# UNIVERSITÀ DEGLI STUDI DI ROMA "TOR VERGATA"

FACOLTA' DI INGEGNERIA

DOTTORATO DI RICERCA IN
MATERIALI PER L'AMBIENTE E L'ENERGIA


XXII CICLO

# EXPLOITING THE PROPERTIES OF MESOPOROUS THIN FILMS


LUCA MALFATTI


A.A. 2009/2010


Docente Guida/Tutor: Prof. Plinio Innocenzi

Coordinatore: Prof.ssa Silvia Licoccia

# Abstract

Questa tesi di dottorato si pone l'obbiettivo di esplorare le potenzialità offerte dai film sottili mesoporosi. Questi sistemi, infatti, offrono la possibilità di modulare molte delle loro caratteristiche più peculiari come la composizione chimica delle pareti dei pori, la struttura dei pori e la loro organizzazione e sono inoltre eccellenti matrici per strutture *host-guest*. Inizialmente, sono stati svolti diversi esperimenti *in-situ* durante l'auto-organizzazione dei film per indagare alcuni aspetti fondamentali di tale processo e per studiare le proprietà chimico-fisiche delle pareti dei pori. In seguito, sono state sfruttate le proprietà di questi materiali attraverso la funzionalizzazione delle loro strutture porose con coloranti, molecole organiche fotoattive e complessi inorganici. E' stata anche testata la possibilità di utilizzare i pori come stampi monodispersi per la sintesi di nanoparticelle metalliche. Grazie all'elevata area superficiale e ad una particolare composizione chimica delle pareti dei pori, sono stati realizzati film mesoporosi a base di ossidi misti con proprietà ottiche modulabili. Infine, si è cercato di indurre più di un grado di auto-organizzazione all'interno dello stesso materiale per realizzare film a porosità gerarchica. Tre diverse strategie sono state impiegate per ottenere simultaneamente una macro- e una meso-porosità: stampaggio diretto con nanoparticelle fluorurate, separazione di fase controllata mediante l'aggiunta di un agente co-stampante e cristallizzazione controllata di un sale inorganico. I risultati presentati in questa tesi di dottorato dimostrano la versatilità dei sistemi mesoporosi per la realizzazione di materiali avanzati funzionali con un'ampia varietà di proprietà chimiche e morfologiche.

# Abstract

Mesoporous materials show the possibility to tailor several of their characteristic features such as pore structure and arrangement, chemical composition of the pore walls, and, in addition, are excellent matrixes for host-guest systems. This doctoral work explores many of the potentialities offered by mesoporous thin films to produce advanced functional materials with a wide range of tunability in terms of properties and morphology. The first aim was to promote a basic study of self-assembly by *in-situ* experiments to reveal some fundamental aspects of the process and some chemical-physical properties of the pore walls. Then, a full set of experiments was dedicated to exploit the mesoporous materials by functionalizing their porous structures with dyes, organic photoactive molecules and inorganic complexes. The pores were also used as a nanoreactor for controlled growth of metallic nanoparticles. Mesoporous mixed oxides films with tunable optical properties were obtained by using the high surface area and controlling the chemical composition of the pore walls. Finally, the possibility of inducing more than one degree of self-organization in the same material, to design hierarchical porous films, was also explored. Three different strategies were used to obtain macro- and meso-porosity, which include direct templating with fluorinated nanoparticles, controlled phase separation using a co-templating agent and controlled crystallization of an inorganic salt.

# Index

# List of Symbols and Abbreviations

| | |
|---|---|
| AFM | atomic force microscopy |
| BuOH | butanol |
| CCD | charge-coupled device |
| *cmc* | critical micelle concentration, |
| CTAB | cetyltrimethylammonium bromide [$C_{16}H_{33}(CH_3)_3N^+Br^-$] |
| DHT | delayed humidity treatment |
| DTGS | deuterated triglycine sulfate |
| EISA | evaporation-induced self-assembly |
| EtOH | ethanol |
| FEG | field-emission gun |
| FE-SEM | field-emission scanning electron microscopy |
| FIR | far infrared spectroscopy |
| FTIR | Fourier-transform infrared spectroscopy |
| FWHM | full width at half maximum |
| GISAXS | grazing incidence small-angle X-ray scattering |
| LC | liquid crystalline |
| MCT | mercury cadmium telluride |
| MCM | Mobil composition of matter |
| MRI | magnetic resonance imaging |
| MTES | methyl-triethoxysilane [$CH_3Si(OCH_2CH_3)_3$] |
| MW | molecular weight |
| NBB | nano-building block |
| NCS | nanoparticles colloidal solution |
| NMR | nuclear magnetic resonance |
| PEO | polyethylene oxide |
| PPG | polypropylene glycol |
| PPO | polyisoprene |
| PS | polystyrene |
| RH | relative humidity |
| Rh6G | rhodamine 6G |
| SA-XRD | small angle X-ray diffraction |

| | |
|---|---|
| SAXS | small-angle X-ray scattering |
| SDS | sodium dodecyl sulfate |
| SEM | scanning electron microscopy |
| TEM | transmission electron microscopy |
| TEOS | tetraethoxysilane [$Si(OCH_2CH_3)_4$] |
| THF | tetrahydrofuran |
| TIPB | triisopropylbenzene |
| TLCT | true liquid crystal templating |
| TSS | tunable steady state |
| UV | ultraviolet |
| VAE | vacuum-assisted evaporation |
| WA-XRD | wide angle X-ray diffraction |
| XPS | X-ray photoelectron spectroscopy |
| XRD | X-ray diffraction |

# Chapter 1:
# Introduction to mesoporous thin films

This first part is dedicated to a basic introduction of mesoporous materials with a particular attention to thin films. The purpose of this chapter is not to provide a complete and exhaustive perspective on the wide and fascinating “meso-world”, but to give some essential tools to the readers that are not familiar with this topic. The first section is dedicated to a really condensed history of mesoporous films, starting from the first discovery of a mesoporous materials. Then, the Section 1.2 explores the most important technique, at least from the viewpoint of published works, used to produce mesoporous films: the evaporation induced self-assembly. To allow a better reading, this part is divided in several paragraphs analysing the most crucial parameters to control the self-assembly process. The third section is dedicated to an overview on the concept of order in mesoporous silica films. The order is analysed as a morphological aspect, then in relation with the synthetic pathways, and finally in correlation with the material properties. Furthermore a brief part is dedicated to non-siliceous systems, which are knowing a growing interest due to their stability in water, their enhanced mechanical resistance and their functional properties in the pore walls. The Chapter 1 closes with an outlook on the future perspectives of self-assembly, in particular some future developments and applications of mesoporous materials are described.

## 1.1 Mesoporous films: a brief chronology

Periodically ordered mesoporous [*] materials are a notable example of functional materials which recently aroused a great interest due to their interesting features, such as extremely high specific surface area, possibility to tailor pore size and geometry and to functionalise the pore surface. Mesoporous materials are obtained by the templated self-assembly of inorganic nano-building blocks and an organic phase, such as low-molecular weight surfactants or amphiphilic block copolymers. At first, a periodic ordered structure is created in the inorganic matrix by organic self-assembled micelles, afterwards the micelles are removed by thermal treatment to yield an ordered mesoporous structure. Mesoporous materials are characterised by the presence of ordered porosity in the 2 to 50 nm range (**Figure 1.1**) and they can be reproducibly synthesized in a variety of shapes (thin or thick films, membranes, powders, microspheres) and compositions (silicates, transition metal oxides, etc.). These systems are extremely interesting from a technological viewpoint due to the very high specific surface area (as much as $\approx 1000\ m^2 \cdot g^{-1}$) and the possibility to tune important parameters such as pore size and shape, pore accessibility, etc.

The first family of mesoporous materials, M41S, were synthesised by a Mobil Oil research Group in the form of powders through precipitation mechanism, at that time this represented an adequate solution in applications such as catalysis and sorption, for which they were invented[2,3]. From the first application, mesoporous materials were used in all technological fields where ordered nanometric porosity and high specific surface area were crucial. After few years, the synthesis of mesoporous films opened the way to new advanced applications for which powders were unsuitable. The first self-supporting mesoporous films appeared between 1994 and 1996. These first syntheses consisted in

[*] According to IUPAC classification[1] porous solids fall into three categories depending on the pore size, $d$: microporous ($d < 2$ nm), mesoporous (2 nm < $d$ < 50 nm) and macroporous ($d > 50$ nm). Microporous and mesoporous materials are generally referred to as nanoporous materials, which fall into the general class of nanostructured materials, since they possess features (pores) which are defined on the nanoscale. The distinction between the attributes mesoporous and mesostructured is not univocal. Whereas in the literature "mesoporous material" univocally refers to the presence of porosity in the 2–50 nm range, the term "mesostructured material" is less clear, referring to either "a mesoporous material with ordered disposition of pores" or "a material containing an organic mesophase in the 2–50 nm range". In the former case "mesostructured" is a special case of "mesoporous" where the pores are ordered, whereas in the latter case "mesostructured" means "containing a mesophase". In this thesis we follow the latter case, therefore we define a "mesostructured material" as a material containing a (organic) phase in the 2–50 nm range. In this sense, the synthesis of a mesoporous film proceeds through the formation of a mesostructured film, which is then submitted to a treatment in order to remove the mesophase, yielding mesoporosity.

the precipitation of the precursors at the solution air interface, involving transport of the precursors in the liquid phase towards the interface.[4,5] Supported mesoporous silica films were also grown on a substrate immersed in a solution with high surfactant concentration by a so-called *True Liquid Crystalline Templating* approach.[6]

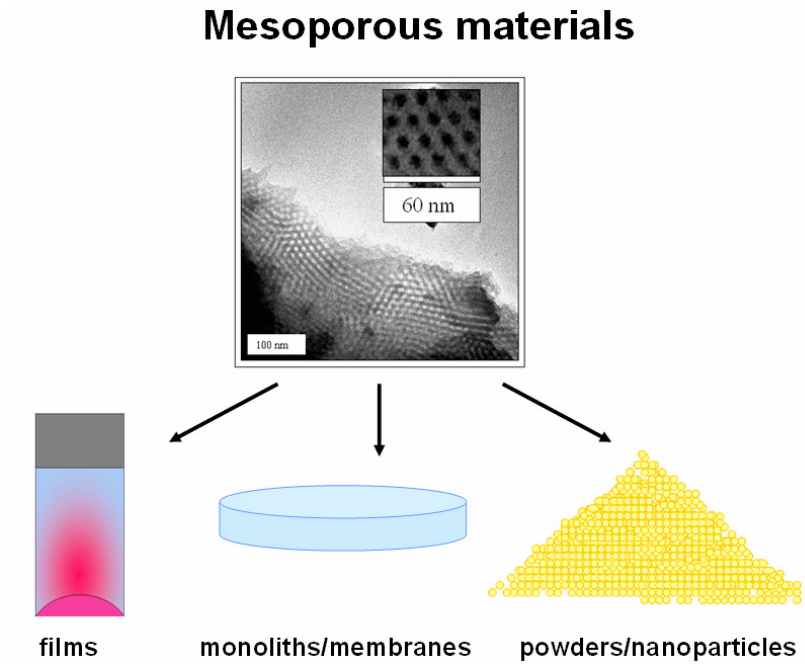


Fig. 1.1 Transmission electron micrograph of a mesoporous material (upper image). These materials can be prepared under different sizes and shapes depending by the purposes (lower images).

Growth and coalescence of the solid phase on the substrate occurs on a time scale between few hours and several weeks. However, the films prepared according to these procedures are inhomogeneous even on a micron scale and have a bad optical quality, which makes them unsuitable for advanced applications. In 1997, Lu et al. obtained mesopores with 2d-hexagonal and cubic phases in silica films prepared by dip-coating.[7] Here, surfactant concentration was lower than *critical micelle concentration* (*cmc*[†]), and self-assembly occurred as a consequence of solvent evaporation which progressively increased the non-volatile species concentration.

The idea of using a very dilute solution, where the concentration $c_0 < cmc$, was developed in the same research group at the Sandia National Laboratories (US) and is the basis of the most widely employed technique, to date, in the synthesis of

[†] The critical micelle concentration is defined as that concentration about which the surfactant molecules in solutions undergo a nanophase segregation process in order to minimise the free Gibbs energy, forming supramolecular aggregates called *micelles*.

mesoporous films: *evaporation-induced self assembly* (EISA). This definition was coined by Brinker and coworkers in 1999 to indicate a new synthesis process where mesophase formation is triggered by solvent evaporation rather than precipitation reactions.[8]

If it considers the publications on mesoporous films, it can note that siliceous systems constitute the largest part. The reasons are manifold: first, there is a historical reason, as many researchers come from the zeolite world and as they are much more familiar with the silicon and the aluminium chemistry rather than transition metal chemistry. Second, silica films obtained by sol-gel routes are less problematic with respect to other oxides, because the self-assembly process can be controlled more easily due to low hydrolysis-condensation rates of silica precursors (e.g. alkoxides, chlorides). Transition metal precursors are more prone to hydrolysis, redox reactions or phase transitions involving thermal breakdown of the structure, which makes much more difficult to remove the template and create an ordered mesoporosity maintaining the optical quality of the film.[9] Third, the stability of the Si-C bond opens several perspectives on hybrid organic-inorganic materials[‡], as well as on the possibility of grafting a number of chemical functionalities on the mesopore surface due to the presence of Si-OH groups.

Despite the higher complexity of the synthesis, mesoporous materials based on transition metal oxides are recently attracting an increasing interest because of their particular optical, electronic and magnetic properties (e.g. high refractive index, semiconductivity, photocatalytic properties).[10,11]

[‡] A material is defined as *hybrid* if it includes two types of functions bonded at molecular scale; one of the two is organic while the other is inorganic. These materials are proved to be very versatile because of the wide combinations of functions they can contain and their improved thermal and mechanical stability. Hybrid material can be also divided in two sub-classes: *class I* if the interactions between organic and inorganic components are weak (such as hydrogen bonding, Van-der-Waals interactions, etc.) and *class II* if the interactions are strong such as covalent or coordination bonds. An as-deposited mesostructured film belongs to the first class while an ordered porous film with organic functionalities attached to the pore surface belongs to the second class.

## 1.2 Evaporation-Induced Self-Assembly

The starting point in the EISA technique is the preparation of a dilute solution containing the inorganic precursors (generally a metal/metalloid alkoxide or salt) and the organic templating agents (surfactant or macromolecular amphiphilic block copolymers). The solvent is an alcohol (generally ethanol or methanol) and small amounts of water may be added. EISA is most often used in combination with the dip-coating deposition technique (or, less frequently, with spin-coating). In dip-coating, a substrate is dipped into the solution and extracted at a constant speed (typically, few $mm \cdot s^{-1}$). Due to the solution-substrate wettability, a liquid layer is formed on the substrate, whose thickness depends on the extraction speed and the viscosity of the solution.

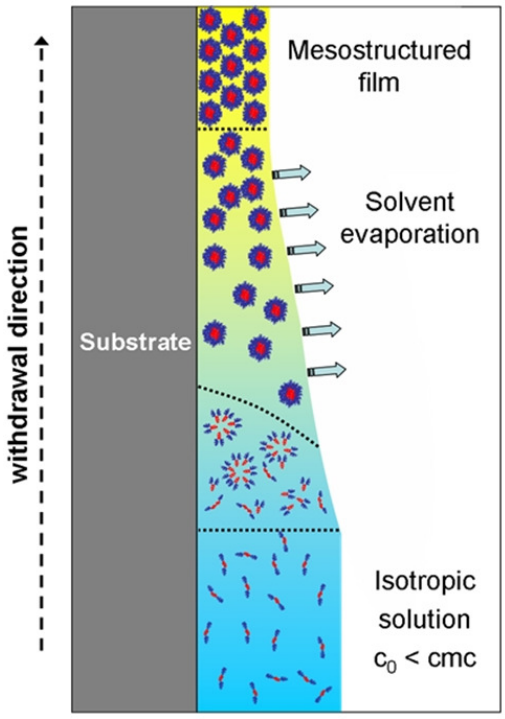


Fig. 1.2 Scheme of the formation of a mesostructured film by evaporation-induced self-assembly. The arrow indicates both the time line and withdrawal direction. In the isotropic solution, condensation is slowed down and the non-volatile precursors are free surfactant molecules and inorganic oligomers. During dip-coating, solvent evaporation triggers the formation of surfactant-inorganic units. When evaporation is complete, the film equilibrates its water content with the environment (tunable steady state, TSS). A final thermal treatment stabilises the mesostructured film.

As the solvent evaporates from the liquid layer, the inorganic precursors undergo condensation and crosslinking processes, thus forming a gel, which can be defined as a phase constituted by a more or less condensed inorganic network within which residual solvent molecules form an interconnected liquid phase (see **Figure 1.2**). In spin-coating, few drops of the precursor solution are placed on a substrate, which is then spinned at a constant angular speed (typical values: few thousands of revolutions per minute, rpm). Thus, a homogeneous film is spread on the substrate due to the centrifugal force. Because in this doctorate work mesoporous films are prepared exclusively by dip-coating (as in most works in the literature), hereafter we will refer to this deposition technique.

In the EISA technique, solvent evaporation occurring in the first seconds after deposition causes an increase in the concentration of non-volatile (organic and inorganic) species in the film. This triggers both self-assembly and inorganic crosslinking, which therefore act concurrently. Thus, evaporation is not the driving force for self-assembly as such, but rather keeps the system on a pathway where self-assembly can occur during film formation. A more thermodynamic synthetic control allows for the formation of better ordered mesostructures, whereas an increasing kinetic control leads to the formation of ill-defined or disordered mesostructures. The complexity and the rapidity of the concurring phenomena during solvent evaporation justify what can be defined as "race towards order": therefore, it is a sort of challenge in that the organic phase must form an ordered self-assembled mesophase before inorganic polycondensation stops it. That is why one needs to decrease inorganic reactivity, for example adjusting the pH near to the isoelectric point (e.g. in the case of silica alkoxide precursors) or using complexing agents (e.g. in the case of titania) and working in dilute conditions. EISA is a technique that can be readily adapted to perform these tasks: the chemical composition and the processing parameters can be adjusted in order to form well-ordered mesostructures, as well as to obtain the properties that are required for functional applications (i.e. homogeneity, transparency, etc.). Besides, EISA can be used in such different preparation processes based on solvent evaporation (e.g. dip- and spin-coating,[8] inkjet printing,[12] aerosol[13]) and self-assembly can be tuned by a careful control of the solvent evaporation process.[14] In this way, mesoporous materials in forms other than films can be prepared (e.g. mesoporous micro- and nano-spheres,[13,15] monolayers,[16,17,18] nanoscale islands[11]). Thermal treatments can follow the deposition step in order to promote further condensation, mechanically stabilise the mesostructure

and remove the surfactant. Further operations that may be performed on films include chemical grafting of functional groups or molecules on the mesopore surface to change the physicochemical properties (e.g. grafting of fluorinated groups in order to increase hydrophobicity) or the functional properties (e.g. inclusion of metallic or semiconductor nanoparticles within the mesopores for non-linear optics, photocatalysis and sensing[19,20,21]).

To sum up, mesoporous films prepared by EISA require an adequate composition of the initial solution (inorganic precursors, templating agents, volatile media), the organization can be achieved by controlling the evaporation rate and the physicochemical and functional properties can be created or tuned by a thermal treatment or chemical post-synthesis modification. As a consequence, a reproducible synthesis of mesoporous materials via EISA requires control on three levels: (1) chemical composition of the precursor solution, (2) deposition process, (3) post-treatments performed on the film.

### 1.2.1 Solution of precursors

A careful design of the solution of precursors is fundamental to obtain a highly degree of organization in the self-assembled materials. It is therefore very important to know the roles of the principal components of this mixture: solvent, inorganic precursors, templating agent, water and catalyst.

*- Solvent*

The choice of solvent has to meet at least three requirements: the solution has to completely wet the substrate in order to ensure good film homogeneity; furthermore, the solvent must be volatile to promote a fast increase in concentration of the non-volatile species; and it should be a good solvent for the organic and inorganic precursors. Generally, ethanol is the preferred choice, as it can wet both hydrophilic and hydrophobic substrates, it is volatile, and it can easily dissolve amphiphilic block copolymers as well as inorganic alkoxides and metal salts.

*- Inorganic precursors*

Inorganic precursors alkoxysilanes such as tetraethoxysilane (TEOS) are widely employed in the synthesis of mesoporous silica. Small quantities of an organically-

substituted alkoxysilane, called organo-alkoxysilane, may be added to TEOS. In organo-alkoxysilanes one or more hydrolysable groups are substituted by organic groups which are not hydrolysable due to the high stability of the Si-C bond. Therefore, these organic groups eventually end up covalently linked to the final inorganic framework, and a wide variety of mesoporous or mesostructured hybrid organosilica products can be obtained.[22] Inorganic reactivity can be controlled by varying the pH. This is most clear in silicon alkoxides: less ordered mesophases are obtained at high pH values (5–7), where condensation is fast and prevails over mesostructure formation. A low pH favours hydrolysis and inhibits condensation, therefore permitting a better mesostructure organisation. Working in high dilution conditions, silica condensation is further inhibited and the solution is very stable in time (up to several months). Transition metal alkoxides are much more reactive, according to the series: $Si(OR)_4$ < $Sn(OR)_4$ < $Ti(OR)_4$ < $Zr(OR)_4$ < $Ce(OR)_4$.[23] This is because the reactivity of transition metal precursors is strongly dependent on the electrophilicity of the metal centre (hydrolysis and condensation proceed through nucleophilic attack by water molecules), therefore the reactivity trend is Si < Ti < Zr < Hf.[24] Condensation can be inhibited by introducing complexing agents, such as acetyl acetone, which are effective in sequestering the transition metal ion.

*- Templating agent*

The choice of type and quantity of templating agent has shown to be a key parameter to obtain a final mesostructure with a given symmetry. Both ionic or non-ionic surfactant can be used to induce self-organization. To the first class belong surfactants such as cetyltrimethylammonium bromide (CTAB) or sodium dodecyl sulfate (SDS); to the second class, diblock or triblock copolymers such as Brij or Pluronic type. In particular, for non-ionic surfactant, the size, architecture and chemical composition of the amphiphilic block copolymers deeply affect the final mesostructure. In this doctoral work a particular type of block copolymer with a commercial name of Pluronic F127 has been used. This polymer is formed by one core made by poly-oxypropylene (PPO) and two tails of poly-oxyethylene (PEO) having the following chemical formula $EO_{106}$–$PO_{70}$–$EO_{106}$.

When an ionic surfactant is used, the geometric packing factor $g$[‡] can predict whether high-curvature cubic or low-curvature 2d-hexagonal mesostructures will form. A calculation of the quantity to be introduced into the precursors solution can be made by inspection of the surfactant/water phase diagram, considering the surfactant volume fraction

$$\Phi = V_{surf} / (V_{surf} + V_{inorg}) \quad (1.1)$$

This formula is a good predictive model that allows calculating the quantities of inorganic and organic precursors to mix into the solution in order to reach a given mesophase symmetry, in line with the phase diagram approach of true liquid crystals templating. However, a work on oriented silica membranes templated by Pluronic F127[25] has revealed that wormlike or hexagonal phases can be obtained in conditions where cubic phases are expected ($\Phi < 70\%$). In these "silicatropic" hybrids, the final mesostructure can be tailored by the water content in solution, keeping $\Phi$ constant. The crucial role of water can be rationalised in this way: $\Phi$ is not the only parameter that directs mesophase formation, as the extent of the silica-template interface should be taken into account. Water helps to fold the hybrid interface with a higher curvature radius,[26] and also generates more hydrophilic silanol ends; a more hydrophilic hybrid interface tends to maximise interactions with the hydrophilic parts of the micelles and enhance curvature. Therefore, the final mesophase symmetry cannot be predicted only on the grounds of the inorganic-template fraction ($\Phi$), thus predictions made purely with phase diagrams may be misleading and care should be exerted when using this model.

It has been demonstrated[27] that in the case of films $V_{inorg}$ should take into account also the presence of water as relative humidity in the deposition chamber, beside water contained in the precursor solution. In fact the amount of relative humidity is crucial in determining mesostructure formation, in that it can diffuse from the environment into the film, affecting the interactions at the hybrid interface and exerting a critical role on micelle curvature. Furthermore, the presence of additives or solvents other than those reported in the phase diagrams can influence the chemistry of these systems, and mesophase symmetries different than those reported in the phase diagram have been reported. For example, mesoporous silica films with a rhombohedral $R\bar{3}m$ symmetry

‡ The packing factor $g$ correlates the structure of the surfactant with the resulting aggregate morphology. If we consider the surfactant as formed by hydrophilic head and an hydrophobic tail, $g$ can be defined as the volume of the hydrophobic tail divided by the product of its maximum length with the area of the hydrophilic head.

have been obtained from a solution containing TEOS and CTAB to which 1,3,5-triisopropylbenzene (TIPB) was added.[28] $R\bar{3}m$ structures in mesoporous $TiO_2$ have been obtained using 1-butanol as the solvent: this enhances microphase segregation increasing the curvature at the hybrid interface, because the polar end of 1-butanol is reported to be localised at the hydrophilic/hydrophobic interface between the poly(ethylene oxide) and poly(propylene oxide) blocks, thereby helping to stabilise the mesophase with the required surface curvature.[29] Another factor that has to be kept in mind is that EISA synthesis conditions are dramatically affected by kinetic factors, whereas a phase diagram refers to a system in its thermodynamic equilibrium. Polycondensation increases film viscosity and reduces micelle mobility, therefore the mesophase in a film is typically in a metastable state, out of thermodynamic equilibrium. To summarise, the synthesis parameters that are used to predict mesophase symmetry can be overwhelmed by other factors (e.g. water content in solution, relative humidity, evaporation rate, presence of a solvent with different polarity) that force the structure into an unpredicted phase.[30] In practice, the molar ratio $s$ = [surfactant]/[inorganic] is generally reported in research works rather than the surfactant/inorganic volume fraction. In fact, $s$ is considered more as a heuristic parameter, often determined through educated guesses in a trial-and-error fashion, where different quantities of surfactant are systematically varied, and the characterisation of the films thus obtained are used as a feedback to formulate a "working recipe". The $s$ values are on the order of magnitude of 0.01 for ionic surfactants (e.g. CTAB), whereas for high MW block copolymers (e.g. Pluronic type) they can be as low as $10^{-3}$ or $10^{-4}$.

- *Water*

Water is a truly multipurpose component of the precursor solution. In silica-based systems it takes part in alkoxide hydrolysis and condensation. For small values of $h$ =[$H_2O$]/[Si], no mesostructure or a wormlike mesophase is obtained, whereas too high $h$ values may lead to uncontrolled condensation and poor order. A typical value found in the synthesis of silica is $h$ = 5–10, which is relatively independent of the type of inorganic precursor (a silicon alkoxide or a salt). Water molecules are adsorbed on the hydrophilic crown of the micelles, increasing the hydrophilic headgroup area and thus decreasing the geometric packing factor $g$. In this way an increase in hybrid interface curvature is observed and the formation of spherical micelles rather than cylindrical is favoured. Besides, water favours the formation of silanols at the hybrid interface which

contribute to strengthening the interactions between inorganic precursors and surfactant. In general, the role of water at the hybrid interface is of key importance in the synthesis of all mesostructured films. A notable example is mesostructured $TiO_2$ obtained from $TiCl_4$, where the presence of significant amounts of water is essential in order to form an ordered mesostructure. In this system, water can be supplied either by direct adding to the precursor solution, either by treating as-deposited films with high relative humidity for a short time since solvent evaporation.[31,32] At least three effects can be discerned: (1) water promotes Ti(IV) hydrolysis and favours the formation of hydrophilic species such as $TiCl_{4-x}(OEt)_x$.[26] (2) Water favours phase separation by increasing the entity of the interactions at the interface, swelling the hydrophilic corona, thus increasing its curvature. (3) Water lowers viscosity acting as a lubricant by forming a layer around each micelle, permitting structural rearrangements in the mesophase which lead to a better degree of order.[27]

- *Catalyst*

When an alkoxide is used as the inorganic precursor, a catalyst increases the kinetics of hydrolysis or condensation. There is a fundamental difference between basic and acid catalysts, in that the former favour hydrolysis and inhibit condensation, whereas the latter favour condensation and inhibit hydrolysis.[33] In the synthesis of mesoporous films, an acid catalyst is generally used, as it ensures good quality and homogeneity of the film. In particular, HCl is the choice in most cases as its high volatility ensures full evaporation once its function is not required any more and therefore it does not remain in the film as impurity. Furthermore, its evaporation causes the pH inside the film to increase, which favours condensation reactions, stiffening the mesostructure. When transition metal salts are used as the inorganic precursors, the presence of $Cl^-$ ions in the solution controls condensation kinetics by forming coordinated species, e.g. $TiCl_{4-x}(OEt)_x$. After deposition, hydrolysis and condensation are accelerated by HCl evaporation.[34] In the case of silica, pH is generally set near the isoelectric point, which is defined as the pH of a solution or dispersion at which the net charge on the macromolecules or colloidal particles is zero ($pH_{iep} \approx 2$ for silica, $pH_{iep} \approx 6$ for titania): in this way, the inorganic colloids in the solution do not aggregate, and the solution can be stable even for several months.

Once the chemical design of the solution of precursors has been selected, it remains to choose the right ageing of the mixture. In fact experimental results have demonstrated

that ageing is a critical parameter which can affect deeply the degree of order of the final mesostructure. This is due to the hydrolysis and polycondensation reactions of inorganic precursors that cause the formation and growth of oligomeric species (nanobuilding blocks, NBBs). In the case of silica, these can be constituted by cyclic, linear or branched structures, depending on the composition and pH. The size of these oligomers increases as a function of time. Because the size of these NBBs is critical in mesostructure formation, it is of crucial importance to control ageing of the coating solution (at a first approximation, ageing can be identified as the time interval between preparation of the solution and its use in the dip-coating). Structural information on silica oligomers can be inferred from $^{29}$Si NMR measurements on solutions containing the EISA precursors aged for different times, by relating the observed chemical shift to the number of O atoms to which a Si atom is bonded. The notation $Q_i$ is generally adopted, where i represents the number of O atoms bonded to a single Si atom and $0 \leq i \leq 4$. Grosso et al. have observed a trend in $Q_i$ concentration depending on the solution (TEOS, CTAB, HCl, $H_2O$ in EtOH) ageing time[35] (**Figure 1.3**).

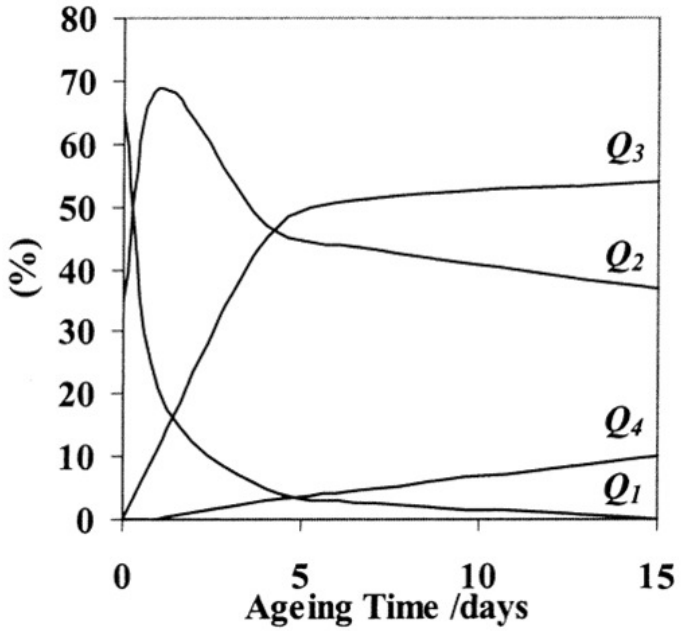


Fig. 1.3 Ageing time dependence of the relative amounts of $Q_1$, $Q_2$, $Q_3$ and $Q_4$ silica species in a solution containing CTAB/TEOS = 0.10. These evolutions were deduced from the $^{29}$Si liquid-phase NMR spectra by integrating and adding $Q_i$ peaks. Reproduced from ref. 35.

.

This trend was compared to the degree of order of the final mesostructure in films obtained by dip-coating with the aged solutions, which was estimated by the intensity of the main low-angle X-ray diffraction peak. The most ordered mesostructures are observed when the concentration of $Q_2$ and $Q_3$ is highest, corresponding to an ageing time of 6–7 days.[36] If ageing is either shortened or protracted, the resulting mesostructure is less ordered or absent. Too long an ageing leads to the formation of large silica oligomers that are not capable of accommodating the curvature at the hybrid interface during mesophase formation, whereas too short an ageing does not result in the formation of well-defined NBBs, which again leads to poor order. Most likely, the NBBs cannot exceed the feature size of a mesostructure, typically 1-20 nm. Optimal ageing times strongly depend on solution composition as well as its temperature. For a similar TEOS/ CTAB / EtOH system but with a higher [$H_2O$] / [Si] ratio and a lower [EtOH] / [Si] ratio, Klotz et al. estimate an optimum ageing time of 200 minutes, which is lower of a factor of 50 than that reported by Grosso.[36]

In short, controlling ageing permits controlling the size of the NBBs that build up a hybrid interface, thus it turns out to be a key requisite in the design of a synthesis process. For each system, an optimum ageing time must be determined, depending on the type and concentration of surfactant, water and inorganic precursor.

### 1.2.2 Film deposition

Whereas control of the precursors solution requires understanding the chemistry of the inorganic species and the self-assembly properties of the surfactant, in the deposition process control is transferred to the external conditions. The deposition step is no less critical than the preparation of the precursor solution, because in this stage inorganic condensation and self-assembly take place, driven by the local thermodynamic and kinetic conditions and ultimately triggered by the fast evaporation of the solvent.

It has been suggested that the depart of solvent from the film-air interface causes an increase in concentration of the inorganic and the organic non-volatile species, which undergo self-assembly and condensation reactions and form a mesostructure. As the rate of evaporation is faster at the film-air than at the film-substrate interface, non-volatile species become more concentrated in the former than in the latter regions, triggering diffusive processes due to the concentration gradient within the film. Therefore, while solvent evaporates, the composition of the film is not univocally determined, but rather

there exist several compositions in different regions, which constantly evolve with time until most solvent is evaporated (typically within 10–30 seconds). Though it is practically impossible to calculate the exact composition as a function of space and time; there is one phenomenon that can give insight on what occurs within the film during the evaporation process: mesophase transition. Performing *in situ* small angle X-ray scattering (SAXS) measurements during dip-coating, one can obtain a time-resolved sequence of diffraction patterns which inform on the structural evolution of the forming mesophase. The sequence: lamellar phase → 3d hexagonal → cubic is typically observed, corresponding to the sequence: isotropic → spherical micelles → cylindrical micelles → lamellar phase observed in the surfactant/solvent phase diagram for increasing concentrations.[37] Different mesophases can be obtained by varying solvent evaporation rate: in an interesting study, a vacuum pump was connected to a cylindrical pipe sitting at given distances from a substrate covered with the desired solution, which was let to evaporate. By varying the pipe-to-sample distance, it was possible to adjust the evaporation rate of the liquid film (this procedure is called "vacuum-assisted evaporation", VAE).[38] For high evaporation rates, the simultaneous presence of different mesophases can be observed, an effect that can be ascribed to different compositions at different depths caused by high concentration gradient: since evaporation occurs at the film-air interface, nonvolatile concentration is higher in this region, thus giving an ordered phase sooner than in the region close to the substrate. As different compositions generally correspond to different stable symmetries in the phase diagram, different or overlapped diffraction patterns are observed. Where solvent is less present (close to the film-air interface) inorganic condensation may form a solid barrier that prevents further evaporation, thus multiple mesostructures are likely to be "frozen" in their metastable states. This can explain an aspect that is sometimes observed in transmission electron microscopy (TEM) cross-sectional images of mesoporous films, that is an ordered structure near the surface and a wormlike or totally disordered region within the film (see **Figure 1.9**).

There is evidence for structural rearrangements in the mesophase occurring even long after the solvent evaporation step. Experimentally, *in situ* SAXS measurements pointed out that mesophase transitions can be induced by the external environment well after solvent evaporation, most typically by a variation in relative humidity. Mesophase transitions reflect structural rearrangements in mesophase architecture, which are observed to be reversible as long as the film viscosity is low (i.e. as long as the

inorganic network has a low degree of crosslinking). Therefore, we can identify a time span between film deposition and when inorganic condensation hinders mesophase rearrangements; this latter represents a broad time interval itself since inorganic condensation is a continuous process, in which kinetics varies according to the system in question. One of the most notable examples where this effect is reported is a work by Cagnol et al., who first demonstrated the very important role of water originating from external humidity (relative humidity, RH) in the texturation of the hybrid mesostructure.[39] In this work, the effect of relative humidity during dip-coating was observed and the mesostructure organisation was demonstrated to be affected by the diffusion of volatile molecules equilibrating between the environment and film media. More precisely, high RH (70%) favours the formation of a $Pm\bar{3}n$ cubic phase, whereas low RH (20%) leads to lower quantity of water inside the film, which promotes the two-dimensional hexagonal *p6mm* mesostructure. Too low RH may lead to poorly-defined structures. If RH is sufficiently high, water is encouraged to stay inside the film, or a diffusive motion occurs from the environment into the coating (water is preferentially localised in the hydrophilic part of the film, i.e. on the hydrophilic coronas of micelles and in between). During this dynamic equilibrium state, condensation progressively takes place, stabilising the inorganic framework around the spherical micelles and avoiding further phase transitions when the viscosity is too high. This state of as-deposited mesostructured films is called *tunable steady state* (TSS). This time interval depends on the chemical composition of the film and may last up to few hours. To sum up, we can identify a threefold role of RH: 1) it acts as a swelling agent with respect to the hydrophilic headgroups, thus increasing the micelle curvature and creating a well-defined hybrid interface; 2) it contributes to lowering the film viscosity, acting as a lubricant and favouring mobility of nanobuilding blocks and mesophase rearrangements. This ultimately leads to a better degree of order and sometimes to mesophase symmetries not immediately predicted by phase diagrams: different symmetries can be obtained with different RH values, in particular cubic structure are favoured for high RH. 3) In films obtained from inorganic salts (e.g. $TiO_2$ from $TiCl_4$) the departure of water from the film allows for HCl evaporation through diffusive motion, thus increasing inorganic polycondensation. Because the amount of water in a film depends critically on RH, it is useful to derive a relation between them, especially if an estimation of $V_{inorg}$ is needed in order to calculate the copolymer volume fraction $\Phi$. This is often accomplished by resorting to experimental techniques; unfortunately, the

quantity of matter in films is too low, so determining the total volume fraction of water is a difficult task and other systems than thin films are used. For example, Karl-Fischer titration measurements have been performed on a small amount of solution let to evaporate in the presence of an air flux with a preset RH.[39] Indicatively a correspondence between RH and water content expressed as $h$ = [$H_2O$] / [Si] can be found, corresponding to $h$ = 0.5, 4, 7 for RH = 20%, 40%, 70%, respectively. Another way is to measure the film thickness by ellipsometric spectroscopy at different RH values: the variation in thickness is related to different concentrations of water in the film.[14] Based on these considerations, it is straightforward to conclude that one major key issue is determining the temporal extent of the TSS in order to understand and direct the physicochemical phenomena occurring in this time frame. This is why dip-coaters are generally enclosed in a cabinet or in a glove box, in which air with controlled RH can be fluxed.

The film thickness bears a direct proportion with the speed at which the substrate is extracted from the solution (pulling rate) in the dip-coating process (in spin-coating this parameter is rotation speed, usually expressed in revolutions per minute, rpm). This well-known effect is due to surface tension effects occurring at the solution-film-air interface, which become less critical when extraction speed is increased.[33] In terms of mesostructure order, a lower degree of order is generally observed when extraction speed is increased. This can be explained considering that condensation is faster at the film-air interface: a high concentration gradient is set up and further evaporation from the bottom of the film is inhibited if the topmost layer is too crosslinked.

### 1.2.3 Post-treatment

Post-treatments have the double purpose of promoting inorganic condensation and decomposing the organic phase in order to free the mesopores (calcination). Generally, mild treatments with thermal ramps and steps are preferred: abrupt treatments at high temperatures may cause mechanical stress in the sample which can damage the mesostructure and lead to macroscopic cracking. A phenomenon that is always observed is thermal shrinkage: because the film is pinned to the substrate, the contraction occurs exclusively along the direction perpendicular to the substrate (out of plane), whereas the contraction parallel to the substrate (in plane) is negligible. As a consequence, calcination somewhat alters the shape of mesopores: this is evident in

spherical pores, which become oblate spheroids. In addition, the thermal treatment may lead to the fusion of pores along those crystallographic directions where packing is most dense (e.g. [111] in cubic structures) forming structures that may resemble cylindrical pores when observed with TEM (see **Figure 1.4**). In transition metal oxides, thermal treatment may lead to phenomena related to inorganic crystallisation. This is often a very critical step, in that crystallisation and phase transitions can cause mesostructure collapse, especially if the surfactant is decomposing or has already decomposed: in this case the role of surfactant as a "supramolecular scaffold", ensuring stability while inorganic condensation/ crystallization are in progress. These phenomena can be controlled by performing suitable thermal treatments, and mesoporous oxides can be obtained with nanocrystalline inorganic walls,[29] combining the physicochemical properties of crystalline metal oxides with a high specific surface area.

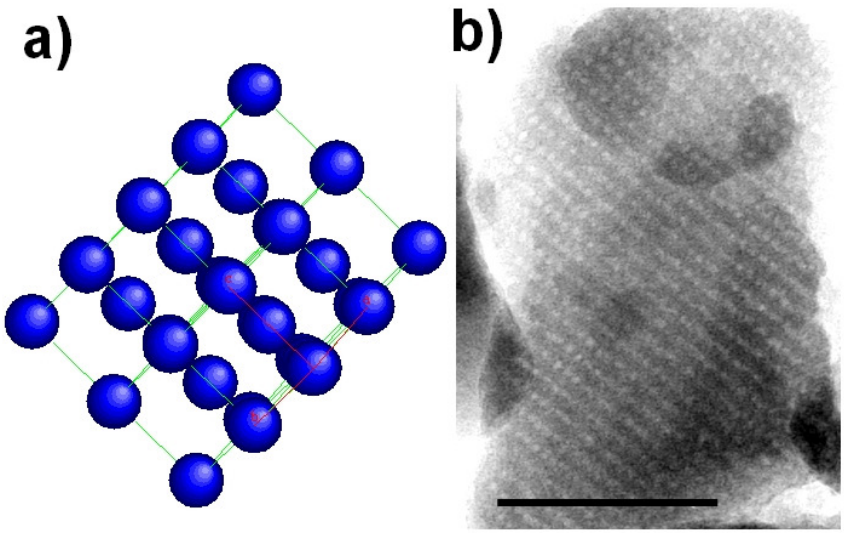


Fig. 1.4 a) Scheme of the stacking pore view from [111] direction. b) Corresponding TEM image showing [111] orientation of the cubic pore system in a F127-silica film. Scale bar represents 75 nm.

*In situ* simultaneous small- and wide- angle X-ray scattering (SAXS/WAXS) experiments using synchrotron radiation have been performed on as-deposited mesostructured titania films[40] and, by using this approach, the mechanisms involved during the thermal crystallisation of mesoporous $TiO_2$ films have been elucidated, casting light on mesostructure formation and inorganic crystallisation. For titania system, the growth of anatase particles was shown to be controllable to prevent mesostructure collapse. In particular, a fast and short treatment at elevated temperature

applied to the cubic initial mesostructure allows rapid growing of the anatase particles up to the limit imposed by the mesostructure. Furthermore SAXS measurements have suggested that pores merge along the directions where the mesopore density is the highest and large single crystallised particles are formed through epitaxial fusion / nucleation.

Recent studies, especially based on transition metal oxides, have underlined the importance of keeping the as-deposited mesostructured films in controlled-RH conditions for a few days before performing thermal treatment.[29] For example, mesoporous yttria-zirconia and ceria-zirconia films with 2d-hexagonal and cubic structures show a relation between mesostructure order and humidity post-treatment.[41] Mesoporous tin oxide films with an orthorhombic F*mmm* symmetry have been prepared by the Hillhouse research group.[42] The as-deposited samples show no long-range order. However, if the films are aged at high RH (≈ 80%) for a time span between 30 minutes and 48 hours, an ordered mesophase appears (a treatment called delayed humidity treatment, DHT). The mechanisms leading to self-assembly have not been fully elucidated. What is sure, is that in this case we cannot speak of EISA, in that solvent evaporation is considered to have ceased when DHT begins, and self-assembly appears to be triggered by some unclear process during DHT itself.

## 1.3 Order in mesoporous silica thin films

This section tackles the concepts behind order and disorder in mesoporous silica films. We have focused on silica because it is the most popular and common oxide to be prepared as mesoporous thin films and it has some peculiar properties that make it a really interesting system to explore order in small scale. Finally, the most part of the experimental work in this thesis is dedicated to hybrid silica-based mesostructured films.

### 1.3.1 Types of order

The first question we have to deal with discussing organization from self-assembly of mesoporous silica films, is what type of order we can obtain. Order is clearly depending on mutual interactions during processing of several parameters, the kind of "chemical-physical" symphony described by Soler-Illia[43]; however at the moment, the scientist-director can only write the music but can not direct the orchestra. Making an *a priori*

prevision of the porous ordered phase[44] is still, in fact, difficult and our ability of producing specific phases largely relies on a trial and error process. Several types of porous structures have been obtained and described by different groups for silica mesostructured films; we can divide the mesophases in two groups of lower and higher symmetry, i.e. two-dimensional (2D) and three-dimensional (3D) phases, respectively. A wormlike disordered phase, with only a local correlation, is also commonly observed as a result of poor ability to self-assemble to an ordered structure; this structure is generally formed when the condensation of the silica backbone is too high or the amount of surfactant too low. Typical 2D structures that have been reported are lamellar[45] and 2D-hexagonal (2D-hex); in general the stability, chemical and mechanical, of the 2D porous phases is much lower than 3D phases but the possibility of orienting the channels of 2D-hex structures make them quite appealing for several applications.

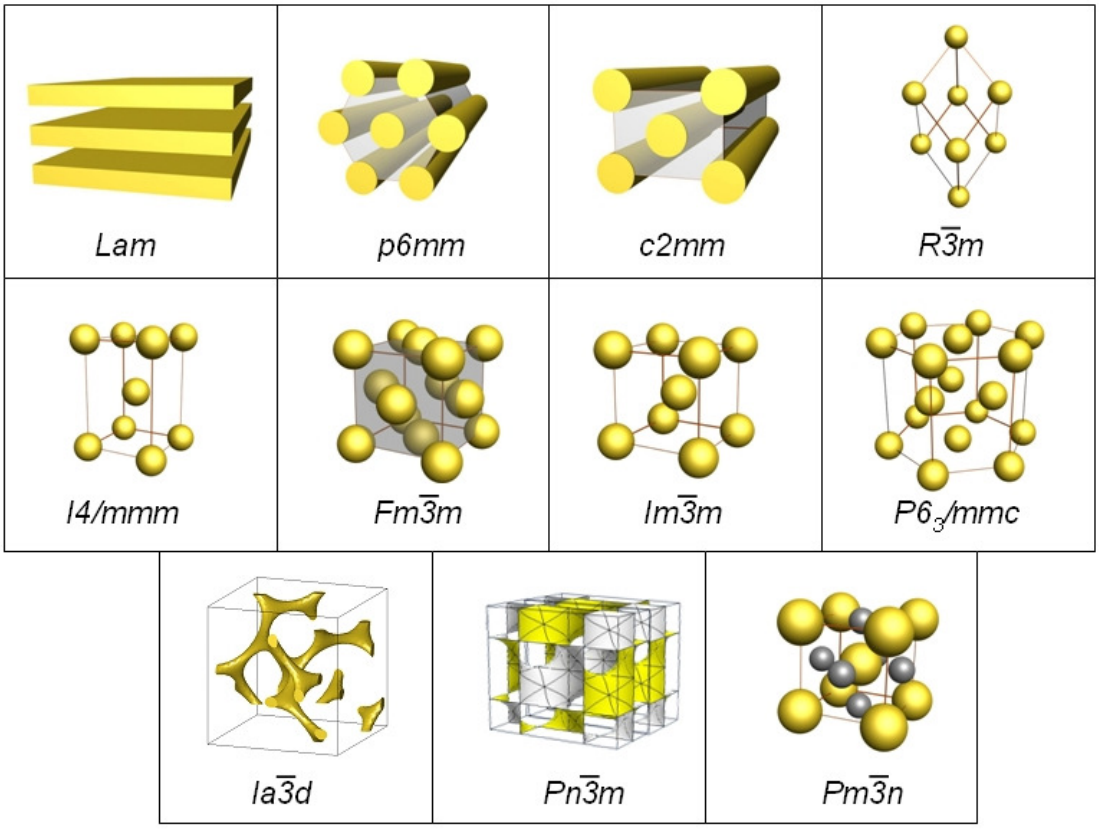


Fig. 1.5 Scheme reproducing the 2D and 3D pore structures obtained in silica mesoporous thin films.

A typical 2D order is represented by the 2D-hex porous phase with hexagonal plane group *p6mm*,[7,46] which, under thermal shrinkage, produces the planar rectangular *c2mm* mesophase. Several types of 3D structures have been also reported for mesoporous silica films: the 3D hexagonal (3D-hex) phase, $P6_3/mmc$ in the space group,[48,49] is one common example. Other cubic structures are formed by different types of cells: a primitive cubic phase, $Pm\bar{3}n$ in the space group;[14,50] bicontinuos cubic, *Pn3m*;[51,52] a body centred cubic phase, ($Im\bar{3}m$);[53,54] a body-centred tetragonal phase ($I\bar{4}/mmm$);[55] a face-centred cubic phase ($Fm\bar{3}m$),[32] rhombohedral $R\bar{3}m$[56] and a double-gyroid cubic phase with space group ($Ia\bar{3}d$).[47,57] The different phases are illustrated in **Figure 1.5**. What will be the degree of organization of the final mesostructure depends on the ability of the micelle to form and organize in a system where the kinetic of the process is a key parameter. The fast evaporation of the solvent induces the micelle formation but the nature of the interface, such as micelle curvature, and the interaction at the hybrid interface has also a predominant role.[58] In general, the difficulty to take into account the multiple effects of the many parameters[59] that have been described to affect self-assembly hampers our ability to predict and control the mesophase that will be formed.[60] The process of organization involves the formation of intermediate species, as it has been shown studying the structural evolution taking place during the processing of silica self-assembled film; the final $Pm\bar{3}n$ cubic structure, for instance, is obtained via the formation of lamellar and hexagonal intermediate structures.[37] The formation of a surfactant concentration gradient, from the air-liquid interface to the film substrate, which is larger in thicker films, is responsible for the presence of the intermediate species[61] and this is the reason why several different phases can be found in the same film. In general the chemical-physical phenomena during evaporation are kinetically controlled[62,63]; a water-surfactant richer liquid-air interface is formed during EISA and this produces different mesophases in the films. However, not only several mesophases can coexist but is even possible to observe one type of mesophase with two well defined preferential orientations. An example that has been reported is the formation of $Pm\bar{3}n$ phases with (211) and (210) orientations together with the mono-oriented *p6mm* mesophase. The presence of epitaxial relationships between the different phases, such as that one between the $Pm\bar{3}n$ and the *p6mm* phases along the (211) and (01) directions, respectively, favours the presence of different phases.[64]

After film deposition, if self-organization has been achieved, a mesostructure is finally formed; however the material is not stable, at least until a thermal treatment has been done to induce a higher degree of condensation in the silica pore walls. The thermal stabilization process produces a film shrinkage in the direction normal to the substrate which can have two different effects on the structure: a distortion of the pore shape, generally from spherical to ellipsoidal and / or a change in the mesophase, i.e. in the pore organization. Even if phase transition of the mesostructure is not observed, a strong distortion of the cell parameters can occur upon shrinkage. However, the phase change has to follow the symmetry rules and only some transitions are allowed; only few of these transitions have been identified, in particular: from an oriented (10) planar hexagonal *p6mm* to an oriented (10) planar rectangular *c2mm* mesophase[36]; from an oriented (110) body centred cubic $Im\bar{3}m$ to an oriented (010) orthorhombic *Fmmm*[54], and from an oriented (111) face centred cubic $Fm\bar{3}m$ to an oriented (111) rhombohedral $R\bar{3}m$ phase.[56] **Figure 1.6** shows a scheme of the transitions that have been described. A systematic study has been done by Hillhouse and cowokers[65] that reproduces the known structures of mesoporous silica films and investigates the change in the mesophase after contraction.

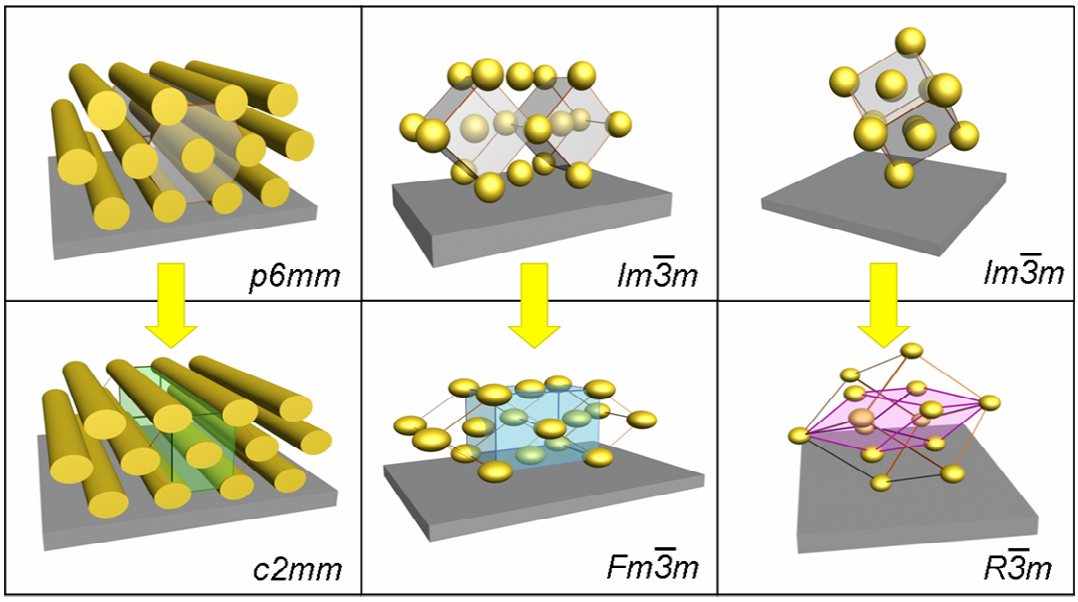


Fig. 1.6 Scheme reproducing the allowed mesophase transitions in ordered mesoporous silica films.

One important observation from this work and from a comparison of the data in literature is that not all the known pore topologies can be obtained from the same type

of surfactant even if different surfactants can produce the same mesophase. This is an indication that if we were able to keep constant all the other variables during EISA processing, the curvature of the micelle and the interactions at the interface would have the key role to control ordering. The structure that is obtained at the end of EISA processing[58] is the product of an allowed transition between different porous phases that is thermally induced on the mesophase. The possibility to change the organization in mesoporous films upon external intervention is one of their most striking properties. As said before, until the structure is not finally condensed and rearrangement of the micelles is allowed, the film remains in a kind of tunable state and the organization can be controlled even in a reversible way. In particular the film mesostructure can be modulated by changing the relative humidity in the deposition room.[39] The water absorption induces a micelle swelling and promotes a change in the micelle organization, if the silica backbone is still enough compliant to allow these transitions. Besides, the tunable steady state allows film patterning by specific lithographic techniques that are based on mesophase change induced immediately after film deposition.[66] An example is the hexagonal-to-tetragonal phase transformation observed in photosensitive silica mesoporous films after UV illumination observed by Brinker and co-authors.[67]

EISA is not the only method to obtain ordered porous oxide films, it is possible somehow to reverse the approach and use a pre-ordered template film instead of trying to obtain order during processing. This method has been proposed by Watkins et al. that have used selective deposition of silica in a block copolymer film dialyzed by supercritical carbon dioxide.[68] Unlike EISA, this strategy allows pre-organization of the template by decoupling the metal-oxide condensation and the template self-assembly. Mesoporous silica films with well ordered nanochannels oriented parallel to the substrate have been also produced by this method.[69]

### 1.3.2 Defects at the mesoscale order

*- Point defects and linear defects*

We have seen that several types of porous structures can be obtained and it is also possible to identify a unit cell of specific dimensions which generates a three-dimensional order. In general, the ordered array of pores in mesostructured films is well described in terms of a “crystalline-like” structure; even if the silica films are not

crystalline, they give diffraction patterns when irradiated by X-rays (**Figure 1.7**). This is due to the periodic voids in the amorphous network, or if the material is not calcined, to the periodic contrast in the electronic density in correspondence of the surfactant periodic array.[70] However in the case of mesoporous ordered materials the dimensions of the unit cells are quite large in comparison with ordinary crystalline materials; instead of a lattice of atoms (0.1 - 0.2 nm), there is an ordered structure of pores and walls (both in the 2 - 6 nm range) and consequently the lattice parameters are in the order of 4 - 12 nm, which is much higher than the typical dimension of a crystalline structure (~ 0.5 nm). If we treat mesoporous ordered materials like crystals, we should also face the presence of several types of defects at different length scale, exactly such as the case of ordinary crystals. At this point it is important to realize that obtaining defects free and monocrystalline-like self-assembled mesostructured films means to deal with the ambitious challenge of mastering a process mainly driven by kinetics. We can analyze the defects starting from point defects, which in crystalline materials are intrinsic defects that must be present on a thermodynamic basis, such as atomic vacancies.

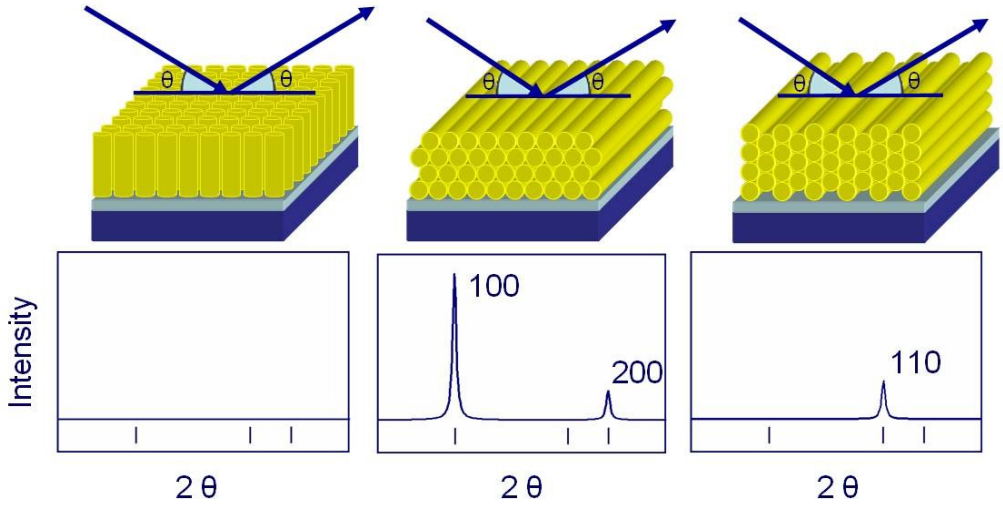


Fig. 1.7 Orientations of 2D hexagonal pore structures (above) and corresponding reflection mode X-ray diffraction pattern (below). Right: mesophase with channels oriented perpendicular to the substrate. Centre: mesophase with channels oriented with the 100 face parallel to the surface. Left: mesophase with channels oriented with the 110 face parallel to the surface.

In mesostructured materials vacancies in the ordered array of pores are not thermodynamic defects and are less common to be observed; nevertheless the defects generated by the coalescence of adjacent micelles, which are often observed in mesoporous materials, can be properly considered point defects. This type of defect is generated during the film formation, when the polycondensation reactions are not completed yet. A direct probe of defects has been realized by applying single molecule microscopy to hexagonal mesoporous silica films; closing of pores and small opening in the silica walls between neighboring channels have been observed.[71]

Beside these point defects, which can be considered peculiar of mesostructured films, line defects such as dislocations that are typical of crystalline materials, have been also described. Even if the term "dislocation" has been used to describe linear defects in mesostructured materials,[72,73] these defects can not move under mechanical stress such as the case for the dislocations in crystalline materials and are only defects in the structural arrangements of pores. The first clear observation of dislocation defects in the pore array has been reported by Feng et al.,[72] for mesoporous silica powders with hexagonal mesophase (*p6mm*). Two types of dislocations were described, longitudinal edge dislocations and mixed dipole dislocations; the nature of the dislocations, which is similar to those observed in liquid crystals, suggested they formed in the liquid-crystal like stage before formation of the silica backbone through polycondensation.[74] This hypothesis has been confirmed by other studies on defects in cubic mesoporous films that revealed the presence of bending deformation, which are also typical of liquid crystals.[75] A specific study of linear defects in silica mesostructured films, which have been synthesized by cohydrolysis of tetraethoxysilane (TEOS) and methyl-triethoxysilane (MTES), has been reported by Brinker et al.;[73] the origin of this type of defects seems correlated with the presence of strain in mesostructured films (**Figure 1.8**). The formation of a residual strain in sol-gel films is also an effect that involves several processing parameters;[76] in general, the uniaxial shrinkage of the film in the direction normal to the substrate, which arises because the film is constrained to the substrate, produces a tensile stress in the films and a compressive stress in the substrate. In mesoporous films the presence of the surfactant does not avoid the formation of strained films at the end of the process and residual stress is generally present, such as the more general case of sol-gel coatings.

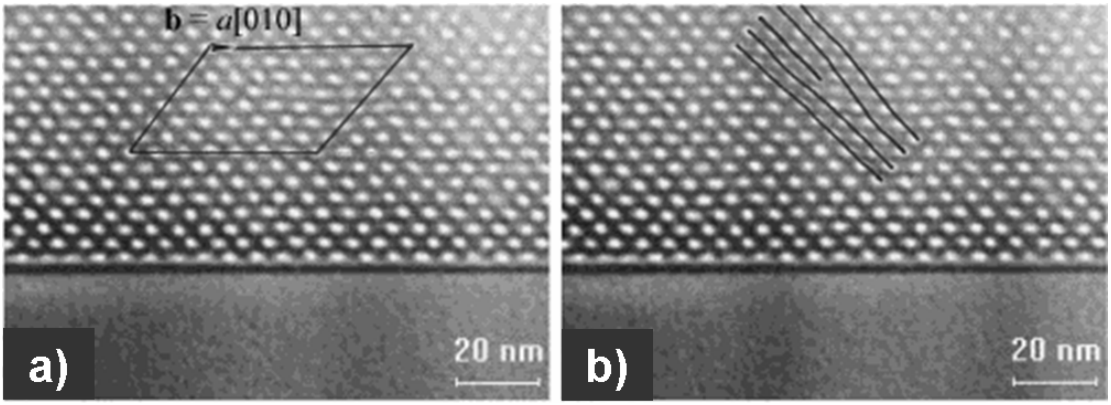


Fig. 1.8 Bright-field TEM images showing some examples of linear defects in mesoporous films.

*- Grain boundaries, polycrystals – monocrystals*

If we describe the mesoporous silica films in terms of crystalline-like materials the similarity is not restricted to point and unidimensional defects but we can also observe defects that are typical of polycristalline materials which are composed by different grains. TEM and SAXS analysis on mesostructured silica films have revealed that there is a poly-distribution of ordered porous domains, "*polycristalline like*", which are well oriented along the substrate, but all possible in-plane orientations are also present. Detailed TEM analysis have shown the presence of grain boundaries of different angles at the mesoscale. Quantitative analysis of defects and grain boundaries in mesostructured films of cubic structure ($Im\bar{3}m$) have revealed that low angle, high angle and translational anti-phase domain boundaries are formed in the films.[75] The domains are extended in a range of several hundreds nanometers and exhibit edge dislocations at the boundaries and within the ordered domains. Bend deformations similar to those of nematics liquid crystals have been reported in accordance with the work of Brinker et al.[73] On the other hand, the presence of domains and therefore grain boundaries is even more complex for mesoporous films because domains of different mesostructures can coexist: the same film can show disordered domains or lamellar structures together with cubic or hexagonal mesophases.[61] Even if this case represents somehow an extreme, it is clear that the interfaces (solid-liquid and liquid-air) favor this type of multi-mesostructures; an good example is **Figure 1.9** where a high resolution TEM image of a mesoporous silica film section is reported. The film shows the coexistence of different types of ordered domains, lamellar (at the silicon-film interface), wormlike in the middle and cubic at the film-air interface. The preparation of a

"*monocrystal*", in which the order is extended on the whole film, or at least on a longer scale (mm to cm) by a simple and reproducible route remains one of the main challenges for the exploitation of mesoporous silica films in industrial applications.

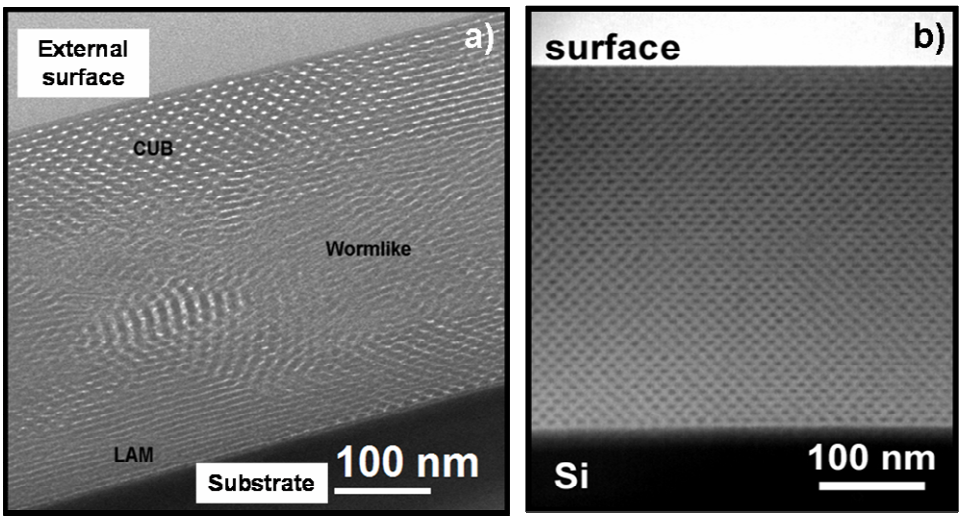


Figure 1.9 a) HRTEM image of a mesoporous silica film showing the coexistence of lamellar (LAM), wormlike and cubic (CUB) pore domains. b) HRTEM image of a hybrid mesoporous MTES-TEOS silica film with highly ordered tetragonal pore structure.

Clearly if we are not able to master the pore order on a bigger scale we loose some of the main advantages of the material property. Basically we can think about two different strategies to extend the scale order, one is trying to manage the film formation process by pre-patterning the surface that allows a controlled epitaxial growth, while another one is based on the chemical-physical process control during film formation. Two examples of these different strategies have been shown by Kuroda et al.[77] who obtained highly ordered mesoporous films whose organization is extended for several centimeters and Falcaro et al.[55] that have fabricated defect-free hybrid silica films even if in a shorter range. The two examples are important to withdraw some basic information about mesoporous film formation, because if clearly the epitaxial controlled growth allows alignment of pores on a rubbed surface, adjusting the kinetic of EISA parameters allows also moving a step ahead on the route of self-assembly.

### 1.3.3 Order-disorder in the pore walls

The dimension of the pore walls is an important parameter for controlling the mechanical properties[78] and the durability of mesoporous films.[79] In general, increasing the pore wall thickness is seen as the simplest route to enhance the overall performance of the material; especially in the case of silica films it is important not to focus only on the dimensions, but also on the structure of the silica network that forms the mesoporous film backbone. One of the critical issues in the field of mesoporous self-assembled films remains the inability to obtain crystalline silica films with an organized porosity. This target has been somehow achieved in the synthesis of hybrid silica powders, but it still remains a kind of "holy grail" for films. This is also a clear indication that the different conditions of preparation between monoliths and films change the chemical-physical conditions during material processing. On the other hand crystalline walls are easily obtained in films based on transition metal oxides and several examples, such as perovskite mesostructured films, are reported in literature.[11] The pore walls are generally formed by crystals of dimensions up to few nanometers and crystal growth is achieved by a controlled thermal treatment. In the case of mesoporous silica crystallization of the walls has not been reported yet, but because of the poor hydrolytic stability of silica the achievement of this goal could really boost applications for mesoporous films. Even if real silica "crystalline" walls have not been synthesized in mesoporous films, several noticeable works have been dedicated to achieve a control of the material property by managing the silica structure at a very fine level. The dimension of the silica pore wall is still relevant to affect the materials properties, in particular we can distinguish three different length scales: an atomic scale, over 1.5 – 2.5 Å, a molecular one, from 2.5 to 4.5 Å, and finally a ''network'' scale, within few nanometres. The molecular scale is particular interesting because it is associated to medium-range order, at this scale the crosslinking of the glass network, with the occurrence of clusters and rings, can be studied. Medium range order can be observed at the molecular scale with the formation of rings of different dimensions, which range from 2-fold up to 6-fold rings. The role of these basic units in the silica network is not trivial, in the sense that several of the material properties are affected by their presence. It is noticeable that the dimensions of the silica pore walls are in the mesoscopic range, which is exactly the scale for silica glasses that would develop some local order through the formation of organized domains.[78] In silica glasses the size of

the ‘‘domains’’ which are likely to be amorphous, is typically <10 nm and can be estimated from the frequency of the ‘‘Boson’’ peak observed in the 3 – 50 $cm^{-1}$ Raman frequency range[79]. The presence of cyclic species in silica precursor solutions has been described by $^{29}Si$ nuclear magnetic resonance (NMR) experiments[80]; the particular processing conditions used for self-assembly of silica films (the low pH) can produce the formation of medium-range ordered units, such as four-fold and three-fold rings. To assess the presence of these structures in thin films is, however, not a simple task because the only techniques that can give a direct *in situ* indication of the presence of silica rings are FTIR and Raman[81], which are quite difficult to perform on thin films (Raman) or can give only limited information (FTIR). The spectra of as-deposited mesoporous silica films have shown that some of these cyclic species are retained in the structure after deposition even if, at temperatures higher than 350 °C, they generally disappear. Cyclic species, especially those of lower dimensions such as 2-fold, 3-fold and 4-fold rings are, in fact, thermodynamically unstable and during thermal treatment the medium-range order is easily lost. In particular, the presence of specific vibrational bands associated with disorder-order transitions in the silica structure have been reported upon FTIR analysis of silica mesoporous thin films. These disorder-induced optical modes are due to the large interface in mesoporous silica films and correlated to bond strains. In the case of mesostructured porous films the pores are ordered, the pore walls are amorphous but a medium-range order (the silica rings) is present in their structure. This is not just an “academic” classification because it has been demonstrated that the presence of silica rings in the pore walls strongly influences the mechanical properties, such as the elastic modulus. An excellent demonstration of how much the presence of medium-range order can affect the properties of the films has been reported by Brinker at al.[83] It is interesting to notice that the reduced dimensions of the silica walls (typically in the range of 2-3 nm) somehow force the formation of a large population of four-member rings and a decreased population of larger rings. The reduced dimensions push the medium-range order with respect to amorphous bulk silica and xerogel materials. The formation of small silica rings is also the product of the dehydroxilation[84] of the silica surface and the thermal history of the sample is strongly affecting their concentration. The presence of these medium-range order species is also assessed for silica mesoporous powders[85] and can be taken as a peculiar characteristic of silica networks in small dimensions.

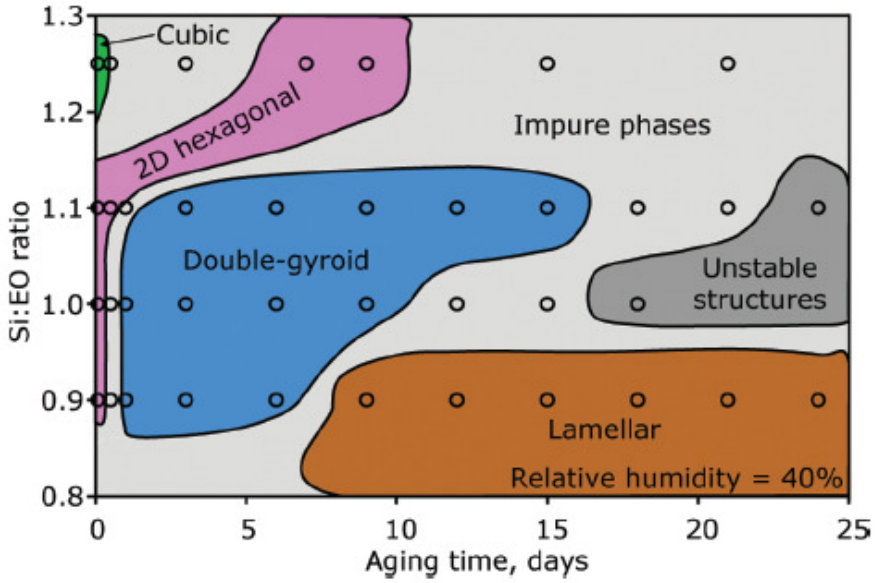


Figure 1.10 Influence of the processing parameters on self-assembled silica films obtained via EISA. Effect of the [Si]/[EO] ratio and ageing time on the structure of the resulting ordered mesoporous structure at relative humidity of 40%. From ref 89.

Getting the control of medium range structures, such as silica rings, within the silica network in mesoporous films is, however, a difficult task. Mastering the material properties through the structure at this scale is limited by the difficult detection of silica rings into the mesoporous film network. On the other hand silica cyclic species are already present in the precursor solution; their nature and amount are strongly dependent on ageing which is an important parameter to take into account to design the right mesophase[86] (see Paragraph 1.2.1). The silica sol is formed of small oligomeric rings and cage-like species that with ageing time are linked to form larger silica clusters. A good experimental evidence of the effect of ageing has been reported by Hillhouse and co-workers: silica condensation and cluster growth in the precursors sol have been found to be unambiguously correlated with the formation of different mesophases in the film; ageing of the silica sol decreases the interfacial curvature and gives a different order topology.[88] **Figure 1.10** from ref. 88, shows the effect of ageing as a function of Si:EO (EO=ethyleneoxide) ratio in silica mesostructured films; if the ratio is fixed, different mesophases are produced in the film by changing the ageing time. It is also possible to design the silica network structure using pre-defined framework units, an elegant approach has been proposed by Kuroda and co-workers who synthesised specific building blocks.[89] Siloxane cages are a good example of symmetrical units that can be used as molecular building blocks for silica and hybrid networks; the molecular

design of these building blocks with alkoxy-functionality allows formation of a siloxane network with well defined silica units.

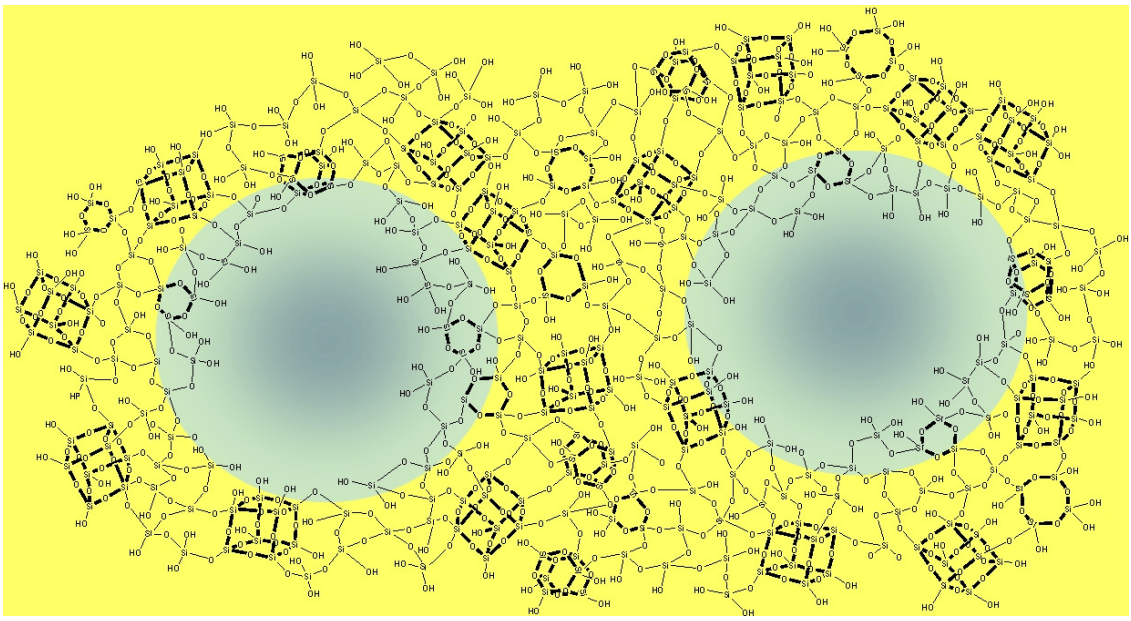

Figure 1.11 Picture of mesopore walls made with embedded silica cyclic species.

A sketch of the possible structural building blocks, cyclic species, and cages that can form the silica backbone is shown in **Figure 1.11**. This represents an extension of the concept of order in the silica mesoporous film framework where "bricks" of specific geometry are used to build up the network.[90] The pore walls are still amorphous but some order is given by the presence of cage-like units; enhanced properties could be expected for this type of silica mesoporous films made by molecularly designed building units even if experimental support has still to be clearly shown.

### 1.3.4 Pores Orientation

We have seen that different types of porous structures can be obtained in mesoporous silica films and it is possible to design, within some limits, the material properties that are connected to the porous topology. Mesoporous films showing a 2D phase organization, such as the 2D rectangular *c2mm* and the 2D-hex *p6mm,* have a lower symmetry with respect to 3D structures, but the possibility of controlling the mesophase alignment make them very attractive. Therefore the question is how to obtain a preferential orientation of the channels. Many researchers have applied a plenty of strategies to achieve this goal. Just some examples of the different opportunities to

obtain oriented mesochannels in silica films through the highly flexible bottom up EISA route are: electrochemical driven self-assembly,[91] dip-coating under a steady-homogeneous high magnetic field parallel to a substrate[92] and photo-orientation on a photocrosslinkable polymer film.[93] We can align the mesochannels along the orthogonal and parallel directions with respect to the substrate and the strategy to control orientation of 2D mesophases depends on the direction of the channels. In general, to achieve a macroscopic orientation with in-plane alignment is easier and several synthesis based on epitaxial growth have been reported.[94,95] A true fully ordered mesostructure is, however, obtained only if the channels show the same in-plane uniaxial orientation in a large length scale and do not result only generally aligned in directions parallel with respect to the substrate as illustrated in **Figure 1.12**. The group of Kuroda has done a systematic work on the subject and they have successfully obtained oriented silica mesochannels in 2D hexagonal structures using polyimide Langmuir-Blodgett films[96] or rubbing treated polyimide films[97] to coat the substrate. Clearly the surface properties govern the alignment process and the channels orientation appears strongly influenced by the interactions between the substrate surface and surfactant molecules.[10]

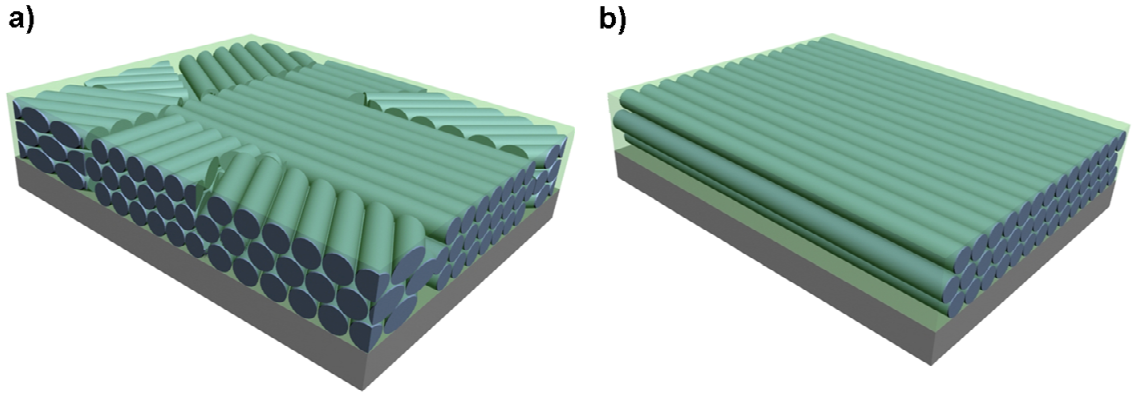


Figure 1.12 Different possible orientations of 2D hexagonal stacks of mesopores in a self-assembled silica film: random (a) and full (b) uniaxial in-plane orientation.

Alignment of mesochannels of different extents, has been reported for mesoporous silica films deposited on graphite, mica[98] and oriented silicon wafers (110).[99] In this case the substrate itself, without any modification, is able to orient the mesophase; an example is the full in-plane and out-of-plane alignment of hexagonal cylinders that has been observed on freshly cleaved mica substrates.[98] The methods of orientation that do not require a pre-treatment of the substrate are clearly more feasible for applications; a

more generic method is the application of a hot jet air flow[100] to a droplet of precursors solution after deposition on the substrate. In this case because the mesochannels will be oriented along the direction of the air flow, orientation of multilayered mesostructured films can be achieved; different layers can be oriented in different directions independently on the type and even shape of the substrate. Uniaxial alignment of the channels is not the only possible form of in-plane orientation;[101] steric hindrance effects between the hydrophilic head of adsorbed surfactant molecules and silica oligomers on an aligned rubbing-treated polyimide film give two distinct alignment directions with a zig-zag porous structure and a fixed kinky angle, as illustrated in **Figure 1.13**.[101] Obtaining ordered arrays of channels that are orthogonally oriented with respect to the substrate is more tricky but some successful examples have been reported so far; one possible route is self-assembly in a confined environment with 1D orientation and controlled growth on a pre-patterned substrate. Porous alumina membranes, showing ordered and vertical monodimensional (1D) channel structures have been used as templating environment for mesoporous silica;[102] TEM and X-ray diffraction (XRD) have shown that the pores within the membrane are oriented in a parallel direction with respect to the alumina channels.[103]

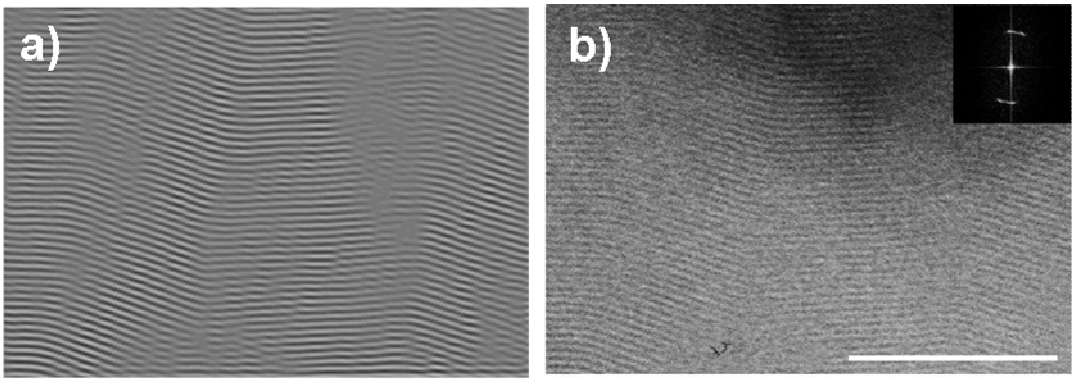


Figure 1.13 a) Top view TEM image of silica film having zigzag mesoporous structures with fixed kink angles. b) Reconstructed image of (a) from the fast Fourier transform image (inset), scale bar: 100 nm. From ref 101.

However, this route is not suitable for films and other specific methods based on electrochemically assisted self-assembly[91] and nanometre-scale epitaxial growth[104] have been developed. Both the methods allow achieving vertically alignment of oriented hexagonal channels even if they have some limitations given by the need of a specific substrate. The control of pore orientation in 2D-hex structures is not restricted to the

choice of orthogonal-parallel directions with respect to the substrate; it is also possible to produce tilted mesochannels by modifying the substrate with PEO-PPO copolymers to obtain a chemical neutral surface that promotes the alignment.[105]

We have observed that the role of the interfaces in the alignment process is crucial and most of the successfully examples are due to controlled epitaxial growth of the films; it has to be underlined, however, that the orientation is controlled by both interfaces, air-film and film-substrate, and homogeneous layers can be obtained only balancing the interfacial energies.[106] It is otherwise quite common to observe different structures or different levels of organization at the two interfaces and in the middle of the film, which is a clear indication that not only the solid-liquid interface plays a major role to direct organization during EISA.

### 1.3.5 Order and properties

What is the advantage of the pore order and how the order does affect the film properties are among of the main questions which arise by approaching ordered mesoporous films. These are clearly critical issues and deserve a strong experimental evidence to reply in a proper way because, in general, the supporting experiments require a high level of sophistication. The clear advantage of getting ordered porous structures has been shown by Brinker et al. that measured the elastic modulus of thin mesoporous silica films.[83] They have found a modulus–density scaling relationship for cubic (C), hexagonal (H) and worm-like disordered (D) mesoporous silica prepared by surfactant directed self-assembly. Mesostructured porous silica films have shown a hierarchy of modulus values, $D < H < C$, which depends on the specific pores topology; order vs. disorder changes the mechanical properties,[78] the higher is the symmetry and the higher is the elastic modulus of the material.

The advantage of getting an ordered porous structure is not only linked to changes of some general properties of the material; the possibility of obtaining ordered pores is also intuitively correlated to diffusive processes; interconnected and ordered paths represent an intrinsic advantage for effective mass transport. Many studies have been devoted to asses how the topology of the ordered porosity affects the diffusion within the films and the order has been found to be the most important factor to deal with for efficient design of a high diffusivity material.[108,109] The experimental data from different researchers indicate that there is a general correlation between diffusion and topological order of the

pores; the diffusivity decreases following this order: gyroid bicontinuos → orthorhombic and cubic → 3D-hex → 2D-hex and rhomboedral.[110] Diffusion in 2D-hex structures has clearly shown a strong dependence on the orientation of the channels with respect to the film substrate; films with cylindrical mesopores oriented parallel to the substrate[32] have been found to block the sensing element. In this case the effect of disorder-order in the mesostructure has been specifically evaluated by electrochemical impedance spectroscopy experiments. Accessibility in 2D rectangular *c2mm* films (which are finally obtained upon shrinkage of *p6mm* 2D-hex films) with a full alignment of the channels parallel to the substrate has been compared with respect to *c2mm* films with only oriented domains. The disordered *c2mm* films have shown a higher accessibility than well organized *c2mm* silica mesoporous films. In the evaluation of these results it should also considered that not only order but also accessibility and the presence of microporosity, which is generally present in films synthesised from block copolymers,[111] have an important role. Besides electrochemical evaluation of diffusion some sophisticated experiments have also been performed by single molecule fluorescence microscopy[71,112,113] and positronium time of flight spectroscopy to test the accessibility of mesoporous films.[114] In particular, the experiment of Mills et al. has been realized on 2D-hex and cubic mesoporous silica films[114] also in this case the experiments performed on 2D-hex films have revealed that the diffusion coefficient is an order of magnitude higher in the system with the mesochannels aligned to beam direction.

## 1.4 Mesoporous non-siliceous thin films

Short after the discovery of periodically organized mesoporous silica, the scientific community strove to extend the mesoporous family to non-silicate materials. These systems, consisting on oxides or phosphates of transition metals, were interesting because of their varied framework properties, which should permit development of several applications, particularly in catalysis, photocatalysis, sensors, optics, separation techniques, smart coatings, etc. Despite the important improvements in the synthesis of non-siliceous mesoporous materials, at present the reported works on transition metal porous materials are still considerably lower than on silica.

Soler-Illia et al.[115] have summarized the reasons of the slower advancement in this field as follows:

1) as already mentioned (see Section 1.1), the pioneer groups in mesoporous materials had a scientific background related to zeolites; therefore, they were mainly familiar with silicon and aluminium chemistry;
2) the high reactivity towards hydrolysis and condensation of transition metal oxide precursors increases the extent of uncontrolled phase separation between organic and inorganic components, yielding non-mesostructured materials, but porous gels;
3) structural integrity of mesoporous materials made with non-silica systems is often undermined by redox reactions, phase transitions, and the crystallization processes that can happened during thermal treatments;
4) synthesis procedures are extremely sensitive to external parameters such as the relative humidity. In some cases, this leads to an intrinsic difficulty in reproducing results.

The first studies concerning non-silica mesostructured materials have been presented by researchers of the University of Santa Barbara[34,116,117] and nowadays, research groups all over the world are developing this field. A great variety of oxide-based hybrids containing surfactant templates and metal cations have been synthesized in the form of powders or "bulk gels": non-silica main block (Al, Ga, Sn, Sb, Pb), transition metals (Ti, V, Fe, Mn, Zr, Hf, Nb, Ta, W, Y) and rare earths. Some methods can even be generalized for more than one metal cation or mixed oxides.

Production of organized porous films were also obtained for many chemical elements: Al,[119] Ti,[27,29] Zr,[27] V,[120] Hf,[121] W,[122]Ce,[123] Nb[124] and multi-metal-oxide systems.[11] Films present the paramount advantage to be directly shaped in any substrate for a targeted application but it is important to point out that many papers reported synthesis conditions which are sometimes difficult to reproduce, leading to a lack of reproducibility. We can found an explanation of this if we consider that most of the syntheses are under kinetical control, which in turn means a enhanced complexity in reproducing the dynamic conditions. Sometimes, uncontrolled (i.e., very fast) inorganic polymerization can "freeze" a metastable mesostructure (even a non-organized one) in an "irreversible" way. As a consequence, the study of transition metal oxides mesoporous films is still an intriguing field, and not many papers has been devoted to the formation mechanisms of these materials. **Figure 1.14** displays selected TEM micrographs of non-silica ordered mesoporous films; hexagonal, wormlike, rhombohedric and cubic mesophases are obtained.

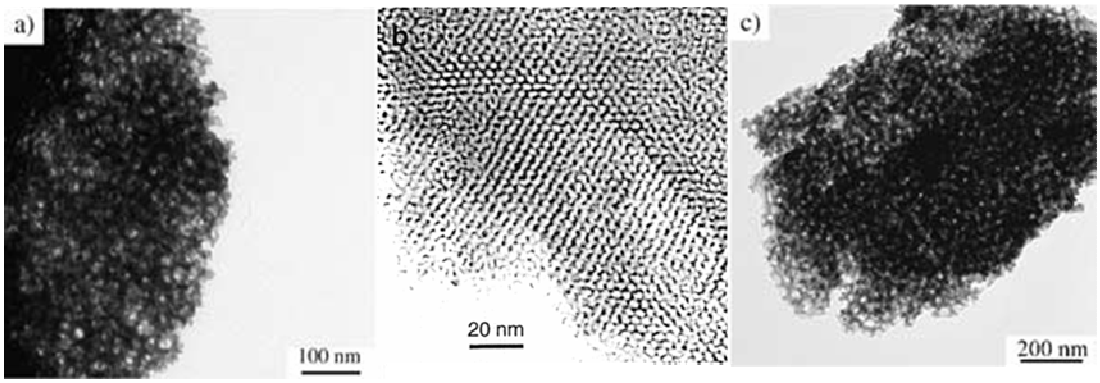


Fig. 1.14 TEM images of some transition metal mesoporous thin films made with hafnium (a), titanium (b), and zirconium oxides. Pictures are taken from ref 29 and 27.

Regarding to their synthesis and processing, we can identify at least five differences among silica- and non-silica oxide based systems:

a) metallic alkoxide precursors are more reactive toward hydrolysis and condensation than Si counterparts;
b) inorganic polymerization has to be partially blocked, because of the high reactivity. In some cases, clusters or nanoparticles may result, which lower the film quality upon drying;
c) the degree of organization and the extension of the porous domains are often lower for transition metals than for silica-based systems;
d) the obtained structures are often unstable towards template removal. This is particularly marked for metals capable of presenting various oxidation states such as tungsten, vanadium or manganese;
e) once that hydrolysis and polycondensation have been concluded, most part of metal centres present a higher coordination than tetrahedral silicon.

Considering what exposed before, controlling the precursors reactivity becomes the most important and hard task to get an ordered porous films formed by transition metal oxides. The reactivity of the precursors can be efficiently controlled by many different means, for example, by using preformed nano-objects or by using alkoxides or other salts in the presence of condensation inhibitors (acids, complexing agents) or by working in non-aqueous solvents and limited quantities of water. In particular the use of chlorides dissolved in ethanol has proved to be a very effective non-hydrolitic pathway to prepare non-siliceous mesoporous film. Under these conditions generally associated with high hydrolysis ratios ($[H_2O]/[metal] > 2$), condensation is hindered by protonation of the

metal-OH nucleophilic species present in the medium.[26] At the same time, depolymerization processes (the inverse of polycondensation) are promoted. Both processes generally lead to the formation of small hydrophilic oligomers: clusters or nano-objects. As a result, both organic and mineral building blocks present a hydrophilic character, due to the presence of water, which favors micelle formation. This procedure of "matching the hydrophilic domains" allows mesophase formation using both neutral (Pluronic or Brij block-copolymers) or cationic templates (CTAB, SDS, etc.) upon solvent evaporation or precipitation. A typical example of this pathway is the synthesis of mesoporous titania starting from a solution of precursor with ethanol, surfactant and $TiCl_4$.

$$TiCl_4 + X\ EtOH \rightarrow TiCl_{4-x}(OEt)_x + X\ HCl$$

The addition of a strong Lewis acid such as titanium chloride to the alcohol is a very effective way to introduce acid into the initial solution without adding water, slowing noticeably the condensation process.

We have already mentioned the EISA process, initially proposed by Brinker and colleagues.[33] This technique is based on the processes that lead to the formation of mesostructured silica films upon evaporation of the solvent: starting from dilute solutions, a liquid crystalline (LC) mesophase is gradually formed upon solvent evaporation. The formation of an inorganic network around this LC phase permits the formation of a well-defined hybrid mesostructured which present a segregation of organic and mineral domains at the nanoscale. In the case of non-silica systems, inorganic condensation can be "turned on" after deposition by post-treatments, leading to a condensed inorganic framework. EISA technique, therefore, has been successfully applied to non-silica systems to produce ordered porous films but some additional procedures have been used to increase the degree of order and stabilize the inorganic framework. Due to the incomplete inorganic polymerization, in fact, the as-synthesized hybrid structure in the film is still quite flexible. Therefore, a subsequent "locking" step is necessary (by a chemical process, for example, inorganic or organic polymerization, or by mild thermal treatment) in order to obtain a robust and highly ordered mesoporosity. This is a very effective procedure for transition-metal-based materials, because starting solutions are relatively dilute, and the inorganic polymerization can be readily controlled by an acid, subsequently eliminated by evaporation. In addition to the already mentioned parameters, indeed, the formation of a well-defined mesostructured film critically depends on factors such as the synthesis temperature, which controls two processes in competition: solvent evaporation (and, thus, self-assembly) versus inorganic polymerization. Hexagonal $TiO_2$/CTAB hybrids that lead

to mesoporous $TiO_2$ upon thermal treatment were obtained by combining EISA with acid inhibition of the condensation.[125] In this case, the hybrid titania mesostructure have been thermally reinforced, to assist condensation among nano-building blocks, leading to robust hybrid precursors at T > 70 °C. Cubic mesoporous titania were also obtained from non-ionic surfactants by using Pluronic F127[29], P123[126] and KLE[40] block copolymers.

In many applications, such as selective electrodes, sensors, photocatalytic, or electro-chromic devices,[127] crystalline pore walls are required to enhance the functional properties of films. Titania, zirconia, hafnia and perovskite mixed oxides mesoporous films presenting highly ordered porous texture and high crystallinity have been recently obtained by a careful control of the thermal treatment (see Paragraph 1.2.3).[11,40,121]

Finally, organic functionalization of the mesoporous walls is also an important added value for advanced transition-metal oxides mesostructures. Hybridization of the pore surface can be easily performed by post-functionalization, once the oxide network of mesoporous film is consolidated. Organic molecules bearing interesting functions (chromophores, selective solubilization, trapping, etc.) have been anchored to the pore wall by means of complexing groups (carboxylates, phosphonates, α-diketonates, etc.).[128] In particular, an interesting feature of non-siliceous systems is the wide availability of the grafting molecules and the quickness and completion of the grafting reactions; silane-coupling agents, for instance, can also be envisaged for functionalization purposes.

## 1.5 Beyond evaporation-induced self-assembly

Controlling order-disorder transitions and mastering self-organization into ordered structures at nanoscale is still an open task. Self-assembly of mesoporous ordered silica films is an example of such complexity, understanding and controlling the different levels of order that are involved in the process is a stimulating challenge. Order evolves from self-organization of templating micelles, but the large number of parameters to be controlled and the lack of systematic basic data still limit our ability of producing well controlled and oriented pores with specific topologies.

Several issues have to be settled to reach a full exploitation of the potentialities of the material; in particular, the weak chemical durability under hydrolytic conditions is a

major drawback for silica mesoporous films and a future goal should be obtaining ordered (i.e. crystalline) pore walls, at least as hybrid silica. A natural evolution is in the direction of even more complex materials through self-assembly, which means hierarchical porous materials;[129] the different orders of porosity should show both organized structures possibly obtained through self-assembly process.

Controlling the order means also designing the properties as a function of applications and enlarging our perspective on the different complex interactions in the nanoworld. Ozin and Cademartiri[130] have recently given an interesting outlook of the future trends in nanoscience. They have prefigured several emerging applications of nanomaterials where they could provide disruptive and novel solutions and not just incremental improvements over old technology. Among these, there are some specific topics where porous, and specifically hierarchical multi-porous, materials would surely give their contribute;

- sensor for nanodiagnostics, because a cheap production from readily available inorganic materials would make them amenable for use and production in low-resource settings;
- nanophotonics, because the way by which the interaction of light with matter is managed would be dramatically changed by the use of material properties (plasmonics) or architectures (metamaterials, photonic crystals, granular materials) ;
- nanocomposites, for exploiting the unexpected properties of mixtures of well-defined nanoscale building blocks;
- nanocrystallization, for instantly solving most of the problems related to the use of nanomaterials in devices (e.g., heterogeneity, batch-to-batch variations, etc.) and bioapplications (e.g., toxicity screening).

In our opinion, the increased control of self-assembly using bottom-up techniques will build a bridge between the world of biotechnology and nanotechnology allowing powerful but unpredictable developments for the therapeutical and clinical medicine.

## 1.6 References

[1] J. Rouqerol, D. Avnir, C. W. Fairbridge, D. H. Everett, J. H. Haynes, N. Pernicone, J. D. Ramsay, K. S. W. Sing, K. K. Unger, Recommendations for the characterization of porous solids (Technical Report) *Pure Appl. Chem*. **1994**, *66*, 1739 -1758.

[2] S. Beck, J, J. C. Vartuli, W. J. Roth, M. E. Leonowicz, C. T. Kresge, K. D. Schmitt, C. T.-W. Chu, D. H. Olson, E. W. Sheppard, S. B. McCullen, J. B. Higgins, J. L. Schlenker. A new family of mesoporous molecular sieves prepared with liquid crystal templates. *J. Am. Chem. Soc.*, **1992**, *114*, 10834–10843.

[3] C. T. Kresge, M. E. Leonowicz, W. J. Roth, J. C. Vartuli, S. Beck, Ordered mesoporous molecular sieves synthesized by a liquid-crystal template mechanism. *Nature*, **1992**, *359*, 710–711.

[4] A. S. Brown, S. A. Holt, T. Dam, M. Trau, J. W. White. Mesoporous silicate film growth at the air-water interface – Direct observation by X-ray reflectivity. *Langmuir*, **1997**, *13*, 6363–6365.

[5] S. H. Tolbert, T. E. Schaffer, J. Feng, P. K. Hansma, G. D. Stucky. A new phase of oriented mesoporous silicate thin films. *Chem. Mater.*, **1997**, *9*, 1962–1967.

[6] P. Yang, A. Kuperman, N. Coombs, S. Mamiche-Afara, G. A. Ozin. Synthesis of oriented films of mesoporous silica on mica. *Nature*, **1996**, *379*, 703–705.

[7] Y. Lu, R. Ganguli, C. A. Drewien, M. T. Anderson, C. J. Brinker, W. Gong, Y. Guo, H. Soyez, B. Dunn, M. H. Huang, J. I. Zink. Continuous formation of supported cubic and hexagonal mesoporous films by sol-gel dip-coating. *Nature*, **1997**, *389*, 364–368.

[8] C. J. Brinker, Y. Lu, A. Sellinger, H. Fan. Evaporation-induced self-assembly: Nanostructures made easy. *Adv. Mater.*, **1999**, *11*, 579–585.

[9] F. Schüth. Non-siliceous mesostructured and mesoporous materials. *Chem. Mater.*, **2001**, *13*, 3184–3195.

[10] C. J. Brinker, D. R. Dunphy. Morphological control of surfactant-templated metal oxide films. *Curr. Opinion Colloid Interf. Sci.,* **2006**, *11*, 126–132.

[11] D. Grosso, C. Boissière, B. Smarsly, T. Brezesinski, N. Pinna, P. A. Albouy, H. Amenitsch, M. Antonietti, C. Sanchez. Periodically ordered nanoscale islands and mesoporous films composed of nanocrystalline multimetallic oxides. *Nat. Mater.*, **2004**, *3*, 787-792.

[12] H. Fan, Y. Lu, A. Stump, S. T. Reed, T. Baer, R. Schunk, V. Perez-Luna, G. P. López, C. J. Brinker. Rapid prototyping of patterned functional nanostructures. *Nature*, **2000**, *405*, 56–60.

[13] N. Baccile, D. Grosso, C. Sanchez. Aerosol generated mesoporous silica particles. *J. Mater. Chem.,* **2003**, *13*, 3011 – 3016.

[14] D. Grosso, F. Cagnol, G. Soler-Illia, E. L. Crepaldi, H. Amenitsch, A. Brunet-Bruneau, A. Bourgeois, C. Sanchez. Fundamentals of mesostructuring through evaporation-induced self-assembly. *Adv. Funct. Mater.*, **2004**, *14*, 309–322.

[15] D. Grosso, G. Soler-Illia, E. L. Crepaldi, B. Charleux, C. Sanchez. Nanocrystalline. Transition-metal oxide spheres with controlled multi-scale porosity. *Adv. Funct. Mater.*, **2003**, *13*, 37–42.

[16] D. Grosso, C. Boissière, L. Nicole, C. Sanchez. Preparation, treatment and characterisation of nanocrystalline mesoporous ordered layers. *J. Sol-Gel. Sci. Technol*., **2006**, *40*, 141–154.

[17] T. Brezesinski, M. Groenewolt, A. Gibaud, N. Pinna, M. Antonietti, B. Smarsly. Evaporation-induced self-assembly (EISA) at its limit: ultrathin, crystalline patterns by templating of micellar monolayers. *Adv. Mater.*, **2006**, *18*, 2260–2263.

[18] M. Järn, F. J. Brieler, M. Kuemmel, D. Grosso, M. Lindén. Wetting of heterogeneous nanopatterned inorganic surfaces. *Chem. Mater.* **2008**, *20*, 1476–1483.

[19]G. Cortial, M. Siutkowski, F. Goettmann, A. Moores, C. Boissière, D. Grosso, P. Le Floch, C. Sanchez. Metallic nanoparticles hosted in mesoporous oxide thin films for catalytic applications. *Small*, **2006**, *2*, 1042–1045.

[20] S. Besson, T. Gacoin, C. Jacquiod, C. Ricolleau, J.-P. Boilot. 3D periodic arrays of nanoparticles inside mesoporous silica films. *Mat. Res. Soc. Symp. Proc.*, **2002**, *707*, 119-124.

[21] D. Buso, P. Falcaro, S. Costacurta, M. Guglielmi, A. Martucci, P. Innocenzi, L. Malfatti, V. Bello, G. Mattei, C. Sada, H. Amenitsch, I. Gerdova, A. Hache´. PbS-Doped Mesostructured Silica Films with High Optical Nonlinearity. *Chem. Mater.,* **2005**, *17*, 4965-4970.

[22] L. Nicole, C. Boissière, D. Grosso, A. Quach, C. Sanchez. Mesostructured hybrid organic-inorganic thin films. *J. Mater. Chem.*, **2005**, *15*, 3598–3627.

[23] L. G. Hubert-Pfalzgraf. Molecular design of oxide precursors for advanced materials in "Sol-Gel and Polymer Photonic Devices", SPIE Press Book, **1997**, *CR68,* 3-24.

[24] J. Livage, M. Henry, C. Sanchez. Sol-gel chemistry of transition metal oxides. *Prog. Solid State Chem.*, **1988**, *18*, 259–341.

[25] G. Soler-Illia, E. L. Crepaldi, D. Grosso, D. Durand, C. Sanchez. Structural control in self-standing mesostructured silica oriented membranes and xerogels. *Chem. Commun.*, **2002**, 2298–2299.

[26] G. Soler-Illia, C. Sanchez. Interactions between poly(ethylene oxide)-based surfactant and transition metal alkoxides: their role in the templated construction of mesostructured hybrid organic-inorganic composites. *New J. Chem.*, **2000**, *24*, 493–499.

[27] E. L. Crepaldi, G. Soler-Illia, D. Grosso, F. Cagnol, F. Ribot, C. Sanchez. Controlled formation of highly organized mesoporous titania thin films: from mesostructured hybrids to mesoporous anatase $TiO_2$. *J. Am. Chem. Soc.*, **2003**, *125*, 9770–9786.

[28] S. P. Naik, T. Yokoi, W. Fan, Y. Sasaki, T.-C. Wei, H. W. Hillhouse, T. Okubo. Versatile fabrication of distorted cubic mesoporous silica films using CTAB together with a hydrophilic organic additive. *J. Phys. Chem. B*, **2006**, *110*, 9751–9754.

[29] S. Y. Choi, B. Lee, D. B. Carew, M. Mamak, F. C. Peiris, S. Speakman, N. Chopra, G. A. Ozin. 3D hexagonal (R-3m) mesostructured nanocrystalline titania thin films: Synthesis and characterization. *Adv. Funct. Mater.*, **2006**, *16*, 1731–1738.

[30] M. P. Tate, B. W. Eggiman, J. D. Kowalski, H. W. Hillhouse. Order and orientation control of mesoporous silica films on conducting gold substrates formed by dip-coating and self-assembly: A grazing angle of incidence small-angle X-ray scattering and field emission scanning electron microscopy study. *Langmuir*, **2005**, *21*, 10112–10118.

[31] G. Soler-Illia, E. Scolan, A. Louis, P.-A. Albouy, C. Sanchez. Design of mesostructured titanium oxo based hybrid organic-inorganic networks. *New J. Chem.*, **2001**, *25*, 156–165.

[32] E. L. Crepaldi, G. Soler-Illia, D. Grosso, C. Sanchez. Nanocrystallised titania and zirconia mesoporous thin films exhibiting enhanced thermal stability. *New J. Chem.*, **2003**, *27*, 9–13.

[33] C. J. Brinker, G. W. Scherer. Sol-gel science: The physics and chemistry of sol-gel processing. Academic Press, San Diego, 1992.

[34] P. Yang, D. Zhao, D. I. Margolese, B. F. Chmelka, G. D. Stucky. Block copolymer templating syntheses of mesoporous metal oxides with large ordering lengths and semicrystalline framework. *Chem. Mater.*, **1999,** *11*, 2813–2826.

[35] D. Grosso, F. Babonneau, P.-A. Albouy, H. Amenitsch, A. R. Balkenende, A. Brunet-Bruneau, J. Rivory. An *in situ* study of mesostructured CTAB-silica film formation during dip coating using time-resolved SAXS and interferometry measurements. *Chem. Mater.*, **2002**, *14*, 931–939.

[36] M. Klotz, A. Ayral, C. Guizard, L. Cot. Synthesis conditions for hexagonal mesoporous silica layers. *J. Mater. Chem.*, **2000,** *10*, 663–669.

[37] D. Grosso, F. Babonneau, G. Soler-Illia, P.-A. Albouy, H. Amenitsch. Phase transformation during cubic mesostructured silica film formation. *Chem. Commun.*, **2002**, 748–749.

[38] A. Gibaud, D. Grosso, B. Smarsly, A. Baptiste, J. F. Bardeau, F. Babonneau, D. A. Doshi, Z. Chen, C. J. Brinker, C. Sanchez. Evaporation-controlled self-assembly of silica surfactant mesophases. *J. Phys. Chem. B*, **2003**, *107*, 6114–6118.

[39] F. Cagnol, D. Grosso, G. Soler-Illia, E. L. Crepaldi, F. Babonneau, H. Amenitsch, C. Sanchez. Humidity-controlled mesostructuration in CTAB-templated silica thin film processing. The existence of a modulable steady state. *J. Mater. Chem.*, **2003**, *13*, 61–66.

[40] D. Grosso, G. Soler-Illia, E. L. Crepaldi, F. Cagnol, C. Sinturel, A. Bourgeois, A. Brunet-Bruneau, H. Amenitsch, P.-A. Albouy, C. Sanchez. Highly porous $TiO_2$ anatase optical thin films with cubic mesostructure stabilized at 700°C. *Chem. Mater.,* **2003**, *15*, 4562–4570.

[41] E. L. Crepaldi, G. Soler-Illia, A. Bouchara, D. Grosso, D. Durand, C. Sanchez. Controlled formation of highly ordered cubic and hexagonal mesoporous nanocrystalline yttria-zirconia and ceria-zirconia thin films exhibiting high thermal stability. *Angew. Chem. Int. Ed. Engl.*, **2003**, *42*, 347–351.

[42] C. N. Urade, H. W. Hillhouse. Synthesis of thermally stable highly ordered nanoporous tin oxide thin films with a 3D face-centered orthorhombic nanostructure. *J. Phys. Chem. B*, **2005**, *109*, 10538–10541.

[43] G. J A.A. Soler-Illia, P. Innocenzi, Mesoporous hybrid thin films: the physics and chemistry beneath. *Chem.: A Europ. J.*, **2006,** *12*, 4478-4494.

[44] P. C. A. Alberius, K. L. Frindell, R. C. Hayward, E. J. Kramer, G. D. Stucky, B. F. Chmelka, General predictive syntheses of cubic, hexagonal, and lamellar silica and titania mesostructured thin films. *Chem. Mater.* **2002**, *14*, 3284-3294.

[45] M. Ogawa. Formation of novel oriented transparent films of layered silica-surfactant nanocomposites. *J. Am. Chem. Soc.* **1994**, *116*, 7941-7942.

[46] D. Zhao, P. Yang, N. Melosh, J. Feng, B. F. Chmelka, G. D. Stucky, Continuous mesoporous silica films with highly ordered large pore structures. *Adv. Mater.* **1998**, *10*, 1380-1385.

[47] R. C. Hayward, P. C. A. Alberius, E. J. Kramer, B. F. Chmelka. Thin films of bicontinuous cubic mesostructured silica templated by a nonionic surfactant. *Langmuir* **2004**, *20*, 5998-6004.

[48] D. Grosso, A. R. Balkenende, P. A. Albouy, M. Lavergne, L. Mazerolles, F. Babonneau. Highly oriented 3D-hexagonal silica thin films produced with cetyltrimethylammonium bromide. *J. Mater. Chem.* **2000**, *10*, 2085-2089.

[49] S. Besson, C. Ricolleau, T. Gacoin, C. Jacquiod, J. P. A. Boilot. A new 3D organization of mesopores in oriented CTAB silica films. *J. Phys. Chem.* B **2000**, *104*, 12095-12097.

[50] S. Besson, T. Gacoin, C. Ricolleau, C. Jacquiod, J. P. Boilot. Phase diagram for mesoporous CTAB–silica films prepared under dynamic conditions. *J. Mater. Chem.* **2003**, *13*, 404-409.

[51] I. Honma, H. S. Zhou, D. Kundu, A. Endo. Structural control of surfactant-templated hexagonal, cubic, and lamellar mesoporous silicate thin films prepared by spin-casting. *Adv. Mater.* **2000**, *12*, 1529-1533.

[52] H. S. Zhou, D. Kundu, I. Honma. Synthesis of oriented meso-structure silica functional thin film. *J. Europ. Ceram. Soc.* **1999**, *19*, 1361-1364.

[53] S. Besson, C. Ricolleau, T. Gacoin, C. Jacquiod, J. P. Boilot. Highly ordered orthorhombic mesoporous silica films *Microporous Mesoporous Mater.* **2003**, *60*, 43-49.

[54] P. Falcaro, D. Grosso, H. Amenitsch, P. Innocenzi. Silica orthorhombic mesostructured films with low refractive index and high thermal stability. *J. Phys. Chem. B,* **2004**, *108*, 10942-10948.

[55] P. Falcaro, S. Costacurta, G. Mattei, H. Amenitsch, A. Marcelli, M. C. Guidi, M. Piccinini, A. Nucara, L. Malfatti, T. Kidchob, P. Innocenzi. Highly ordered “defect-

free" self-assembled hybrid films with a tetragonal mesostructure. *J. Am. Chem. Soc.* **2005**, *127*, 3838-3846.

[56] B. W. Eggiman, M. P. Tate, H. W. Hillhouse. Rhombohedral structure of highly ordered and oriented self-assembled nanoporous silica thin films. *Chem. Mater.* **2006**, *18*, 723-730.

[57] V. N. Urade, T. C. Wei, M. P. Tate, H. W. Hillhouse. Nanofabrication of double-gyroid thin films. *Chem. Mater*. **2007**, *19*, 768-777.

[58] M. Ogura, H. Miyoshi, S. P. Naik, T. Okubo. Investigation on the drying induced phase transformation of mesoporous silica; a comprehensive understanding toward mesophase determination. *J. Am. Chem. Soc.* **2004**, *126*, 10937-10944.

[59] G. J. A. A. Soler-Illia, E. Crepaldi, D. Grosso, C. Sanchez. Block copolymer-templated mesoporous oxides. *Current Op. Colloid Interf. Sci.* **2003**, *8*, 109-126.

[60] B. Alonso, R. Balkenende, P.-A. Albouy, D. Durand, F. Babonneau. Directing role of pH and ethanol vapour on the formation of 2D or 3D mesostructured silica and hybrid organo-silica thin films. *New J. Chem.* **2002**, *26*, 1270-1272.

[61] N. Yao, A. Y. Ku, N. Nakagawa, T. L. Dudley, A. Saville, I. A. Aksay, Disorder–order transition in mesoscopic silica thin films. *Chem. Mater.* **2000**, *12*, 1536.

[62] P. Innocenzi, L. Malfatti, T. Kidchob, P. Falcaro, M. Cestelli Guidi, M. Piccinini, A. Marcelli. Kinetics of polycondensation reactions during self-assembly of mesostructured films studied by *in situ* infrared spectroscopy *Chem. Comm.*, **2005**, 2384-2386.

[63] P. Innocenzi, T. Kidchob, J. Mio Bertolo, M. Piccinini, M. Cestelli Guidi, A. Marcelli. Time-resolved infrared spectroscopy as an *in situ* tool to study the kinetics during self-assembly of mesostructured films. *J. Phys. Chem. B*, **2006**, *110*, 10837-10841.

[64] S. Che, S. Kamiya, O. Terasaki, T. Tatsumi. The formation of cubic $Pm\bar{3}n$ mesostructure by an epitaxial phase transformation from hexagonal *p6mm* mesophase. *J. Am. Chem. Soc.* **2001,** *123,* 12089-12090.

[65] T.-C., Wei, T.-C., H. W. Hillhouse. Mass transport and electrode accessibility through periodic self-assembled nanoporous silica thin films. *Langmuir* **2007**, *23*, 5689-5699.

[66] P. Falcaro, S. Costacurta, L. Malfatti, T. Kidchob, M. Takahashi, M. F. Casula, M. Piccinini, A. Marcelli, B. Marmiroli, H. Amenitsch, P. Schiavuta, P. Innocenzi,

*Adv. Mater.* Fabrication of mesoporous functionalized arrays by integrating deep x-ray lithography with dip-pen writing. **2008,** *20,* 1864-1869.

[67] D. A. Doshi, N. K. Huesing, M. Lu, H. Fan, Y. Lu, K. Simmons-Potter, B. G. Potter Jr., A. J. Hurd, C. J. Brinker. Optically defined multifunctional patterning of photosensitive thin-film silica mesophases. *Science* **2000**, *290*, 107-111.

[68] R. A. Pai, R. Humayun, M. T. Schulberg, A. Sengupta, J. N. Sun, J. J. Watkins. Mesoporous silicates prepared using preorganized templates in supercritical fluids. *Science*, **2004**, *303*, 507-510.

[69] H.-T. Chen, T. A. Crosby, M.-H. Park, S. Nagarajan, V. M. Rotello, J. J. Watkins. Accessibility of cylindrical channels within patterned mesoporous silica films using nanoparticle diffusion. *J. Mater. Chem.* **2009,** *1*, 70-74.

[70] G. W. Hillhouse, J. W. van Egmond, M. Tsapatsis, J. C. Hanson, J. Z. Larese. The interpretation of X-ray diffraction data for the determination of channel orientation in mesoporous films. *Microp. Mesop. Mater.* **2001**, *44-45*, 639-643.

[71] C. Jung, J. Kirstein, B. Plastchek, T. Bein, M. Budde, I. Frank, K. Mllen, J. Michaelis, C. Bruchle. Diffusion of oriented single molecules with switchable mobility in networks of long unidimensional nanochannels. *J. Am. Chem. Soc.* **2008**, *130*, 1638-1648.

[72] J. Feng, Q. Huo, P. M. Petroff, G. D. Stucky. Morphology definition by disclinations and dislocations in a mesostructured silicate crystal. *Appl. Phys. Lett.* **1997**, *71*, 1887-1889.

[73] X. Wu, K. Yu, C. J. Brinker, J. Ripmeester. Mesostructured mtes-derived silica thin film with spherical voids investigated by tem: 2. dislocations and strain relaxation. *Langmuir*, **2003**, *19*, 7289-7294.

[74] H. Yang, G. A. Ozin, C. T. Kresge. The role of defects in the formation of mesoporous silica fibers, films, and curved shapes. *Adv. Mater.* **1998**, *10*, 883-887.

[75] R. Wang, Q. Chen, F. R. Chen, J. J. Kai, L.-M. Peng. Defects and domain structures in SBA-16 mesoporous films with 3D cubic structure. *Chem. Phys. Lett.* **2005**, *411*, 463-467.

[76] H. Kozuka. Stress evolution on gel-to-ceramic thin film conversion. *J. Sol-Gel Sci. Technol.,* **2006**, *40*, 287-297.

[77] H. Miyata, T. Suzuki, A. Fukuoka, T. Sawada, M. Watanabe, T. Noma, K. Takada, T. Mukaide, K. Kuroda. Silica films with a single-crystalline mesoporous structure. *Nature Mater.* **2004**, *3*, 651-656.

[78] R. E. Williford, X. S. Li, R. S. Addleman, G. E. Fryxell, S. Baskaran, J. C. Birnbaum, C. Coyle, T. S. Zemanian, C. Wang, A. R. Courtney. Mechanical stability of templated mesoporous silica thin films. *Microp. Mesop. Mater.* **2005**, *85*, 260-266.

[79] J. D. Bass, D. Grosso, C. Boissière, E. Belamie, T. Coradin, C. Sanchez. Stability of mesoporous oxide and mixed metal oxide materials under biologically relevant conditions. *Chem. Mater.* **2007**, *19*, 4349-4356.

[78] E. Fois, A. Gamba, G. Tabacchi, S. Colucci, G. Martra. Ab initio study of defect sites at the inner surfaces of mesoporous silicas. *J. Phys. Chem. B*, **2003**, *107,* 10767-10772.

[79] T. Uchino. Structure and Properties of Amorphous Silica and Its Related Materials: Recent Developments and Future Directions. *J. Ceram. Soc. Jpn.* **2005**, *113*, 17-25.

[80] H. Cho, A. R. Felmy, R. Craciun, J. P. Keenum, N. Shah, D. A. Dixon. Solution State Structure Determination of silicate oligomers by $^{29}$Si NMR spectroscopy and molecular modeling. *J. Am. Chem. Soc.*, **2006**, *128*, 2324-2335.

[81] P. Innocenzi. Infrared spectroscopy of sol–gel derived silica-based films: a spectra-microstructure overview. *J. Non-Cryst. Solids*, **2003,** *316*, 309-319.

[82] P. Innocenzi, P. Falcaro, D. Grosso, F. Babonneau. Order-disorder transitions and evolution of silica structure in self-assembled mesostructured silica films studied through FTIR spectroscopy *J. Phys. Chem. B*, **2003,** *107*, 4711-4717.

[83] H. Fan, C. Hartshorn, T. Buchheit, D. Tallant, R. Assink, R. Simpson, D. J. Kissel, D. J. Lacks, S. Torquato, C. J. Brinker. Modulus–density scaling behaviour and framework architecture of nanoporous self-assembled silicas. *Nature Mater.* **2007**, *6*, 418-423.

[84] C. Kinowski, M. Bouazaoui, R. Bechara, L. Hench, J. M. Nedelec, S. J. Turrell. Kinetics of densification of porous silica gels: a structural and textural study. *Non-Cryst. Solids* **2001**, *291*, 143-152.

[85] O. Trofymluk, A. A. Levchenko, S. H. Tolbert, A. Navrotsky. Energetics of mesoporous silica: investigation into pore size and symmetry. *Chem. Mater.* **2005,** *17,* 3772-3783.

[86] J. D. Epping, B. F. Chmelka. Nucleation and growth of zeolites and inorganic mesoporous solids: Molecular insights from magnetic resonance spectroscopy. *Curr. Opin. Colloid Interface Sci.* **2006**, *11*, 81-117.

[87] L. Bollmann, V. N. Urade, H. W. Hillhouse. Controlling interfacial curvature in nanoporous silica films formed by evaporation-induced self-assembly from nonionic surfactants. i. evolution of nanoscale structures in coating solutions. *Langmuir*, **2007**, *23*, 4257-4267.

[88] V. N. Urade, L. Bollmann, J. D. Kowalski, M. P. Tate, H. W. Hillhouse. Controlling interfacial curvature in nanoporous silica films formed by evaporation-induced self-assembly from nonionic surfactants. ii. effect of processing parameters on film structure. *Langmuir*, **2007**, *23*, 4268-4278.

[89] Y. Hagiwara, A. Shimojima, K. Kuroda. Alkoxysilylated-derivatives of double-four-ring silicate as novel building blocks of silica-based materials. *Chem. Mater.* **2008,** *20,* 1147-1153.

[90] L. Zhang, H. C. L. Abbenhuis, Q. Yang, Y.-M. Wang, P. C. M. M. Magusin, B. Mezari, R. A. Van Santen, C. Li. Mesoporous organic-inorganic hybrid materials built using polyhedral oligomeric silsesquioxane blocks. *Angew. Chem. Int. Ed.* **2007**, *46*, 5003-5006.

[91] A. Walcarius, E. Sibottier, J. Ghanbaja. Electrochemically assisted self-assembly of mesoporous silica thin films. *Nature Mater.* **2007**, *6*, 602-608.

[92] Y. Yamauchi, M. Sawada, A. Sugiyama, T. Osaka, Y. Sakka, K. Kuroda. Magnetically induced orientation of mesochannels in 2D-hexagonal mesoporous silica films. *J. Mater. Chem.*, **2006**, *16*, 3693-3700.

[93] H. Fukumoto, S. Nagano, N. Kawatsuki, T. Seki. Photo-orientation of mesoporous silica thin films on photocrosslinkable polymer films. *Adv. Mater* **2005**, *17*, 1035-1039.

[94] H. Yang, A. Kuperman, N. Coombs, S. Mamiche-Afara, G. A. Ozin. Synthesis of oriented films of mesoporous silica on mica. *Nature* **1996,** *379*, 703-705.

[95] H. Miyata. Epitaxial growth of a surfactant-silica mesostructure on oriented polyimide films. *Microp. Mesop. Mater.* **2007**, *101*, 296-302.

[96] H. Miyata, K. Kuroda. Alignment of mesostructured silica on a langmuir-blodgett film. *Adv. Mater.* **1999**, *11*, 1448-1452.

[97] H. Miyata, K. Kuroda. Preparation of mesoporous silica films with fully aligned large mesochannels using nonionic surfactants. *Chem. Mater.* **2002**, *14*, 766-772.

[98] T. Suzuki, Y. Kanno, Y. Morioka, K. Kuroda. Facile unidirectional alignment of mesochannels in a mesoporous silica film on a freshly cleaved mica surface. *Chem. Comm.* **2008,** 3284-3286.

[99] H. Miyata, K. Kuroda. Preferred alignment of mesochannels in a mesoporous silica film grown on a silicon (110) surface. *J. Am. Chem. Soc.,* **1999**, *121*, 7618-7624.

[100] B. Su, Q. Lu. A facile method to prepare macroscopically oriented mesostructured silica film: controlling the orientation of mesochannels in multilayer films by air flow. *J. Am. Chem. Soc.* **2008,** *130,* 14356-14357.

[101] H. Miyata, T. Suzuki, M. Watanabe, T. Noma, K. Takada, T. Mukaide, K. Kuroda. Silica films having zigzag mesoporous structures with fixed kink angles. *Chem. Mater.* **2008**, *20*, 1082-1089.

[102] A. Yamaguchi, F. Uejo, T. Yoda, T. Uchida, Y. Tanamura, T. Yamashita, T. Norio. Self-assembly of a silica–surfactant nanocomposite in a porous alumina membrane. *Nat. Mater.* **2004**, *3*, 337-341.

[103] Q. Lu, F. Gao, S. Komarneni, T. E. Mallouk. Ordered SBA-15 nanorod arrays inside a porous alumina membrane. *J. Am. Chem. Soc.*, **2004**, *126*, 8650-8651.

[104] E. K. Richman, T. Brezesinski, S. H. Tolbert. Vertically oriented hexagonal mesoporous films formed through nanometre-scale epitaxy. *Nat. Mater.* **2008**, *7*, 712-717.

[105] V. R. Koganti, D. Dunph, V. Gowrishankar, M. D. McGehee, X. Li, J. Wang, S. E. Rankin. Generalized coating route to silica and titania films with orthogonally tilted cylindrical nanopore arrays. **2006**, *6*, 2567-2570.

[106] E. M. Freer, L. E. Krupp, W. D. Hinsberg, P. M. Rice, J. L. Hedrick, J. N. Cha, D. R. Miller, H. -C. Kim. Oriented mesoporous organosilicate thin films. *Nano Lett.*, **2005**, *5*, 2014-2018.

[107] R. Kennard, W. J. DeSisto, T. P. Giririjan, M. D. Mason. Intrinsic property measurement of surfactant-templated mesoporous silica films using time-resolved single-molecule imaging. *J. Chem. Phys.* **2008**, *128*, 134710.

[108] M. Etienne, A. Quach, D. Grosso, L. Nicole, C. Sanchez, A. Walcarius. Molecular transport into mesostructured silica thin films: electrochemical monitoring and comparison between *p6m*, *P6₃/mmc*, and P*m3n* structures. *Chem. Mater.*, **2007**, *19*, 844-856.

[109] A. Walcarius, A. Kuhn. Ordered porous thin films in electrochemical analysis. *Trends Anal. Chem.* **2008**, *27*, 593-603.

[110] C. Song, G. Villemure. Electrode modification with spin-coated films of mesoporous molecular sieve silicas. *Microp. Mesop. Mater.* **2008**, *44/45*, 679-689.

[111] M. Imperor-Clerc, P. Davidson, A. Davidson. Existence of a microporous corona around the mesopores of silica-based SBA-15 materials templated by triblock copolymers. *J. Am. Chem. Soc.* **2000**, *122*, 11925-11933.

[112] J. Kirstein, B. Platschek, C. Jung, R. Brown, T. Bein, C. Bräuchle. Exploration of nanostructured channel systems with single-molecule probes *Nat. Mater.* **2007***, 6,* 303-310.

[113] Y. Fu, F. Ye, W. G. Sanders, M. M. Collinson, D. A. Higgins. Single molecule spectroscopy studies of diffusion in mesoporous silica thin films. *J. Phys. Chem. B* **2006**, *110*, 9164-9170.

[114] H. K. M. Tanaka, Y. Yamauchi, T. Kurihara, Y. Sakka, K. Kuroda, A. P. Mills Jr. Exploration of a standing mesochannel system with antimatter/matter atomic probes. *Adv. Mater.* **2008**, *20*, 4728-4733.

[115] G. J. A. A. Soler-Illia, C. Sanchez, B. Lebeau, J. Patarin. Chemical strategies to design textured materials: from microporous and mesoporous oxides to nanonetworks and hierarchical structures. *Chem. Rev.*, **2002**, *102*, 4093-4138.

[116] Q. Huo, D. I. Margolese, U. Ciesla, D. K. Demuth, P. Feng, T. E. Gier, P. Sieger, A. Firouzi, B. F. Chmelka, F. Schüth, F., G. D. Stucky. Organization of organic molecules with inorganic molecular species into nanocomposite biphase arrays. *Chem. Mater.* **1994**, *6*, 1176-1191.

[117] Q. Huo, D. I. Margolese, U. Ciesla, P. Feng, T. E. Gier, P. Sieger, R. Leon, P. M. Petroff, F. Schüth, F., G. D. Stucky. 1.Generalized synthesis of periodic surfactant/inorganic composite materials. *Nature* **1994**, *368*, 317-321.

[118] S. A. Bagshaw, E. Prouzet, T. J. Pinnavaia. Templating of mesoporous molecular sieves by nonionic polyethylene oxide surfactants. *Science* **1995**, *269*, 1242-1244.

[119] E. K. Richman, T. Brezesinski, S. H. Tolbert. Vertically oriented hexagonal mesoporous films formed through nanometre-scale epitaxy. *Nat. Mater.* **2008**, *7*, 712 – 717.

[120] P. Liu, S.-H. Lee, C. E. Tracy, J. A. Turner, J. R. Pitts, S. K. Deb. Electrochromic and chemochromic performance of mesoporous thin-film vanadium oxide. *Solid State Ion.* **2003**, *165*, 223-228.

[121] T. Brezesinski, B. Smarsly, K. Iimura, D. Grosso, C. Boissire, H. Amenitsch, M. Antonietti, C. Sanchez. Self-assembly and crystallization behavior of mesoporous,

crystalline $HfO_2$ thin films:a model system for the generation of mesostructured transition-metal oxides. *Small*, **2005**, *8-9*, 889-898.

[122] T. Brezesinski, D. F. Rohlfing, S. Sallard, M. Antonietti, B. M. Smarsly. Highly crystalline $WO_3$ thin films with ordered 3D mesoporosity and improved electrochromic performance. *Small* **2006**, *2*, 1203-1211.

[123] M. Lundberg, B. Skarman, F. Cesar, R. L. Wallenberg. Mesoporous thin films of high-surface-area crystalline cerium dioxide. *Microp. Mesop. Mater.* **2002**, *54*, 97-103.

[124] X. Xu, B. Z.Tian, J. L. Kong, S. Zhang, B. H. Liu, D. Y. Zhao. Ordered mesoporous niobium oxide film: A novel matrix for assembling functional proteins for bioelectrochemical applications. *Adv. Mater.* **2003**, *15*, 1932-1932.

[125] G. J. A. A. Soler-Illia, A. Louis, C. Sanchez. Synthesis and characterization of mesostructured titania-based materials through evaporation-induced self-assembly *Chem. Mater.* **2002,***14*, 750-759.

[126] F. Bosc, A. Ayral, P. A. Albouy, C. Guizard. A simple route for low-temperature synthesis of mesoporous and nanocrystalline anatase thin films. *Chem. Mater.* **2003**, *15*, 2463-2468.

[127] K. L. Frindell, M. H. Bartl, A. Popitsch, G. D. Stucky. Sensitized Luminescence of Trivalent Europium by Three-Dimensionally Arranged Anatase Nanocrystals in Mesostructured Titania Thin Films. *Angew. Chem., Int. Ed.* **2002**, *41*, 959-962.

[128] A. Calvo, P. C. Angelomé, V. M. Sanchez, D. A. Scherlis, F. J. Williams, G. J. A. A. Soler-Illia. Mesoporous aminopropyl-functionalized hybrid thin films with modulable surface and environment-responsive behavior. *Chem. Mater.*, **2008**, *20*, 4661–4668.

[129] M. Sakurai, A. Shimojima, M. Heishi, K. Kuroda. Preparation of Mesostructured Siloxane–Organic Hybrid Films with Ordered Macropores by Templated Self-Assembly. *Langmuir*, **2007**, *23*, 10788-10792.

[130] G. A. Ozin, L. Cademartiri. Nanochemistry: What is next?. *Small,* **2009**, *11*, 1240-1244.

# Chapter 2:
# Characterization techniques

Mesoporous materials, in particular mesoporous thin films, are a very challenging class of specimens because of their intrinsic chemical and morphological complexity that requires advanced and complementary analytical techniques. In this chapter we review the fundamentals of the main characterizations applied in the experimental section. We have divided this chapter in five sections (infrared based techniques, X-ray based techniques, microscopic techniques, spectroscopic ellipsometry and UV-Visible based techniques) according to the nature and the importance of the characterization techniques used in the experiments.

In the past years the study of the machinery of EISA required the development of *in situ* techniques to follow mesophase formation and evolution during self-assembly. Small angle X-ray scattering (SAXS) and X-ray diffraction (XRD) on thin film have been employed and implemented to carry out this purpose, but, using these techniques, only information about micelle formation and self-organization have been obtained. In fact these analysis do not provide information concerning the chemical changes in the as-deposited film; therefore, *in situ* time resolved infrared spectroscopy (FTIR) has been recently developed. This technique has proved to be a very useful and versatile tool to detect solvent evaporation and all the processes related to water adsorption and evaporation during film formation. Despite of the big results obtained with SAXS, the data interpretation is still not straightforward and some ambiguities in the symmetry of the mesophase can be avoided only by using SAXS in combination with atomic force microscopy (AFM), field emission scanning electron microscopy (FE-SEM) or transmission electron microscopy (TEM). An important spectroscopic techniques that has been recently developed to study mesoporous films, is the ellipsometry. Even if this techniques can be used to extrapolate data concerning the pore volumetric fraction, pore size and the Young modulus of a porous film, in this doctoral work spectroscopic ellipsometry is mainly used for standard characterization obtaining data such as the refractive index and film thickness. Finally optical techniques, such as UV-Visible absorption spectroscopy and spectrofluorimetry, have been employed to study the pore functionalization with inorganic chromophores or organic dyes.

## 2.1 Infrared based technique

### 2.1.1 Fourier transform infrared spectroscopy

Infrared (IR) spectroscopy is related to the interaction of IR radiation with matter. More specifically, it is based on the coupling between the electromagnetic radiation and the resonance frequencies of vibration of chemical bonds (vibrational modes). The infrared portion of the electromagnetic spectrum ranges from 12800 to 10 $cm^{-1}$, corresponding to wavelengths 0.78 to 1000 μm.[§] The IR portion is divided into three regions: the near-, mid- and far- infrared, named for their relation to the visible spectrum. The far-infrared, (400–10 $cm^{-1}$) lying adjacent to the microwave region, has low energy and may be used for rotational spectroscopy. The mid-IR region (4000–400 $cm^{-1}$) may be used to study the fundamental vibrations and associated rotational-vibrational structure. The higher energy near-IR (14000–4000 $cm^{-1}$) can excite overtone or harmonic vibrations.

In Fourier transform infrared spectroscopy (FTIR), spectra are collected by measuring the temporal coherence of a radiative source. In other words, instead of varying the wavelength of the electromagnetic radiation, Fourier transform spectroscopy exposes the sample to a single pulse of broad bandwidth IR radiation and measures the response. The resulting signal is a direct measurement of the temporal coherence of the light and contains a composite of all possible frequencies. In this way the Fourier transform spectrometer can produce the same kind of spectrum as a conventional dispersive spectrometer, but in a much shorter time.

The essential piece of optical hardware in a FTIR spectrometer is the interferometer. This component simultaneously allows source radiation of all wavelengths to reach the detector. **Figure 2.1** illustrates how an interferometer works: radiation from the source is focused on a beam splitter that transmits half of the radiation to a fixed mirror, while reflecting the other half to a movable mirror. The radiation recombines at the beam splitter, where constructive and destructive interference determines, for each wavelength, the intensity of light reaching the detector. As the moving mirror changes position, the wavelengths experiencing maximum constructive interference and maximum destructive interference also change. The signal at the detector, called *interferogram*, shows intensity as a function of the moving mirror position, expressed in units of distance or time. The interferogram is mathematically converted, by a process

[§] The wavenumber, unit length $cm^{-1}$, is defined as the reciprocal of the wavelength expressed in cm, and is traditionally employed in infrared spectroscopies.

called a Fourier transform, to the normal spectrum (also called a frequency domain spectrum) of intensity as a function of the radiation energy.

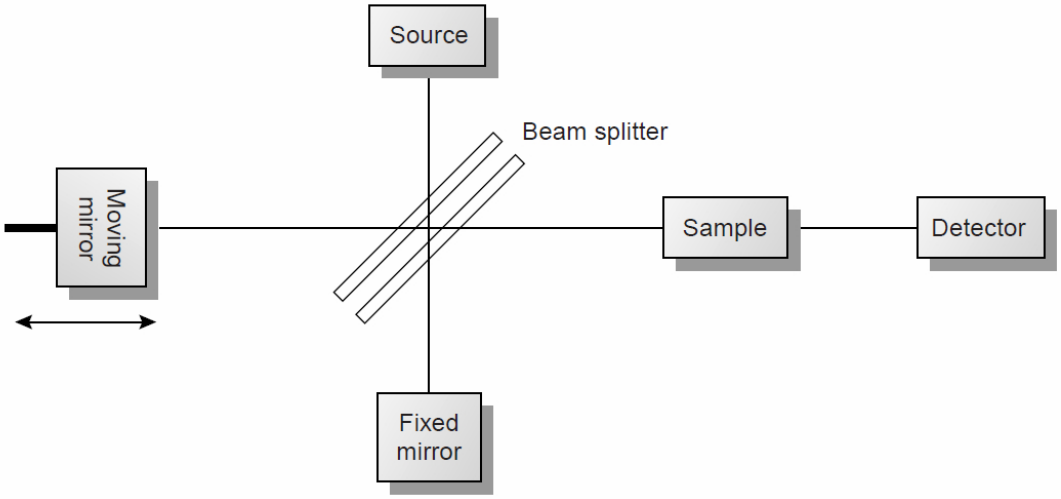


Fig. 2.1 Block diagram of an interferometer.

FTIR spectrometers have many characteristic features which make it superior to conventional dispersive IR. First of all, FTIR spectrometers have a built-in wavenumber calibration of high precision (practically about 0.01 $cm^{-1}$) due to the presence of the interferometer. Another advantage arises from the fact that the circular apertures used in FTIR spectrometers have a larger area than the linear slits used in grating spectrometers, thus enabling higher throughput of radiation. Finally in FTIR, all frequencies emanating from the IR source impinge simultaneously on the detector. This accounts for the so-called multiplex advantage. The measuring time in FTIR is the time which is necessary to move the interferometer mirror over a distance proportional to the desired resolution. As the mirror can be moved very fast, complete spectra can be measured in fractions of a second, so this is a great advantage for fast time-resolved measurements. The combination of all these advantages allows the construction of interferometers having much higher resolving power than dispersive instruments.

Data acquisition yields the digitized interferogram *I(x)*, which must be converted into a spectrum by means of a Fourier transformation (FT). Generally, the FT determines the frequency components making up a continuous waveform numerically calculated by a computer. The final spectrum is obtained from the interferograms not only by

performing the FT, but also by adding other mathematical operations, such as: zero-filling, phase correction and apodization, but they will not be discussed here.

In this doctoral thesis, FTIR absorbance spectra have been used to study chemical properties of the self-assembled thin films. To obtain an absorbance spectrum, four steps are necessary: first an interferogram measured without sample in the optical path is Fourier transformed and yields the so-called single channel reference spectrum $R(\nu)$. Secondly an interferogram measured with a sample in the optical path is Fourier transformed and yields the so-called single channel sample spectrum $S(\nu)$; then the final transmittance spectrum $T(\nu)$ is defined as the ratio $T(\nu)=S(\nu)/R(\nu)$. Finally the absorbance spectrum $A(\nu)$ can be obtained by the equation (2.1).

$$A = -\log_{10} T = \log_{10}\left(\frac{I_0}{I}\right) \tag{2.1}$$

where $T$ is the transmittance, $I_0$ and $I$ are the intensities of the incident beam and of the beam transmitted through the sample, respectively.

### 2.1.2 Measurements at DAΦNE and ELETTRA

Many IR measurements presented in this thesis have been performed at the SINBAD (Synchrotron INfrared Beamline At DAΦNE) beamline installed at the DAΦNE synchrotron of Laboratori Nazionali di Frascati (Istituto Nazionale di Fisica Nucleare, INFN).[2]

The SINBAD beamline (**Figure 2.2**) extracts IR radiation from the electron beam passing through a bending magnet of the DAΦNE electron-positron storage ring. The beam energy is 0.51 MeV and current can reach values up to 1.8 A, which makes this source one of the most brilliant and brightest in the world. The first mirror of the beamline allows the collection of IR radiation from the near-IR through the far-IR, the beam is then collimated and focused into the laboratory by 6 gold mirrors where a Bruker Equinox 55 FTIR interferometer is installed. The interferometer has been modified to work in a maximum vacuum of $10^{-5}$ mbar.

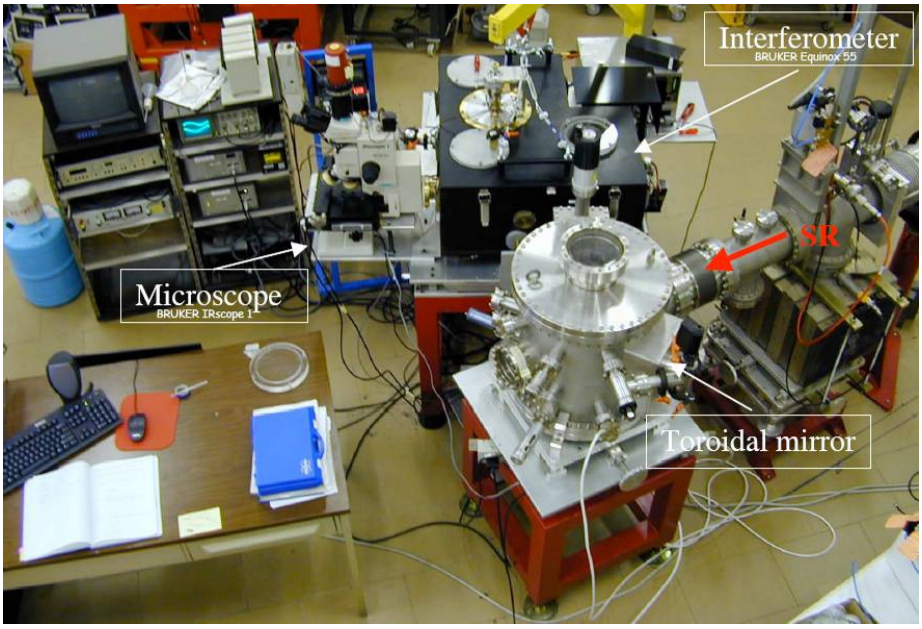


Fig. 2.2 Picture of the SINBAD beamline at DAΦNE.

## 2.2 X-ray based techniques

### 2.2.1 X-ray diffraction

X-ray diffraction is a wide used techniques to perform structural characterisation of solid materials. When an electromagnetic wave impinges on the sample, it interacts with the electron clouds and undergoes elastic scattering phenomena. If the electron density is periodically arranged, as in a crystal lattice, the scattered waves add up and give constructive and destructive interference, and their intensity is recorded by a detector as a function of the exit angle. Diffraction effects are generally only noticeable for waves whose wavelength is in the order of the feature size of the diffracting objects, thus for crystal lattices with periodicity in the order of the angstroms, X-rays are used. A visual way to rationalise X-ray diffraction by an ordered crystal lattice is provided by the so-called Bragg's interpretation (**Figure 2.3**). A given crystal is constituted by regular arrays of atoms spaced by fixed distances *d*. The crystal can be decomposed into any number of different planes, due to the periodicity of the crystal lattice. As the wave enters the crystal, some parts of the wave are reflected by the first layer, while the rest continues through to the second layer, and so on. By the definition of constructing interference, the separately reflected waves remain in phase if the difference in the path length of each wave is equal to an integer multiple of the wavelength.

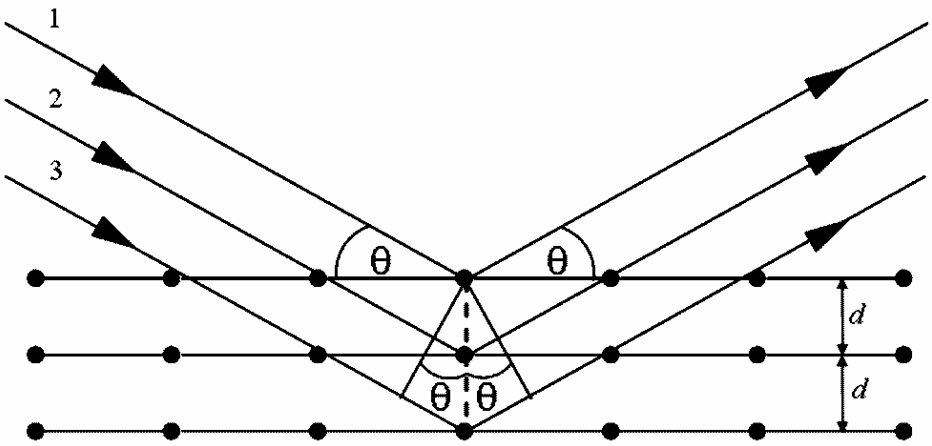


Fig. 2.3 Schematic representation of the Bragg's diffraction.

This condition is expressed by the formula 2.2, the well-known Bragg's law:

$$2d_{hkl} \sin\theta = m\lambda \qquad (2.2)$$

where $d_{hkl}$ is the periodicity of a given family hkl of planes (*d*-spacing), θ is the incidence and exit angle, m is an integer and λ is the wavelength.[3]

### 2.2.2 Small angle X-ray scattering at ELETTRA and ESRF

Mesostructured materials show an ordered arrangement of the mesophase which provides an electron density contrast between the inorganic and the organic phase. As a consequence, the interaction of X-ray radiation with mesostructured and mesoporous materials gives diffraction and information on the symmetry of the ordered mesophase can be inferred. Since the feature size of a mesostructure is typically ~10 nm, using incident X-rays of wavelength ~1 Å will give diffraction at 2θ angles in the range 0.1–1°. On this principle are based small-angle X-ray scattering (SAXS) techniques. The "small-angle" refers to the angular range of the scattered beams, containing information on the structure in the reciprocal space in the nanometre range. SAXS on mesostructured materials is often performed at synchrotron facilities.

Regarding to mesostructured films, there are a few aspects of synchrotron radiation that have made small angle scattering studies very effective: very small beam divergence, high beam flux, and in some cases energy tunability. It is crucial to have small beam divergence in order to isolate weak scattering at very small angles from the direct beam which is orders of magnitude stronger. The flux of a synchrotron source is usually several orders of magnitude higher than those from conventional X-ray sources,

therefore a diffraction pattern can be acquired in short times, typically on the order of 500 ms, making it possible to perform, for instance, time-resolved *in situ* experiments during dip-coating.

The most part of the SAXS experiments presented in this doctoral work were conducted at the Austrian beamline at the ELETTRA synchrotron in Trieste[4] and a minor part of them at ID01 installed at the ESRF synchrotron in Grènoble. The first beamline has a the 57-pole NdFeB hybrid wiggler as the photon source. The wiggler delivers a very intense radiation between 4 and 25 keV, of which three discrete energies (5.4, 8 and 16 keV) can be selected by a flat double crystal (111 Si) monochromator in optics hutch 1 and focused by a double focusing toroidal mirror in optics hutch 2 (**Figure 2.4**).

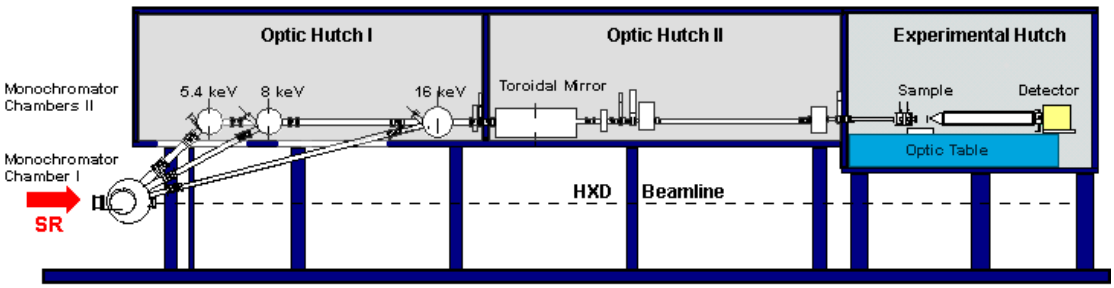


Fig. 2.4 Scheme of the Austrian SAXS beamline at ELETTRA.

The entire beamline is controlled via a software interface developed with LabView programme. The optical table in the experimental hutch allows optimisation of the sample-to-detector distance with respect to SAXS resolution and sample size setup, as well as installation of specialised sample equipment (**Figure 2.5**). A two-dimensional CCD detector (Photonic Science, UK) is used for data acquisition. Before starting a measurement session, the sample-to-detector distance is adjusted in order to ensure that the diffracted beams were well separated from the direct beam, and a sufficiently large area of the reciprocal space be sampled by the CCD detector. The beam stopper has to be correctly positioned for preventing the direct beam from hitting the detector, as this may cause irreversible damage to the CCD array.

The ID01 beamline is mainly dedicated to diffuse scattering experiments near a chemical element's absorption edge using small and/or wide-angle techniques (SAXS and/or WAXS). The optics consists of a double-crystal monochromator located between two mirrors. This arrangement provides a fixed-exit monochromatic beam and maintains the focal spot constant during energy tuning.

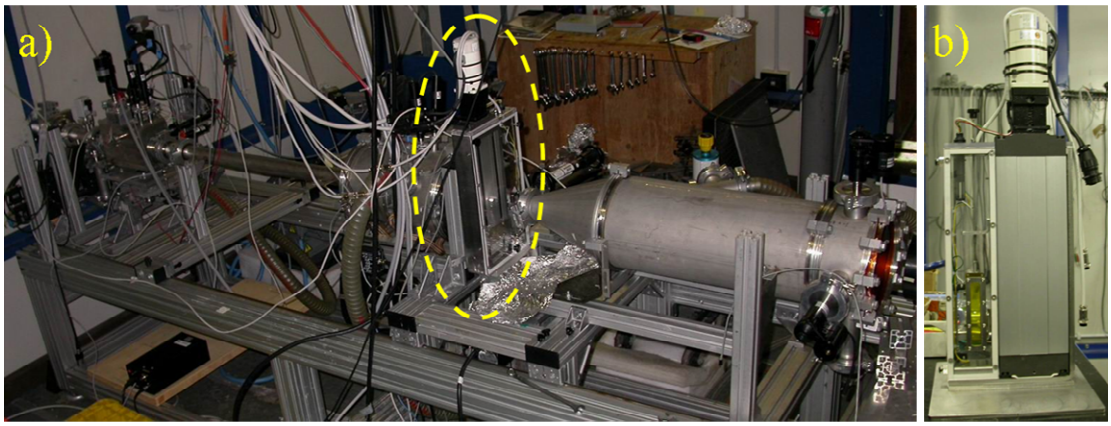


Fig. 2.5 a) Picture of the Austrian SAXS beamline equipped with a dip-coater for *in situ* experiments (indicated by the dotted yellow oval). b) Detail of the dip-coater.

The beamline can operate in a 2 - 42 keV energy range with the possibility to rapidly select several beam energies by adjusting on-line the optics and without changing the set-up in the experimental hutch. During measurements, the specimens are placed on a sample-holder, called "Huber tower", which has up to 7 different translational and rotational degree of freedom and the diffraction patterns are collected on a 2 dimensional CCD detector (Princeton).

In a typical SAXS analysis, the sample is placed on the sample holder, which can be rotated via a servo motor from the control room, so that the angle of incidence can be varied. It is of utmost importance that a diffraction pattern of a calibration standard be acquired for each setup of the beamline. Diffraction standards provide a tool to determine accurately the beam centre position and the sample-to-detector distance. Without such calibration, it is not possible to perform quantitative data analysis such as cell constant calculation. We used a silver behenate powder standard ($CH_3(CH_2)_{20}COOAg$, d-spacing = 58.38 Å) in a capillary glass:[5] the ring-like diffraction pattern is used in the data analysis software (**Figure 2.6**). Diffraction patterns are acquired using the CCD detector provided with a software-triggered fast shutter positioned upstream.

The diffraction pattern of a mesostructured film depends not only on the mesostructure symmetry and orientation, but also on the experimental measurement conditions, such as the angle of incidence. In general, the model of the monocrystal-like mesostructure is not true for "real" films. These are almost always composed by micron-sized

mesostructured domains which show an orientational disorder around the axis perpendicular to the substrate, this is a feature common to nearly all mesostructured films that is also called planar disorder.

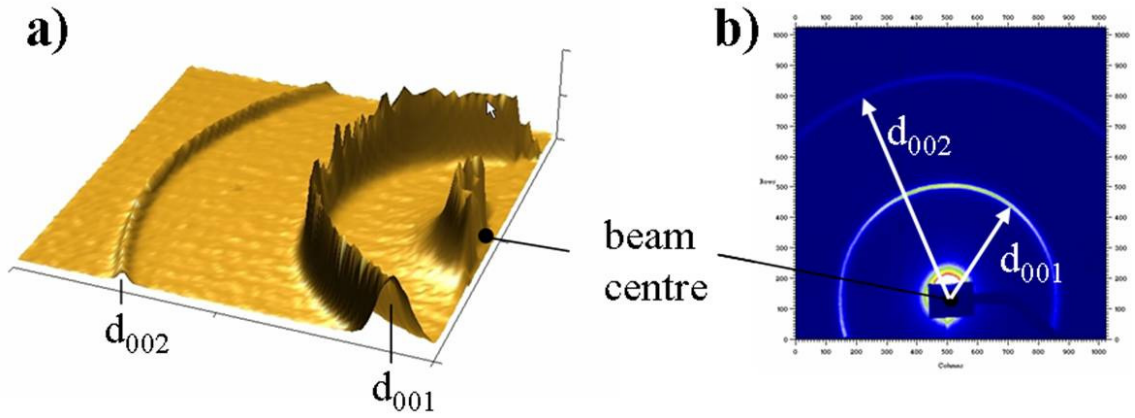


Fig. 2.6 3D and 2D representation of a SAXS pattern obtained from silver behenate powder (a and b respectively).

Thus, mesostructured films have typically out-of-plane order, but lack in-plane order. This is true if we consider a sufficiently large region investigated by the impinging beam. There are essentially two configurations used in the acquisition of SAXS patterns of mesostructured films: the angle of incidence of the X-ray beam impinging on the sample may be set to either small angle (slightly above the critical angle, i.e. 0.2–0.3°) or perpendicular to the film surface (90°). These two configurations are referred to as grazing and transmission incidence, respectively, and yield information on the out-of-plane and in-plane mesostructure order. When the sample is in grazing incidence (grazing incidence SAXS, or GISAXS) the detector acquires out-of-plane reflections that are not accessible by transmission mode, whereas in transmission mode in-plane reflections are sampled which cannot be recorded in grazing incidence. Due to the lack of global in-plane order, the reciprocal lattice is a collection of concentric rings, centred on the axis perpendicular to the substrate. These rings can be thought as the infinite replication of the spots around the axis perpendicular to the substrate and intersecting the origin. The scattering events occurring during the measurement can be modelled by using the Ewald construction.[3] When the Ewald sphere slices the ring-like reciprocal lattice in grazing incidence, the intersection is constituted by spots, whereas in transmission mode the intersection is constituted by rings (**Figure 2.7**), thus the detector records spots in the former case and rings in the latter case.[6] The choice of substrate depends on whether we are working in grazing incidence or transmission mode. In

transmission mode the diffracted beams has to travel through the substrate and towards the detector, therefore a thick substrate (e.g. 400 µm Si wafer, soda-lime glass) cannot be used and thin substrates must be resorted to (e.g. 50 µm Si wafer).

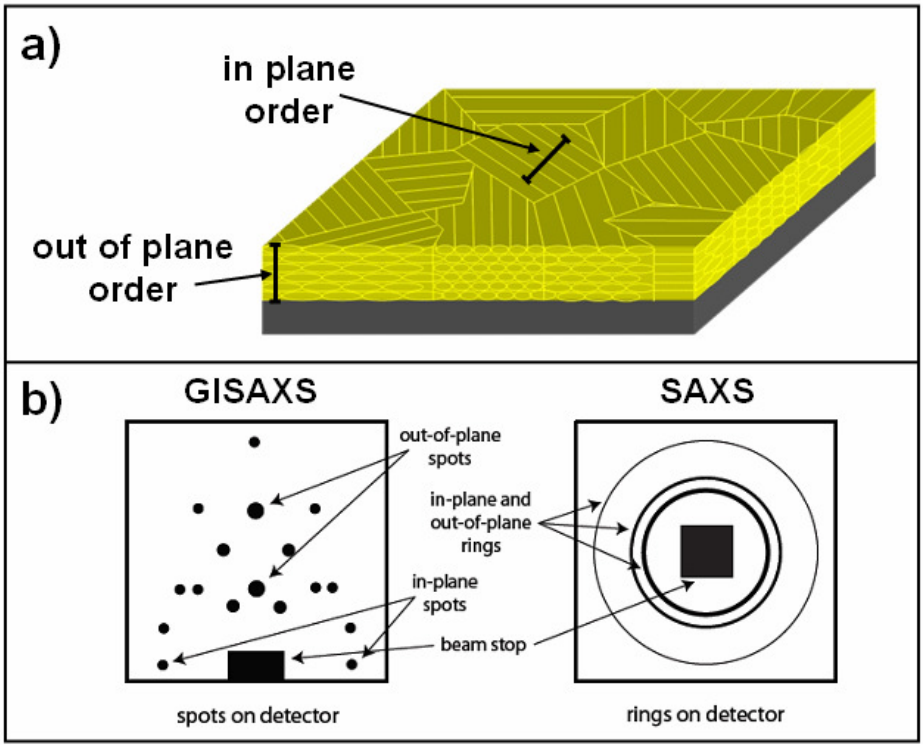


Fig. 2.7 a) Sketch of a real mesostructure with in-plane misorientation of ordered mesostructured domains. b) This type of organized structures produces spots or rings on SAXS pattern depending whether the measurement is performed in grazing incidence (left) or transmission mode (right).

In fact, for a 8 keV radiation (corresponding to a wavelength of 1.54 Å) the intensity transmitted through a 400 µm Si wafer is about one thousandth of the incident intensity. Using a 50 µm Si wafer however the transmitted intensity fraction increases to 0.5. In grazing incidence, substrate thickness is not an issue, as the diffracted beams do not pass through the substrate, therefore either thick or thin substrates can be used.

Diffraction patterns taken in grazing incidence and transmission mode give a first hint on the presence of an ordered mesostructure and its planar disorder. A first visual inspection can give a clue on the mesostructure symmetry group if this is known from the literature or previous data, especially for a trained eye, but a more accurate attribution of the pattern to a space group can be performed only by software simulations. Diffraction patterns can be stored in 12-bit TIFF files which can readily manipulated with proper software. During this doctoral work Fit2d[7] programme, which

includes important image analysis tools such as intensity scaling, one-click d-spacing calculation, 1-d integration, calibration and correction for detector distortions, has been used for both interactive and batch data processing.

## 2.3 Microscopic techniques

### 2.3.1 Transmission electron microscopy

Transmission electron microscope (TEM) is one of the most powerful instruments for investigating the microstructure of materials. By TEM the fine-scale microstructures can be examined in samples sufficiently thin to facilitate transmission of a beam of electrons without a great loss of intensity. The schematic diagram of a TEM is presented in **Figure 2.8**. Electrons are accelerated by a tungsten filament or a $LaB_6$ crystal through an evacuated column containing an assembly of condenser, objective and projector lenses.[8] The interaction of the electron beam with the sample and the subsequent formation of an image can be treated with Abbe's theory of image formation.

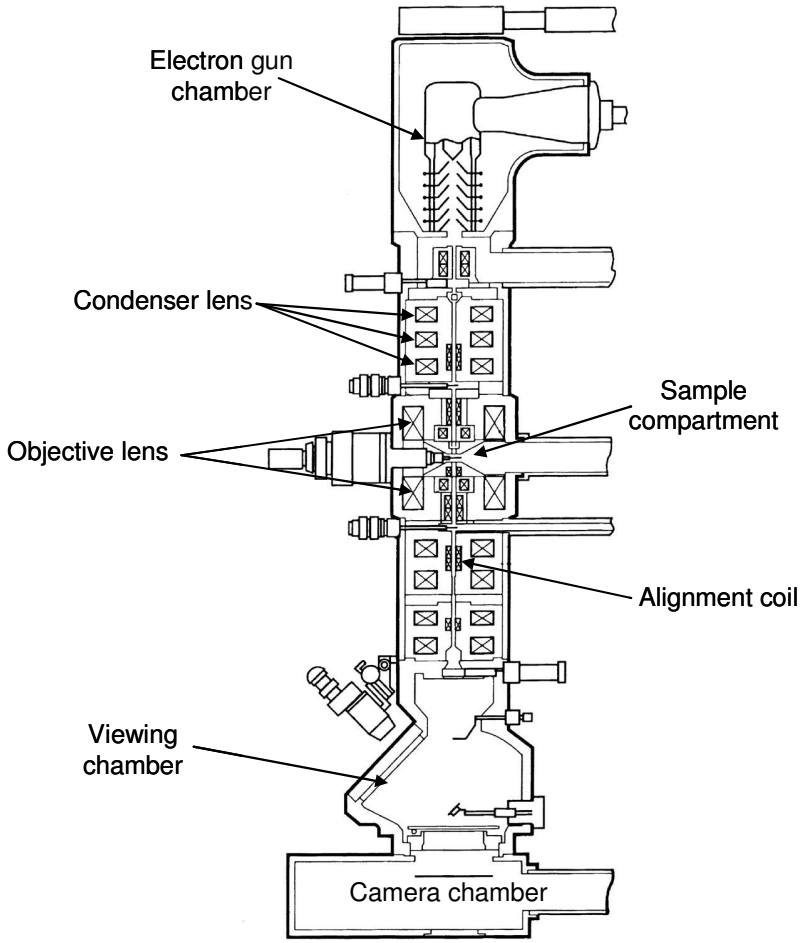


Fig. 2.8 Scheme of a typical TEM microscope.

According to this theory, the incident electromagnetic wave impinges on the grating object and is diffracted, a diffraction pattern then forms in the back focal plane, which corresponds to the object's Fourier transform. The diffraction pattern is then reconverted into a real image in the image plane by the objective lens through an inverse Fourier transform. The intermediate lens then produces a second intermediate image which is magnified at the viewing screen by the final projector lens.

Theoretically, very high resolution can be reached, but in practice this is limited by strong aberration effects, and resolutions on the order of the Å are obtained only in high resolution instruments. Because electron are used, electrostatic lenses are employed to deflect the electron trajectory. In addition, the wavelength of the incident electron beam can be tuned by varying the accelerating voltage. The resolution of the image depends on the number of grating orders that are transmitted through the optical system. Interchangeable objective apertures, typically ≈ 50 μm to ≈ 200 μm are positioned close to the back focal plane of the objective lens to enhance image contrast. If an objective aperture intercepts all the diffracted beams and allows only the direct beam to pass, deficiency contrast occurs and a bright field image is formed. Alternatively, the objective aperture can be used to select a single diffracted beam to produce a dark field image.

TEM in mesoporous films can give direct high quality images of the ordered porous structure. Typically, the film is cut into μm-thick slices by a microtome, and further thinned by $Ar^+$ ion beam milling, until a hole is dug at the centre of the sample[9]. Measurements are then performed close to the edge of the hole, so that a region of the sample with the desired thickness can be observed by moving the sample stage. A more rapid but less effective method is to scratch a film from its substrate and disperse the fragments in an organic solvent. Mesoporous films which have undergone full removal of the template generally give better quality images than samples where the organic mesophase is still present within the film: this is because the former has a high electronic contrast (inorganic-void), whereas the latter provides a lower electronic contrast (inorganic-organic). Furthermore, a mesostructured film that has not undergone thermal treatment is mechanically unstable, and can collapse when the film is cut and drilled before TEM measurements.

TEM can be regarded as a structural technique complementary to SAXS. In fact, in SAXS the probed region extends on the volume of matter interested by the interaction with the impinging X-ray beam, of characteristic length ranging from 500 μm to several

mm. Conversely, TEM describes the structure on a very local scale, typically few tens of nm to ≈ 1 μm. When determining the mesostructure symmetry, TEM measurements may be misleading, in that only a localised area of the specimen is sampled: this can be the case when the film is not homogeneous (i.e. one can find a "lucky" ordered area while the rest of the sample is more or less disordered, or vice versa). Furthermore, different planes merge due to the depth of field of the electron microscope, so that three-dimensional structures are necessarily collapsed into two-dimensional images, and this can lead to wrong conclusions: for instance, cylindrical pores may be observed when in fact this is the superposition of planes where the pores are most densely packed. In order to have reliable information on mesostructure symmetry, different projection planes are accessed by multiple TEM observations, such as cross-section and in-plane views. Thus, the right mesophase symmetry can be sorted out by careful inspection or software simulation. For example, if 6-fold symmetry axes are observed in one image, a two-dimensional hexagonal symmetry is the first guess, with ordered stacks of cylindrical pores. But if a 4-fold symmetry axis is observed in the same sample, one has to call into question the previous guess and suppose the presence of a cubic unit cell unless we are in the presence of multiple phases, in which case we may be observing different domains having different mesostructures. These observations underline, once again, the key importance of having the support of SAXS measurements.

Mesoporous films can be investigated by acquiring TEM images in scanning mode (Scanning Transmission Electron Microscopy, STEM) in which a small electron probe (about 1 nm FWHM) is rastered over the sample. In STEM, a bright field detector is placed in a conjugate plane to the back focal plane to intercept the direct beam while a concentric annular dark field detector intercepts the diffracted electrons. In STEM images the image contrast is proportional to the local atomic number, therefore the contrast between pores and inorganic framework is highly enhanced with respect to conventional bright-field mode. Furthermore, this technique causes a lower radiation damage to the investigated sample, therefore systems that require special care can be studied (STEM is routinely used for biological research).

### 2.3.2 Scanning electron microscopy

Scanning electron microscopy (SEM) is one of the most versatile and widely used among the surface analytical techniques as it allows to be studied both the morphology

and composition of various materials in modern science. It is considered a relatively rapid, inexpensive, and basically non-destructive approach to surface analysis. Nowadays there are many different types of scanning electron microscope designed for specific purposes ranging from routine morphological studies to high-speed compositional analyses or the study of environment-sensitive materials. The main advantages of SEM are the high lateral resolution (1–10 nm), large depth of focus (typically 100 mm at x1000 magnification), and the numerous types of electron–specimen interaction that can be used for imaging or chemical analysis purposes. In contrast to transmission electron microscopy, specimens of largely varying sizes can be examined without elaborate sample preparation. The scanning electron microscope consists of an electron–optical column mounted on a vacuum chamber as depicted in **Figure 2.9**.[10] An electron gun is placed on top of this column; this gun usually consists of a thermionic cathode made of tungsten or $LaB_6$. The pressure in the specimen chamber is $10^{-3}$ – $10^{-5}$ Pa. This pressure is much lower than the saturation vapour pressure of water, requiring special preparation of water-containing biological samples.
During this doctoral work, a modern instruments operating at low voltages and high magnifications has been used: in this equipment the thermionic source is replaced by a field-emission gun (FEG), yielding a higher brightness and lower energy spread in the beam. Field-emission sources require a better vacuum of $10^{-7}$ – $10^{-8}$ Pa as opposed to $10^{-4}$– $10^{-6}$ Pa for thermionic emitters but increase the lateral resolution under the operating conditions. The electron beam formed in the electron gun is demagnified by a set of magnetic and /or electrostatic lenses. The condenser lenses are then used to change the beam divergence angle and thus the probe current. Changes in probe current, in turn, result in changes in probe diameter. The objective lens is finally used to focus the electron beam into a fine spot on the sample surface. The signals generated in the specimen by the incident electron beam are monitored synchronously with the raster scan. The magnification and scan velocity are altered by changing the scan coil excitation. Upon entering the sample, the electron beam interacts with the sample, and both electron and photon signals are generated. These signals are collected by dedicated detectors, amplified, and displayed. The electron beam has many interactions with the specimen; when an electron enters a solid, it is subject to electrostatic interactions with the nuclei and electrons of the target atoms. The angle of the incident electrons is changed in the solid owing to elastic scattering by the shielded target nuclei, and the

electrons lose energy owing to inelastic scattering from the core and valence electrons of the target atoms.

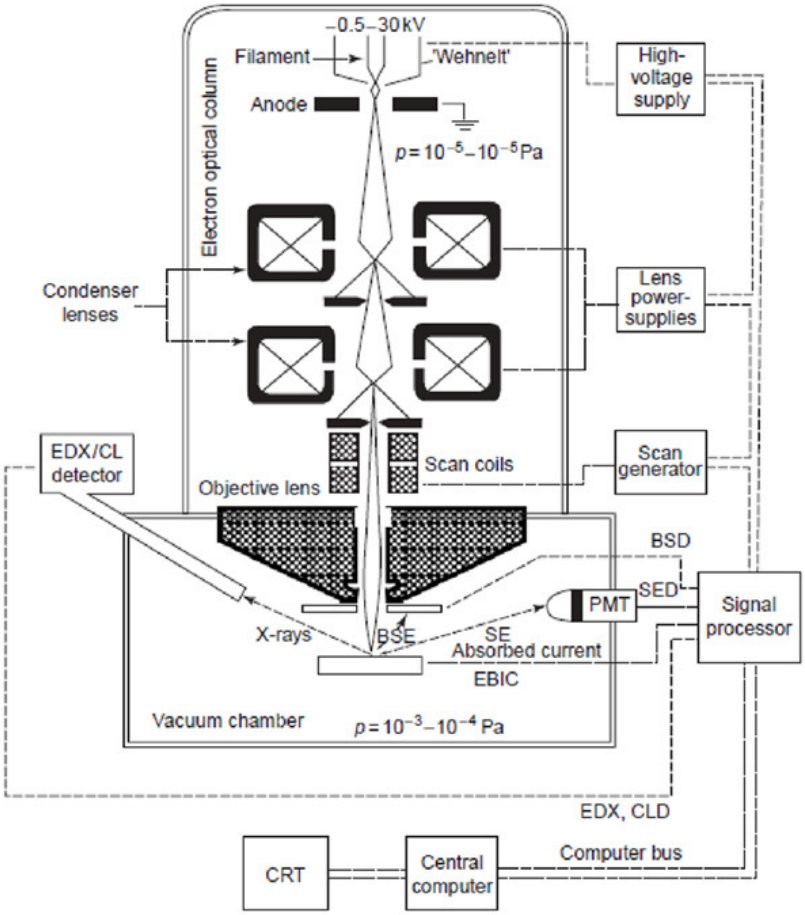


Fig. 2.9 Scheme of a typical SEM microscope.

Besides, because of the elastic scattering events in the solid, a fraction of the incident electrons is scattered back into the vacuum. These electrons are called *backscattered electrons* (BSEs), and the backscatter yield, Z, depends on the target atomic number, Z. By convention the term BSE applies to all electrons that escape into the vacuum with energy E > 50 eV. During inelastic scattering events, a primary electron can ionize target atoms. The ionized atoms fall back into a lower energy state with the emission of Auger electrons or X-rays. The energy of the X-rays is characteristic of the atom involved and is used in most scanning electron microscopes for elemental identification. Measurements of the energies or wavelengths of these X-rays gives information about the chemical composition of the specimen. Depending on whether an energy-dispersive or wavelength-dispersive X-ray analyzer is mounted on a SEM equipment, it is possible to perform the so called EDX or WDX spectrometry.

During inelastic scattering events with the incoming electron beam, some excited valence electrons called *secondary electrons* (SEs) can be formed. By convention, all electrons that leave the surface with energy E < 50 eV are called SEs. Because of the small mean escape depth λ of an SE (λ = 2–10 nm), only those electrons that are generated close to the surface can escape into the vacuum and be detected. This offers the possibility of obtaining high-lateral resolution SE images. The topographic contrast observed in most SE micrographs gives these images a clear 3D appearance (**Figure 2.10**).

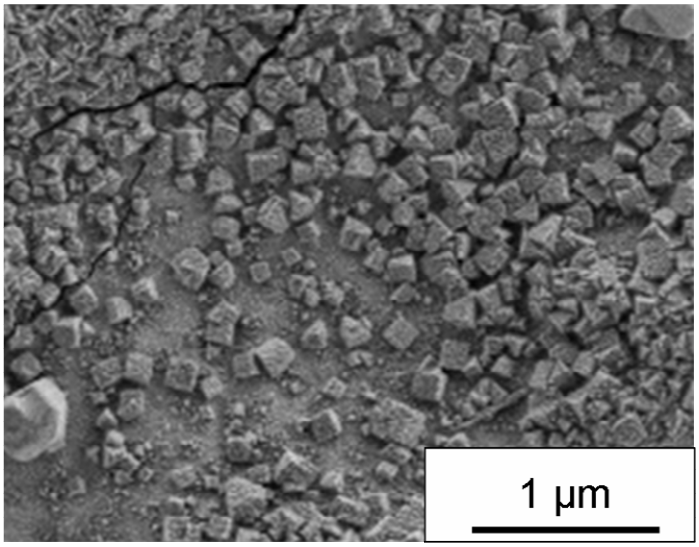


Fig. 2.10 SEM picture of gold nanocrystals growth on a mesoporous silica film.

The observed contrast is mainly due to three effects:[10]

1.tilt contrast: the SE yield, δ, depends on the local tilt angle of the surface θ. For voltages 45 kV the dependence of δ on local tilt angle, θ, is given approximately by

$$\delta(\theta) = \delta_0 / \cos(\theta) \qquad (2.3)$$

where $\delta_0$ is the SE coefficient at 0° tilt. At low voltages, when the distance travelled by the beam electrons within the solid becomes comparable with the mean escape depth, λ of the SEs, this surface tilt contrast is greatly reduced;

2. shadow contrast: this is the shadowing of the SE signal due to holes or protrusions. The amount of shadowing depends on the presence of electrostatic and magnetic extraction fields on the surface;

3. edge effect contrast: this is due to SEs that penetrate through the edges of structures. This contrast is observed in most micrographs as white edges extending over a

distance of the order of the electron range. Therefore, the width and magnitude of the observed edge contrast depend on the beam energy and are greatly reduced at low voltages. This effect is most disturbing when the spatial variation of the background due to the edge effect is comparable with the size of the surface structures to be examined. At high voltages this situation occurs at medium magnifications. Low voltages are therefore preferred when observing cross-sections or details on small topographic structures, such as patterns on integrated circuits.

### 2.3.3 Atomic force microscopy

Scanning probe atomic techniques refer to a general class of microscopy techniques that produce high-resolution and high-magnification images by scanning a sharp probe back and forth over a specimen. In particular, atomic force microscopy (AFM), uses a force-sensing probe to track sample topography. The topographic resolution of AFM ranges from 1 to 20 Å and does not depend on the electrical conductivity of the specimen but rather on the operation mode and the specific sample characteristics; under favourable conditions true atomic resolution can be obtained, more than 1000 times better than the optical diffraction limit.[11]

Atomic force microscopy uses the repulsive or attractive forces between the probe and sample. **Figure 2.11** shows an illustration of a typical AFM apparatus. The probe, consists of a sharp tip on the end of a small cantilever a few hundred micrometers in length. Forces exerted on the tip cause the cantilever to bend. The force F is directly proportional to the cantilever deflection and is given by

$$F = k\Delta z \tag{2.4}$$

where $k$ is the cantilever force constant (in N/m, analogous to a spring constant) and $\Delta z$ is the vertical deflection. Cantilevers can be fabricated with force constants as low as 0.01 N/m, so that forces as small as 0.1 nN give nanometric deflections that can be detected easily. The sensitivity of AFM to forces smaller than the bonding forces between individual atoms was the motivation for the name “atomic force” microscopy.

Resolution in AFM is governed principally by the sharpness of the probe tip, although the sample characteristics and specific operating mode are also important. Commercial cantilever-tip assemblies are made from silicon or silicon nitride using conventional microfabrication methods common to the semiconductor industry. **Figure 2.12** shows the specific of a typical micro-fabricated silicon nitride probe. Commercial probes can

be made with tip radii as small as 10 nm, but 20–40 nm is more common. With a 20-nm-radius tip it is possible to obtain images of surfaces that show topographic corrugation due to atomic or molecular packing.

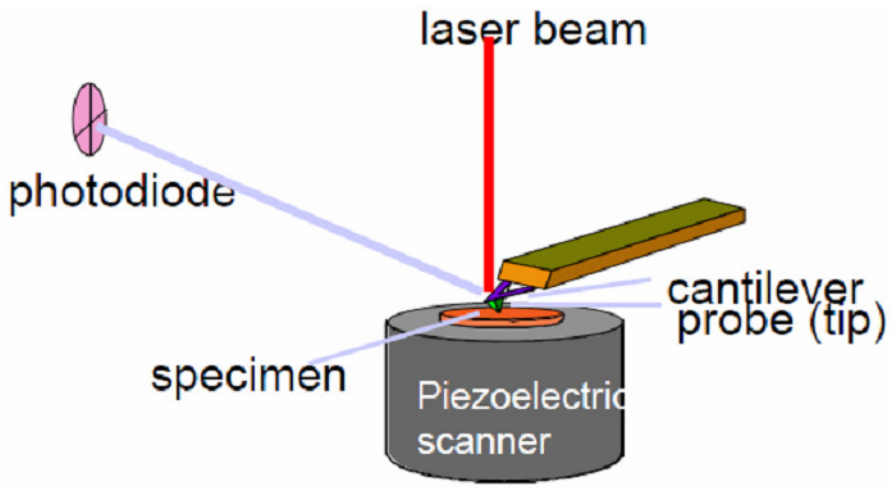


Fig. 2.11 Schematic representation of an atomic force microscopy (AFM).

There are three main modes used to perform AFM imaging: contact mode, tapping mode and force modulation mode. In the *contact mode*, also called normal force mode, the tip is brought into hard contact with the sample surface such that the cantilever bends due to the tip–sample repulsion. The cantilever deflection can be measured in several ways, but the most common is the optical beam method. In this approach, a laser beam from a semiconductor laser is focused on the back side of the cantilever, as shown in **Figure 2.11**.

| Cantilever series | Cantilever lenght, L±5µm | Cantilever width, W±3µm | Cantilever thickness, T±0.5 µm | Resonant frequency, kHz | | | Force constant, N/m | | |
|---|---|---|---|---|---|---|---|---|---|
| | | | | min | typical | max | min | typical | max |
| NSG01 | 125 | 30 | 2.0 | 87 | 150 | 230 | 1.45 | 5.1 | 15.1 |

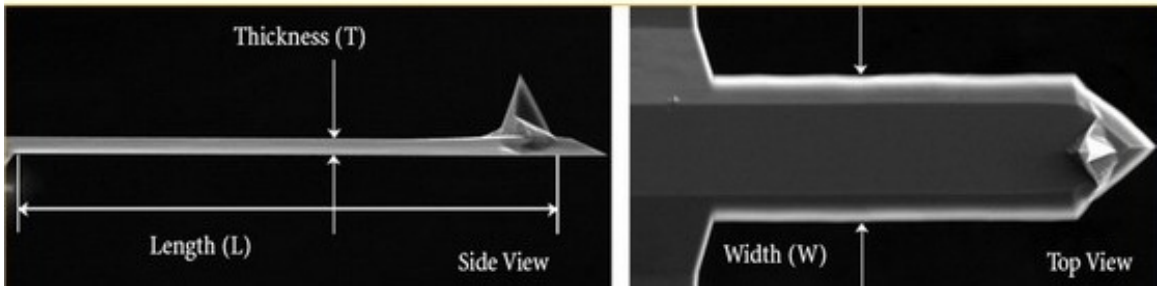


Fig. 2.12 Typical performances of a AFM probe [from ref. 12].

The reflected light hits a position-sensitive detector that produces a voltage indicating how much the cantilever has deflected up or down. The optical beam method allows deflections as small as an angstrom to be detected.

Other popular scanning modes involve oscillating the cantilever-tip assembly while the sample is scanned; in *tapping mode* the tip is oscillated vertically with an amplitude of 50 to several hundred nanometres and makes contact with the sample at the bottom of every downstroke. The optical beam and photodetector assembly is used to detect the oscillation amplitude, which is dependent on how close the tip is to the sample. The feedback control electronics maintains the oscillation amplitude at a user-defined set-point value and a topographic image is generated in the same fashion as in contact mode, i.e. by recording the height position of the sample as a function of X and Y coordinates. The advantage of this intermittent contact method is that shear forces that are always exerted on the sample in contact mode are eliminated. For imaging soft samples, such as biological specimens or dried mesostructured thin films, this has proved to be an advantage. Also by using the so called *non-contact mode* the tip is allowed to oscillate near the surface, but not to touch it: in this way, under favourable circumstances, it is possible to obtain true atomic resolution.

Another operation mode is known as *force modulation mode*. This is a contact mode technique, but, instead of maintaining fixed cantilever deflection, the tip is periodically pushed into the sample. This periodic force modulation is accomplished by oscillating the height position of the sample at a known amplitude (typically 2–5 nm). If the region under the tip is stiff, the probe will not compress the sample and the cantilever will deflect by the oscillation amplitude (e.g. 2 nm). If the sample is soft, the probe will push into the sample and the cantilever will deflect somewhat less than the full oscillation amplitude producing a stiffness map of the sample.

AFM finds important applications in the fields of biology for imaging of DNA folding and unfolding and crystallization processes in solution such as the topographic images of growing insulin crystals. AFM is also used as a tool to investigate frictional and mechanical properties of thin films on the nanoscale. AFM images were seldom reported for mesoporous thin film because it is very difficult to image the pore arrangement on film surface. Nevertheless, in some particular applications, such as monolayer porous thin films, this technique has proved to be very effective for revealing the real morphology of the surface. [12]

## 2.4 Spectroscopic ellipsometry

Ellipsometry is a method based on analysis of elliptical polarization, to determine the properties of thin films (particularly the thickness and refractive index) on dielectric or metal surfaces. The basic theory derives from the work of Rayleigh and Drude in the late 19th century. A plane wave incident on a surface at an oblique angle can in general be decomposed into two polarization components, which are typically referred to as the *p* and *s* waves, whose electric field vectors lie in and normal to the plane of incidence, respectively. Upon reflection, these two waves may each undergo changes of amplitude and phase. In ellipsometric measurement it is the change in the relative amplitude and phase of the two components that is measured. If we designate phases and amplitudes by β and *A*, respectively, and denote *p* and *s* waves by the corresponding subscripts, we can determine the two quantities Δ and Ψ

$$\Delta = \left(\beta_p - \beta_s\right)_{reflected} - \left(\beta_p - \beta_s\right)_{incident} \tag{2.5}$$

$$\Psi = \tan^{-1}\left[\frac{\left(A_p / A_s\right)_{reflected}}{\left(A_p / A_s\right)_{incident}}\right] \tag{2.6}$$

Δ and Ψ can be related to the film properties according to the Drude relations

$$\tan(\Psi)e^{i\Delta} = \left(\frac{r_{1p} + r_{2p}e^{-2i\delta}}{1 + r_{1p}r_{2p}e^{-2i\delta}}\right)\left(\frac{1 + r_{1s}r_{2s}e^{-2i\delta}}{r_{1s} + r_{2s}e^{-2i\delta}}\right) \tag{2.7}$$

Where $r_{1p}$ and $r_{1s}$ and are the Fresnel reflection coefficients of the film surface, and $r_{2p}$ and $r_{2s}$ the Fresnel coefficients at the film–substrate interface. These in turn can be calculated from the material properties and wave directions, so that:

$$r_{1p} = \frac{n_a \cos\varphi_f - n_f \cos\varphi_a}{n_a \cos\varphi_f + n_f \cos\varphi_a} \tag{2.8}$$

$$r_{1s} = \frac{n_a \cos\varphi_a - n_f \cos\varphi_f}{n_a \cos\varphi_a + n_f \cos\varphi_f} \tag{2.9}$$

with $n_a$ and $n_f$ the ambient and film refractive indices, and $\varphi_a$ and $\varphi_f$ the angle of incidence, and angle of refraction in the film, respectively. The two angles are related by Snell's Law, and the coefficients $r_{2p}$ and $r_{2s}$ can be found by substituting the subscripts *f* and *s* (film and substrate) for *a* and *f* in (2.8) and (2.9). It is important to stress that both the indices and the angles may be complex if the materials are lossy, as

will often be the case. In equation (2.7), δ is the phase change caused by the propagation through the film (in both directions) according to

$$\delta = k_0 d \sqrt{n_f^2 - n_a^2 \sin^2 \varphi_a} \tag{2.10}$$

where $d$ is the film thickness and $k_0 = 2\pi / \lambda$.

Since we have two measurable variables Δ and Ψ we can derive two unknown quantities of the system, for example $d$ and $n_f$ (if we assume is real). While this gives an immediate benefit over more straightforward interferometric measurements, it is mainly the attainable precision that has made ellipsometry an important technique.[13]

The basis of the ellipsometer measurement is to determine the state of polarization of the reflected beam, i.e. its ellipticity and the orientation of the ellipse. If a λ/4 plate is placed in the beam path such that its principal directions are aligned with the major axis of the ellipse, the light emerging is linearly polarized and can be extinguished by an analyzer at the appropriate angle. The angles of the λ/4 plate and analyzer thus indicate Δ and Ψ. In practice, this simple and basic approach lacks precision, and a number of variants of the instrument architecture and operation have been derived: in particular additional information can be acquired if the angle of incidence or wavelength is varied, and this information can allow a larger number of film parameters to be calculated. Angle variation tends to add complexity to the instrument operation because of the need to know the angle very precisely at every measurement point, so that use of a few fixed angles rather than continuous variation is often preferred. On the contrary, by using a continuously variable wavelength, usually called *spectroscopic ellipsometry*, it is possible to include chromatic dispersion of the film obtained from the experimental measurements in the fitting parameters. A block diagram of a spectroscopic ellipsometer with variable angle is depicted in **Figure 2.13**. Spectroscopic ellipsometry has been extensively used to characterizes many features of thin and thick films. The most advanced equipments, in fact, allowed to estimate not only refractive index and thickness but also, surface roughness, gradient of optical density and film porosity.[14] This last property is very important for sol-gel films which can show porosity from nano- to meso-scale range and have a mass not sufficient for characterization with common BET methods based on $N_2$ absorption/desorption.

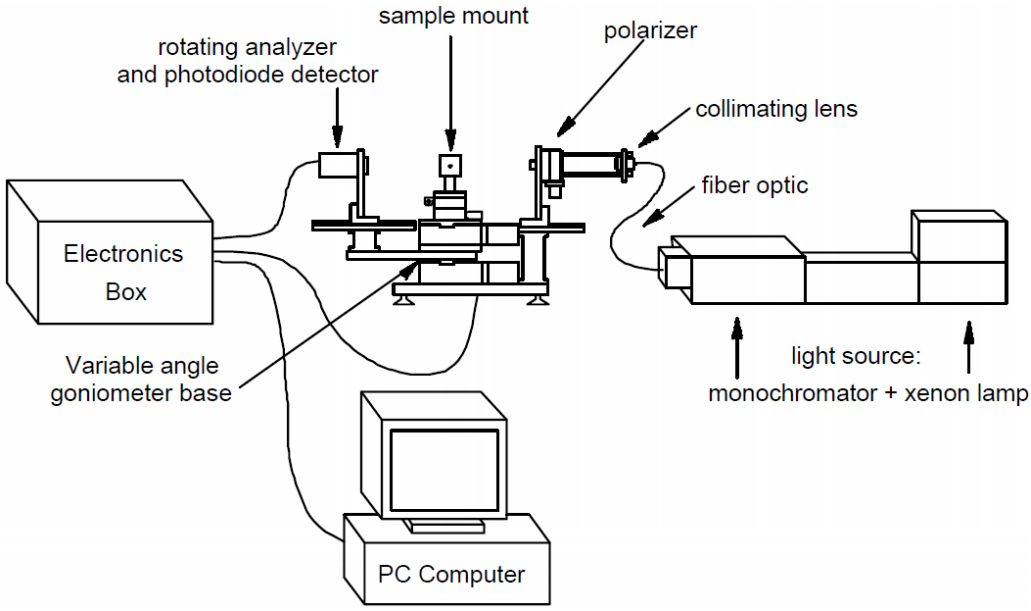


Fig. 2.13 Block diagram of a spectroscopic ellipsometer with variable angle.

## 2.5 UV-Vis based techniques: spectrofluorimetry and absorption spectroscopy

Spectrofluorimetry has been extensively employed because of its sensitivity, selectivity and fast response. Spectrofluorimeters are instruments capable of measuring excitation and emission spectra as well as fluorescence intensities.[15] The most important components layout of this type of equipment is shown in **Figure 2.14**. The characteristic feature of this arrangement is that any fluorescence emitted by the sample is detected at 90° to the incident light beam. The crucial advantages are that photons transmitted by the sample (the majority of the incident photons when dilute solutions are studied) are not detected, and that Rayleigh scattered light has a minimum intensity in the 90° direction. The key optical elements of the layout are the light source, the excitation monochromator or filter (M1), the sample cell, the emission monochromator or filter (M2), and the detector. Separate power supplies are normally provided for the light source and the detector, and additional power may be needed for such items as a reference detector, sample stirrer, etc. Fluorescence can also be measured in steady-state mode or in time-resolved to evaluate the decay of chromophores species. The measurements can be conducted both on liquid and solid specimens. For liquid, a fused-silica cuvette is often used while for thin films the instruments must be equipped with a

particular attachment which allows the orientation of the samples respect to the incident beam according to their properties of absorption and reflection in the UV-Visible range.

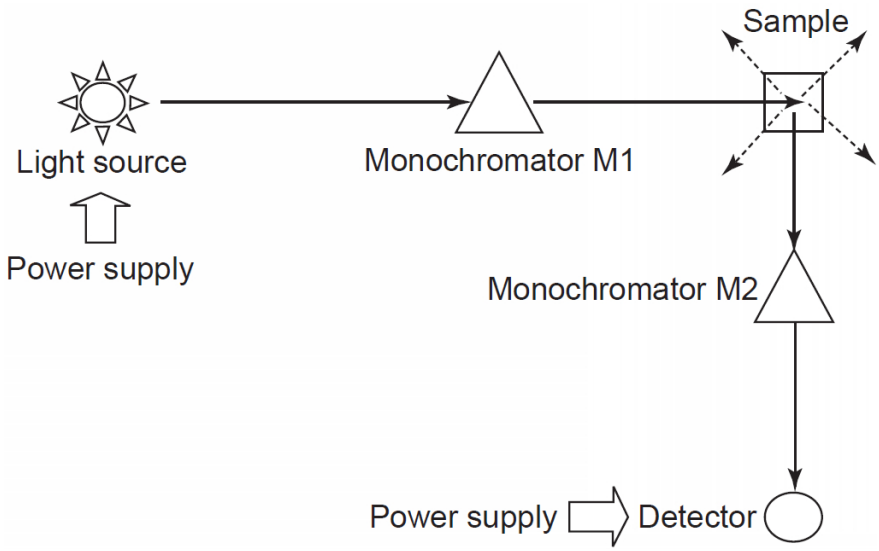


Fig. 2.14 Block diagram of a spectrofluorimeter.

A striking feature of the optical layout in **Figure 2.14** is that a fluorescence spectrometer is essentially a single-beam instrument. Thus fluctuations in light source intensity cause corresponding changes in fluorescence signals. Moreover, the efficiency of the grating in the monochromator M1 is wavelength dependent; therefore all spectrometers with an excitation monochromator also have to include a reference beam system which allows a correct calibration of the incident intensity.

The selectivity of fluorescence analysis can be attributed to the multiparametric properties of the measurement. This is because even the simplest of the luminescence measurements will involve the use of two parameters: an excitation wavelength and an emission wavelength. In a conventional fluorescence characterization, the excitation wavelength is set at a particular value and the emission wavelengths are scanned. To overcome the limitations of single-wavelength measurements in evaluating multicomponent samples, multidimensional luminescence measurements can be used. The multidimensional approach allows for a better estimation of minor differences between the individual components of the mixture and can ultimately lead to well-resolved spectra of multicomponent mixtures. Of significant importance is the fact that multidimensional luminescence measurements can be a viable technique for detecting very small and distinct spectral perturbations from a particular chemical environment such as the case, for instance, of a fluorescent molecules enclosed in a micelle.

Ultraviolet-Visible (UV-Vis) spectroscopy is a standard and cheap technique to characterize the absorption properties of solid and liquid samples. In a typical UV-Vis absorption spectra, the absorbance (see equation 2.1 of Paragraph 2.1.1) is reported as a function of the wavelength transmitted through the sample. **Figure 2.15** shows a block scheme of a double beam spectrometer.[15]

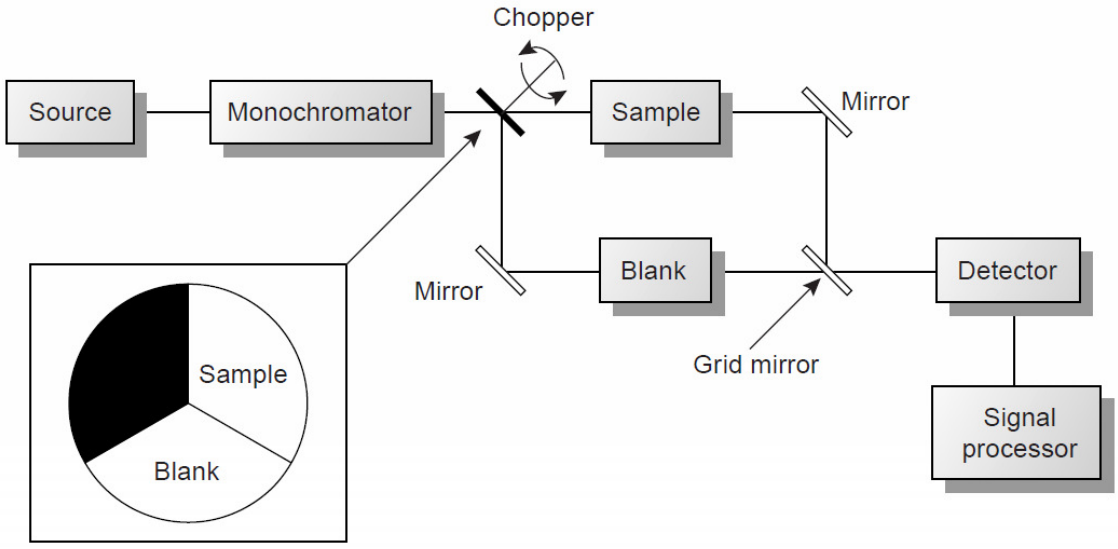


Fig. 2.15 Block diagram of a double-beam scanning spectrophotometer.

Double-beam instruments are more versatile than single-beam instruments, being useful for both quantitative and qualitative analyses. A chopper, similar to that shown in the figure, controls the radiation path, alternating it between the sample, the blank, and a shutter. The signal processor uses the chopper's known speed of rotation to resolve whether the signal reaching the detector is coming to the transmission of the blank ($P_0$) or the sample ($P_T$). By including an opaque surface as a shutter it is also possible to continuously adjust the 0% transmittance response of the detector. The effective bandwidth of a double-beam spectrophotometer is controlled by means of adjustable slits at the entrance and exit of the monochromator. Effective bandwidths of between 0.2 nm and 3.0 nm are common. In these doctoral work, UV-grade fused silica slides have been used as the substrate to perform UV-Vis spectroscopy on self-assembled mesostructured thin films.

## 2.6 References

[1] B. Stuart. Infrared spectroscopy: fundamentals and applications. **2004**, Chichester, Wiley.

[2] M. Cestelli Guidi, M. Piccinini, A. Marcelli, A. Nucara, P. Calvani, E. Burattini. Optical performances of SINBAD, the Synchrotron INfrared Beamline At DAΦNE. *J. Opt. Soc. Am. A* **2005**, *22*, 2810-2817.

[3] N. W. Ashcroft, N. D. Mermin. Solid state physics. **1976**, Orlando, Harcourt College Publishers.

[4] H. Amenitsch, M. Rappolt, M. Kriechbaum, H. Mio, P. Laggner, S. Bernstoff. First performance assessment of the small-angle X-ray scattering beamline at ELETTRA. *J. Synchrotron Rad.*, **1998**, *5*, 506–508.

[5] T. N. Blanton, T. C. Huang, H. Toraya, C. R. Hubbard, S. B. Robie, D. Louer, H. E. Gobel, G. Will, R. Gilles, T. Raftery. JCPDS-International center for diffraction data round robin study of silver behenate. A possible low-angle X-ray diffraction calibration standard. *Powder Diffr.*, **1995**, *10*, 91–95.

[6] P. Dubček. Nanostructure as seen by the SAXS. *Vacuum*, **2005**, *80*, 92–97.

[7] http://www.esrf.eu/computing/scientific/FIT2D/ (accessed November 2009)

[8] D. B. Williams, C. B. Carter CB. Transmission Electron Microscopy, A Textbook for Materials Science. **1996,** New York, Plenum.

[9] B. Fultz, J. H. Howe. Transmission Electron Microscopy and Diffractometry of Materials. **2000,** Berlin, Springer.

[10] S. Amelinckx, D. van Dyck, J. van Landuyt, G. van Tendeloo. Handbook of Microscopy. **1997**, Weinheim, VCH.

[11] B. Bhushan, H. Fuchs, S. Hosaka. Applied scanning probe methods. **2004**, Heidelberg, Springer.

[12] T. Brezesinski, M. Groenewolt, A. Gibaud, N. Pinna, M. Antonietti, B. M. Smarsly M. Evaporation-Induced Self-Assembly (EISA) at Its Limit: Ultrathin, Crystalline Patterns by Templating of Micellar Monolayers. *Adv. Mater.* **2006**, *18*, 2260-2263.

[13] R. M. A. Azzam, N. M. Bashara. Ellipsometry and polarized light. **1987,** Oxford, Elsevier.

[14] C. Boissière, D. Grosso,S. Lepoutre, L. Nicole, A. Brunet Bruneau, C. Sanchez. Porosity and Mechanical Properties of Mesoporous Thin Films Assessed by Environmental Ellipsometric Porosimetry. *Langmuir*, **2005**, *21*, 12362–12371.

[15] D. A. Skoog. Fundamentals of analytical chemistry. **1995** ($7^{th}$ edition), Philadelphia, Harcourt Brace College Publishers.

# Chapter 3:
# Experimental results

This thesis is focused on the possibilities offered by the mesoporous films properties; therefore it is important to describe what are the peculiar features of mesoporous material and how they can be tuned belonging to the prospected applications. The most evident characteristic is the porous structure; the architecture of ordered pores is responsible of the accessibility into the inorganic matrix. As described in Paragraph 1.3.5, the increased control of pore morphology and arrangements allows tuning the film accessibility and opens the route for the use of mesoporous films for molecular capture and detection. The key of an ordered structure is kept into the fundamental chemical-physical processes that controls self-organization. Because self-assembly is mainly kinetically-driven, it is mandatory to study it with advanced techniques which allow to cross chemical and morphological information at the same time. After a first part dedicated to materials synthesis (Section 3.1), in Section 3.2 we have reported the results of two *in situ* experiments in order to elucidate some mechanisms behind the self-assembly of siliceous and non-siliceous thin films. Mesopores are important for the high surface area they provide to the materials. Section 3.3 is dedicated to a basic study on the pores surface and in particular to analyse the chemical bonding of water into the pores. The surface of a mesoporous film can be functionalized following different strategies to obtain functional hybrid porous materials (Paragraphs 3.4.1-3.4.3). Pore surface can act as a catalytic site to promote nucleation of metallic and oxides nanoparticles; in this case the tailoring of pore size and shape is fundamental to obtain particle showing monodisperse dimensions (Paragraph 3.4.4).

Mesoporous materials can be also attractive for the properties given by the pore walls. In Section 3.5 is reported the case of a mixed silica-germania films with photoactive properties.

Last section is dedicated to the natural evolution of self-assembled thin films; nano-engineering means to fill the gap between nano- and macro-dimension by controlling the matter organization at every length scales. To reach this goal, one possibility is mastering several self-assembly processes at the same time so that different degree of organization into the final material can be obtained. This is still a very difficult task to

achieve, nevertheless, in Section 3.6 are resumed three strategies that we followed to obtain hierarchical porous films via EISA at different length scales.

## 3.1 Materials synthesis

*- Mesostructured hafnium oxide films*

The precursors solution has been prepared by the slow addition of $HfCl_4$ (6.33 g) to 46.13 $cm^3$ of ethanol and 1.26 g of surfactant. Finally 7.12 $cm^3$ of water have been added to this sol under stirring. The molar ratios were: $HfCl_4$ : EtOH : Pluronic F127 : $H_2O$ = 1 : 40 : $5 \cdot 10^{-3}$ : 20. Silicon wafers have been used as the substrates. The substrates, previously cleaned with hydrofluoric acid, water, EtOH, and acetone, have been dip-coated in the fresh solution (no ageing). The films have been prepared by dip-coating in a controlled-humidity environment at the pulling rate of 2.3 $mm \cdot s^{-1}$ at room temperature. The RH during deposition has been set to ≈ 20%. After deposition, the films have been allowed to dry for about 1 minute, until the drying line disappeared. Soon afterwards, the films have been exposed to high RH (≈ 80–90%) for around 5 seconds, and aged for 24 hours in a controlled humidity environment (RH = 50%). Some samples have been also thermally treated at 150 °C for 1 hour and at 60 °C for 40 min for GISAXS and AFM measurements, respectively.

*- TEOS-MTES films for in situ combined FTIR-SAXS*

Films have been obtained from a precursor solution where the Si source was a mixture of tetraethoxysilane (TEOS) and methyl-triethoxysilane (MTES), and the templating agent was Pluronic F127 block copolymer. The precursors solution has been prepared as follows: a solution containing 3.08 $cm^3$ of EtOH, 2.84 $cm^3$ of TEOS, 1.42 $cm^3$ of MTES and 0.355 $cm^3$ of HCl 0.77 M has been stirred for 45 minutes, then added to a solution containing 15 $cm^3$ of EtOH, 1.3 $cm^3$ of HCl 0.057 M and 1.3 g of F127. The final solution has been stirred for 10 minutes and used for *in-situ* dip-coating and measurements.

*- TEOS and TEOS-MTES membranes for pores surface characterization*

Transparent inorganic and hybrid organic/inorganic mesoporous silica membranes have been synthesized starting from two different acidic sols obtained by using two different

silicon alkoxides as the silica sources, and containing Pluronic F127 amphiphilic block copolymer as the templating agent. A first precursors sol (*mother solution*) has been prepared by adding in the following order: ethanol (EtOH), tetraethyl orthosilicate (TEOS), water and HCl in the molar ratios TEOS : EtOH : $H_2O$ : HCl = 1 : 2.78 : 1.04 : $1.43 \cdot 10^{-2}$. This sol has been stirred for 1 h at room temperature to allow pre-hydrolysis and slight condensation of the silicon alkoxide. Another solution (templating solution) has been prepared dissolving 1.3 g of Pluronic F127 in a mixture of 15 $cm^3$ EtOH and 1.5 $cm^3$ weakly acidic aqueous solution ($5.7 \cdot 10^{-2}$ M). The final precursors sol, which has been obtained by adding 7.7 $cm^3$ of the mother solution to the templating solution, has been reacted under stirring for 24 h (final molar ratios TEOS : EtOH : $H_2O$ : HCl : F127 = 1 : 16.3 : 5.4 : $1.88 \cdot 10^{-2}$ : $5 \cdot 10^{-3}$). The precursors sol of the hybrid membrane has been prepared using the same procedure, the silica source being a mixture of TEOS and methyl triethoxysilane (MTES) in the molar ratios TEOS : MTES = 0.66 : 0.33, instead of 1 mol TEOS.

To prepare the mesostructured membranes, the two sols have been poured into polystyrene Petri dishes to allow solvent evaporation for around 60 days. The evaporation rate can be changed using Petri dishes of different dimensions or changing the amount of solution. The conditions of preparation have been controlled during the evaporation stage, the temperature has been maintained at 25 °C and the relative humidity at 40%. Membranes have been calcined in an oven, with a heating ramp from room temperature to 350 °C of 1 °C·$min^{-1}$, and have been maintained at 350 °C for 12 h. The samples have been then cooled to room temperature within 24 h.

*- Rhodamine 6G-doped films*

The samples have been prepared adding different amounts of *Rh6G* and Pluronic F127 to a solution of tetraethoxysilane (TEOS), ethanol (EtOH), water and HCl. A precursor sol containing the silica source has been prepared by adding in the following order: 3.08 $cm^3$ of EtOH, 4.26 $cm^3$ of TEOS, 0.355 $cm^3$ of HCl aqueous solution (0.77 M). This sol has been stirred for 1 h at room temperature to allow pre-hydrolysis and slight condensation of the silicon alkoxide. Templating solutions have been prepared dissolving different amounts of Pluronic F127 in a mixture of 10 $cm^3$ EtOH and 1.5 $cm^3$ weakly acidic HCl aqueous solution ($5.7 \cdot 10^{-2}$ M). The amount of Pluronic F127 has been varied from 0 to 1.3 g. After adding 7.7 $cm^3$ the precursors sol to the templating

solutions, the final dip-coating solutions have been obtained by introducing increasing amounts of *Rh6G* and stirring for 2 hours. All the solutions have been protected from the environmental light. At the end, the molar ratios of the dip coating solutions were TEOS : EtOH : $H_2O$ : F127 : *Rh6G* = 1 : 40 : 20 : *s* : *c* with *s* ranging from 0 to $5 \cdot 10^{-3}$ and *c* from $5 \cdot 10^{-5}$ to $5 \cdot 10^{-2}$. Silica films doped with *Rh6G* have been also prepared as the reference: the precursor silica sol has been prepared with the same procedure described for mesostructured films but without the addition of the surfactant. Thin films have been obtained using a home made dip-coating system working at the pulling rate of 2 $mm \cdot s^{-1}$; the relative humidity in the deposition chamber has been set to (27± 2)%. Fused silica slides (UV-grade, thickness 1 mm) have been used as substrates for dip-coating. The substrates, previously cleaned with detergent solution, EtOH, and acetone, have been dip-coated in the fresh solutions. The films, after deposition, have been dried at 60°C for 24 h.

- *Spiropyran-doped films*

*Spiropyran 1* (**Figure 3.1**) has been synthesized by the organic chemistry group of Prof. Michele Maggini (University of Padua) using commercially available compounds and following a previously reported recipe.[1]

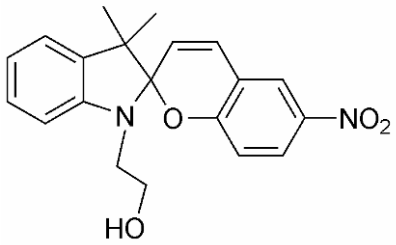


Figure 3.1 Structure of *spiropyran 1*.

Mesostructured silica films have been prepared adding different amounts of *spiropyran 1* to a solution of TEOS, EtOH, water, Pluronic F127 and HCl. A precursor sol containing the silica source has been prepared by adding in the following order: 3.08 $cm^3$ of EtOH, 4.26 $cm^3$ of TEOS, 0.355 $cm^3$ of HCl aqueous solution (0.77 M). The sol has been stirred for 1 h at room temperature, then it has been added to a solution containing 1.3 g of Pluronic F127 in a mixture of EtOH (10 $cm^3$) and HCl ($5.7 \cdot 10^{-2}$ M) aqueous solution (1.5 $cm^3$). For UV–Vis and fluorescence measurements on films, the

final sol has been obtained by introducing 48 mg of *Spiropyran 1* ($1.43 \cdot 10^{-4}$ mol) and stirring for 1 h; the solution has been protected from light during and after films deposition. The final molar ratios were TEOS : EtOH : $H_2O$ : F127 : *spiropyran 1* = 1 : 40 : 20 : $5 \cdot 10^{-3}$ : $7.5 \cdot 10^{-3}$. For SAXS and TEM measurements, the final precursors sols have been obtained by introducing increasing amounts of *spiropyran 1* and stirring for 1 h; also in this case, the solutions have been protected from light during and after the preparation of the samples. The final molar ratios were TEOS : EtOH : $H_2O$ : F127 : *spiropyran 1* = 1 : 40 : 20 : $5 \cdot 10^{-3}$ : X with X ranging from $1.5 \cdot 10^{-3}$ to $7.5 \cdot 10^{-3}$.

Silicon wafers (thickness 500 μm, test grade) or silica slides (UV grade) have been used as the substrates that have been dip-coated with a pulling rate of 2.5 $mm \cdot s^{-1}$ at the relative humidity of 27 ± 3%. The substrates, previously cleaned with detergent solution, EtOH, and acetone, have been dip-coated into the sol. The films, after deposition, have been dried at 60 °C for 24 h.

*- Zinc complex-doped films*

Mesoporous silica films have been deposited from a silica sol. This solution has been obtained from a stock solution with ETOH, TEOS, $H_2O$ and HCl having the following molar ratios TEOS : EtOH : $H_2O$ : HCl = 1 : 2.78 : 1.04 : $1.43 \cdot 10^{-2}$. The sol has been left to react under stirring 75 min at room temperature. A second solution has been prepared by dissolving 1.3 g of Pluronic F127 in 15 $cm^3$ of EtOH and 1.5 $cm^3$ of HCl acid aqueous solution ($5.7 \cdot 10^{-2}$ M). The final molar ratios were TEOS : EtOH : $H_2O$ : HCl : Pluronic F127 = 1 : 16.3 : 5.4 : 1.88 : $9 \cdot 10^{-2}$ : $5 \cdot 10^{-3}$. The sol has been stirred at room temperature for 10 min and immediately used for film deposition.

The films have been deposited on the substrates (silicon wafers and silica glass slides) via dip-coating at room temperature. The film depositions have been performed at 24% relative humidity and at the withdrawal speed of 2.5 $mm \cdot s^{-1}$. After the deposition, the films have been put directly in the pre-heated oven and dried at 60 °C for 12 h, then they have been calcined in air for 60 min at 350 °C.

The Schiff base zinc complex ($ZnL_2$) for films functionalization has been synthesized by Prof. Mauro Ghedini research group of Università della Calabria following the scheme of **Figure 3.2**; at first the ligand HL has been prepared by condensation of aminopropyltriethoxy silane (APTES) with salicylaldehyde, then zinc(II) acetate

dihydrate (0.50 mmol, 0.11 g) and HL (1 mmol, 0.33 g) have been mixed in 30 $cm^3$ of EtOH and left stirring for 5 hours under reflux at 80 °C.

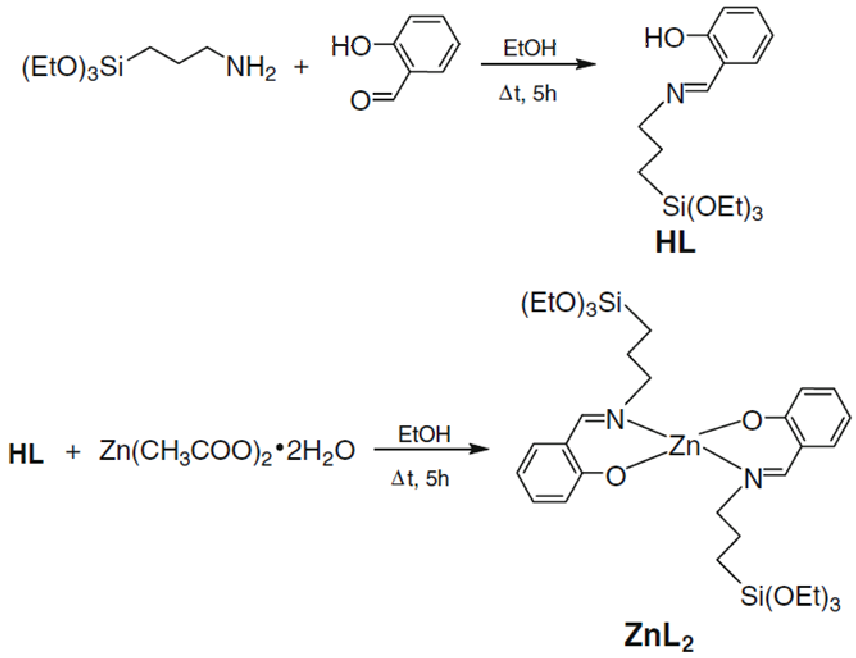


Figure 3.2 Synthesis of the ligand HL (upper sketch) and of the complex $ZnL_2$ (lower sketch).

*- Fe-Co $SiO_2$ nanocomposites*

Mesoporous silica thin films have been prepared using two different templating agents in order to have porous structures with different pore size, for this reason the precursor solution contained TEOS as the silica source and either block copolymer Pluronic F127 ($EO_{106}$–$PO_{70}$–$EO_{106}$) or Pluronic F68 ($EO_{80}$–$PO_{30}$–$EO_{80}$) as the structure-directing agent. A starting solution has been prepared by mixing 4.2 $cm^3$ of TEOS, 3 $cm^3$ of EtOH and 0.35 $cm^3$ of a 0.768 M HCl solution. This solution has been stirred for 45 min, then it has been added to a solution containing 15 $cm^3$ of EtOH, 1.3 g of block copolymer and 1.5 $cm^3$ of a 0.057 M HCl solution. This has been stirred for 15 min before dip-coating. Silicon substrates (thickness 400 μm) have been dip-coated at constant relative humidity (≈ 40%), the pulling rate have been set to 2.5 $mm \cdot s^{-1}$. The films have been directly calcined at 350 °C for 2 hours. The mesoporous silica films have been impregnated with an aqueous solution of $Fe(NO_3)_3 \cdot 9H_2O$ and $Co(NO_3)_2 \cdot 6H_2O$ having an overall metal molar concentration of 0.4 M. The [Co] / [Fe] ratio has been set to 0.5 in order to obtain a FeCo alloy with the desired composition in the final composite ($Fe_{67}Co_{33}$). Impregnation has been carried out for 30 min under stirring. Afterwards the samples have been treated at 450 °C for 1 h in air to remove residual nitrate ions and solvent.

The samples have been finally reduced at 600 °C for 2 h under a hydrogen flow (80 $mL \cdot min^{-1}$) in a quartz tubular reactor in order to promote formation of the metal phase.

*- Mesoporous $SiO_2$-$GeO_2$ films*

Four precursors solutions have been obtained by adding different amounts of anhydrous $SiCl_4$ and $GeCl_4$ under stirring to a stock solution of Pluronic F127 dissolved in ethanol. The molar ratios have been set to EtOH : $GeCl_4$ : $SiCl_4$ : F127 = 30 : $x$ : (1 - $x$) : $5 \cdot 10^{-3}$, where $x$ has been varied between 0.1 and 0.4. Then, substrates have been dip-coated on the fresh solutions at the pulling rate of 2 $mm \cdot s^{-1}$; the relative humidity (RH) in the deposition chamber has been set to 24 ± 2%. The substrates were either silicon wafers (100-oriented, B-doped test grade, nominal thickness 500 $\mu$m) or fused silica slides (UV grade, thickness 1 mm). The precursors solutions have been maintained under stirring to avoid they would become turbid, and a white precipitate, probably due to aggregation between surfactant block copolymers, would form. Solutions have been also sonicated for 5 min prior to each dip-coating in order to re-dissolve eventual aggregates and ensure films homogeneity. After dip-coating the films have been stabilized in the deposition room at low RH for a at least 10 minutes, the they have been transferred into a oven at the temperature of 100 °C, and calcined at 350 or 550 °C for 1 h; the thermal treatments have been all performed in air.

*- Hierachical porous hybrid TEOS-MTES films by direct templating*

Colloidal nanoparticles (NCS) solution has been developed in collaboration with CIVEN (Centro Interuniversitario Veneto per le Nanotecnologie) researchers. The NCS has been prepared by seeded semi-continuous emulsion polymerization by adapting a procedure described by Castelvetro et al.[2] The polymerization has been carried out under a nitrogen atmosphere in a conventional 250 $cm^3$ jacketed glass reactor equipped with thermostated bath circulator, reflux condenser, mechanical stirrer, and thermocouple. The seed latex has been prepared directly *in situ* by a batch process. The reactor containing a solution of sodium dodecylsulfate (0.6 g) in 90 $cm^3$ of deionized water has been loaded with the monomer (2,2,2-trifluoroethylmethacrylate, 10 g), purged with nitrogen for 30 min, and then heated at 70 °C under stirring (250 rpm) prior to addition of the initiator (0.15 g of $K_2S_2O_8$ in 5 $cm^3$ of water). After 2 h of polymerization at 70 °C, two distinct and individually deoxygenated feeds with 2,2,2-

trifluoroethylmethacrylate (20 g) and the aqueous solution of surfactant (Brij 58P, 0.15 g), buffer ($NaHCO_3$, 0.035 g; $NaH_2PO_4$, 0.035 g), and initiator ($K_2S_2O_8$ 0.06 g), respectively, have been added by means of metering syringe pumps. During the feeding stage and throughout the polymerization the mixture in the reactor has been stirred at 250 rpm and the circulating thermostated fluid maintained at 70 °C. The feeds have been added simultaneously for 3 h, and the polymerization has been then allowed to proceed for an additional 2 h. The resulting seed latex, with 19.9 wt % solids have been analysed by photon correlation spectroscopy (PCS) using a dynamic laser light scattering instrument. Particle size, particle size distribution, and polydispersity index have been calculated from the autocorrelation function using CONTIN and NNLS data elaboration. The solutions contained monodispersed polymer particles of average diameter $d_p$ = 69 nm and polydispersity index equal to 0.036 according to PCS analysis. No additional peak due to surfactant micellization has been observed in the intensity distribution. The number of particles contained in 1 Kg of NCS has been estimated by the following formula

$$N_p = \frac{6wt\%}{\pi\rho \cdot d_p^3} \tag{3.1}$$

where wt % is the weight fraction of polymer in the NCS (19.9%), $\rho$ is the polymer density (estimated as 1.39 $g \cdot cm^{-3}$), and $d_p$ is the intensity-average particle diameter as determined by PCS (69 nm). The density of NCS has not been determined, but it can be reasonably approximated as 1 $g \cdot cm^{-3}$ so that volume and weight have been used interchangeably. Once prepared the NCS, in order to deposit hierarchical porous film a precursors solution has been prepared as it follows. A stock solution has been obtained by adding EtOH (31 $cm^3$), TEOS (29 $cm^3$), MTES (13 $cm^3$), and HCl (4 $cm^3$, 0.9 M). This sol has been left to react under stirring in a closed vial for 45 min at room temperature. Seven different precursor solutions have been prepared as a function of nanoparticles concentration adding respectively 0.3, 0.6, 0.9, 1.2, 1.5, 3, and 6 $cm^3$ of NCS to a mixture of Pluronic F127 (1.3 g), EtOH (15 $cm^3$), and HCl aqueous solution ($5.7 \cdot 10^{-2}$ M, 1.5 $cm^3$). The final precursor solutions have been obtained by adding 7.7 $cm^3$ of stock solution to the templating solutions and reacting the sols under stirring for 1 h at room temperature; the [F127] / [Si] molar ratio in the final sol was $\approx 5 \cdot 10^{-3}$ M. To prepare hierarchical films, silicon substrates, previously cleaned with water and EtOH and rinsed with acetone, have been dip-coated in the precursor solutions using a

withdrawal speed of 2.3 $mm \cdot s^{-1}$ and a RH between 20 and 40% in the deposition room. After dip coating, the samples have been dried at 60 °C for 1 h and then calcined at 350 °C for 1 h.

*- Hierarchical porous titania films*

The precursor sols containing the titania source have been prepared by adding, in the following order, 14.6 $cm^3$ of BuOH, 0.44 $cm^3$ of $TiCl_4$ and Pluronic F127. After 5 min stirring, 0.72 $cm^3$ of water and PPG have been added to obtain the solutions for film preparation; solutions have been prepared under ordinary laboratory conditions, at room temperature and atmospheric pressure, and stored in closed glass or plastic bottles. The relative concentrations of Pluronic F127 and PPG have been systematically changed to optimize the synthesis parameters. Molar ratios for the precursor sols were $TiCl_4$ / BuOH / $H_2O$ / PPG / F127 = 1 : 40 : 10 : $P$ : $S$, where $P$ = [PPG] / [Ti] and $S$ = [F127] / [Ti]. $P$ has been varied between 0 and $2.25 \cdot 10^{-2}$, $S$ between $4 \cdot 10^{-3}$ and $1.6 \cdot 10^{-2}$. $V_{THF}$ has been defined as the percentage volume ratio between the volume of THF and the final volume of the solution. $V_{THF}$ has been systematically varied between 0% and 37%. When THF has been added to the solutions, an intense orange color has been observed in solutions containing Ti(IV) upon THF addition, indicating formation of the well-known Ti(IV) chloride-THF complex. Titania films have been produced by dip-coating at a withdrawal speed of 0.5 $mm \cdot s^{-1}$. Silicon substrates have been pre-treated by a 5 min immersion in KOH ethanol solution (10% m/m) and subsequent thorough rinsing with distilled water, to improve wetting. Prior to deposition, soda-lime glass slides or silicon wafer substrates have been thoroughly washed with a suitable surfactant-based cleaning agent, followed by successive rinsing in water, ethanol, and acetone.

The relative humidity during dip-coating has been set at 20%. After deposition, films have been aged at RH 50% for 24 h and then dried in an oven at 60 and 130 °C (24 h at each temperature). Finally, the samples have been calcined in air at temperatures between 130 and 350 °C (1 $°C \cdot min^{-1}$ ramp) with a final 2 h step at 350 °C.

*- Hierarchical porous hybrid TEOS-MTES films by controlled salt crystallization*

Pluronic F127, TEOS, MTES, EtOH, sodium chloride (NaCl), and sodium phosphate monoacid ($Na_2HPO_4$) have been used to prepare the solution of precursors by using different steps: at first a well established recipe to obtain a sol for the deposition of

MTES-TEOS hybrid mesoporous films has been used.[3] The sol has been prepared in two stages; in the first one a stock solution has been obtained by mixing 3.08 $cm^3$of EtOH, 2.84 $cm^3$ of TEOS, 0.42 $cm^3$ of MTES, and 0.36 $cm^3$ of an acidic water solution (HCl $7.68 \cdot 10^{-1}$ M); the solution has been stirred for 1 h at 25 °C in a closed vessel. In the second stage a solution containing the surfactant has been prepared by dissolving 1.3 g of Pluronic F127 in 15 $cm^3$ of EtOH and 1.5 $cm^3$ of acidic water (HCl $5.7 \cdot 10^{-2}$ M). Finally the two solutions have been mixed together and stirred for 15 min at 25 °C in a closed vessel. The final molar ratios of the mixture have been set as it follows: TEOS : MTES: EtOH : $H_2O$ : HCl : F127 = 1 : 0.56 : 24.48 : 8.13 : 0.11 : $7.6 \cdot 10^{-3}$. Then, salts solutions have been prepared by dissolving NaCl and $Na_2HPO_4$ in water at different relative concentrations. Finally, the salts solutions have been added to the hybrid silica sol. When the solution of NaCl and $Na_2HPO_4$ has been added, the MTES-TEOS-F127 sol remained transparent and allowed to dip-coat optically homogeneous and transparent films. In a typical preparation, 20 $cm^3$ of the MTES-TEOS-F127 solution have been added to 3.6 $cm^3$ of salts aqueous solution. To compare the effects induced by the salts, other 2 precursors sols containing only NaCl or $Na_2HPO_4$ have been also prepared using the same recipe and molar ratios. Silicon substrates, previously cleaned with water and EtOH, have been dip-coated at a 2.5 $mm \cdot s^{-1}$ withdrawal rate; the temperature in the deposition room has been kept at 25 °C and the relative humidity at 25%. The films, immediately after their deposition, have been dried at 80 °C for 18 h in air, then at 150 °C for 2 h, and finally calcined in air at room pressure at 350 °C for 3 h. To remove the salt nanocrystals from the films, the samples have been immersed in water and sonicated for 5 min.

## 3.2 *In situ* experiments

The synthesis of mesoporous films is generally regarded as a combination of inorganic sol-gel and colloidal chemistry, consisting in the so-called templated self-assembly of organized matter. Due to the many factors cooperating during the short time of a typical synthesis (usually a few seconds or minutes by dip- or spin-coating), it is difficult to sort out the role of each synthesis and processing parameter. This requires characterisation techniques which are not always readily available, such as synchrotron facilities for *in situ* studies.

In this section are collected two *in situ* experiments regarding self-assembly of mesostructured hafnia and organosilica films. We have faced the problems related to mesophase self-assembly by attempting to synthesise mesoporous hafnium oxide (*hafnia*) films during *in situ* experiments conducted at the SAXS beamline at the ELETTRA synchrotron facility. As-deposited mesostructured hafnia films have shown to be highly sensitive, in terms of self-organisation of micelles and degree of order, to processing parameters such as relative humidity (RH) and external factors such as the synchrotron high-flux X-rays used in the *in situ* experiments. In a first set of experiments, mesostructured hafnia films have been found to be highly sensitive to relative humidity changes in the deposition chamber, in the so-called tunable steady state. Changes in the relative humidity have caused mesostructure assembly and de-assembly, observing order-to-disorder reversible transitions. Furthermore, a second set of experiments has revealed the local mesostructure disruption and restoration, induced by changes in the X-ray incident beam. These phenomena have been observed for the first time and have been explained by entropic effects.

The formation of an ordered mesophase is a process resulting from a delicate balance between kinetic and thermodynamic effects: in the synthesis of mesoporous organo-silica films, for instance, the ageing of the precursor solution affects the size of the inorganic starting units, resulting in higher or lower degrees of order. Several new techniques have been developed with the purpose of studying the phenomena occurring during self-assembly. The most popular among these techniques is *in situ* SAXS using synchrotron radiation, which is used to assess structural changes and rearrangements in the mesostructure. However, this technique yields only structural information such as presence of an ordered mesostructure and the degree of order, but it does not allow

collecting time-resolved data about the chemistry of the process. Spectroscopic information can be obtained only *ex-situ* in as-prepared films, but in this case the chemical information regarding the phenomena occurring during the dip-coating stage is lost. Therefore, the lack of a spectroscopic *in situ* technique appears to be a weak point in the understanding of the process that leads to the mesostructure formation. In order to obtain structural and chemical information on the physicochemical processes occurring during dip-coating, we have decided to couple the FTIR and the SAXS techniques at the synchrotron facility. Paragraph 3.1.2 reports on the simultaneous *in situ* FTIR and SAXS experiments conducted at the ELETTRA synchrotron in order to study and correlate the structural and chemical processes occurring during dip-coating of mesostructured organosilica films obtained from MTES-TEOS solutions.

### 3.2.1 Mesostructured hafnium oxide

Mesoporous hafnia films can be synthesised starting from chloride precursors as the Hf source. Generally, the synthetic strategies to mesoporous transition metal oxides do not make use of alkoxides because of their high reactivity, which hinders the formation of an ordered mesostructure. Therefore, metal chlorides are often used as the precursors either in hydrolytic or in non-hydrolytic synthetic pathways (see Section 1.4). In the present case, the templating agent is triblock copolymer Pluronic F127 and the Hf source is anhydrous hafnium chloride (details on the preparation of precursors solution and film deposition can be found in Section 3.1, page 37). In previous experiments on mesostructured transition metal oxides, such as titania and zirconia, exposure to high RH has been found to affect critically both the optical quality of the films and the degree of order of the resulting mesostructure.[4,5] This fact has been explained by the extended inorganic polycondensation induced by water which ensures homogeneity of the inorganic framework, resulting in less optical scattering and better optical quality. The high degree of order observed in films treated with high RH has been attributed to the creation of a well-defined "hybrid interface" between organic (template) and inorganic (framework) phases.

*- Experimental set-up at the SAXS beamline*

The dip-coating system is a home-made device customised for *in situ* experiments. In this dip-coater, the substrate has been mounted on a fixed sample holder, whereas the

beaker containing the solution has been moved using a linear guide which has been remotely controlled from the experimental hutch. Using this configuration, the sample remains in a fixed position to ensure that the selected area of the film is irradiated during the whole experiment, while the solution can be raised and lowered for the dip-coating process. The dip-coating apparatus has been provided with a closed deposition chamber so that RH has been either maintained constant during film deposition or varied through an air flow. Because the deposition process required RH to be varied in a wide range (20% to ≈ 80%) the dip-coating chamber has been connected with a system flowing air with controlled RH. This has been accomplished connecting a tube from a dry air compressor (RH ≈ 0%) to a bubbler containing hot water: in this way the air flow has become saturated with water vapour. In order to control RH, the tube with saturated water vapour has been connected by means of a T-connector with a dry-air tube originating from the air compressor: the two air flows (high-RH and low-RH) have been finally mixed into a tube carrying the flow from the T-connector to the dip-coating chamber. Two valves have allowed to control the high-RH (through the bubbler) and low-RH (from compressor) air flows, so that humidity has been readily varied by opening or closing the two "wet air" and "dry air" valves. A humidity probe inside the deposition chamber has been connected to a hygrometer in the control room, to ensure an accurate readout of RH throughout the whole experiment.

*- In situ SAXS measurements*

To minimize the X-ray absorption due to the substrate, we deposited the film on a 50 μm-thick Si wafer. A Si substrate with this thickness is difficult to work with because it is very fragile and even the small pressure of tweezers can break it into fragments. Acquisition of SAXS diffraction patterns has been started during dip-coating, as soon as the substrate has been outside the solution vessel, with an integration time of 500 ms and a delay time of 1 s between two acquisitions. Because the storage time of the images into the computer hard drive was 500 ms, the total time between two acquisition was 2 s. **Figure 3.3** contains four selected diffraction patterns showing the different degrees of organisation in the mesostructured hafnia film: a diffraction ring appeared a few seconds after dip-coating, indicating the presence of disordered micellar structures with monodisperse size in the meso-range. This phase has been found to be stable because in other experiments we have obtained this disordered state by simply keeping low RH inside the deposition chamber. When high-RH air has been pumped inside the

deposition chamber ("dry air" valve close and "wet air" valve fully open) a sudden increase in the RH in the deposition chamber has been displayed in the hygrometer readout (from 20% to ≈ 80% in a few seconds).

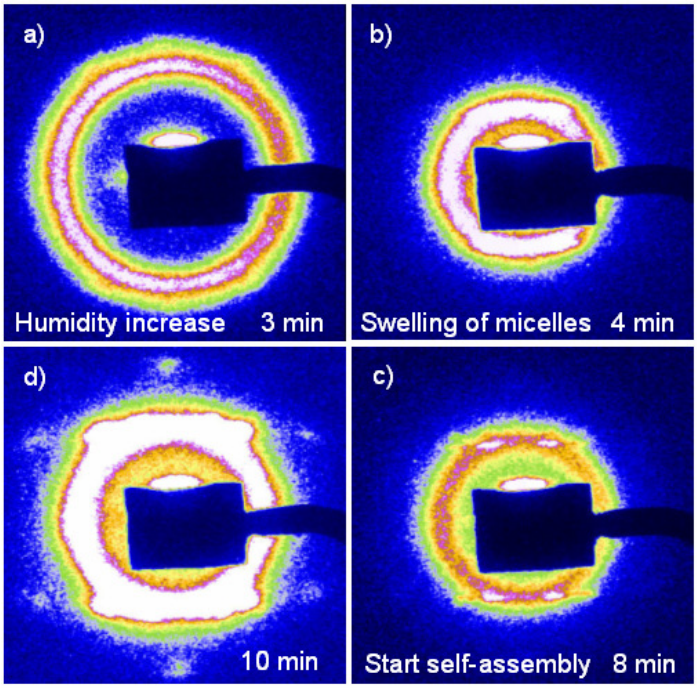


Fig. 3.3 The SAXS patterns recorded during self-assembly of a hafnia thin film. The increase in humidity (a) causes a micelle swelling (b) that, after 8 min, (c) produces self-assembly of the film (d). The conditions of instrumental acquisition have been maintained constant during self-assembly process. For this reason, in snapshot d the first order of the diffraction spots is totally saturated and appears as a bright ring.

At the same time, a marked shrinkage in the diffraction ring has been observed (**Figure 3.3b**). The ring shrinkage has been attributed to the increase in the size of the disordered micelles in the film (as the micelles swell, the diffraction ring decreases its diameter), which has been caused by water adsorption in the hydrophilic crown at the organic-inorganic hybrid interface.[4,6] The duration of the "wet air" flow has been approximately 5 seconds and both valves have been closed soon after the diffraction ring shrinkage has been observed. A few minutes later, diffraction spots have appeared, accompanied by a decrease in RH (**Figure 3.3c**). This has been likely caused by the diffusion of vapours out of the deposition chamber: because the deposition chamber is not airtight, the

system equilibrates with the external environment in the absence of a controlled air flow. After a few minutes we have observed the presence of well-defined spots and no diffraction ring (**Figure 3.3d**). This indicates a high degree of self-organisation; if we consider that the setup is in transmission mode: the mesostructure not only has out-of-plane order, commonly observed in mesostructured films, but it also shows high in-plane order. This experiment has been repeated few times in order to ensure reproducibility. We have noted that the disorder-order transition induced by RH changes is reversible: changing the humidity inside the deposition chamber from low to high RH (and vice versa) results in self-organisation and loss of order. These changes could be repeated a few times (at least 5 cycles) with little or no apparent loss of degree of order in the resulting mesostructure at high RH. These experimental results show that micelle swelling is directly related to organisation and rearrangement of the mesophase. The overall process is shown in **Figure 3.4**: the precursor solution is an isotropic sol in which block copolymer concentration *c* is lower than the critical micelle concentration *cmc*. When the solvent evaporates, *c* becomes greater than *cmc* and micelles self-assemble. At this stage, when a weakly condensed film is formed, a disordered array of micelles can self-organise upon increase of the external humidity. Water absorption by the micelles causes their swelling and this effect pushes the system to self-organize.

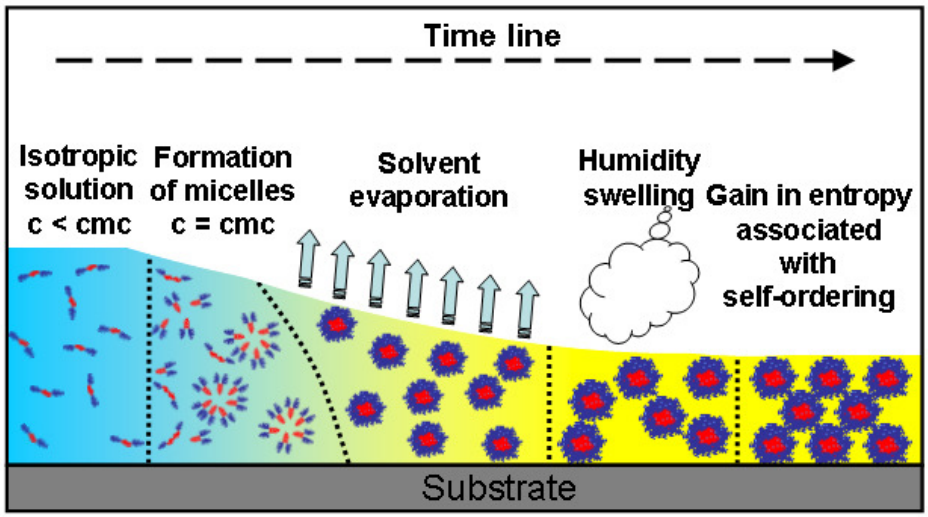


Fig. 3.4 Scheme of the self-assembly in a mesostructured hafnia film. The organization is caused by humidity swelling of the micelles.

This phenomenon can be related to the tunable steady state (TSS), a particular state of as-deposited mesostructured films that allows for micellar reorganisation by external sources (such as RH, as in this case).[7] Therefore, the system can be driven towards order as long as the flexibility of the oxide network allows a rearrangement of the templating micelles when their size increases. When inorganic condensation leads to the formation of large oxo- or hydroxo- clusters, the TSS ends. The possibility of rearranging (order-disorder transitions) has been observed for up to 5 hours since film deposition, which indicates a much longer TSS than that observed in silica (lasting approximately a few minutes). This is due to much faster condensation rate in TEOS than in chloride precursors.[8]

*- Mesophase symmetry*

After these *in situ* experiments, mesostructured hafnia films have been synthesised offline following the same experimental procedure, including the treatment at high RH leading to self-organisation as observed in the *in situ* experiments, and have been thermally treated at 150 °C for 1 hour in order to stabilise the inorganic framework and inhibit further mesophase rearrangements (i.e. suppress the TSS). These films have been studied by grazing incidence SAXS (GISAXS). The grazing incidence configuration has been chosen because the films have been deposited on thick substrates (500 µm-thick Si wafers). The GISAXS pattern of a mesostructured hafnia film treated at 150 °C is shown in **Figure 3.5c**.

The diffraction patterns have been simulated with the software Nanocell, a code written for Mathematica® which outputs the simulated SAXS pattern of a mesostructure given initial parameters such as mesophase symmetry, d-spacings and experimental setup.[9,10] Different space groups have been considered for the simulations, varying systematically the orientation of the unit cell with respect to the substrate. The only matching simulated patterns have been found to be (1) a rhombohedral unit cell with $R\bar{3}m$ symmetry, oriented with the [111] 3-fold axis perpendicular to the substrate, (2) a face-centred cubic cell with $Fm\bar{3}m$ symmetry having the same orientation with respect to the substrate as the rhombohedral cell. In fact, these two descriptions are fully compatible, because a rhombohedral unit is the primitive cell of a FCC cell, provided that the angle between the axes of the rhombohedral cell a is 60°.[11] If we consider the rhombohedral $R\bar{3}m$ cell, the thermal shrinkage perpendicular to the substrate causes the variation of

the cell parameters (axis a and angle α); alternatively, if we consider the cubic $Fm\bar{3}m$ cell, a contraction along the [111] direction (i.e. 3-fold axis) is observed.

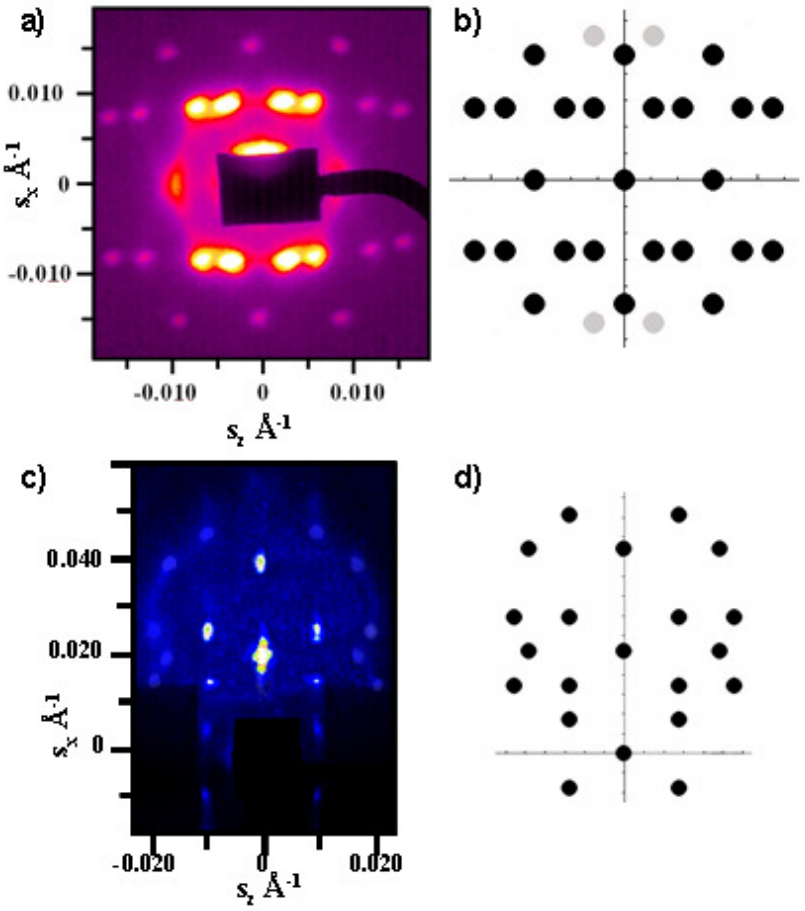


Fig. 3.5 Transmission mode SAXS pattern of an as-deposited hafnia film (a) and results of a Nanocell simulation (b); the grey spots are barely visible on the SAXS measurement (a). Grazing incidence SAXS pattern of a hafnia film treated at 150 °C (c) and its Nanocell simulation for the same unit cell.

These two descriptions can be considered equivalent, although the most correct choice from a crystallographic viewpoint is considered the rhombohedral $R\bar{3}m$ symmetry. The ordered mesophase can also be thought as composed of three different micelle planes in a close-packing stack with packing factor $f$ = 0.74. The calculation of cell parameters for both as-deposited and thermally treated mesostructured hafnia films has been performed by a numerical routine written for the rhombohedral $R\bar{3}m$ symmetry. The cell parameters for the as-deposited film are a = 20.80 ± 2.0 nm and α = 62.0 ± 6.2°. The constants for the film treated at 150 °C are a = 14.3 ± 1.4 nm and α = 83.2 ± 8.4°.

This confirmed that a uniaxial shrinkage occurs during thermal treatment along the [111] direction. Even after a weak thermal treatment, the mesophase retains the same symmetry: this is in agreement with our findings because a uniaxial contraction of a rhombohedral cell along the [111] direction does not reduce the symmetry operations of this type of structure. Considering the reported error bar, the angle $\alpha = 62°$ calculated for the rhombohedral cell of the as-deposited film is close to that of the undistorted $Fm\bar{3}m$ cell, that is $\alpha = 60°$. This confirms that the rhombohedral structure of the as-deposited film can be described by a cubic $Fm\bar{3}m$ cell.

*- Self-organization as an entropy-driven process*

The synthesis of mesoporous films used in these experiments is known as evaporation-induced self-assembly. The underlying concept is that solvent evaporation causes an increase in the nonvolatile (inorganic and organic) species. This triggers both self-assembly, because of the increase in surfactant concentration above the critical micellar concentration, and formation of bridged oxo- or hydroxo- species by the metal centres. However, this is in partial disagreement with our findings: the TSS duration of hafnia films is on the order of hours because the formation of an ordered structure can be observed even minutes after dip-coating. At the same time, we can reasonably assume that all solvent has been evaporated during the first minutes after dip-coating; therefore, the formation of an ordered mesostructure might appear uncorrelated to solvent evaporation. A solution to this contrast can be found in the fact that self-assembly describes the formation of micellar structures by the aggregation of surfactant molecules when $c > cmc$: this is observed in the first seconds after deposition, when solvent evaporation takes place and can be considered to cause the self-assembly of disordered micelles (formation of a ring, **Figure 3.3a**). We now consider another phenomenon, self-organisation, as separate from self-assembly, because it involves the formation of ordered arrays of pre-formed micelles. Therefore a first conclusion is: solvent evaporation triggers self-assembly, but not self-organisation, because we can observe self-organisation even hours after solvent evaporation. Another case where self-organisation is observed as a distinct phenomenon from self-assembly can be found in the synthesis of mesoporous tin oxide reported by Hillhouse's research group.[12] In this work, a mesostructured tin oxide films is formed upon ageing at high RH for hours (delayed humidity treatment, DHT). In the cited publication the authors state "it is clear

that the self-assembly process reported here is not EISA [. . . ] The mesostructure is formed while the films are still in the high-humidity environment, in the presence of excess water incorporated during the DHT". However, no structural information on self-assembly regarding the first seconds and minutes after dip-coating is reported.

Our experiments suggest a thermodynamic interpretation of the self-organisation of the process (self-assembly is still assumed to be driven by solvent evaporation). The film in its TSS is in a temporal window in which randomly distributed micelles can self-organise in ordered arrays without solvent evaporation. If we model the micelles as spheres in which interpenetration is forbidden and the interaction energy is zero, the enthalpy variation of the system during self-assembly can be neglected. This is a reasonable assumption because the spheres are not in contact due to inorganic species which condense on micellar hydrophilic surfaces.[13] It is important to stress that even if enthalpy plays an important role during solvent evaporation, once the micelles and the solid inorganic network are formed, we assume that it does not change significantly. As a consequence, only the entropic term in $\Delta G = \Delta H - T\Delta S$ should be responsible for the decrease in $\Delta G$ that pushes the system to self-organisation. The counterintuitive idea that entropy is the source of order can be used to explain the experimental findings in the tunable state of self-organisation. In fact, the loss in entropy with ordering is more than compensated by the gain in entropy due to the increased free volume[*] of the micelles into an ordered array.[14,15] The swelling of micelles increases the volumetric fraction of the organic mesophase within the film, so that the micelles have lower translational entropy. In these conditions, the only way to maximise the entropy of the whole system is to increase free volume by packing the micelles in an ordered structure. Self-organisation is thus an entropy-driven process, provided that the inorganic framework is flexible enough to allow micelle self-organisation.

*- Mesostructure damage induced by synchrotron radiation*

During the *in situ* experiments on mesostructured hafnia, an interesting phenomenon has been observed while the preview of SAXS acquisition has been operating. The preview system allows to continuously capture and display SAXS patterns on the computer monitor, so as to follow structural evolutions in real-time. The interesting observation is that the mesostructure degree of order has appeared to decrease with

[*] The free volume is defined as the volume within which a given hard sphere centre can move without requiring alterations in the positions of the other surrounding spheres.

time: at first this has been related to a change in RH that caused a mesophase transition towards a disordered state. A few adjustments have been made to the experiments, for example RH has been controlled more carefully, the solution vessel has been removed from the chamber in order to prevent solvent and HCl vapours to come into contact with the film. However, the disordering phenomena have been remained and no satisfying explanation has been provided. We have obtained a clue of what has been happening when we have moved the sample a few mm to one of its sides, so that the incident beam has probed a different region of the film: the mesostructure in this "new region" has shown a much higher degree of order with respect to the "old region", comparable to the degree of order of the "old region" before observing mesostructure degradation. We have found that this degradation is fully reproducible in mesostructured hafnia films: mesostructure degradation takes place only in the irradiated area and does affect the adjacent regions, so that after observing mesostructure degradation, an ordered region has been detected simply by shifting the sample. The most likely reason of this local mesostructure disruption phenomenon has been assumed to be radiation damage induced by the incident X-rays. The preview system requires that a X-ray beam impinges on the sample continuously - typical values are 500 ms acquisition and 1500 ms delay - controlled by a fast shutter, therefore the sample has been continuously irradiated with the incident X-ray beam. Furthermore, the effect has not been observed when few acquisitions have been made instead of many continuous acquisitions in preview mode. Another effect has been visible in the irradiated samples: at the end of the experiments the films presented a change in colour in the irradiated region. In transmission mode, this is a spot having the same shape of the incident X-ray beam, whereas in grazing incidence configuration this is a stripe extending on the whole film. We can formulate two hypotheses: (1) the block copolymer backbones have been chemically broken by the incident X-rays, so that the micelles have been disrupted. (2) A local increase in temperature caused micelles to de-assemble: *cmc* is highly sensitive to temperature and even a slight increase in temperature may cause the loss of self-assembly conditions, favouring the "single-chain state" of the unassembled molecules of surfactant. A number of publications support the first conclusion. In particular, damage to biological structures is often induced by high-flux synchrotron radiation due to the formation of free radicals from water molecules. The free radicals act as initiators for the de-polymerisation of these biological species e.g. lipids, proteins.[16,17,18] To check whether the radiation affects the total thickness or the surface roughness of the film, we

have compared the morphology of both the irradiated and the unirradiated areas by atomic force microscopy (AFM). To perform the measurements, a NT-MDT Ntegra instrument working in contact mode has been used. The curvature radius of the AFM tip is 10 nm, and the elastic constant of the cantilever is 0.2 $N \cdot m^{-1}$. Both large area (50 µm × 50 µm) and small area (1 µm × 1 µm) scans have been acquired to verify the roughness on different length scales.

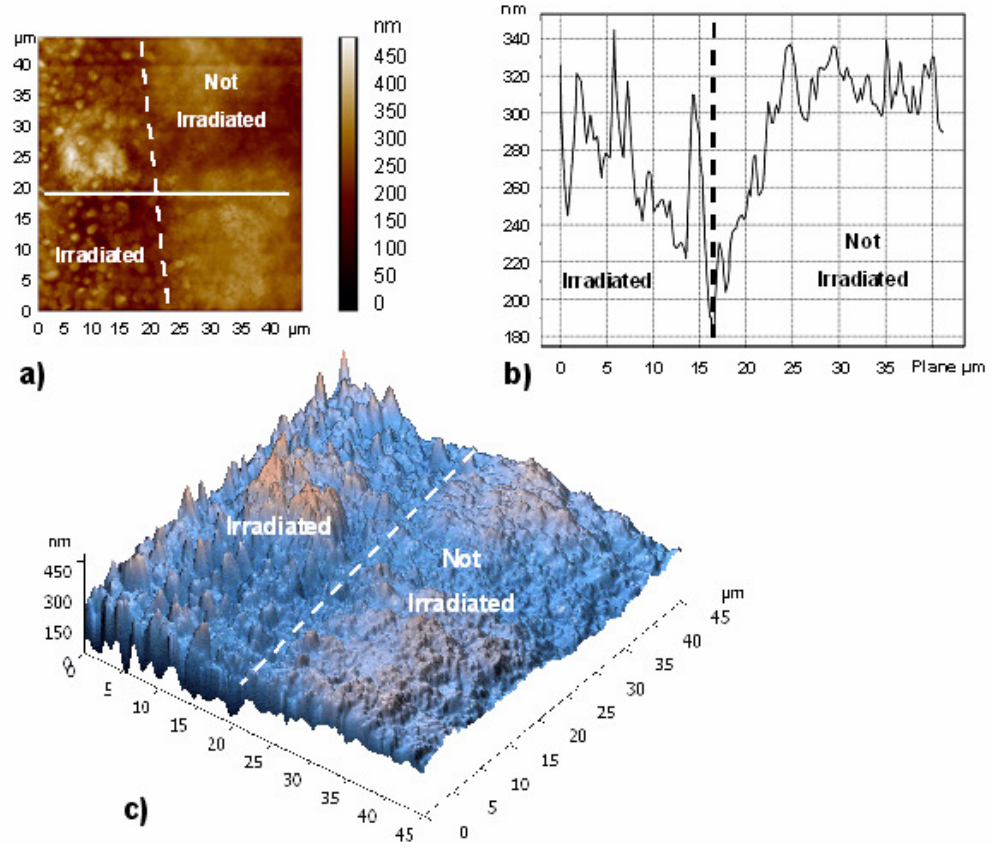


Fig. 3.6 AFM image of a mesostructured hafnia film after X-ray exposure on a stabilized film (40 min at 60 °C). Plane and perspective views of the boundary region between irradiated and non-irradiated areas (a and c). Depth profile of the film across the irradiation boundary (b).

We have found that the thickness is not affected by radiation while the roughness increases after X-ray irradiation (sampled on 10 different points on the surface); such difference has been related to a loss of micellar organisation, which takes place without any crack or damage to the sample. Images of **Figure 3.6**, taken close to the border between the irradiated and unirradiated regions, show no substantial difference on the average height of the surface. This provided evidence that the observed disordering phenomenon can be related to mesostructure de-assembly and does not consist in a mere ablation of the film from the substrate. Even more surprisingly, we have found that this mesostructure deformation is reversible. The results of an experiment, which are

reported in **Figure 3.7**, show that after mesostructure disruption, if the film is left at controlled RH for a certain amount of time with no irradiation, it would recover a highly ordered mesostructure.

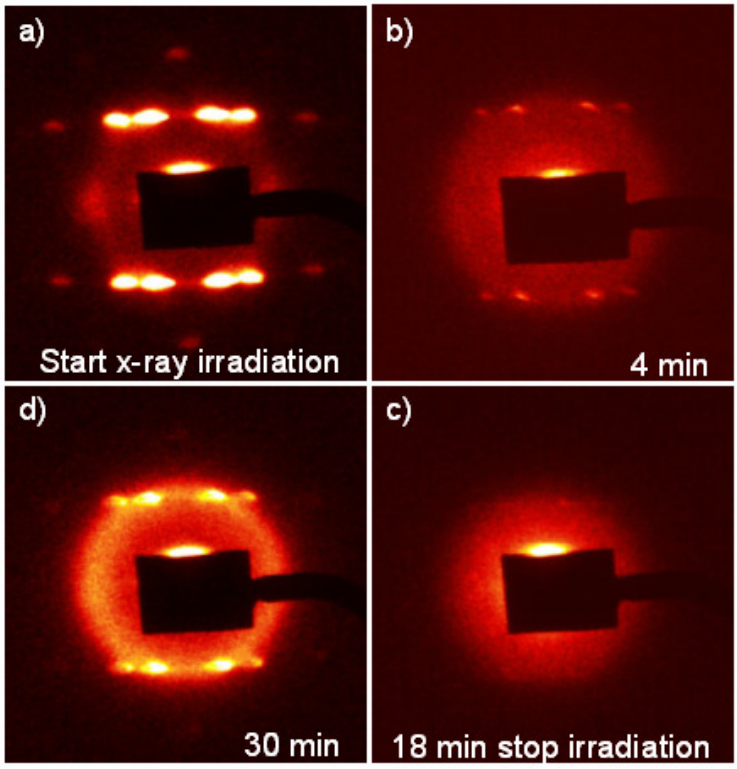


Fig. 3.7 Organization disarray induced by intense X-ray radiation and disorder-to-order transition. In situ SAXS patterns recorded at different irradiation times. A high flux radiation causes on a highly organized film (a) the disarray of the rhombohedral mesophase (b). After 18 min of irradiation the organization is completely disrupted (c). Self-assembly is again observed after switching off the X-ray flux and maintaining the film in stationary conditions of humidity and temperature (d).

In other words, the mesostructure undergoes a process of re-organisation. The possibility of cycling between ordered and disordered states has been confirmed by further experiments, although some hysteresis has been observed, so that the phenomenon cannot be said to be fully reversible. This is caused by the stiffening of the inorganic network (polycondensation) which puts a time limit on the TSS and inhibits further micellar rearrangements.

The mesostructure disruption-restoration phenomenon has a particular importance because - as in the previous case, when mesophase changes have been induced by RH variations - the self-organisation process is never pushed by solvent evaporation but it

appears another entropy-driven process. If we admit that mesostructure disruption is caused by cleavage of the copolymer backbones, mesostructure restoration can be thought of involving the diffusion of undamaged block copolymer molecules and the self-assembly and self-organisation of new supramolecular structures. This is the most reasonable assumption but to date no experimental data have been acquired to provide support to this hypothesis, and further experiments are planned. In any case, self-assembly and self-organisation appear as separate mechanisms leading to different phenomena: formation of micelles and formation of order, respectively.

To sum up, self-assembly and self-organisation in mesostructured films appear as highly tunable processes: evaporation-induced self-assembly drives the templating species towards a first intermediate stage when micelles are formed upon solvent evaporation and increase of nonvolatile media. The flexible nature of the inorganic network, which is composed of oxo- and hydroxo- bridges and has a low degree of condensation, allows for micellar self-organisation driven by external parameters. These can be either changes in relative humidity or high-flux X-rays, leading to entropic effects. A direct application of this phenomenon is the possibility of inducing disordered regions into the mesostructured film with the aim, for example, to produce materials with a gap in the refractive index (after calcination, the mesoporous unirradiated region is expected to have a lower refractive index than the irradiated non-porous region). It is also possible to perform several write-erase cycles as long as the degree of condensation of the film allows mobility of the micelles. These changes in the mesophase become permanent once the mesostructure is thermally stabilised.

### 3.1.2 *In situ* combined FTIR-SAXS studies

Several groups have successfully coupled SAXS with other *in situ* techniques to correlate the structural data and the chemical processes that occur during dip-coating. An interesting example is reported by Grosso and co-workers who performed time-resolved *in situ* GISAXS using synchrotron light combined with interferometry measurements on a mesostructured silica film templated by cetyltriethylammonium bromide.[19] This combined interferometry-SAXS technique allowed correlating mesophase organisation occurring during dip-coating with film thickness. Here, the evolution of thickness with time follows a triple regime, where a first rapid evaporation step is attributed to the evaporation of (mainly) ethanol; the second step is slower, due

essentially to the departure of water, and a third regime involves the loss of residual water and ethanol molecules. However, the departure of solvent molecules is just an educated guess which is not completely supported by experimental data. Another example of a combined technique has been reported by Doshi et al. who performed time-resolved *in situ* GISAXS using synchrotron light combined with gravimetric analysis to study the self-assembly of a slowly evaporating cast film.[20] In another work, *in situ* Karl Fischer titration measurements have been used to estimate the content of water in as-deposited silica films as a function of RH, obtaining increasing $h = [H_2O] / [Si]$ values with increasing RH values, even though titrations have not been made on films but on solutions, which have been assumed to be representative of the corresponding films.[7] Mass spectrometry of vapour fraction, Karl Fischer titration, ellipsometry and interferometry data acquired *in situ* on mesostructured titania thick films have been used to follow the evolution of volatile species and film composition.[5] Crossing these data has led to the comprehension of the role of each variable involved in the self-organisation. Thanks to these central works, fundamental solution and processing parameters, such as the manifold role of water and the importance of the tunable steady state, have been sorted out. FTIR technique has proved to be very effective to monitor the evaporation of water and ethanol and the polycondensation reactions in silica mesostructured materials; for this reason we have used a combined SAXS-FTIR characterization to monitor the chemical processes during self-assembly in dip-coated films.

*- Experimental set-up for simultaneous analyses*

The experimental setup is shown in **Figure 3.8**. FTIR measurements have been performed using the optical system of the IRCube™ interferometer.[21] This is a very compact commercial spectrometer produced by Bruker Optics, working in the middle infrared (mid-IR) with a KBr beamsplitter and a Globar source. The setup has been designed so that simultaneous FTIR and GISAXS measurements could be performed on the film, using the conventional Globar source and the synchrotron radiation, respectively. The optical components of the FTIR spectrometer have been set so that a parallel IR beam has been focused by an additional external parabolic mirror onto the sample in transmission mode at normal incidence. The transmitted signal has been reflected by a flat mirror towards another elliptical mirror focusing the signal onto the liquid nitrogen-cooled MCT detector. A GISAXS configuration has required that the

correct angle of incidence has been set carefully: the optimum angle of incidence $\alpha_i$ is slightly above the critical angle of a mesostructured film (≈ 0.2°), and small variation off this optimum angle can deeply affect the GISAXS measurements, because too small $\alpha_i$ can cause total reflection, whereas too large $\alpha_i$ can cause insufficient scattering.

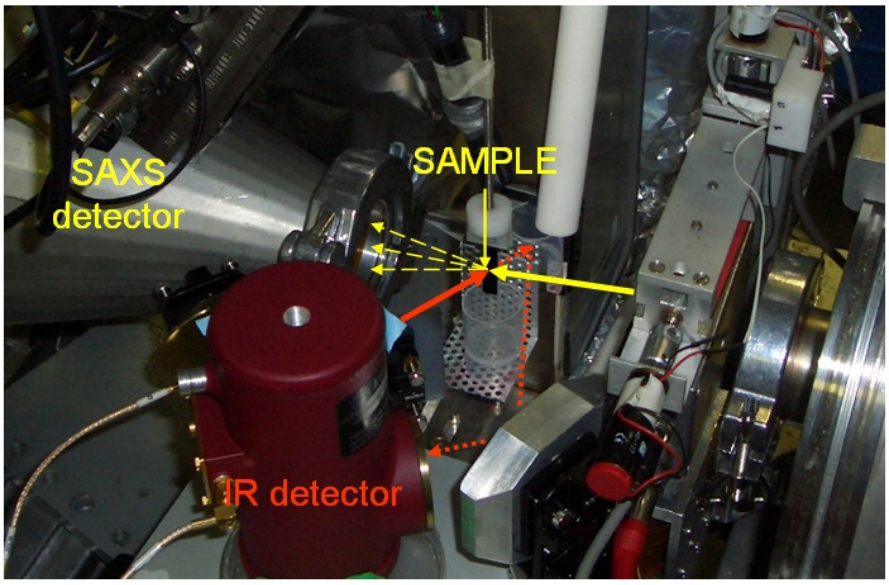


Fig. 3.8 Experimental set-up for simultaneous FTIR-SAXS at the Austrian SAXS beamline at the ELETTRA synchrotron.

The dip-coater's sample holder can be rotated so that the angle of incidence of the impinging X-ray can be readily varied. However, because accessing the experimental hutch during the measurement is forbidden, the sample holder rotation must be performed before the experiment is started. Therefore, we have used a freshly-coated mesostructured silica sample for the adjustment of $\alpha_i$, which has been left unaltered during the whole experiment by fixing the sample holder. Following this experimental configuration, the incident IR and X-ray beams probe the very same region of the sample. The interval between successive acquisitions has been set to 2 seconds, since from preliminary tests we have evaluated that the time scale of these processes is in the order of seconds both in terms of self-assembly and chemical processes. The sequences of GISAXS and FTIR spectra acquisitions have been simultaneously launched immediately after the solution vessel has been lowered. FTIR data have been collected using the Bruker OPUS™ software, and each FTIR spectrum has been obtained by averaging 16 interferograms having at a resolution of 8 $cm^{-1}$. Background has been

collected prior to each measurement session as the average of 100 spectra on a bare silicon substrate. The procedure followed in GISAXS data acquisition is the same used for the *in situ* experiments conducted on mesostructured hafnia films described in the previous paragraph. Here we present an *in situ* FTIR-SAXS experiment using a hybrid silica precursor solution (details of the synthesis are reported in Section 3.1, page 37). We used a 400 μm-thick, p-type B-doped (100) Si wafer as the substrate because it ensures transparency in the mid-IR range. Simultaneous FTIR and SAXS acquisitions have been launched after lowering the solution vessel (pulling rate 2.3 $mm \cdot s^{-1}$), as soon as the silicon substrate has been fully coated. The relative humidity in the deposition chamber has been set to ≈10% and kept throughout the whole experiment.

*- GISAXS results*

**Figure 3.9** shows the time-resolved GISAXS two-dimensional patterns recorded at intervals of two seconds.

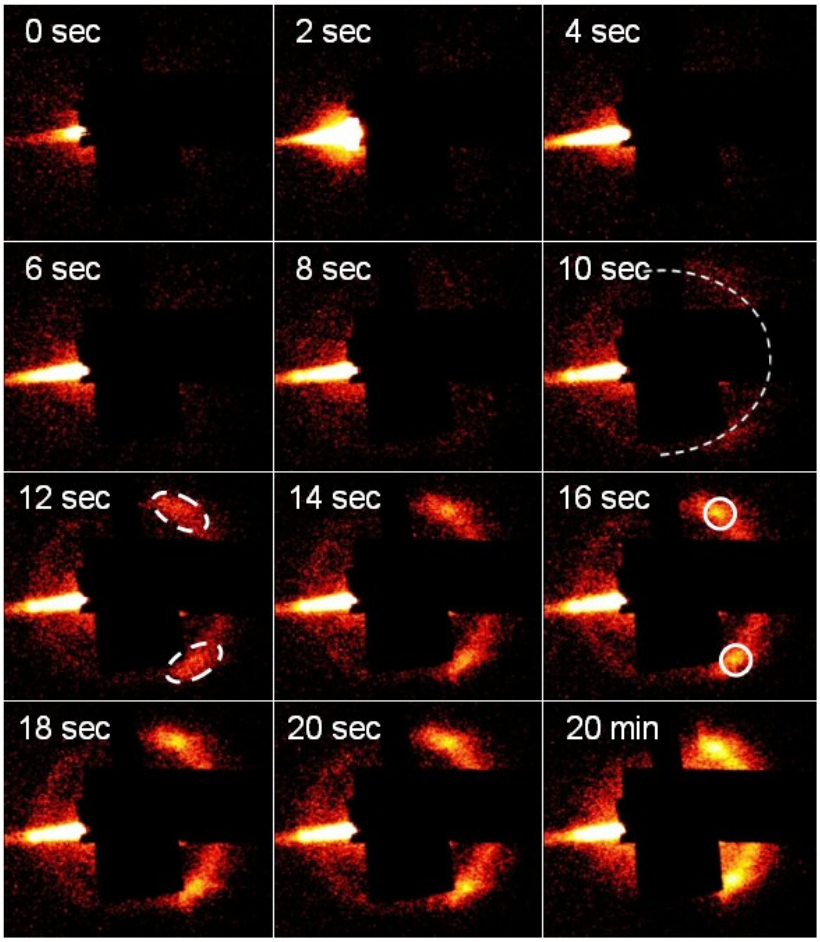


Fig. 3.9 GISAXS images recorded at different times after the dip-coating.

The first significant snapshots are shown, from t = 0 (acquisition start) to t = 20 sec. Another GISAXS snapshot, recorded at t = 20 min, is also reported. The GISAXS and FTIR spectra have been recorded for times as long as 40 minutes from dip-coating. Within this time frame the RH inside the deposition chamber has been maintained constant at 10 ± 5%.

The GISAXS patterns show that in the first 8 seconds no mesophase organisation takes place, and after 10 seconds the presence of a ring (dotted line in the figure) indicates that organisation is starting, even though a mesophase is not still well defined. At 12 seconds the detection of well-defined spots reveals the presence of an ordered mesostructure. Whereas these spots increase in sharpness and intensity with time, negligible changes are observed at times longer than 20 seconds. These *in situ* GISAXS data show only two diffraction spots, which makes the unambiguous identification of the space group impossible. This is because the integration time for each GISAXS pattern has been limited to 500 ms in order to have good time resolution, and higher-order diffraction spots requiring longer integration times could not be recorded. Nevertheless, these spots could be used to quantify the degree of mesophase order.

*- FTIR results*

**Figure 3.10** shows the FTIR spectra recorded simultaneously with the GISAXS patterns shown in **Figure 3.9**. In this experiment, we expected to detected the kinetics of solvent and water evaporation. The raw spectra appear well resolved and exhibit good signal-to-noise ratio even if they have not been smoothed and the baseline has not been corrected. We can recognize two main regions, at high wavenumbers (3700–2800 $cm^{-1}$) and at low wavenumbers (1700–800 $cm^{-1}$) where different chemical species overlap. The first stages of the FTIR spectra are dominated by the vibrational modes attributed to ethanol. Its intense signals at 2973, 2927, 2885 $cm^{-1}$, at 1460–1270 $cm^{-1}$, at 1088 and 1050 $cm^{-1}$, and at 880 $cm^{-1}$ allow following solvent evaporation with time. After about 8 seconds this process is completed (the residual signal after 10 seconds observed in the C-H stretching region around 2700–3000 $cm^{-1}$ has been assigned to the surfactant). The decrease in intensity of the 1640 $cm^{-1}$ vibrational mode, attributed to water ($\nu_b(H_2O)$), indicates that evaporation of water is also observed in the first seconds of dip-coating, but after this fast initial stage, a slower evaporation rate follows.

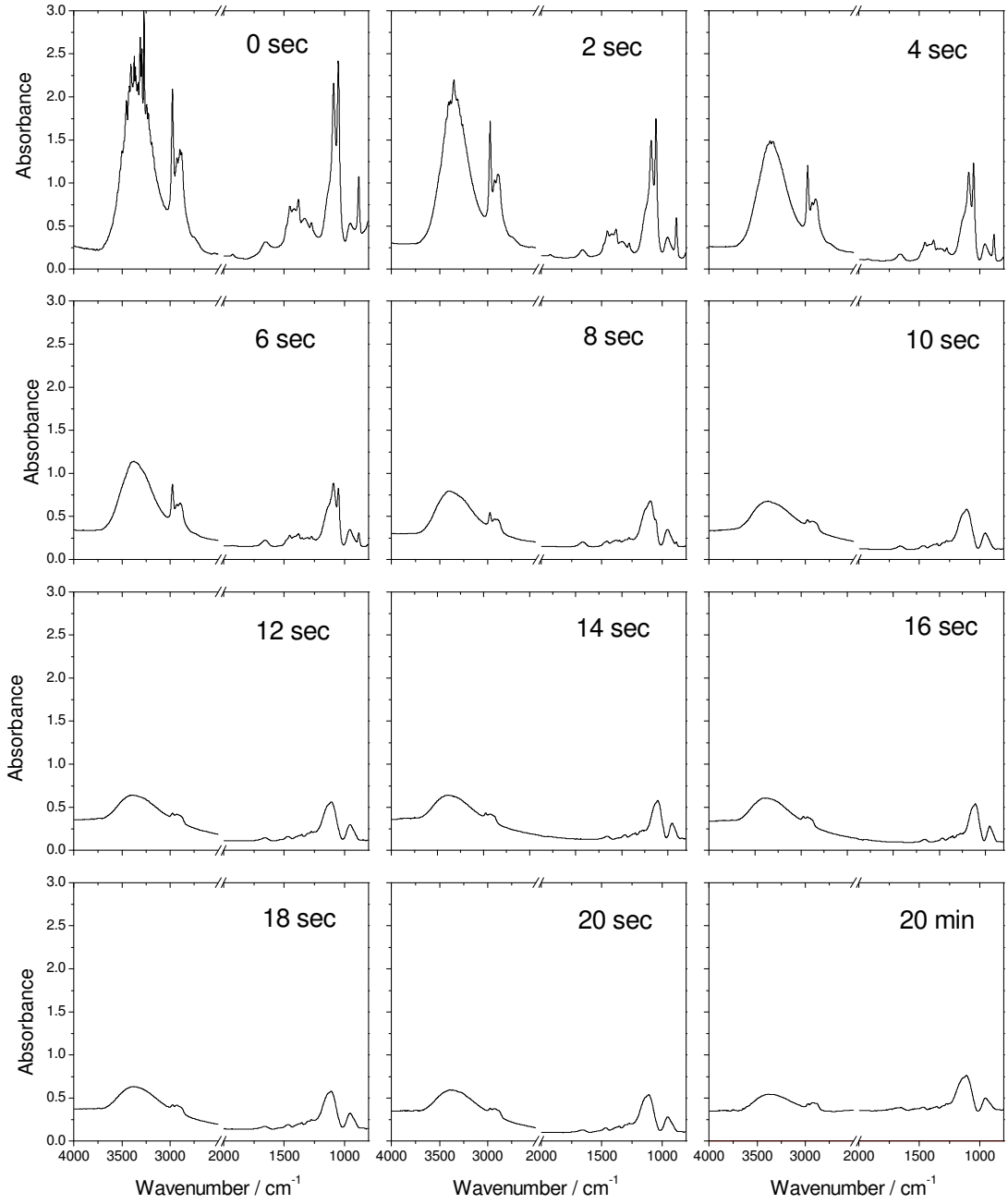


Fig. 3.10 Transmission FTIR absorption spectra recorded at different times after the dip-coating.

*- Comparison between SAXS and FTIR data*

**Figure 3.11** shows the content of ethanol and water in the film as a function of time (dip-coating has been set as t = 0). The content of ethanol and water has been estimated considering the areas subtended by two specific absorption bands that are well resolved

and not overlapped with other vibrational modes, that is around 880 and 1640 $cm^{-1}$ for ethanol and water, respectively.

The area of the two bands has been plotted as a function of time, assuming that the areas at t = 0 correspond to 100% water and 100% ethanol in the film. From this graph, the evaporation of ethanol appears fast, following a linear trend: after 10 seconds the residual ethanol in the film can be approximated to 0%, so that the process can be considered to be complete.

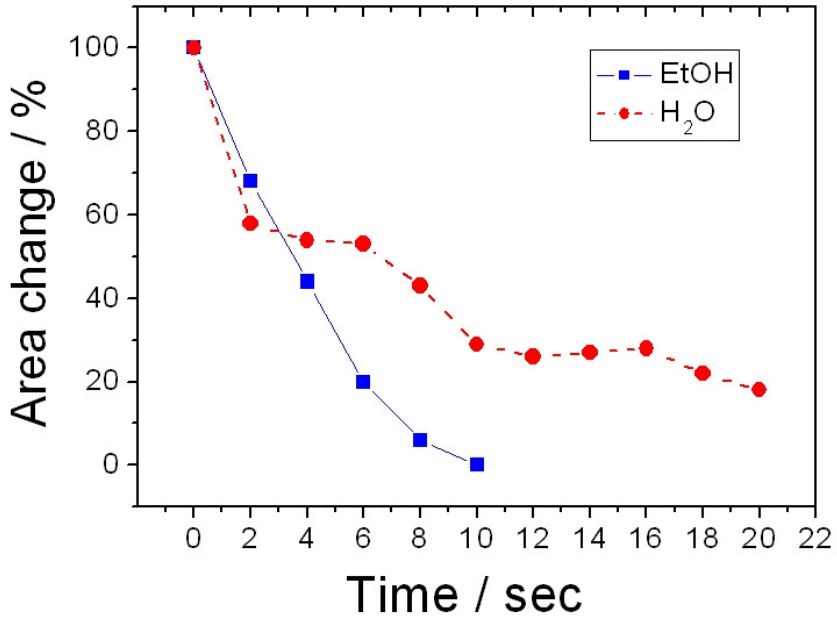


Fig. 3.11 Change in the area of the 1640 $cm^{-1}$ band attributed to water and of the 880 $cm^{-1}$ band attributed to ethanol as a function of time after dip-coating.

The evaporation of water has a more complex trend: a fast initial evaporation in the first 2–3 seconds, similar to ethanol, is followed by a slower intermediate stage between 3 and 6 sec, then a third phase of water enrichment between 6 and 10 sec is followed by another evaporation stage from 16 sec onwards. More specifically, at t = 10 sec, around 30% of the initial water is present in the film, whereas all ethanol is evaporated. At t = 20 sec, around 20% of the initial water is still detected in the film. The water enrichment stage (third point in the above description) is attributed to the polycondensation reactions that occur after ethanol evaporation. From GISAXS data, we observe that the organisation into an ordered mesophase starts only after ≈ 10 seconds. Comparing these structural data with the spectroscopic data from FTIR measurements, we infer that an ordered mesostructure is formed after ethanol

evaporation is complete and 70% water has departed from the film: at this stage the SAXS diffraction spot intensity increases showing a sigmoidal trend with time. **Figure 3.12** shows the change in the average intensity of a GISAXS diffraction spot (upper spot in the snapshots of **Figure 3.9**) as a function of time. To obtain these data, the intensity of a selected diffraction spot in a SAXS pattern has been calculated as the average intensity calculated in a rectangular area around the spot, composed of 1148 pixels. These data have been used for a semi-quantitative evaluation, in that they can not be normalised with respect to the intensity of the background. Nevertheless, this has given a reliable indication on how the mesophase evolves with time. The appearance of the asymmetric stretching $\nu_{as}$(Si-O-Si) band at around 1100 $cm^{-1}$ in the FTIR spectra after 10 – 12 seconds indicates that at this time polycondensation reactions are almost complete and an interconnected silica network is formed. However, at this stage the silica network is still flexible enough to allow spatial reorganisation of micelles. It is worth to underline that mesophase organisation starts only after ethanol evaporation. This is in agreement with the well-known role of ethanol evaporation as the trigger to mesophase formation. However, as described in the introduction, there is no direct evidence of this, as there is no *in situ* experiment in the literature capable of providing simultaneous unambiguous spectroscopic and structural information on mesophase organisation.

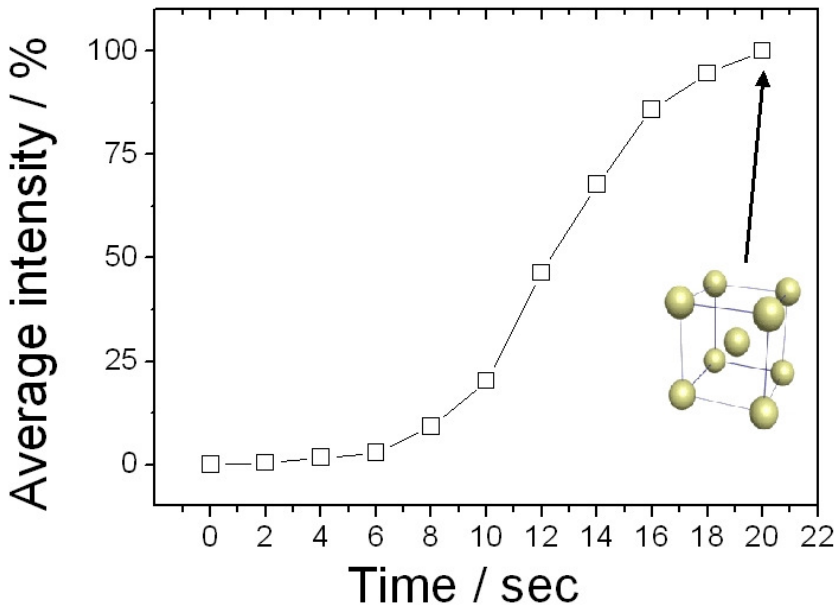


Fig. 3.12 Average intensity of a GISAXS diffraction spot as a function of time.

Therefore, this is the first time that evidence is provided regarding the time correlation between ethanol evaporation and mesophase formation. This is the most exciting finding of this FTIR-SAXS *in situ* technique. The major advantage of simultaneous FTIR and SAXS analysis is the possibility to discriminate between the evaporation rates of ethanol (or any other solvent) and water, as well as to obtain semi-quantitative data that can be examined in the light of the structural data provided by SAXS. The discrimination between different chemical species can be readily attained by FTIR spectra, because vibrational modes are attributed to different chemical species (e.g. the amount of free water, the degree of condensation of the inorganic walls).

In this case, it has been proved that the formation of an organised mesophase occurs after all ethanol and 70% of water have evaporated. At this stage, the presence of water in the film can be estimated as $h = [H_2O] / [Si] = 1.56$ (i.e. 30% of $h$ in the precursor solution), which is close to the values obtained through other *in situ* experimental techniques such as Karl-Fischer titration.[5] This leads us to identify another application of the present technique, in that the water content (expressed as $h$) can be simply calculated from FTIR data, and correlated quantitatively with RH. As we have said, this has been done previously by means of rough estimates from Karl-Fischer titrations on cast films rather on dip-coated films, but the FTIR-SAXS technique can be considered to be more accurate. Other advantages of this FTIR-SAXS combined technique are that it is not invasive, can be applied to thin films instead of thick films, cast drops or solutions, and does not require altering the chemistry of the self-assembling system. It also takes into account the presence of atmospheric water, as a reference background is taken prior to each FTIR measurement session.

To summarise, in this paragraph we have presented a new combined FTIR-SAXS technique, where the IR source is a conventional Globar lamp, and monochromated synchrotron light is used as the X-ray source. This technique has been applied to the study of mesostructured organosilica films with an experiment providing insight on basic structural and chemical aspects of self-assembly. The formation of an ordered mesostructure has been correlated with ethanol and water evaporation from the film; the amount of residual water within the film has been estimated to be 30% in correspondence to the onset of self-assembly, whereas all ethanol is already departed from the film. This opens a new affordable route to calculate the amount of residual solvent in the films. Besides, the presence of water vapour in the environment is accounted for by the background spectrum, acquired prior to each measurement session.

This is important because a direct correlation can be established between the RH value in the deposition chamber and the quantity of water present in the film: this correlation has been previously studied in the literature, but using experimental techniques based on thick films or cast films, whose behaviour is quite different from thin films obtained by dip-coating and studied by in situ SAXS. The simultaneous recording of different types of information allows correlating different phenomena that contribute to a complex process such as self-assembly in mesostructured films. This is particularly relevant when the kinetics of some chemical reactions can affect other chemical or physical processes involved in the phenomenon. Another advantage provided by the in situ FTIR-SAXS technique is that different vibrational modes can be attributed to different species in the FTIR spectra (provided that they do not overlap). Therefore, different chemical information can be obtained, for example on water content, ethanol content, inorganic condensation, copolymer content, etc.

## 3.3 Pores surface properties

The ability of mesoporous materials to graft different types of molecules or show functional properties (e.g. sensing) is strictly related to the physicochemical properties of the pore surface; an important issue, therefore, concerns its nature and the related mechanism of water adsorption–desorption. With these experiments we have first synthesized highly ordered mesoporous membrane and then we have studied their pore surface chemistry as a function of the environmental pressure. We have also changed the chemical composition of the mesoporous membrane using either pure, either organically modified silica precursors to elucidate the interactions between surface and water molecules in the pores.

Transparent inorganic and hybrid organic/inorganic mesoporous silica membranes have been synthesized as reported in Section 3.1, page 37. After 60 days of ageing, before thermal treatment, transparent and self-standing membranes have been obtained, in the shape of disks with about 30 μm thickness and 80 mm diameter (**Figure 3.13**). Membranes have been also calcined in an oven, with a heating ramp from room temperature to 350 °C. After the thermal treatment, the membranes remained transparent even though they broke in fragments of some centimetres. TEOS–MTES–F127 and TEOS–F127 membranes will be hereafter referred to M and T, respectively.

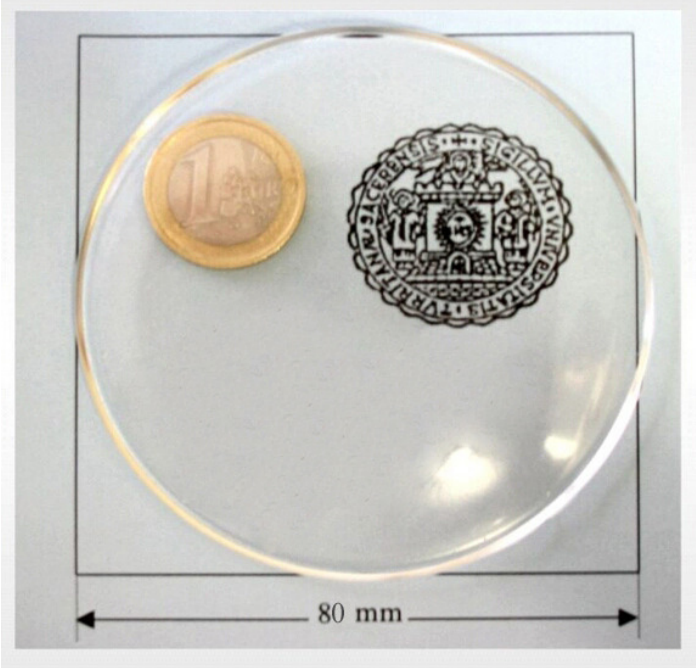


Fig. 3.13 Optical appearance of an as-prepared mesostructured organosilica membrane.

- *Morphological characterization: SAXS and TEM*

As-prepared and thermally treated membranes have been investigated by grazing incidence and transmission SAXS at the Austrian beamline of ELETTRA. SAXS. Patterns have been acquired with different exposition times to obtain the *d*-spacings of the ordered mesostructures with good signal-to-noise ratio for both low-order and high-order diffraction spots. **Figure 3.14a** and **c** shows a representative GISAXS patterns of uncalcined pure silica and organosilica membranes. Nanocell code for Mathematica®, developed by the Hillhouse research group,[9,10] has been used to simulate the diffraction patterns (**Figure 3.14b** and **d**). Based on this analysis, we can conclude that the experimental GISAXS patterns of both M and T membranes are consistent with a slightly distorted cubic $Im\bar{3}m$ phase (space group #229 in Crystallographic Tables) oriented with the (110) plane parallel to the surface of the membrane. The cell constants of the ordered mesostructure have been calculated using a numerical routine developed for the $Im\bar{3}m$ cubic cell; they are a = 16.3 ± 1.1 nm for the as-prepared M membrane and a = 11.8 ± 1.0 nm for the calcined M membrane. This corresponds to a contraction in the cell parameter of 28% upon calcination. In the silica membranes the cell constants are a = 18.0 ± 1.0 nm and a = 14.2 ± 1.0 nm for the as-prepared and calcined membranes, respectively, with a contraction of 22% induced by calcination. Note that in

this case the shrinkage is isotropic, contrary to films, where uniaxial contraction perpendicular to the substrate is always observed. In another experiment we have tried to increase the evaporation rate by placing the Petri dishes containing the precursor solutions under a chemical hood.

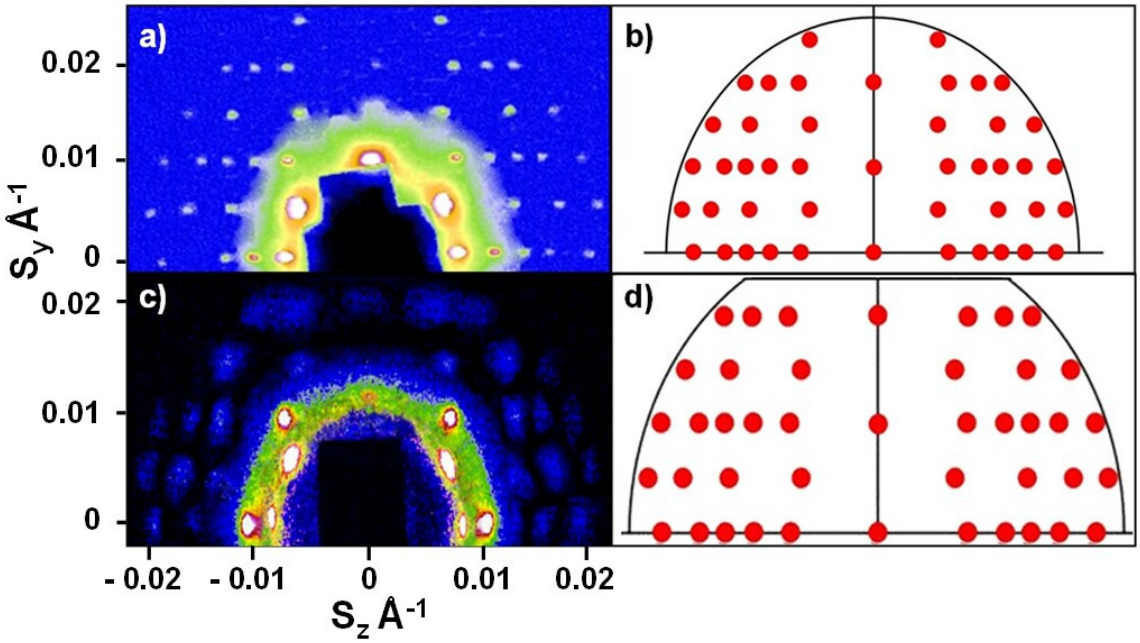


Fig. 3.14 GISAXS diffraction patterns of TEOS–MTES–F127 (a), and TEOS–F127 membranes (c). The relative diffraction patterns obtained by simulation with Nanocell code are shown on the right side: (b) TEOS–MTES–F127 and (d) TEOS–F127.

In a few days the membranes have dried, however they have not given appreciable signal in GISAXS measurements. This indicates that there has been no ordered mesostructure in the membrane otherwise a diffuse ring should be visible in the pattern, corresponding to a wormlike mesophase. Two conclusions can be deduced from this evidence: 1) solvent evaporation has to be slow in order to occur self-assembly and create an ordered pore array; 2) objects thicker than films, prepared under similar conditions, require slower solvent evaporation to reach a comparable degree of pore organization.

It should also be noted that both the inorganic silica and the organosilica membranes show the same mesophase symmetry with a high degree of order and only a slight difference in the cell parameters. On the other hand, it is quite well established that hybrid films prepared from a mixture of TEOS and MTES are more ordered with respect to films prepared from TEOS.[3] In the corresponding membranes the role of the

methyl groups does not seem to be so critical to affect the final structure. This is probably due to the specific synthesis conditions: in particular, a slow solvent evaporation may favour a more thermodynamic and less kinetic control on the formation of the mesostructure. The use of a specific sample holder equipped with an *x*–*y* stage system (parallel to the membrane surface) has allowed the sampling of the T membrane along two orthogonal directions with steps of 5 mm (**Figure 3.15**). A structural mapping of the samples is required to ensure that the ordered mesophase extends in the whole membrane and is not restricted to some regions. Nine different SAXS diffraction patterns, recorded in transmission mode, are shown in **Figure 3.15a** while the corresponding positions in the membrane are reported in **Figure 3.15b**. Comparing the SAXS patterns taken starting from the centre of the membranes towards the outer region, it is possible to detect the presence of the ordered mesophase in the central region of the membrane within a radius of 30 mm. The presence of spots both in the transmission and grazing diffraction patterns relative to this inner region show that the mesostructure has both *in-plane* and *out-of-plane* order: this is a feature that is not commonly observed in mesoporous materials, where ordered mesoporous domains have no in-plane preferential orientation (planar disorder).

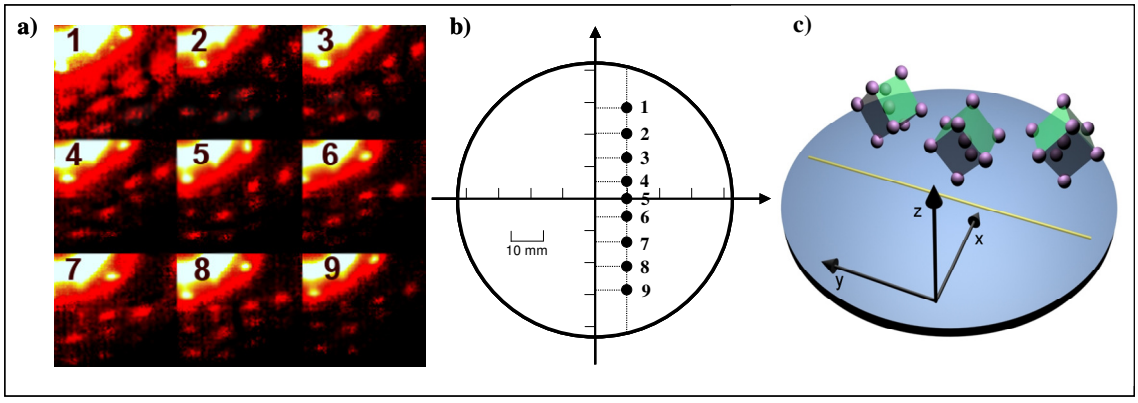


Fig. 3.15 SAXS sampling (transmission mode) of the T membrane with steps of 5 mm (a) and drawing of the corresponding positions along the membrane diameter (b). (c) Picture of the rotation of the mesostructure from the centre of the membranes (snapshot 5) towards the outer regions.

Because the SAXS patterns do not change within this central region, we conclude that the long range order is preserved. The SAXS patterns only show a small rotation (3–4°)

from the centre of the membranes (snapshot 5) to the external areas.[*] This rotation corresponds to an in-plane rotation of the mesostructure which may be caused by a small difference between the evaporation rates in the centre of the membrane and in the regions that are closer to the container walls (**Figure 3.15c**). In the outer region of the membrane (indicatively beyond the zone delimited by the 30 mm radius), the in-plane order is lost but the out-of-plane order of the mesostructure is retained, as confirmed by the presence of diffraction rings (not shown in the figure). This phenomenon is probably caused by an increase in the radius of curvature of the membrane surface, affecting the peripheral regions of the samples. Because the radius of curvature of the air-sample interface is smaller in the region closer to the edge of the container than in the central region, the thickness rises from 30 μm in the membrane centre to 48 μm at the edges. As already reported,[22] the self-organization of micelles starts from the interfaces (we assume this as a reasonable hypothesis based on the literature even if we have only a direct experimental evidence in the present system), therefore the smaller radius of curvature can determine a gradient in the evaporation rate of solvent and, in turn, the loss of order.

TEM images have been collected to support the information provided by SAXS data. A JEOL 200C× microscope equipped with a tungsten cathode operating at 200 kV has been used to analyse the samples. The membrane have been finely ground on a mortar, then dispersed in n-octane and finally evaporated on a carbon-coated copper grid. Bright field TEM images for mesoporous silica and organosilica membranes thermally treated at 350°C are reported, whereas images referred to the uncalcined samples are not shown because they are not significant. This can be due either to the small electronic contrast between the framework and the templating phase, either to electron beam damage on the weakly condensed membrane framework during observation. **Figure 3.16** shows four representative TEM images of the silica and organosilica membranes. The presence of 4-fold symmetry axes suggests that the structure is cubic. In both membranes an $Im\bar{3}m$ body-centred cubic organized porous structure is compatible with the TEM images, which refer to different sample orientations corresponding to different projection planes of the porous array. In particular, **Figure 3.16a, c and d** show the (100) face and **Figure 3.16b** shows the (110) face. The (110) face appears as a sequence

[*] The rotation of the whole SAXS pattern, from the snapshots 5–1 and 5–9, can be visualized taking as reference the central snapshot 5.

of channels because the depth of field of the electron microscopy merges different mesopores located on different levels.

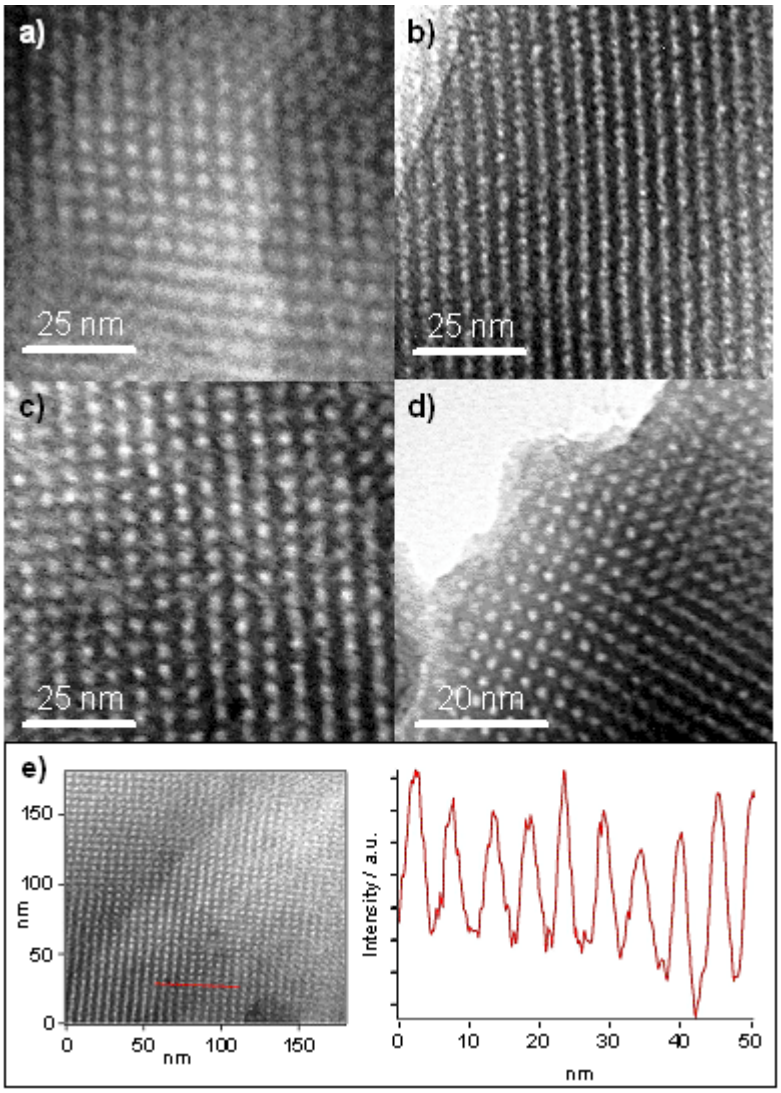


Figure 3.16 Bright field TEM images for samples calcined at 350°C. Four different images of inorganic T (a and b) and hybrid M (c and d) membranes are shown. In particular (a), (c) and (d) show the (100) faces, (b) shows the (110) face. (e) represents the line profile analysis (right side) to evaluate pore and walls dimensions. The TEM image on the bottom left refers to a hybrid M membrane.

By a line profile analysis on a representative TEM image showing the (100) projection plane (**Figure 3.16e**) we have estimated pore diameter and wall thickness as the average FWHM of the intensity distribution along a line passing through the pore centres (red line in figure). Pore diameter in organosilica membranes is 6 ± 1 nm and wall thickness

is 3.3 ± 0.5 nm. Thus the average centre-to-centre distance of two adjacent pores is ≈ 4.5 nm. Due to the merging of planes, the (100) projection plane shows the pores both at the cube vertices and at the centre of the unit cell. Therefore, the interpore distance represents half the diagonal of a face of the cubic unit cell and must be multiplied by 2 $\sqrt{2}$ in order to get the cell parameter a, which gives a ≈ 12 nm, a value in agreement with SAXS data. Similar results have been obtained for the inorganic silica membranes.

*- Chemical characterization by infrared spectroscopy*

Fourier-transform infrared analysis has been performed at the synchrotron infrared beamline SINBAD at the INFN Laboratori Nazionali at Frascati (Rome). The equipment used has been a Bruker Equinox 55 spectrometer with a conventional Globar source. To investigate the desorption kinetics of chemical moieties physically adsorbed on the pore surface, the spectrometer has been set to work in vacuum down to $10^{-2}$ mbar. Measurements have been carried out at different pressures in transmission mode using the interferometer working in the 500–6000 $cm^{-1}$ range at a resolution of 4 $cm^{-1}$. A nitrogen-cooled MCT detector and a KBr beamsplitter have been used.

**Figure 3.17a** shows the FTIR absorption spectra of the T sample, calcined at 350 °C, recorded in the 2800–3800 $cm^{-1}$ range as a function of the pressure within the vacuum chamber. At atmospheric pressure the spectra have been saturated so that the first significant spectrum has been collected at 0.5 mbar. The relative intensities of the main vibrational modes[23,24] observed around 3500, 3650 and 3750 $cm^{-1}$, are directly affected by pressure. The broad band peaking around 3500 $cm^{-1}$ decreases in intensity and 3750 $cm^{-1}$ and shifts to higher energies as vacuum pressure is increased. The maximum of the band shifts from 3494 $cm^{-1}$ in the spectrum recorded at 0.5 mbar, to 3547 $cm^{-1}$ in the spectrum measured at 0.001 mbar. The shape of the ≈ 3500 $cm^{-1}$ band and its changes versus pressure suggest that different contributions are responsible for these variations. At ≈ 3500 $cm^{-1}$ there is a contribution from OH stretching of silanols that are hydrogen bonded to the oxygen of neighbouring silanols ($\nu_s(OH^{\cdot\cdot\cdot H}OSi)$)[24], while the presence of adsorbed water vapours from the atmosphere gives rise to two bands in the 3000–3500 $cm^{-1}$ region that overlap with the $\nu_s$ (OH) band of silanols. A first water band falls at higher energies, around 3450 $cm^{-1}$, and is assigned to molecular water directly bonded to the silica network ($\nu_{as}$ ($H_2O$)) or hydrogen-bonded to the silanol groups ($\nu_s$ ($H_2O$)). In general, the molecular water directly attached to the silica network shows chemical

bonds which are stronger than those of the silanol bonded water, but the two contributions are very difficult to separate.

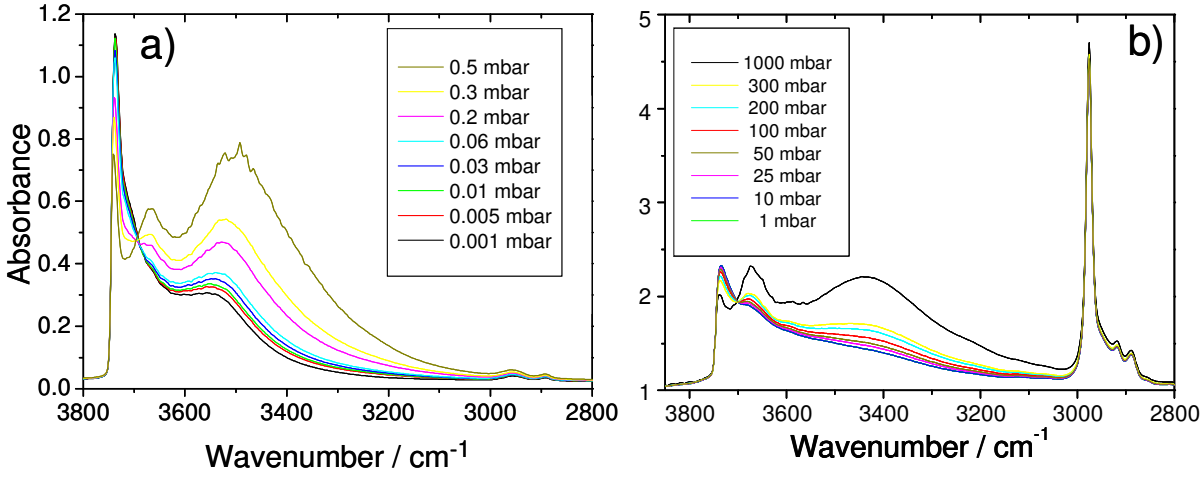


Figure 3.17 FTIR absorption spectra of T (a) and M (b) silica membranes after calcination at 350 °C, in the 2800–3800 $cm^{-1}$ range, taken at decreasing pressures within the experimental chamber.

The second band due to molecular water, assigned to the first overtone of the bending mode of H-bonded water ($2\nu_b$), falls at lower energy, around 3200 $cm^{-1}$. The changes observed in the low wavenumbers tail of the 3500 $cm^{-1}$ band (the band shrinks and the tail disappears in the spectra from 0.5 up to 0.06 mbar) indicate the water removal at lower pressures. In accordance to this, the intensity decrease and shift of the 3500 $cm^{-1}$ band is also attributed to removal of residual H-bonded water.

The FTIR spectra of M sample show a trend similar to that observed in the T membrane, but with some important differences. **Figure 17b** shows the FTIR absorption spectra of the M membrane after calcination at 350 °C, in the 2800–3800 $cm^{-1}$ range vs. pressure. The calcination temperature is effective in removing the surfactant, but at this temperature the methyl groups are not removed from the mesoporous membrane, as shown by the band at 2980 $cm^{-1}$. The thermal treatment temperature, in fact, has been selected to allow surfactant removing without degradation of the methyl species.[3]

The different behaviour with respect to water adsorption can give a clue about the location of the hydrophobic methyl groups since the spectra are not saturated at ambient pressure, and at 300 mbar all the traces of residual adsorbed atmospheric water (≈3200 $cm^{-1}$ band) are removed. This suggests that the most part of pore surface is covered by

methyl groups which makes the M membranes partially hydrophobic. Thus, in M membranes a weaker signal is observed for adsorbed water, as opposed to T membranes where adsorbed water may even cause saturation of the FTIR spectra. This supports the fact that after removal of residual water no other changes on the pore surface can be observed. We have used the band at 1628 $cm^{-1}$ ($\nu_b$, water bending)[25] of the T membrane FTIR spectrum to follow the desorption of water induced by the pressure changes (**Figure 3.18**).

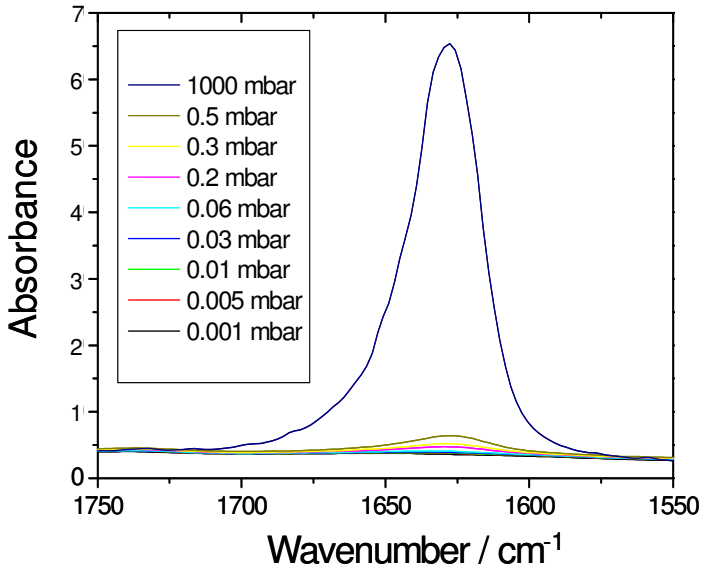


Figure 3.18 Evolution of the 1628 $cm^{-1}$ band ($\nu_b$, water bending) as a function of the pressure changes in the experimental chamber.

This band is not overlapped to other species and can give a direct semi-quantitative indication of water desorption. The asymmetric shape of the band suggests that different types of water are present within the membrane pores at ambient pressure. Following the literature, three different vibrational components due to molecular water can be observed: water molecules that aggregate with strong hydrogen bonding (≈1676 $cm^{-1}$) (type I), water molecule clusters with moderate intensity of hydrogen bonding (≈1654 $cm^{-1}$) (type II) and water molecules that interact with each other with weak hydrogen bonding (≈1592 $cm^{-1}$) (type III) .[26]

Generally, a lower absorption wavenumber is an indication of a decrease in the strength of the hydrogen bonding, and type III of hydrogen bond is so weak that the water involved can be considered as ‘‘free’’ water. **Figure 3.19** shows a fitting of the water band where three components of water bending modes can be resolved by Gaussian curves. Only two components show a significant intensity (I and II). The component III

is, instead, very weak, which is an indication that almost no ‘‘free’’ water is present within the pores.

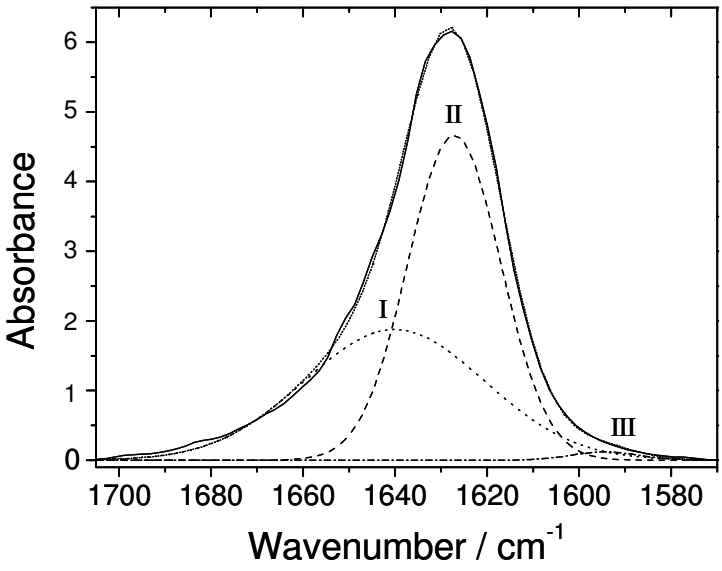


Figure 3.19 Fitting of the water band in the 1700-1580 $cm^{-1}$ range. The three components (I dot line, II dash line and III dash-dot line) of water bending modes have been resolved by Gaussian curves. The short dot line represents the three components Gaussian fit of the experimental data.

While at ambient pressure the sample adsorbs water that is hydrogen bonded on the pore surface through the silanols, at 0.06 mbar the water is completely removed, in accordance with the spectra in **Figure 3.17a**. Furthermore, because most of the water is easily desorbed at 0.5 mbar, the amount of water directly bonded to the silica network is negligible. At higher wavenumbers, in the 3800–2800 $cm^{-1}$ region, the FTIR spectra show three other vibrational modes, which change in intensity with the variation of the pressure: at 3670, at 3708 (shoulder) and at 3737 $cm^{-1}$ (sharp). The 3670 $cm^{-1}$ band is assigned to OH stretching of Si-OH with a contribution from antisymmetric stretching of hydrogen bonded molecular water ($\nu_{as}$ ($H_2O$)).[24] The decrease in intensity of this band at higher vacuum pressures indicates that the contribution from molecular water is predominant. On the other hand, the intensity decrease of this mode is accompanied by a simultaneous increase of the 3708 and 3737 $cm^{-1}$ bands. We attribute the 3708 $cm^{-1}$ band to geminal silanols and the 3737 $cm^{-1}$ to isolated silanols.[27] In fact, the removal of the bridging water can induce a condensation between adjacent silanols that can form twin species or give new isolated silanols. The FTIR measurements performed in vacuum vs. pressure directly confirm that the pores of the membranes are fully

accessible from the external environment, as shown by the full removal of the adsorbed atmospheric water. The process of adsorption–desorption is also reversible and it appears related to the nature of the pore surface. On the basis of FTIR data it should be noted that at ambient pressure the pore surface of silica based mesoporous materials is, in any case, covered by at least one layer of hydrogen bonded atmospheric water linked to the residual silanols. Such layer is responsible for the high protonic conductivity of silica mesoporous materials and their application as electrochemical sensors.[28]

## 3.4 Pores functionalization

The most direct and exploited property of mesoporous films is the possibility to functionalize their pores with either organic or inorganic functionalities. Three main approaches are commonly used to reach this goal: direct grafting by reaction with surface hydroxy species; indirect grafting providing anchoring groups to the guest-molecules and *one-pot* route in which the functions are dissolved in the sol-gel solution during the synthesis and remain entrapped in the material after film deposition. In Paragraph 3.4.1 is reported a *one-pot* synthesis to obtain highly fluorescent silica-rhodamine 6G mesostructured films. The material has shown peculiar luminescence properties related to the chemical environment of the organic dye into the films. The same *one-pot* approach has been used to incorporate spiropyrans into mesostructured films (Paragraph 3.4.2). Spiropyrans are chemical compounds that may switch in two thermodynamically stable states by external stimuli. We have obtained a material with both thermo-and photochromic responses by coupling the characteristic properties of these organic molecules with those of mesostructred silica films.

Unlike one-pot synthesis, chemical grafting of functional groups to the pore surface ensures a better stability of the guest moieties towards leaching. Post-functionalization by indirect grafting has been used to incorporate into mesoporous silica films a fluorescent zinc Schiff base in order to fabricate nanocomposites which are highly fluorescent and show a good stability of the emitting properties (Paragraph 3.4.3).

Mesoporous films can act not only as an active substrate for chromophores, but also as a nanoreactor to growth particles of defined size of metal, alloys and semiconductors. Paragraph 3.4.4 reports on a reproducible route to obtain $SiO_2$-FeCo nanocomposites, with controlled particle size. TEM characterizations have shown that the mesopore

dimension limits the nanocrystals size, allowing the possibility to control the nanoparticle growth by choosing a specific mesoporous matrix.

### 3.4.1 Rhodamine 6G-doped films

Rhodamine 6G (*Rh6G*) is one of the most popular fluorescent dyes and is widely used to fabricate several types of luminescent materials for its lasing ability.[29,30] Dye lasers are generally based on dyes in solution (typically in ethanol, methanol, and less commonly water) or on dye-doped solids such as sol-gel materials.[31] Sol-gel route, because of the low processing temperature, is particularly suitable for incorporation of organic dyes in thin films; several examples of inorganic and hybrid organic-inorganic films doped by rhodamine 6G have been reported so far.[29] One of the main difficulties to deal with, is controlling the aggregation states; in fact *Rh6G* in concentrated solutions or after incorporation into solid state matrixes shows a strong tendency to form aggregates. Stable ground state dimers are formed in water via π-π mixing of xanthene ring orbitals at concentrations around $10^{-5}$ M and, at $10^{-4}$ M, the solution does not show any lasing capability. In alcohols, such as ethanol and methanol, the tendency to form dimers is much reduced and they are not observed before quite high concentrations (up to 0.1 M) are reached.[32] *Rh6G* forms dimers through van der Waals dye-dye interactions and rhodamine–water (counterions) interactions;[33] coexistence of parallel and anti-parallel dimers is also assumed.[34] Sandwich type (*H-dimers*) or head-to-tail dimers[35] (*J-type*) are formed in accordance to the exciton theory. *H*-dimers are characterized by a strong absorption band of higher energy with respect to the monomer band, but this aggregated species is not fluorescent and is the main responsible of the monomer fluorescence quenching. *J*-aggregates, instead, are still fluorescent and have absorption and fluorescent bands at lower energy (*J*-band) with respect to the monomer band.[36]
Controlling the aggregation state of *Rh6G* upon incorporation into a solid state matrix is, therefore, a very challenging task and has been the subject of several works.[37] While incorporation of *Rh6G* in sol-gel materials[38,39] is now quite well understood and characterized, both in inorganic and organic-inorganic hybrid host materials, the preparation of self-assembled mesoporous materials containing fluorescent dyes has still to be completely explored. In mesoporous materials an ordered porosity in the meso-scale is available, but the processing route by self-assembly through supramolecular templates should allow, in principle, to achieve a higher and more sophisticated control

of the dye doping process. A porous host material can be doped by *Rh6G* via post-synthesis impregnation,[40] in this case a secondary bond is formed between the pore surface and the dye. Alternatively, organic dyes with alkoxy functionalities can be also used for post impregnation in order to obtain a direct covalent bonding to the pore surface. Post synthesis doping route is simple, but not very effective; low controlling of the dye aggregation state, pore blocking, phase separation, and leaching effects are the main drawbacks.[41] Another possibility is represented by one-pot route, the dye is introduced in the precursor solution during the synthesis and remains entrapped in the material after the film deposition. This route is widely used to incorporate organic dyes in hybrid organic-inorganic films but a full control of aggregation state is still difficult. In the case of mesostructured thin films obtained via one-pot route, the presence of a surfactant plays a fundamental role and strongly affects the aggregation state of the dye.[42] It has been demonstrated that mesostructures thin films doped by *Rh6G* show stimulated emission and micron scale devices have been fabricated.[43] An interesting result is that the dye exhibited a lower tendency to aggregate after incorporation in mesostructured materials; the confinement effect in a nano-scale structure and the presence of the surfactant affect the aggregation state of the dye. In particular, dimer-to-monomer transformations have been reported for some types of rhodamine derivatives in micellar solutions of surfactants such as sodium dodecyl sulphate.[44] Tri-block copolymer surfactants, consisting of polyoxyethylene-polyoxypropylene-polyoxy-ethylene blocks, have been used to suppress the aggregation of *Rh6G* by emulsifying the monomeric dye and creating an effective partitioning in the solution.[45] In general, the chemical environment strongly affects the aggregation state of rhodamine 6G, and a case by case study has to be performed. A fascinating feature of using mesostructured material as a host for optically active organic molecules is represented by the wide choice of environments.[46] The dye can be placed in specific regions, such as the pore walls, the micelles interior and the hybrid interface, and several strategies can be envisaged to differentiate the dye localization.[47] In the case of *Rh6G*, some studies indicate that during self-assembly by a supramolecular template the dye is incorporated within the hydrophobic core of the micelle. Prevention or limitation of aggregation has been observed, but details of the process are not available yet. By these experiments we have studied the aggregation states of the dye after incorporation into a mesostructured film.

The samples have been prepared as described in Section 3.1, page 80. Mesostructured silica films can be obtained with different types of mesophase array and in principle the mesophase formation depends on processing and synthesis parameters that can be adjusted, within some limits, to obtain a specific organization (see Paragraph 1.3.1). The introduction of host functional molecules in mesostructured materials via one-pot synthesis does not produce, in general, a disruption of the mesophase.[48]

We have used GISAXS to characterize the mesostructure of the films containing *Rh6G* at different concentrations; as a general trend we observed the same mesophase with no changes at increasing *Rh6G* concentrations. Measurements have been performed at the Austrian SAXS beamline of ELETTRA synchrotron with an incident energy of 8 keV. A typical acquisition is an average of 10 acquisitions with integration time of 500 ms. Measurements have been performed on as-deposited mesostructured films with fixed template concentration ($s = 5 \cdot 10^{-3}$), as a function of the *Rh6G* concentration (from $5 \cdot 10^{-4}$ to$1 \cdot 10^{-2}$). **Figure 3.20** shows a typical GISAXS pattern obtained from those samples. The pattern can be indexed as 2d-hexagonal *p6mm* composed of ordered arrays of tubular micelles with hexagonal cross section.[49] Following this attribution, the cell parameters of the mesophase have been calculated as 6.6 ± 0.9 and 6.1 ± 0.8 nm in the in-plane ($x$) and out-of-plane ($z$) directions, respectively. Increasing amount of *Rh6G* does not affect the mesostructure formation neither the cell parameters that remain almost constant inside the error bar.

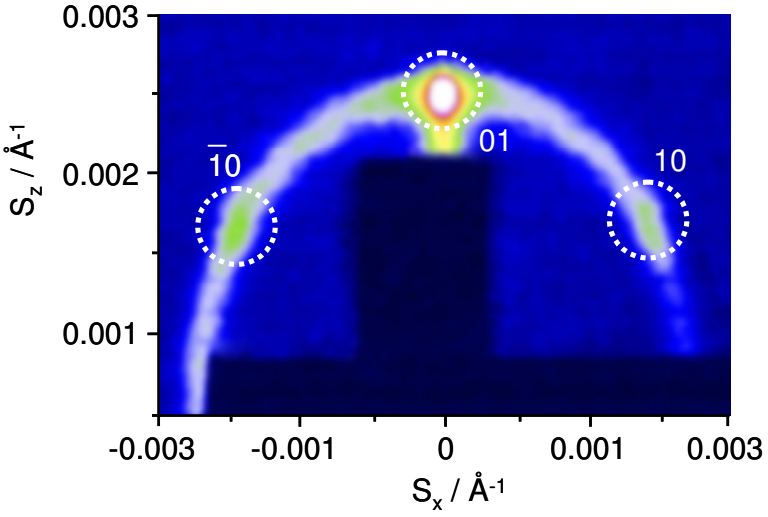


Fig. 3.20 GISAXS pattern obtained from an as-deposited mesostructured doped film with [F127] / [Si] = $5 \cdot 10^{-3}$ and [*Rh6G*] / [Si] = $5 \cdot 10^{-2}$.

*- UV-Vis spectroscopy*

Incorporation of *Rh6G* into a solid state matrix is generally limited by aggregation effects, formation of non-fluorescent dimers (*H-type* dimers) is observed even at relatively low concentrations. The absorption spectrum of *Rh6G* in the monomeric form is characterized by an absorption peak around 530 nm and a vibronic shoulder at lower wavelengths (~500 nm). The molecule is slightly solvathocromic and the absorption maximum red shifts in polar solvents; the intermolecular aggregation strongly depends on the dye concentration and the chemical environment (polarity, charge, etc.). *Rh6G* dimers have two distinct absorption maxima, at higher (*J-type* dimers) and lower (*H-type* dimers) wavelengths with respect to the absorption peak of the monomer band (~530 nm). **Figure 3.21a, b and c** show the absorption spectra of the different types of films doped with *Rh6G* at increasing concentrations (from $5 \cdot 10^{-5}$ up to $10^{-3}$).

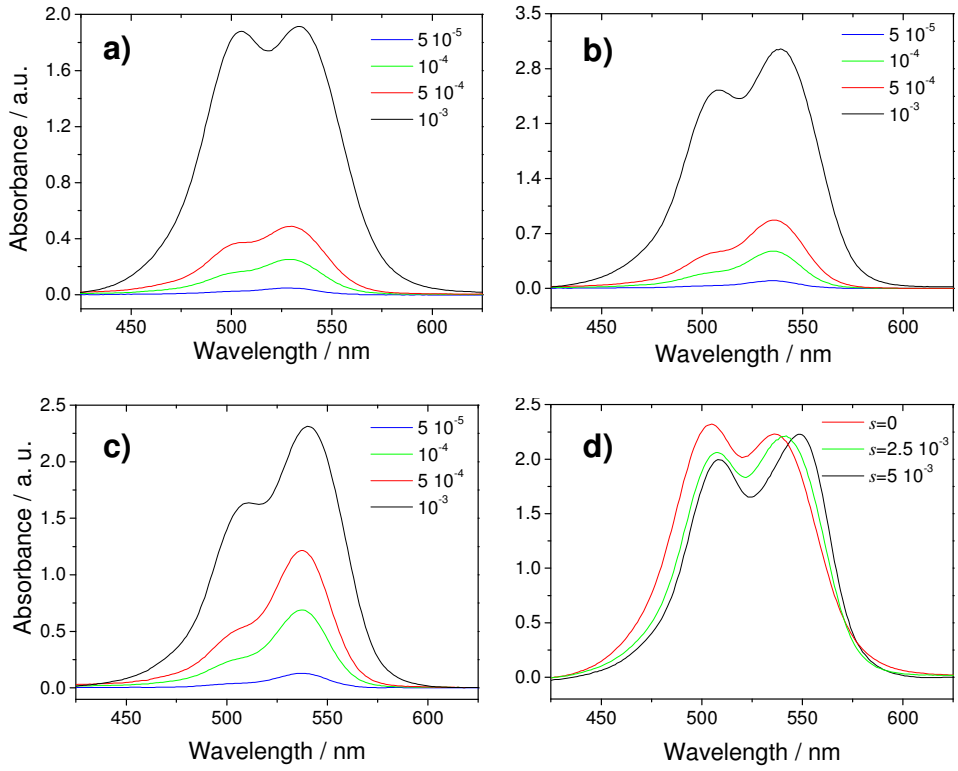


Fig. 3.21 UV-Vis absorption spectra of: (a) sol-gel silica films, (b) mesostructured silica films ($s$ = $2.5 \cdot 10^{-3}$), (c) mesostructured silica films ($s$ = $5 \cdot 10^{-3}$) doped with different amounts of rhodamine 6G. The rhodamine concentrations in the films are: $c$ = $5 \cdot 10^{-5}$, blue line; $c$ = $10^{-4}$, green line; $c$ = $5 \cdot 10^{-4}$ red line; and $c$ = $10^{-3}$, black line. (d) Difference spectra obtained by subtracting the data of the films doped with $5 \cdot 10^{-4}$ *Rh6G* from those of $10^{-3}$ *Rh6G* concentration. The legend in figure (d) indicates the surfactant concentration (red line, $s$ = 0 sol-gel film; green line, $s$ = $2.5 \cdot 10^{-3}$; black line, $s$ = $5 \cdot 10^{-3}$).

Absorption spectra have been measured in 190-900 nm wavelength range using a UV-Vis Nicolet Evolution 300 spectrophotometer, at 500 $nm \cdot min^{-1}$ scan rate. Each acquisition is the average of 3 different scans collected with a bandwidth of 1.5 nm. At the highest dye concentration, $c = 1 \cdot 10^{-3}$, a *H-type* dimer absorption band around 500 nm has been observed in all the samples. This dimer band is overlapped to the vibronic band but can be clearly detected; the *H-type* dimer band has the highest relative intensity in the sol-gel silica sample and the lowest one in the mesostructured film prepared with the highest surfactant concentration.

The formation of *J-type* dimers can not be evaluated from the absorption spectra because of the overlapping with the monomer band. Therefore, we have subtracted the absorption spectra of the films with $c = 5 \cdot 10^{-4}$ from those with $c = 1 \cdot 10^{-3}$ to separate the contributions of the different types of dimers. **Figure 3.21d** shows the spectra that resulted from the subtraction; two different absorption peaks are observed around 505 and 540 nm, which are assigned to *H-type* and *J-type* dimers, respectively.[36,50] The spectra have been normalized with respect to the *J-dimer* peak for comparison; it is interesting to observe that the relative intensity of the *H-type* and *J-type* dimer bands changes with a specific trend. The *J-type* dimer band has the lowest relative intensity in the silica films and the highest in the sample with the highest surfactant concentration: this is an indication that the amount of *J-type* dimers with respect to *H*-dimers is higher in mesostructured films with respect to the dense samples. The two dimer bands, *H* and *J*, appear partially overlapped, which is similar to what observed in the case of the dimer absorption spectrum in water,[51] but differs from that in methanol[52] and ethylene glycol,[36] where two well separated *H* and *J* bands are observed.

*- Fluorescence spectroscopy*

To get a better insight to the effects of *Rh6G* aggregation on the optical properties, fluorescence spectra have been recorded using an excitation at 480 nm on samples as a function of the dye concentration from $5 \cdot 10^{-5}$ up to $5 \cdot 10^{-2}$ M. Fluorescence analysis has been performed using a FluoroMax-3 Horiba Jobin-Yvon spectrofluorometer. The probing beam has been set to impinge on one side of the sample (incidence angle of 2-3°) so that the sample acted as a waveguide for the incident light wave, while the luminescence has been collected at 90° with respect to the incident beam. This configuration enhances the signal-to-noise ratio and limits the reflection effects. Each

acquisition has been the average of 3 different accumulations. **Figures 3.22a, b and c** show the normalized emission spectra, in the 500–800 nm range, of the different samples. The increase of *Rh6G* concentration within the films produces a broadening and red shift of the emission spectra. This effect is in accordance with previous findings;[35] red shift and broadening of the emission band are characteristic of fluorescent *J-type* dimer formation.[50]

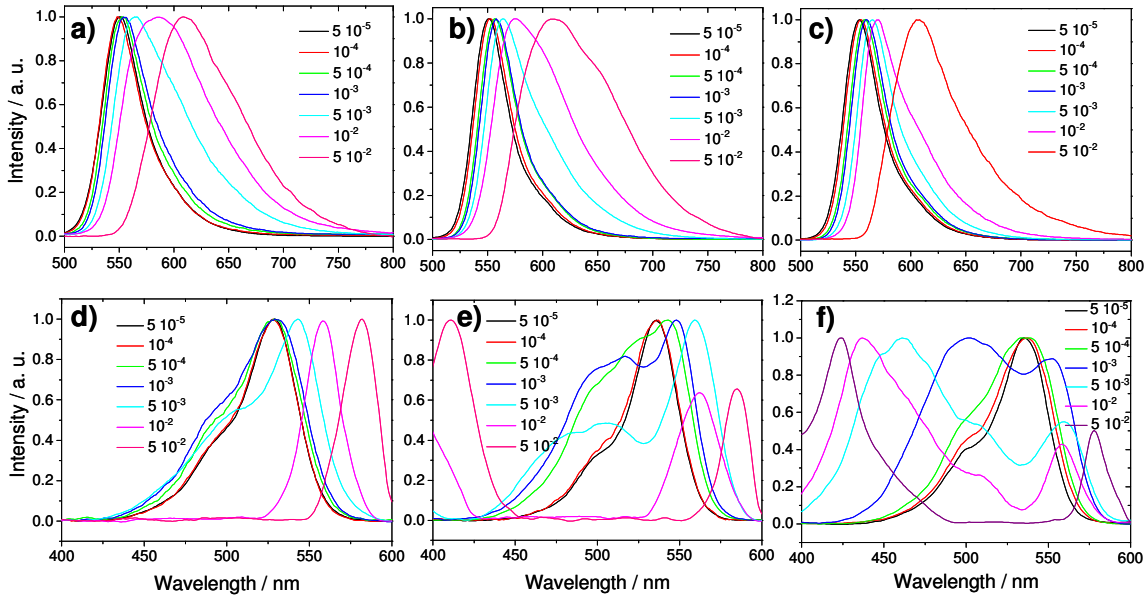


Figure 3.22 Emission spectra of *Rh6G* doped sol-gel silica films (a); *Rh6G* doped mesostructured silica films (s = $2.5 \cdot 10^{-3}$) (b); and *Rh6G* doped mesostructured silica films (s = $5 \cdot 10^{-3}$) obtained by excitation at λ = 480 nm. Excitation spectra of *Rh6G* doped sol-gel silica films (d); *Rh6G* doped mesostructured silica films (s = $2.5 \cdot 10^{-3}$) (e); and *Rh6G* doped mesostructured silica films (s = $5 \cdot 10^{-3}$) (f) obtained by emission at λ = 620 nm.

A red shift has been observed in all the samples; the value of this shift, calculated from the samples at highest concentration ($c = 5 \cdot 10^{-2}$) with respect to the samples at the lowest one ($c = 5 \cdot 10^{-5}$), is 61 nm (**Figures 3.22a**), 58 nm (**Figures 3.22b**), and 53 nm (**Figures 3.22c**). A direct evidence of the red shift effect is given by the picture of the as-prepared samples (**Figure 3.23**); it shows three doped mesostructured silica films (*s* = $5 \cdot 10^{-3}$) at decreasing *Rh6G* concentrations from left to right, illuminated by visible light and by UV light at 365 nm. Upon exposure to UV light, an intense coloration due to red-shifted emission is observed. In accordance with the literature the emission peak

at 550 nm is assigned to the monomeric form of *Rh6G* within the films, and the red-shifted emission around 600 nm to fluorescent *J-type* dimers.[35,36]

The formation of *Rh6G* aggregates (*H-type*) is clearly revealed by absorption spectra, they also indicate the presence of fluorescent dimers (*J-type*) whose formation is enhanced in mesostructured films; this evidence is well supported by the emission spectra. The extremes of these types of dimers are represented by a perfect sandwich structure (*H-type*) and a perfectly aligned head-to-tail dimer (*J-type*). However, these are only idealized configurations and a distribution of dimer geometries is the most realistic description; a "magic angle" around 55° represents the limit between luminescent and non-luminescent dye aggregates.[32,34]

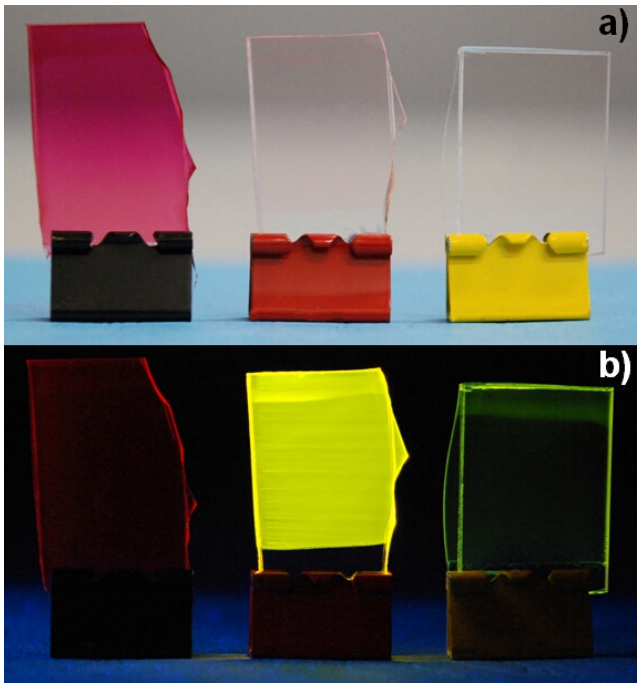


Figure 3.23 Picture of *Rh6G* doped mesostructured silica films ($s = 5 \cdot 10^{-3}$) at decreasing rhodamine 6G concentrations ($c = 5 \cdot 10^{-2}$, $c = 5 \cdot 10^{-3}$ and $c = 5 \cdot 10^{-4}$), from left to right, illuminated by visible light (a) and by UV light at 365 nm (b).

Excitation spectra have been employed to follow the formation of fluorescent aggregates in the films as a function of the dye concentration. **Figure 3.22d, e and f** show the excitation spectra recorded by monitoring the emission at 620 nm in the silica and mesostructured films doped with increasing concentrations of *Rh6G*. The excitation

spectra of silica films (**Figure 3.22d**) show one band at 525 nm, which red shifts in the samples with the higher *Rh6G* concentrations ($c$ = $5{\cdot}10^{-3}$, $10^{-2}$, $5{\cdot}10^{-2}$). The excitation spectra of the mesoporous films appear very different; they are characterized by three main excitation bands, one at 525 nm due to the monomer, a red shift excitation band and a blue shifted excitation band. The red and blue shift increases as a function of the rhodamine concentration, while the monomer excitation strongly decreases at concentrations around $c$ = $5{\cdot}10^{-4}$.

A general overview of the response to excitation at different wavelengths is given by 3D excitation-emission-intensity spectra reported in **Figure 3.24** for the mesostructured sample ($s$ = $5{\cdot}10^{-3}$) prepared with the higher surfactant concentration and six different *Rh6G* concentrations ($c$ = $5{\cdot}10^{-5}$, $5{\cdot}10^{-4}$, $10^{-3}$, $5{\cdot}10^{-3}$, $10^{-2}$, $5{\cdot}10^{-2}$). The spectra show the excitation (x-axis) versus emission (y-axis), intensity is reported in a colour scale; oblique lines in some images are due to scattering effects.

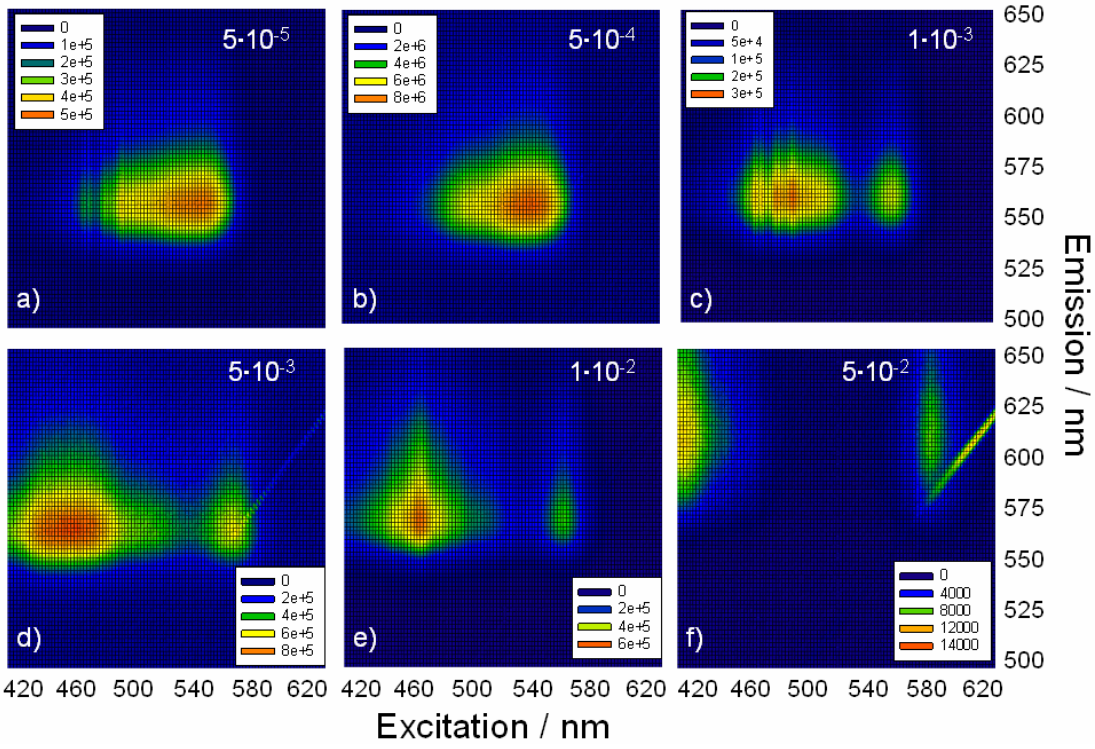


Figure 3.24 3D excitation-emission-intensity spectra of *Rh6G* doped mesostructured ($s$ = $5{\cdot}10^{-3}$) silica films as a function of the dye concentration.

The effect of *Rh6G* concentration on the fluorescence emission and excitation can be clearly observed. At the lower concentrations the main contribution to the fluorescence is given by the monomeric form of rhodamine 6G, but the slightly distorted shape of the

image indicates that even at very low concentrations a contribution from different fluorescent species (*J*-dimers) is present. The image of the sample with the lowest *Rh6G* concentration ($c = 5 \cdot 10^{-5}$) shows that the emission has an intensity peak around 560 nm in correspondence to an excitation of 540 nm. The emission appears asymmetrically red shifted and the excitation ranges from 570 to 460 nm; this is an indication that the fluorescence is due to monomeric species as far as fluorescent aggregates. At $c = 5 \cdot 10^{-4}$ concentration, the red shift of emission fluorescence increases and an asymmetric image is generated. At $c = 1 \cdot 10^{-3}$ concentration, exciton splitting is observed and the fluorescence emission is mainly due to *J-type* aggregates (**Figure 3.24c**). The maximum of *J-type* dimer fluorescence is observed in the $c = 5 \cdot 10^{-3}$ samples, with a strong excitation splitting (**Figure 3.24c**); the large excitation range indicates a large distribution of *J*-dimer aggregates. At higher dye concentrations the fluorescence decreases in intensity and formation of *H*-dimer aggregates prevails. A comparison of the different fluorescence response shown by *Rh6G* doped mesostructured and silica dense films can be done by observing the 3D spectra of the silica samples in **Figure 3.25**.

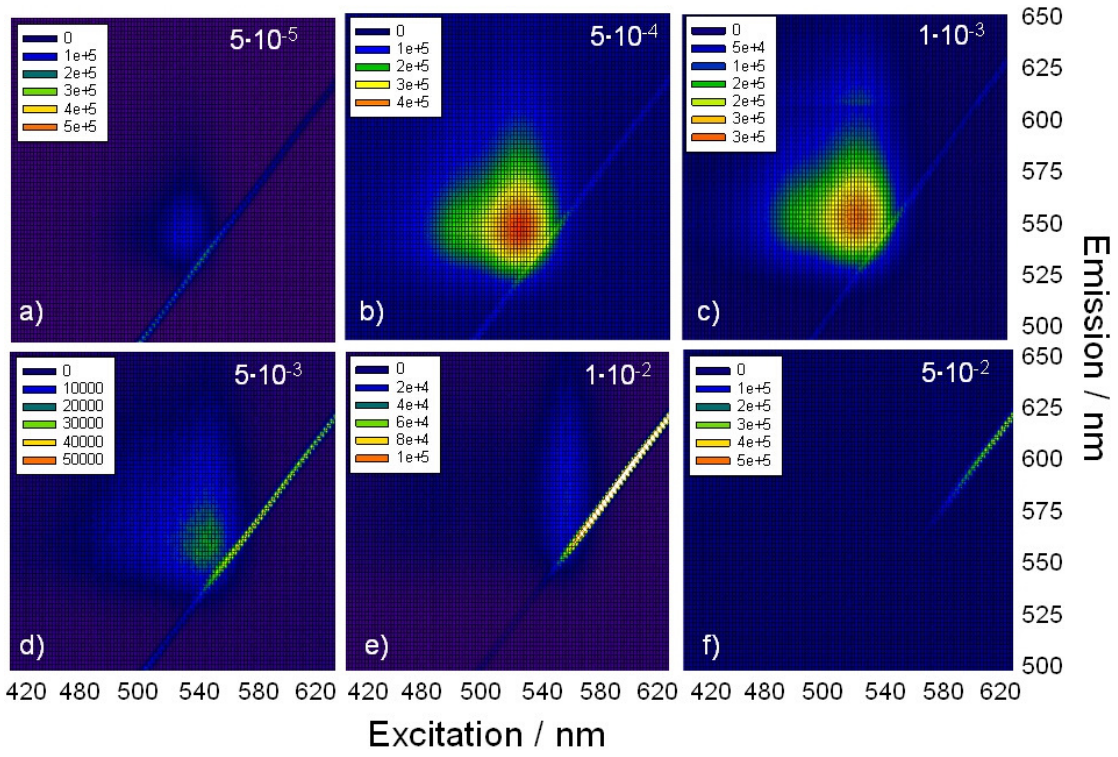


Figure 3.25 3D excitation-emission-intensity spectra of *Rh6G* doped sol-gel silica films as a function of the dye concentration.

These excitation-emission-intensity images appear very different from those observed in mesostructured silica films. In this set of samples only a weak fluorescence is observed at the lowest dye concentration ($c = 5 \cdot 10^{-5}$). At $c = 5 \cdot 10^{-4}$ concentration an intense fluorescence peaking at 550 nm in correspondence to an excitation at 520 nm is observed. The asymmetry of the image, which appears slightly distorted to red for emission and to blue for excitation, indicates that also in this sample a partial contribution to fluorescence emission due to *J*-type aggregates is present. At higher concentrations ($c = 1 \cdot 10^{-3}$) the fluorescence intensity only slightly decreases maintaining the asymmetric shape. Beyond this concentration, the fluorescence abruptly decreases due to the formation of non-fluorescent aggregates. It is worth to underline that the re-absorption of emitted light could also cause red shift of the emission spectra because, in the present system, the partial overlapping of absorption (**Figure 3.21**) and emission (**Figure 3.22**) spectra indicates that this effect should be considered. The changes of excitation spectra as a function of dye concentrations indicate, however, that the formation of fluorescent dye aggregates is the main responsible of the emission changes.

*- Aggregation states in mesostructured films*

The formation of non-fluorescent aggregates (*H-type*) of *Rh6G* upon incorporation in sol-gel films is a well known effect, which is the main responsible of the fluorescence quenching at high *Rh6G* concentrations. The aggregation state in these films depends on dye concentration and interactions with the pore walls, and the presence of residual water and solvents. In the case of mesostructured films, *Rh6G* can be introduced using a one-pot synthesis and it participates to the self-assembly process. The presence of the surfactant in this case is very important, several studies have shown that introduction of surfactants in the sol-gel precursor solution reduces the dye aggregation.[53] It has been reported that when a dye is dissolved in aqueous surfactant solution, the monomer associates to the hydrophobic chain of the surfactant and is included into the micelle.[54] The inclusion in the micelle core has the effect of preventing or limiting the dye aggregation, especially in presence of water that may bridge two monomers to form *H-type* dimers. However, in the case of mesostructured films, the role of the surfactant is quite complex, because it gives a special chemical environment to the guest dye, but also acts as the templating agent of the mesostructure during self-assembly. Therefore,

after film deposition the guest dye is in a highly restricted environment which is very different from that one of a corresponding sol-gel silica films.

To resume, the previous data show several differences and give some indications about the origin of the fluorescence in the different samples:

1) the concentration of surfactant affects the dye aggregation, higher concentrations give more fluorescent films, but mainly from *J-type* dimers;
2) the inclusion in a mesostructured film gives preferential formation of *J-type* with respect to *H-type* dimers;
3) a distribution of dimers is present, corresponding to two extreme configurations, which have been attributed to sandwich *H-type* dimers and head-to tail *J-type* aggregates;
4) the formation of fluorescent aggregates is promoted by the presence of the surfactant that favours the formation of head-to tail dimers within the micelles. In this constrained environment *H-type* dimers are distorted and give rise to oblique *J-type* aggregates.

### 3.4.2 Spiropyran-doped films

Spiropyrans are an important example of chemical compounds that may exist in two thermodynamically stable states and are capable of interconversion under the action of different external sources. Reversible rearrangements of the molecules between two forms (**Figure 3.26**) can be induced by light (photochromism[55]) or heat (thermochromism[56]).

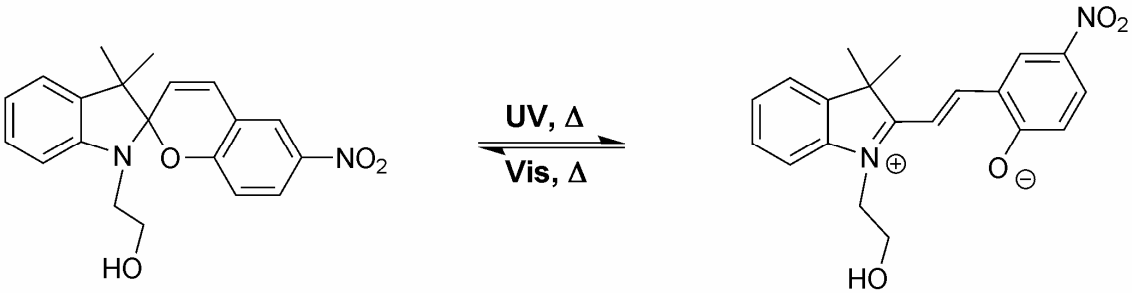


Figure 3.26 Open and closed structures of *spiropyran 1*. The isomerization can also occur thermally. When it is in its open form, the molecule is also called *merocyanine*.

Molecular systems that act as on–off bistable systems have raised a high interest because of the different potential applications in molecular electronics, photonics, computing and chemical sensing.[57] Upon incorporation of spiropyrans into a solid state matrix, stimuli-responsive materials such as heat and pH-sensitive materials can be fabricated. Photochromic materials, in particular, require that either the nanostructure or the molecular structure respond to an external stimulus, in this case, light. On the other hand, because of their peculiar porous topology, mesostructured materials represent an ideal system for developing guest-host functional materials and some examples of incorporation of spiropyrans have been also reported so far.[58] The high interest in porous materials containing spiropyrans relies in the possibility of optical properties fine tuning: antireflective, photochromic and thermochromic properties can be modulated through the control of material processing. However, the porous environment in mesostructured materials is a complex system because of the restriction in the dimension, the pore surface coverage and the presence of surfactant or other guest molecules. Therefore a careful engineering of the system is required and detailed studies on the effect of the several parameters have to be carried out in order to design the material functional properties. The optical response and the stability of the material performances are, in fact, strongly dependent on a set of different parameters; this is especially true in the case of mesostructured materials that contain organic templates. We have prepared silica mesostructured thin films containing *spiropyran 1* (see **Figure 3.26**) through one-pot synthesis. Mesostructured silica films have been used as a host matrix to incorporate spiropyran molecules via one-pot synthesis. The photophysical characterization has shown that the materials have a reversible photo and thermal response: a colour transition from transparent to yellow or purple has been induced by heat or light, respectively; both colour changes are reversible under room temperature or visible light exposure. The colour transition has shown to be specific of the source that has been used: it has been impossible to turn the colour of the films from transparent to yellow using UV light and from transparent to purple using a thermal treatment.

*- Morphological characterization*

Samples have been prepared by using the one-pot procedure resumed in Section 3.1, page 81. Previous reports have shown that, by using one-pot synthesis, spiropyrans preferentially are located within the hydrophobic core of the templating micelle.[58] Therefore we have at first investigated the mesostructure obtained in the films, to verify

if the doping dye has been affecting the mesophase formation. GISAXS and TEM analysis have been used on *spiropyran 1*-doped films to identify the mesostructures obtained by evaporation-induced self-assembly. TEM images have been obtained on a JEOL 200C× microscope equipped with a tungsten cathode operating at 200 kV. To observe the mesopores array, the samples have been further treated at 250 °C for 30 min because dried films showed a poor electronic density contrast that do not allow a direct observation of the pores arrangement. Finely ground films scratched from the silicon substrates have been dispersed in n-octane by sonication, then have been dropped on a carbon-coated copper grid and dried for analysis. TEM picture in **Figures 3.27a** shows the front view of an ordered array of mesopores having a 6-fold rotational axis typical of a hexagonal symmetry; this attribution is confirmed by the observation of stacks of well-aligned tubular micelles (**Figures 3.27b**). These results are consistent with previous studies on self-assembly mesoporous films templated by Pluronic F127, where a mesophase with two-dimensional hexagonal *p6mm* symmetry has been obtained.[49] From TEM pictures, we have evaluated the average pore diameter and pore walls thickness. The average centre-to-centre distance between two adjacent cylindrical pores is 6.2 ± 1.0 nm in the direction perpendicular to their axes; the pores diameter is 3.5 ± 1.0 nm and the inorganic pore wall thickness is 4.6 ± 1.0 nm.

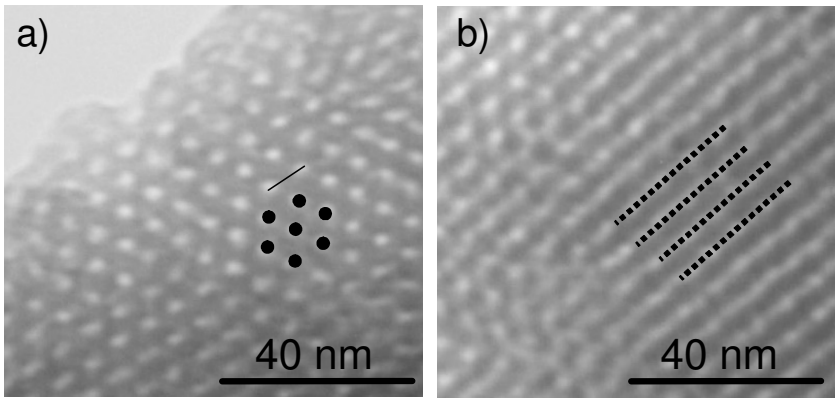


Figure 3.27 Representative TEM bright-field images of mesostructured silica films doped with *spiropyran 1* and treated at 250 °C (a and b); black dots and dotted lines indicate the 2d-hexagonal symmetry of the mesostructure.

To evaluate local order of the mesophase as well as cell parameters, GISAXS measurements have been done on dried mesostructured films. Measurements have been performed at the Austrian SAXS beamline of ELETTRA synchrotron with an incident

energy of 8 keV. A typical measure consisted in an average of 10 acquisitions with integration time of 500 ms. **Figure 3.28** shows a typical GISAXS pattern that can be indexed as 2d-hexagonal *p6mm*. Following this attribution the cell parameter has been calculated as 6.1 ± 0.9 and 6.5 ± 0.9 nm in the in-plane (x) and out-of-plane (z) directions, respectively. The presence of a distorted ring intersecting the spots shows the coexistence in the film of ordered domains together with some disordered or wormlike regions.

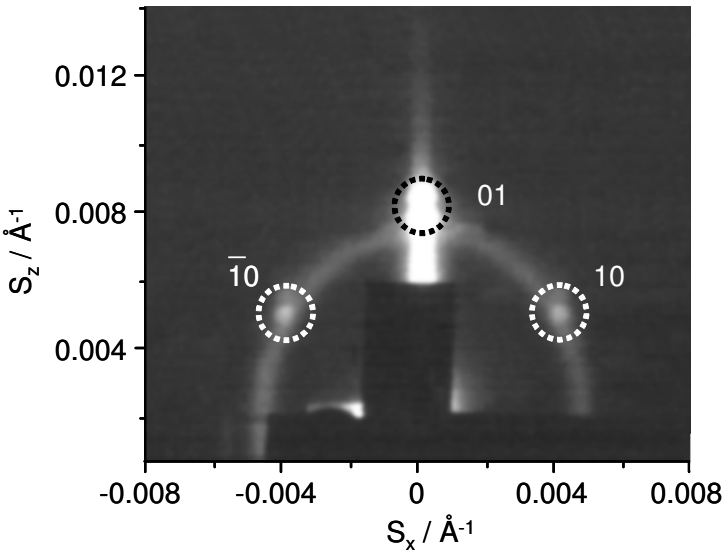


Figure 3.28 GISAXS pattern of the as-deposited spiropyran-doped mesostructured silica films. The diffraction peaks are indexed and indicated by dotted circles.

By comparing the measurements recorded from samples with increasing amounts of spiropyran, we conclude that the compositional variation does not affect neither the cell parameters nor the degree of order in the mesophase; this means that the organic molecules, at least in the concentration range we have used, do not influence the formation of the interface between the micelles and the inorganic network.

*- Photochemical properties*

To study the photochemical properties of the molecules, we have prepared several solutions dissolving *spiropyran 1* in solvents of different polarity. Fluorescence emission measurements in solution have been performed using a FluoroMax-3 Horiba Jobin-Yvon spectrofluorometer and a fused-silica cuvette: 1 mg of *spiropyran 1* has

been dissolved in 40 $cm^3$ of the solvent for the measure; ethanol, water and tetrahydrofuran (THF) have been used as solvents. Emission spectra have been collected between 550 and 800 nm, using an excitation wavelength of 365 nm with an integration time of 0.1 s. **Figure 3.29** shows the photoluminescence emission spectra of *spiropyran 1* in the 550–800 nm range. The organic molecule in water shows the lowest intensity with an emission band peaking around 670 nm (green line), the emission band of *spiropyran 1* in THF (red line) increases in intensity with respect to what obtained in water and shifts to lower wavelengths. The band of *spiropyran 1* in THF appears the sum of two contributions: one centred around 660 nm and the other around 640 nm.

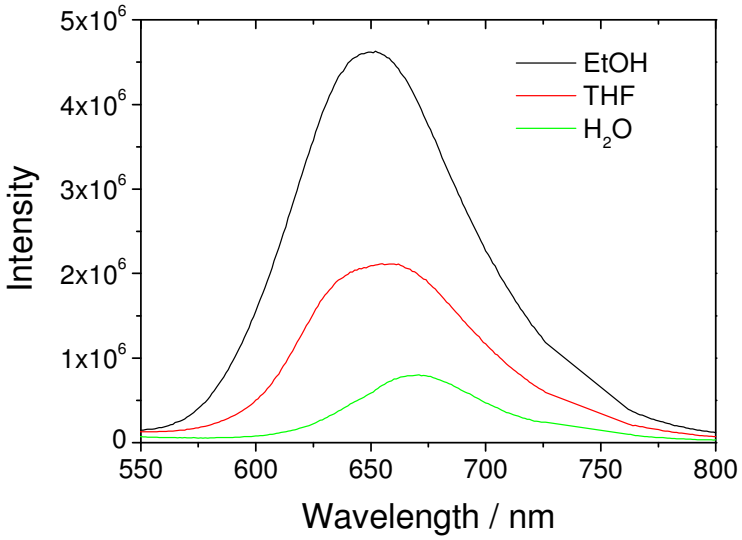


Figure 3.29 Fluorescence emission spectra of *spiropyran 1* in ethanol (black line), tetrahydrofuran (red line) and water (green line). The spectra have been obtained by excitation at 365 nm.

These data are consistent with previous studies reporting that neither *spiro-* (closed) nor *mero-* (open) forms of the dye show an intense fluorescence in water, although the *mero*-form has a higher fluorescence in polar organic solvents and within self-assembled films.[1,59] The maximum of fluorescence intensity is reached when *spiropyran 1* is dissolved in ethanol: the fluorescence spectra (**Figure 3.29**, black line) show a strong emission band centred around 650 nm. This emission is attributed to the merocyanine form even if the interpretation is not straightforward because this form has several geometrical isomers. Each isomer has different fluorescence quantum yields and lifetimes that interconvert on the same time scale as fluorescence decay.[60] To confirm this hypothesis, we have performed a comparative measurement of spiropyran

in ethanol before and after exposure to UV light for a short time; the UV irradiation should in fact increase the concentration of the merocyanine form in solution. **Figure 3.30a** shows the emission spectra in the 550–800 nm range of *spiropyran 1* in ethanol before (black line) and after irradiation (red line) with a UV lamp at 365 nm for 60 s. After irradiation, the fluorescence intensity increases confirming that the fluorescence response can be ascribed to the open form of spiropyrans. The same trend can be found in the emission of as-deposited mesostructured films (**Figure 3.30b**).

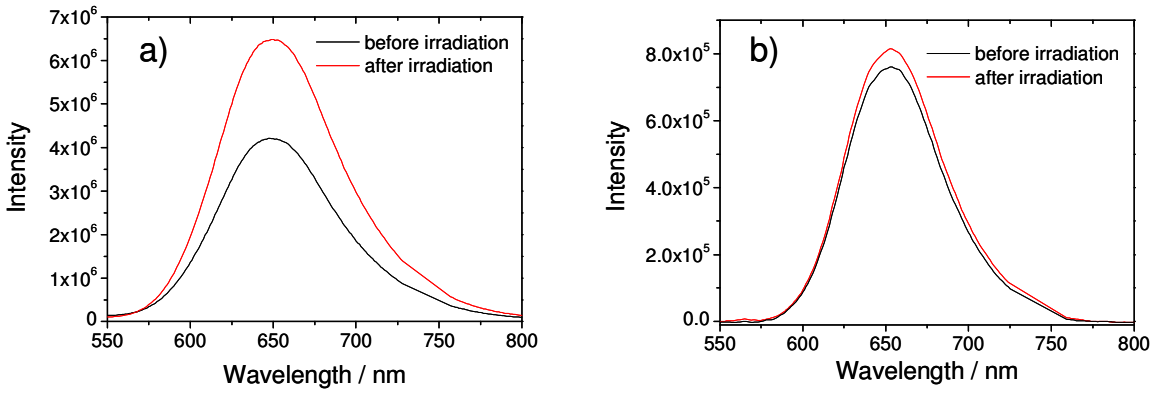


Figure 3.30 a) Photoluminescence emission spectra of *spiropyran 1* dissolved in ethanol before (black line) and after irradiation (red line) at 365 nm for 1 minute; b) photoluminescence emission spectra of spiropyran-doped mesostructured silica films before (black line) and after irradiation (red line) at 365 nm for 5 minute.

Photoluminescence measurements on thin films have been performed using a particular orientation of the samples in order to avoid reflection on the detector and increase the signal-to-noise ratio. The probing beam has been set to impinge on one side of the sample (incidence angle of 2–3°) so that the sample acted as a waveguide for the incident light wave, while the luminescence has been collected at 90° with respect to the incident beam. The incorporation of *spiropyran 1* in the mesostructured films slows down the kinetic of isomerization from the open to the close form; this is reflected in the small difference between photoluminescence spectra of film before (black line) and after UV irradiation (red line).

The same film has been also analysed by spectroscopic ellipsometry to measure thickness and refractive index. Before irradiation, the film appears transparent and consequently the polarization changes of the incident wavelength measured by the

spectroscopic ellipsometry can be fitted using a non-absorbing Cauchy model.* **Figure 3.31a** shows the dispersion curves as a function of wavelength of imaginary *k*, and real part *n* of the refractive index in as-deposited spiropyran-doped films. The real part of the refractive index *n* at 632.8 nm is 1.489 while the extinction coefficient *k* remains constant to zero on the basis of the assumption of non-absorbing film. After irradiation, the sample absorbs in the visible range and therefore a specific model (spline) has to be applied in order to fit the behaviour of the film on a transparent substrate.

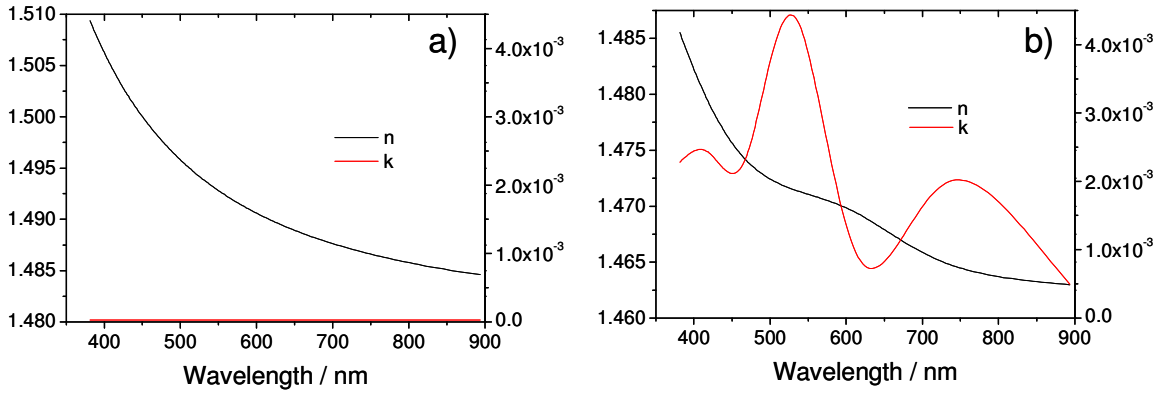


Figure 3.31 Real (*n*, black line, left side scale) and imaginary part (*k*, red line, right side scale) of the refractive index of a spiropyran-doped mesostructured silica film as a function of the wavelength. The measurements have been conducted on the as-deposited film (a) and on the film after 15 min of UV exposure at 365 nm (b).

The extinction coefficient *k* (**Figure 3.31b**, right scale, red line) shows a broad absorption band centred at 525 nm, which is in agreement with the UV–Vis spectra measured on films after UV irradiation (see below). When *spiropyran 1* is embedded in a mesostructured matrix, the local environment affects the photo- and the thermochromic properties of the molecules. **Figure 3.32** shows representative pictures of as-deposited (transparent), thermally treated (yellow) and UV irradiated (purple) films; it is important to note that both colour changes are reversible under room temperature or visible light exposure. Moreover, it has been impossible to turn the colour of the film from transparent to yellow using UV light and from transparent to purple using thermal treatment. These different coloured states of the films can be assigned to different equilibria among the various forms of merocyanine. The colours of

* The Cauchy dispersion equation: $n(\lambda) = A_n + B_n/\lambda^2 + C_n/\lambda^4$, allows calculating the refractive index as a function of the wavelength. $A_n$ is a parameter related to the average refractive index of the material, while $B_n$ and $C_n$ are parameters that provide the shape and curvature of the $n(\lambda)$ curve.

a spiropyran-based system are due to an equilibrium mixture of a number of possible stereoisomers between cis-merocyanine and more stable *s*-trans-merocyanine.[61] Despite many authors reported photochromism response of spiropyran-functionalized materials,[62,63,64] to the best of our knowledge this is the first time that nanocomposite self-assembled films show a different colour change depending on thermal or photo stimuli.

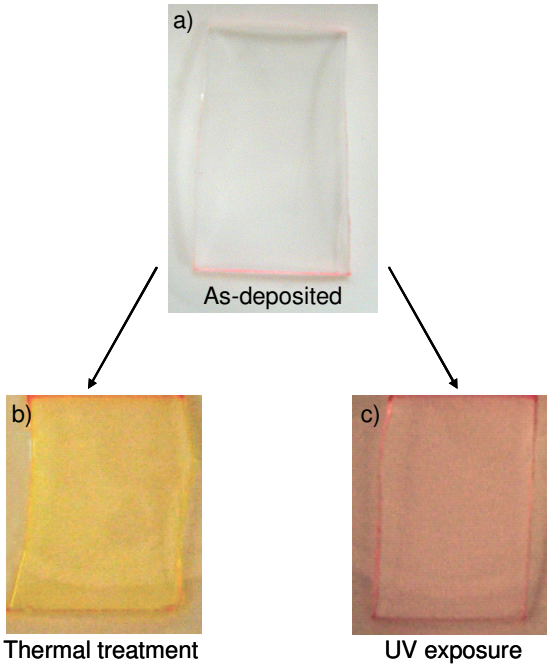


Figure 3.32 Pictures of spiropyran-doped mesostructured silica films as-deposited (a), before thermal treatment (b) and after illumination by UV light at 365 nm for 5 minutes (c).

During the experiments we observed a fast colour transition in the films after exposure to UV light; to follow up the time-dependent colour transition from purple to transparent, we have set a specific protocol of measurement. We have exposed the films to a UV lamp (365 nm) for 5 min, then we hev recorded the UV-Vis absorption spectra every 15 min to obtain the intensity decay. The samples have been exposed to ambient light between each measurement. Absorption spectra have been measured in 250-650 nm wavelength range using a UV-Vis Nicolet Evolution 300 spectrophotometer, at 500 $nm \cdot min^{-1}$ scan rate with a bandwidth of 1.5 nm. **Figure 3.33a** shows the different absorption curves obtained at the various exposure time. The UV–Vis spectra show a complex feature with a band peaking around 520 nm, which is assigned to the ring-opened photoisomer; this band decreases in intensity with the time and after 60 min is very weakly detectable, this decolouration effect is caused by the closing of the

spiropyran molecules. The photochromic decay of the absorption intensity at 520 nm is reported in **Figure 3.33b**, the points are well fitted by a first order exponential decay curve. These results have been compared with the colour change induced by thermal treatments at 100 °C for increasing times, **Figure 3.34** shows the UV–Vis absorption spectra of the film as a function of the time of thermal treatment at 100 °C, from 0 to 210 min.

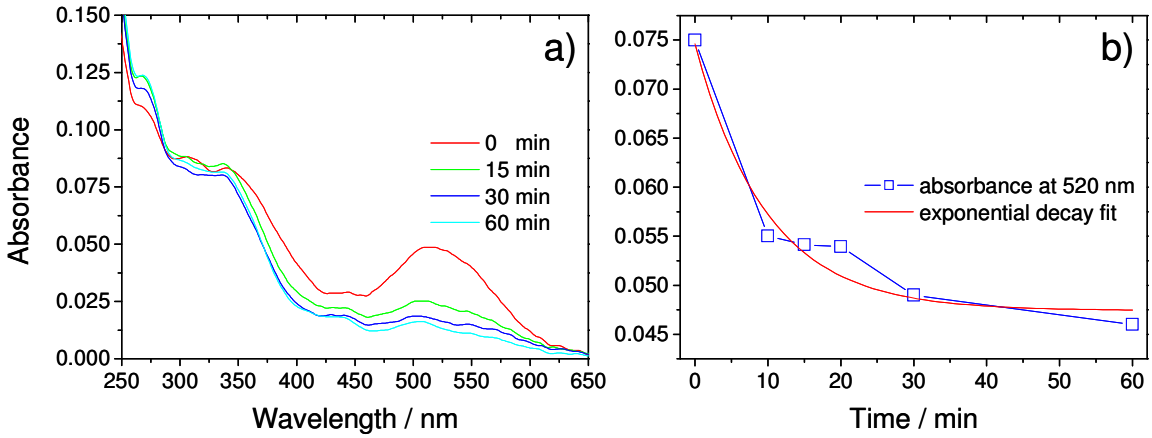


Figure 3.33 (a) UV-Vis absorption spectra of a spiropyran-doped mesostructured silica film after UV exposure at λ= 365 nm for 5 min as a function of time; (b) variation of absorbance at 520 nm as a function of time (the blue line is a guide for eyes) and exponential decay fit of the direct photochromic behaviour (red line).

When the as-deposited films are thermally treated, the response of the material appears different with respect to the films exposed to UV light.

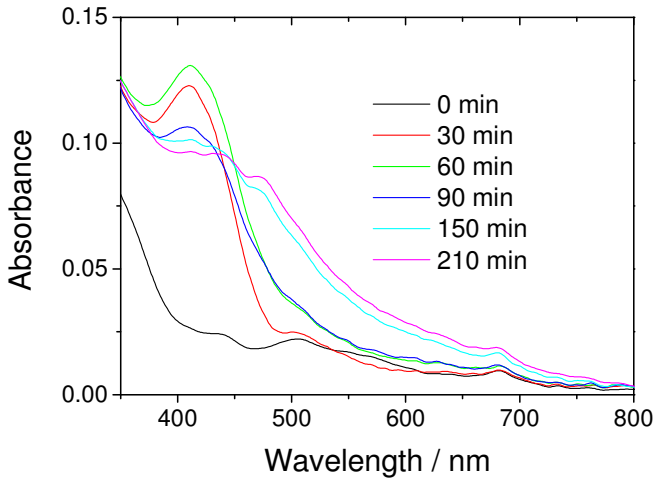


Figure 3.34 UV-Vis absorption spectra of a spiropyran-doped meso-structured silica film as a function of time of thermal treatment at 100 °C.

Even in this case, the film exhibits a direct photochromism, but the absorption maxima resulted shifted to shorter wavelength. This absorption results into a final yellowish colour. At the beginning, the samples show an absorption band at 410 nm that is gradually bleached as the system reaches the thermal equilibrium between open and closed forms of spiropyrans. At the end, a general absorption increase in the 400-500 nm range causes the final appearance of the film.

To sum up, the host system made by mesostructured silica film has proved to be a very peculiar environment for a bi-stable stimuli responsive guest molecules such as the spiropyran. The spiropyran-doped films, which appear transparent before external stimuli is applied, show a colour change to yellow, thermally induced or purple, light induced. Both the colour changes are reversible under room temperature or visible light exposure; the colour transitions have been attributed to different equilibria among the various forms of merocyanine which has different kinetic and thermodynamic stability when nano-confined inside micelles.

### 3.4.3 Zinc complex-doped films

Zinc complexes have received considerable attention for the preparation of electroluminescent thin films[65,66] because they are promising key color components (as blue emitting molecules) for the fabrication of full-color displays.[67] The incorporation of luminescent complexes into a solid state matrix is therefore a mandatory step for technological applications; the immobilization of luminescent organic molecules on rigid supports can lead, in fact, to an enhancement of the emission efficiency[68,69] and a greater temporal stability of the fluorescence properties.

Mesoporous materials, thanks to their pore accessibility and functionalization of catalytic sites within the pores, can be successfully exploited to design highly fluorescent nanocomposites. Host-guest systems such as organic luminescent molecules in silica mesoporous films, combine the chemical stability and mechanical strength of the inorganic matrix together with the functional properties of the active organic guests. Grafting of metal complexes onto the inner walls of mesoporous silica can be obtained using three main approaches:[70,71] (1) direct grafting by reaction with surface silanol groups; (2) indirect grafting via the functionalization of the silanol groups with silane coupling agents followed by the anchoring of metal complexes to the surface; (3) ship-in-a-bottle immobilization of metal complexes.

In these paragraph we report on the introduction of a zinc complex as light emitting guest species into a mesoporous silica acting as host matrix. We have used mesoporous thin films to incorporate a highly luminescent species preserving, at the same time, the ordered porosity and the high surface area of the matrixes. The synthesis of the luminescent material has been performed by addition to the zinc complex of a Schiff-base ligand bearing triethoxysilane functions; this has allowed to graft the molecule directly to the surface of the mesoporous materials through covalent bonding. The structure of the anchoring groups gives high stability to the complex within the mesoporous matrix, avoiding leaching effects.

- *Films functionalization*

Mesoporous films and Schiff base zinc complex ($ZnL_2$) have been prepared as reported in Section 3.1, page 82. The stability of $ZnL_2$ in EtOH has been tested by monitoring the evolution of the absorption spectra with time. Absorption spectra have been measured in 200-500 nm wavelength range using a UV-Vis Nicolet Evolution 300 spectrophotometer, at 500 nm·min$^{-1}$ scan rate. The UV-Vis absorption spectra of $ZnL_2$ in EtOH show three main bands peaking at 361, 269 and 238 nm. The complex appears very stable for 32 h, at longer times the $ZnL_2$ spectral features decrease in intensity and a precipitate, likely resulting from $ZnL_2$ condensation phenomena involving the triethoxysilane functions, is observed (**Figure 3.35a**). A similar trend is shown by $ZnL_2$ in THF.

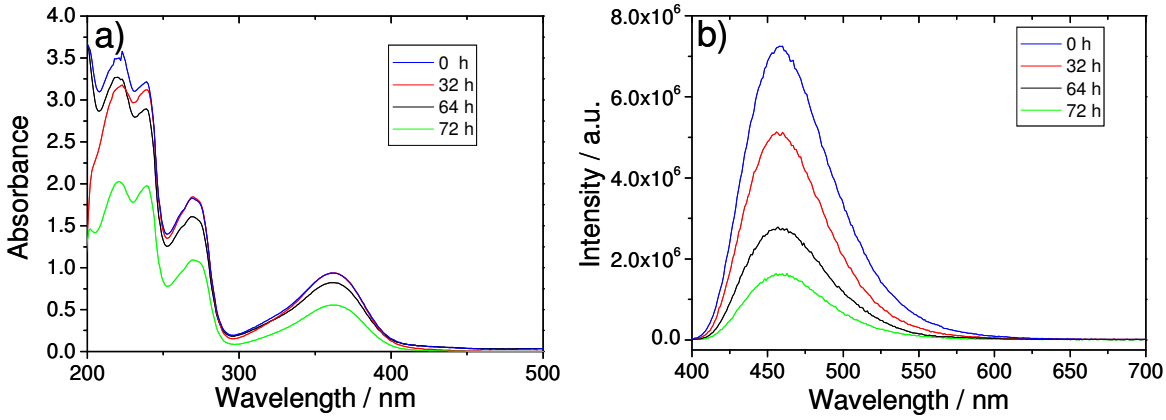


Figure 3.35 a) UV–Vis absorption spectra of the Schiff base zinc(II) complex in ethanol as a function of time. b) Fluorescence emission spectra ($\lambda_{ex}$ = 360 nm) of the Schiff base zinc(II) complex in ethanol as a function of time. Both measurements have been performed on 2 cm$^3$ of ethanol with a concentration of $ZnL_2$ equal to 2.19·10$^{-7}$ mol.

Fluorescence analysis of a solution made with $ZnL_2$ and ethanol has been conducted by using a FluoroMax-3 Horiba Jobin-Yvon spectrofluorometer (**Figure 3.35b**). The spectra show a strong emission band peaking at 457 nm ($\lambda_{ex}$ = 360 nm) which is in the range (440–460 nm) typical for bi- and tetra-dentate HL like Schiff bases coordinated to the zinc(II) ion.[72] The emission arises from the HL complexation to zinc(II) that hampers a non radiative decay pathway by binding the imine nitrogen electrons pairs involved in the metal coordination. HL, in fact, does not show emission, while the complex displays an intense emission band. The decrease in intensity with time of the 457 nm band reveals that the emission spectra are more sensitive than absorption spectra to aging of the complex: after 72 h, with reference to a freshly prepared solution, the emission intensity drops to the 35% nearly.

After its optical characterization, the mesoporous films have been functionalized with the zinc complex. The samples have been introduced into a beaker containing 45 $cm^3$ of THF and $ZnL_2$ (0.21 mmol, 0.113 g) in EtOH (10 $cm^3$) and kept in the solution at different times. Then they have been washed with EtOH and dried at 60 °C for 1 hour.

*- Morphological and optical films characterization*

A ‘‘palette’’ of characterization techniques has been adopted to study the incorporation of the $ZnL_2$ complexes within the host mesoporous films. For mesophase characterization of the resulting films, bright field TEM images have been collected on samples calcined at 350 °C. Finely ground films have been scratched from the substrate, dispersed in n-octane and dropped on a carbon-coated copper grid for analysis. TEM images have been obtained on a JEOL 200C× microscope equipped with a tungsten cathode operating at 200 kV. **Figure 3.36** shows representative direct image of the deposited films. The snapshot suggests that the ordered porous structure is slightly distorted cubic. This periodicity is compatible with an orthorhombic *Fmmm* space group that has been already observed on mesoporous pure silica films by SAXS analysis.[73]

The organized interconnected porous structure is very suitable for post-synthesis grafting of doping molecules. Several examples are reported in literature and show that after incorporation, both via physical adsorption or chemical bonding, the molecules maintain their activity and are well entrapped within the matrix without significant leakage.[74] Infrared absorption spectra collected from a sample as a function of the impregnation time give a direct snapshot of the incorporation of the $ZnL_2$ together with the condensation state of the oxide network. Fourier Transform Infrared (FTIR) analysis

has been performed using a Nicolet Nexus spectrometer. The spectra have been recorded in transmission, using a silicon wafer as the background and averaging 256 scans with 4 $cm^{-1}$ of resolution. The FTIR spectra are characterized by the typical signature of silica[23], which shows three main bands around 1100 ($\nu_{as}$), 800 ($\rho$) and 450 ($\nu_s$) $cm^{-1}$ (**Figure 3.37**).

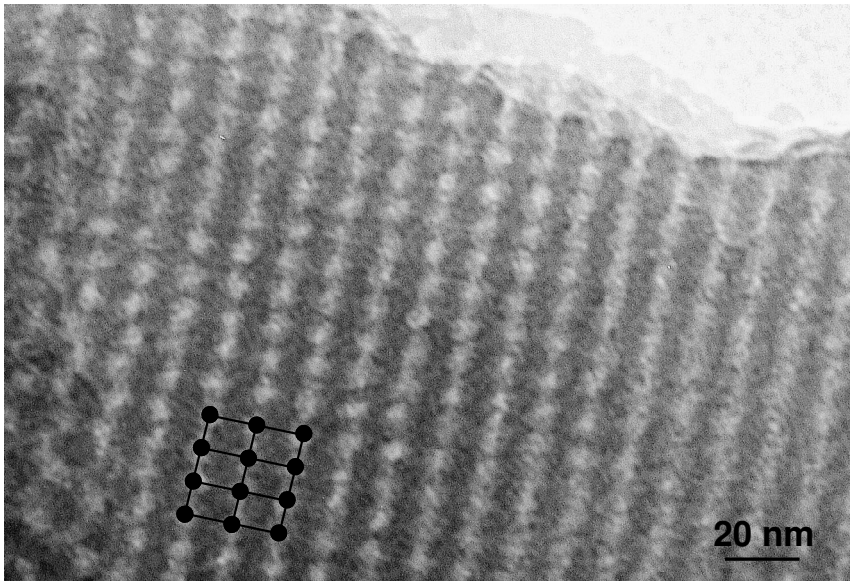


Figure 3.36 Bright field TEM image of the calcined mesoporous silica film.

The wide band peaking around 3300 $cm^{-1}$ is due to O-H stretching of silanol species and adsorbed water. The presence of silanols is also revealed by the band at 940 $cm^{-1}$.

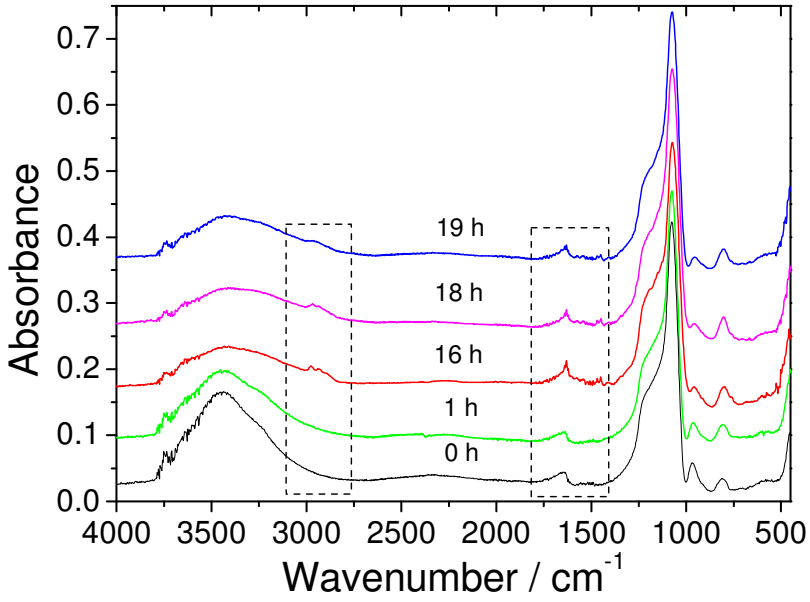


Figure 3.37 FTIR absorption spectra of the mesoporous $SiO_2$ film as a function of impregnation time ($ZnL_2$ in THF).

After calcination at 350 °C, the surfactant is completely removed, as shown by the absence of any signal around 2700–3200 $cm^{-1}$ (spectrum at 0 h). Water absorption is observed in the as-prepared films and in the sample at lower impregnation times (O–H stretching band around 3200 $cm^{-1}$ and H–O–H bending at 1640 $cm^{-1}$).[21] The films show also an absorption band around 3750 $cm^{-1}$ due to isolated silanols which are produced by calcination process.[73] The FTIR spectra of the films after impregnation show, instead, the rise of new signals in the C–H stretching range (2700–3200 $cm^{-1}$). The intensity of this signal can be assumed as an indication of the quality of the porous film impregnation; the spectra show that the best result is obtained after 16 h of impregnation. At times shorter than 16 h, the amount of complexes is much lower, while at longer times a decrease in the impregnation efficiency is observed. This is likely due to leakage effects caused by the hydrolysis of the silica bonds that anchor the zinc complex to the surface of the films. It is important to note that the stability of the films at the impregnation conditions is good; the silica bands do not show any significant change after the films are immersed in the doping solution. The presence of $ZnL_2$ in the films is confirmed by the bands located in the 2750–3050 $cm^{-1}$ range, assigned to the stretching mode of $–CH_2$ group, and the weak bands, barely detectable, at 1639 and 759 $cm^{-1}$ assigned to the vibration of C=N and C–H aromatic.

| **Time of impregnation** | **Thickness / nm** | | **Refractive index λ = 632.8 nm** | |
|---|---|---|---|---|
| | **(before)** | **(after)** | **(before)** | **(after)** |
| 1 h | 458 ± 10 | 448 ± 12 | 1.312 | 1.313 |
| 2 h | 477 ± 9 | 473 ± 10 | 1.358 | 1.371 |
| 16 h | 518 ± 16 | 530 ± 25 | 1.293 | 1.375 |
| 18 h | 477 ± 13 | 470 ± 23 | 1.310 | 1.394 |
| 19 h | 470 ± 15 | 490 ± 24 | 1.315 | 1.351 |

Table 3.1 Changes in thickness and refractive index of mesoporous $SiO_2$ films deposited on silicon before and after introduction of the $ZnL_2$ complexes measured by spectroscopic ellipsometry.

The effect of the introduction of the complex within the mesoporous film has been also monitored by spectroscopic ellipsometry at room temperature. Refractive index and

thickness have been measured by a α-SE Wollam spectroscopic ellipsometry at room temperature. *n*, *k* and the residual porosity have been calculated by 2.03 α-SE Wollam software. **Table 3.1** lists the thickness and the refractive index at λ = 632.8 nm of different samples before and after impregnation. The data have been obtained assuming a fitting model based on the assumption of transparent films on silicon (Cauchy dispersion relation, see note page 136). In fact, the measures have been performed in the 390–900 nm range where the fluorescent zinc complex does not present absorption bands (see **Figure 3.35a**).

A Bruggeman Effective Medium Approximation (EMA)[†] layer with two components (silica and void) has been used to evaluate the optical constants and the residual porosity of the films dried at 60 °C before impregnation; the fit gave a 24% of residual porosity. The data from spectroscopic ellipsometry are well in accordance with the infrared spectra, in fact, only after 16 h a significant change in refractive index is observed, which indicates the successful impregnation of the film. The highest change in refractive index is observed in the films impregnated by $ZnL_2$ for 18 h, in accordance to the FTIR data. We can also note that the thickness is not affected by the doping process and this is a good indication about the stability of the host material in the present conditions of impregnation.

*- Fluorescence films properties*

The fluorescence emission spectra have been measured on film deposited on silica glass slides. The samples have been aligned to have a grazing incidence of the probing beam so that the sample acted as a waveguide for the incident light wave. The luminescence has been then collected at 90° with respect to the incident beam in order to enhance the signal-to-noise ratio and avoid reflection effects.

Emission spectra ($\lambda_{ex}$ = 360 nm) of the $ZnL_2$ grafted films as a function of the doping times are shown in **Figure 3.37**. At higher impregnation times the fluorescence peak shows a shift from 455 to 465 nm and a strong increase of emission intensity. The stability of the fluorescence emission has been tested as a function of aging time; in the

[†] For a two-components material, the refractive index in the Bruggeman approximation is expressed as: $f_v \frac{n_v^2 - n^2}{n_v^2 + 2n^2} + f_{SiO2} \frac{n_{SiO2}^2 - n^2}{n_{SiO2}^2 + 2n^2} = 0$ where $f_v$, $n_v$ and $f_{SiO2}$ , $n_{SiO2}$ are the volume fractions and the refractive index of the pores void and silica, respectively.

case of a sample impregnated for 18 h with a $ZnL_2$ solution, the emission intensity after 7 days is around 80% of the initial one.

The efficiency of the mesoporous host matrix in entrapping the $ZnL_2$ complex has been tested by leaching experiments.

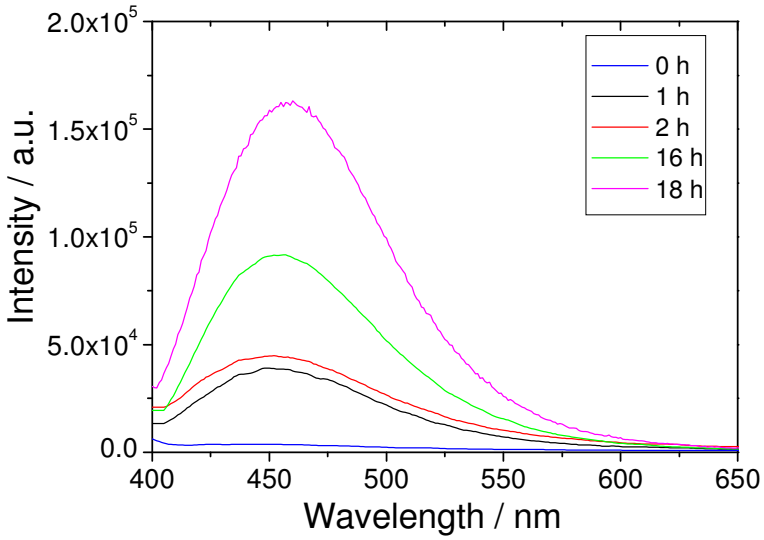


Figure 3.37 Fluorescence emission spectra ($\lambda_{ex}$ = 360 nm) of $ZnL_2$ doped mesoporous $SiO_2$ film as a function of the impregnation time.

The entrapping of the complexes within the mesoporous films should involve the formation of direct silica bonds through the surface silanols, as depicted in **Figure 3.38**.

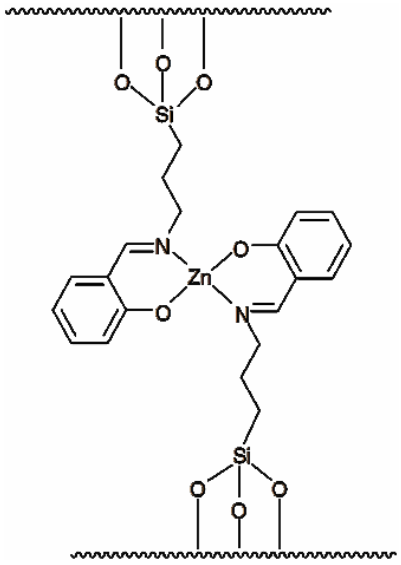


Figure 3.38 Sketch of a possible chemical structure of the $ZnL_2$ doped-mesoporous $SiO_2$ film.

The formation of these bonds should be accompanied by a reduction in silanols, as confirmed by the reduction in intensity of the Si–OH signals in the FTIR spectra of impregnated samples (see **Figure 3.36**). To obtain a direct experimental evidence of the formation of a strong covalent bond between the matrix and the doping complexes in the films is difficult, but leaching experiments can give some indirect clues. Leaching experiments have been performed monitoring the change in intensity of the absorption and emission spectra of the $ZnL_2$ doped mesoporous films as a function of the immersion time in ethanol. **Figure 3.39** shows the emission spectra ($\lambda_{ex}$ = 360 nm) at increasing leaching times. A decrease in emission intensity is observed in the first two hours, after 210 min the samples do not show anymore changes up to 7 days of measure. This result, together with the FTIR data, indicates that grafting of the complex to the silica mesoporous walls has been achieved.

To summarize, mesoporous materials has shown to be a very efficient matrix for the preparation of host-guest systems. The zinc complexes can be used to impregnate porous host materials such as mesoporous silica films: after introduction of the complex, the films are highly fluorescent and a good stability of the emitting properties can be observed as a function of time. Leaching experiments have shown that the complexes incorporated in the film are stable and no significant release of the zinc complex has been detected after several days of immersion of the samples in ethanol.

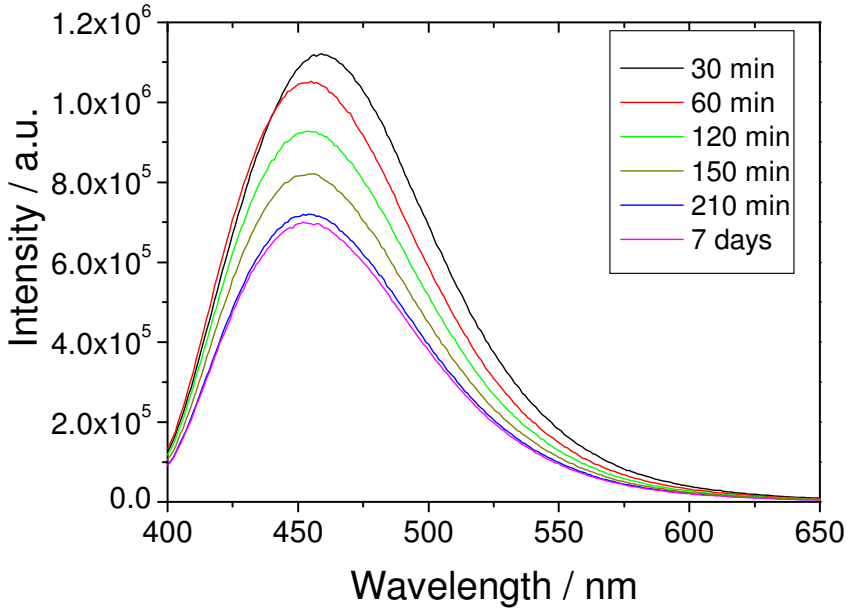


Figure 3.39 Fluorescence emission spectra ($\lambda_{ex}$ = 360 nm) of $ZnL_2$ doped mesoporous $SiO_2$ film as a function of the leaching time.

### 3.4.4 Pores as template for nanoparticles growth

The presence of an ordered porous structure that can be tailored through the control of the synthesis parameters suggests the use of mesoporous films as nanoreactors for the controlled bottom-up synthesis of nanostructured materials. Basically, the mesopores can be filled with suitable liquid or gaseous precursors which subsequently form nucleation seeds, for example by precipitation or oxidation reactions, so that the growth of a solid phase is controlled by the chemical and physical properties in the ordered porous structure (pore size, hydrophobicity, etc.). With spherical mesopores of the order of few nanometres, quantum dots or metal nanoparticles with controlled size and composition can be obtained. There is a large number of publications revolving on this synthetic approach: just to cite a few examples, CdS,[75,76] CdSe,[77] and $Cd_{1-x}Mn_xS$[78] have been grown in mesoporous silica. Techniques other than impregnation can be used to form nanoparticles inside mesopores: for example, CdS and $CuInS_2$ have been obtained by chemical vapour deposition inside mesoporous titania.[79] In a previous study, we have grown PbS nanoparticles by precipitation through a two-step impregnation process by immersing mesoporous silica films in solutions containing $Pb^{2+}$ and $S^{2-}$ species.[80] The films thus contained PbS nanoparticles with size roughly tunable by the immersion time in the Pb or S precursor solutions.

The inclusion of nanoparticles in mesoporous films presents at least three advantages in comparison with other systems (e.g. in a dense sol-gel silica film). First, the size of the nanostructure is controlled by the size of the mesopores, which in turn can be precisely controlled during the synthesis of the mesoporous film; therefore, it is possible to obtain highly monodisperse particles. Secondly, the periodicity of the mesopores allows a more efficient packing, which results in a higher nanoparticle density assuming that (almost) every pore is filled. Thirdly, the presence of micropores in the inorganic walls of the mesoporous films ensures the interconnection between the mesopores, which is an essential condition for a complete film impregnation in the nanoparticle growth process, as well as for permeability in the application of the final product (e.g. a gas or chemical sensor). It has been already observed that in block copolymer-templated mesoporous silica films the ordered mesoporosity is maintained even at temperatures higher than 800 °C.[73] This property makes the mesoporous films an interesting host material for nanoparticles whose preparation requires high temperatures. Furthermore, mesoporous films fulfil the requirement of having good chemical stability to undergo an

impregnation process. Therefore, we have decided to use mesoporous silica film with different pore size in order to growth FeCo nanoparticles. Bulk FeCo alloys are soft ferromagnets whose magnetic properties have been widely investigated as a function of composition and temperature, owing to their technological importance. The major field of application of FeCo alloys is in the technology of transformer cores and electrical generators because of their soft ferromagnetic behaviour combined with high Curie temperatures and large saturation inductions, about 15% larger than pure iron.[81] The preparation of iron-cobalt alloy nanoparticles is usually approached by the use of a coating, in order to avoid agglomeration and coalescence between the nanoparticles. For example, radio frequency plasma torch has been used to produce C-coated FeCo nanoparticles of about 50 nm.[82] Serna et al. made use of hydrolytic routes to produce anisotropic alloy nanoparticles in order to increase the magnetic coercivity: needle-like alumina- and yttria-coated FeCo nanoparticles have been prepared by annealing of YCo-FeOOH nanoparticles obtained by oxidation-precipitation.[83] Monodisperse 15-nm nanoparticles have been recently obtained by co-decomposition in toluene at 150 °C under $H_2$ of appropriate organometallic precursors.[84] An alternative approach lies on embedding the iron-cobalt nanoparticles in an insulating matrix, which acts as a dispersing medium. Sol-gel processing is very suitable for the preparation of such nanocomposites as it offers unique advantages in terms of compositional homogeneity, dispersion of the nanophase within the matrix and purity of the resulting material. Recently, co-gelation sol-gel routes have been successfully exploited for the preparation of FeCo-$Al_2O_3$ nanocomposite materials.[85] The main advantage of this method is the compositional control of the nanocomposite and the high distributional homogeneity of the nanoparticles within the matrix, because the mixing of the precursors occurs at the molecular level in the initial stages of sol preparation. A major drawback of this preparation route is that the microstructure and, in turn, the magnetic properties, are related to many independent processing parameters. For example, an increase in the loading of the nanophase in the composite increases the average size of the nanocrystals, broaden the size distribution and decreases the interparticle distance. Alternatively, if the nanocrystals are grown within a pre-formed matrix with controlled texture, the size, size distribution and dispersion of the nanocrystals is dictated by the porous structure of the host matrix. In principle, the growth of magnetic nanoparticles in a host matrix with controlled pore architecture allows the fine-tuning of the nanocomposite microstructure. Ordered mesoporous matrices prepared by template-assisted sol-gel techniques are

particularly suited to this end in that they exhibit narrow pore size distribution together with pore diameter tunability, well-defined porous structure and high specific surface areas. The major drawback of this approach is that the nanophase is added to the matrix by diffusion and therefore the overall composition and homogeneity are more tricky to control. Mesoporous silica have been shown to be a versatile material to produce nanocomposites with interesting properties. For example, nanocomposites prepared by introducing pre-formed Co nanocrystals of suitable diameter into the pore channels of SBA15 mesoporous matrix have been used to form Co chains within the pore channels; this resulted in magnetic coupling giving rise to a transition from soft to hard magnetic behaviour.[86] In this case, the magnetic behaviour of the Co-SBA15 nanocomposite is directed by the ordered porous structure of the host matrix despite the intrinsic magnetic properties of the individual nanoparticles. Moreover, dissolution of the silica matrix in FeCo-$SiO_2$ nanocomposites has been shown to be an effective way to fabricate FeCo graphitic nanoparticles to be used as MRI (magnetic resonance imaging) contrast agents.[87]

In the following paragraph we have reported on the synthesis of mesoporous silica films with different mesopore size as the host and the template to prepare FeCo-$SiO_2$ nanocomposites. We have used an impregnation process followed by a reduction treatment under $H_2$ flow to grow FeCo nanocrystals inside the mesopores and control their diameter which has been dictated only by the size of the mesopores.

Mesoporous silica thin films have been prepared as described in Section 3.1, page 83. The films have been investigated after the thermal treatment at 600 °C. This study has been conducted both on films previously impregnated with Fe and Co precursors solution and not-impregnated ones. The effects induced by the impregnation process on the silica matrix have been evaluated on the basis of XRD, TEM and GISAXS measurements.

*- XRD and GISAXS films characterization*

A standard powder diffractometer (X3000 Seifert equipped with Cu Kα radiation and a graphite monochromator on the diffracted beam) has been used to gather a first rough indication on the presence of an ordered porous structure in the silica films and its modification with impregnation and reduction treatment by collecting patterns at small angles (0.5 to 3°, SA-XRD). X-ray diffraction experiments also provided evidence on the formation of FeCo nanocrystals by collecting patterns at wide angles (WA-XRD). In

**Figure 3.40a** are reported the SA-XRD patterns of F68-templated unimpregnated and untreated film, the F68-templated film reduced at 600 °C without impregnation and the F68-templated film reduced at 600 °C after being impregnated.

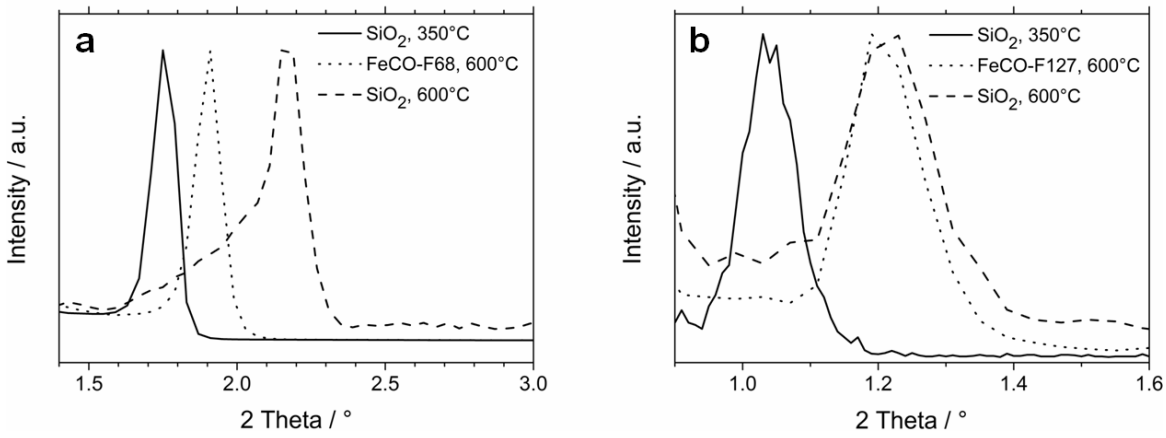


Figure 3.40 SA-XRD patterns of the F68- (a) and F127-templated films (b). The data refer to mesoporous silica films treated at 350 °C before impregnation (solid line), FeCo-$SiO_2$ nanocomposites treated at 600 °C after impregnation (dotted line) and mesoporous silica films treated at 600 °C with no impregnation (dashed line).

The position of the peak is centred around 1.7° in the unimpregnated and untreated film, 2.2° in the film reduced at 600 °C without impregnation and around 1.9° in the film reduced at 600 °C after impregnation. These results indicate that the mesoporous structure is affected by the thermal treatment, which induces a shrinkage of the mesoporous structure. However, the presence of the FeCo nanocrystals hinders the shrinkage, which is less evident in the sample reduced after impregnation. This suggests that the nanocrystals are inside the mesopores: their presence reduces the pores uniaxial shrinkage, most likely due to a steric effect. The mesopores are supported by the nanocrystals which act as a scaffold, therefore the structure is less prone to contract upon thermal treatment. Similar results, even though less evident, have been also obtained from the samples templated by F127 (**Figure 3.40b**). WA-XRD patterns of the samples treated at 600 °C after impregnation, show in both the F68- and F127-templated films a peak around 44°, corresponding to the most intense peak of *bcc* FeCo due to the (110) reflection (**Figure 3.41**). The lattice parameter determined from the (110) peak position is 0.286 nm; this value is in perfect agreement with the lattice parameter for bulk $Fe_{70}Co_{30}$ alloy. [88]

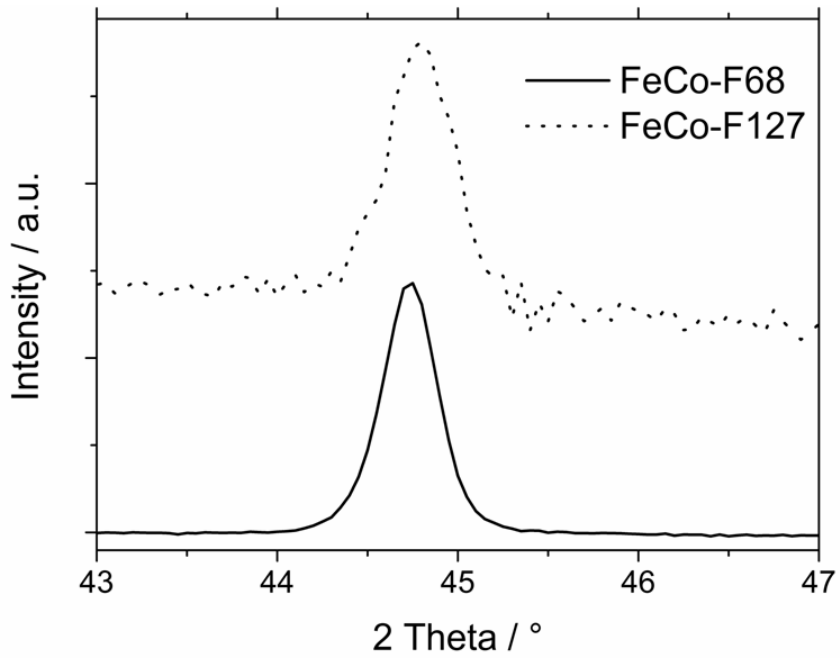


Figure 3.41 WA-XRD patterns of the FeCo-F68 (solid line) and the FeCo-F127 (dotted line) nanocomposites, indicating the presence of FeCo alloy.

Although the XRD patterns at low angle give a first indication on the presence of an ordered porous structure and its behaviour upon impregnation and thermal treatment: the presence of a single peak indicates only the existence of order in the out-of-plane direction but it does not allow determining the symmetry group of the mesostructure. Therefore, a detailed characterisation of the ordered mesoporosity has been performed by collecting two dimensional GISAXS patterns at the Austrian SAXS beamline of ELETTRA synchrotron with a 8 keV incident energy. We used an average of 10 acquisitions with integration time of 500 ms. GISAXS patterns of F68-templated silica films, unimpregnated and untreated, show well-defined spots and no ring, indicating a high degree of order of the porosity within the film (**Figure 3.42a**). The patterns have been assigned to a cubic symmetry (body-centred cubic, space group $Im\bar{3}m$) with the (110) plane oriented perpendicular to the substrate (z direction), uniaxially distorted in the z axis.[27,89] The cell parameter *a* has been calculated according to each single *hkl* reflection from its *d*-spacing $d_{hkl}$ using the formula $a_{hkl} = d_{hkl}\sqrt{h^2 + k^2 + l^2}$ . The distorted cubic symmetry can also be described as an orthorhombic *Fmmm* space group, as reported in Paragraph 1.3.1.

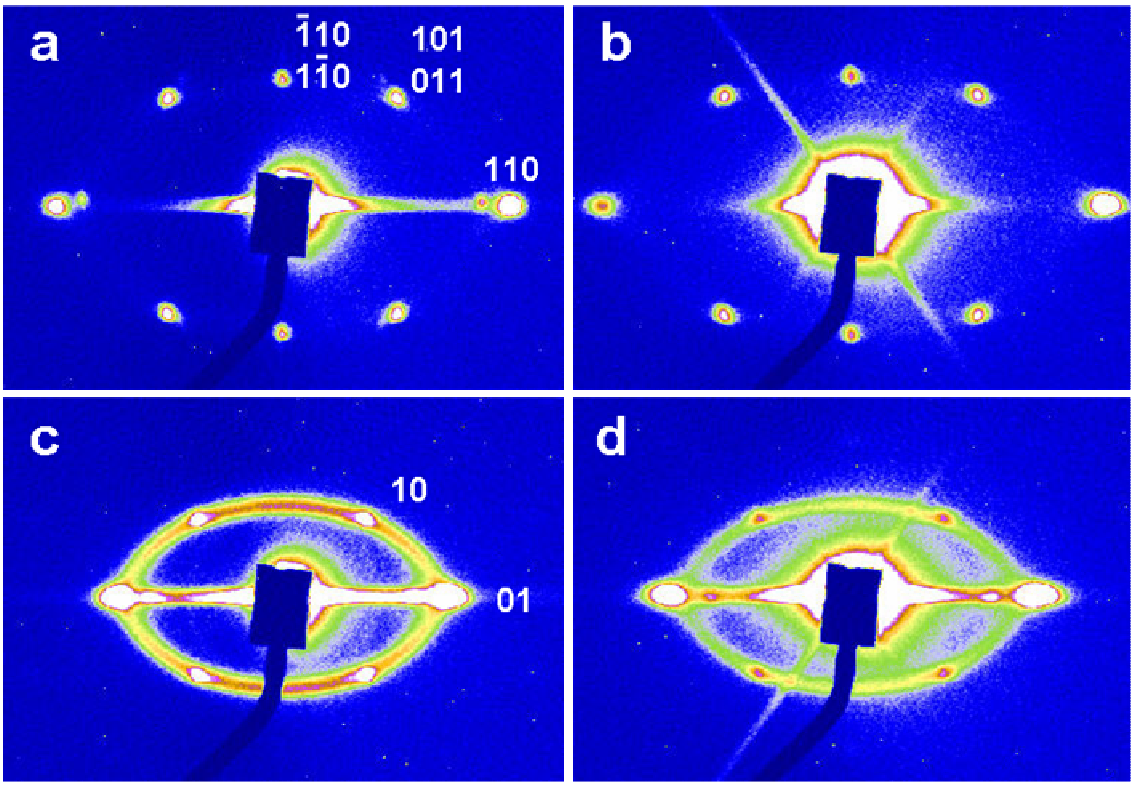


Figure 3.42 GISAXS patterns of F68-templated mesoporous silica films treated at 350 °C (a) and after impregnation and reduction at 600 °C (b). F127-templated mesoporous silica films treated at 350 °C (c) and after impregnation and reduction at 600 °C (d).

However, for practical purposes we can consider the observed porous ordered structure as a slightly z-distorted $Im\bar{3}m$ rather than a lower symmetry orthorhombic structure, and calculate the cell constants accordingly. The distortion is thus a contraction of the unit cell in the out-of-plane [110] direction (normal to the substrate), which is hereafter referred to as $d_{110z}$, whereas the in-plane (parallel to the substrate) cell constant is referred to as $d_{110x}$. The cell parameters of the distorted cubic $Im\bar{3}m$ structure in Pluronic F68-templated films treated at 350 °C that did not undergo any impregnation and reduction treatment are $d_{110x}$ = 14.0 ± 1.4 nm and $d_{110z}$ = 7.8 ± 0.8 nm. The GISAXS patterns of the films templated by Pluronic F68 that have been impregnated with the Fe / Co solution and subsequently reduced at 600 °C, show that no symmetry change occurred upon impregnation (**Figure 3.42b**); in this case the cell parameters are $d_{110x}$ = 14.1 ± 1.4 nm and $d_{110z}$ = 7.1 ± 0.7 nm. We note that the in-plane cell constant is substantially unaltered, whereas the out-of-plane cell constant is smaller in impregnated films treated at 600 °C.

Films templated by Pluronic F127 have a two-dimensional hexagonal *p6mm* symmetry composed of ordered arrays of tubular micelles with hexagonal cross section (**Figure 3.42c and d**). The cell parameters of the 2d-hexagonal *p6mm* mesophase templated by Pluronic F127 are 11.0 ± 1.1 nm and 7.9 ± 0.8 nm in the in-plane (x) and out-of-plane (z) directions, respectively. The presence of a distorted ring intersecting the spots indicates either that a wormlike region coexists with the ordered hexagonal mesophase within the film, or that the hexagonal mesophase is globally not well-ordered (e.g. because there is a short-range order which extends only to the nearest neighbour micelles). The cell constants of the nanocomposite (i.e. impregnated and reduced) films are 10.4 ± 1.0 nm and 7.2 ± 0.7 nm, in the x and z direction, respectively.

*- TEM results*

Transmission electron microscopy images have been acquired to evaluate local order as well as pore size and shape. The samples selected for TEM observation were the starting mesoporous silica films and the final nanocomposites obtained by the impregnation process and annealing at 600 °C. At first, the films have been scratched from their silicon substrates to produce small fragments of the coatings. Then, the fragments have been ground on a mortar, dispersed in n-octane by sonication and dropped on a carbon-coated copper grid. After drying, the grids have been observed on a JEOL 200C× microscope equipped with a tungsten cathode operating at 200 kV. **Figure 3.43b and c** show the ordered arrays of pores in the (100) projection plane of the $Im\bar{3}m$ cubic structure. A line profile analysis has been conducted on the image: the pore diameter and the wall thickness have been calculated as the average FWHM of the intensity distribution along a line intersecting the pore centres (**Figure 3.43d**). The analysis revealed that the pore-to-pore distance is different in the two orthogonal directions, which indicates the presence of a 2-fold symmetry axis, probably originating from the thermal contraction along the [110] direction of the $Im\bar{3}m$ cell (z axis). The average centre-to-centre distance between two adjacent pores is 8.6 ± 1.0 nm in the x (in-plane) direction and 6.3 ± 1. 0 nm in the z (out-of-plane) direction, while the average pore diameter is 4.0 ± 1.0 nm and the inorganic pore wall thickness is 2.3 ± 1.0 nm. Mesoporous films templated by Pluronic F127 show a short-range order, where the hexagonal packing extends only to the nearest neighbour pores, as shown in **Figure**

**3.43a**. In other words, the 6-fold rotational axis describing the cross-sectional symmetry of the nearest neighbour micelles is lost when we consider the next neighbour micelles.

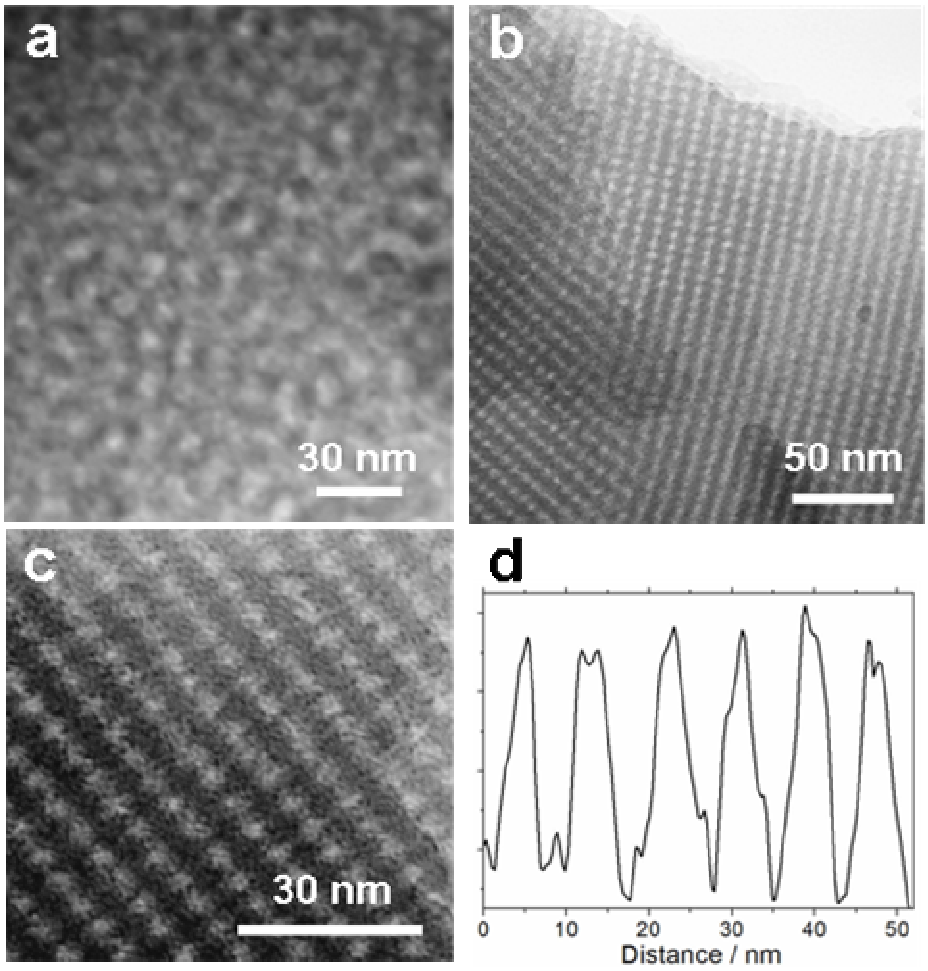


Figure 3.43 Bright-field TEM images of mesoporous silica films templated by F127 (a) and F68 (b). Line profile analysis of a F68-templated film conducted on a representative area with higher magnification (c and d).

This is consistent with the simultaneous presence of spots and a ring observed in the GISAXS patterns (**Figure 3.42c and d**). The line profile analysis showed that the average pore diameter is 7.4 ± 1.0 nm, which is almost double of a Pluronic F68-templated mesopore.

**Figure 3.44** reports representative TEM images of the FeCo-F68 and FeCo-F127 samples obtained in bright field and dark field mode, which show the formation of the FeCo-$SiO_2$ nanocomposite. Due to small nanocrystal size, the alloy nanoparticles are barely detectable as darker spots in the bright field image of FeCo-F68 nanocomposite

(**Figure 3.44a**), whereas they are more evident in the FeCo-F127 sample (**Figure 3.44d**) where larger nanocrystals can be imaged.

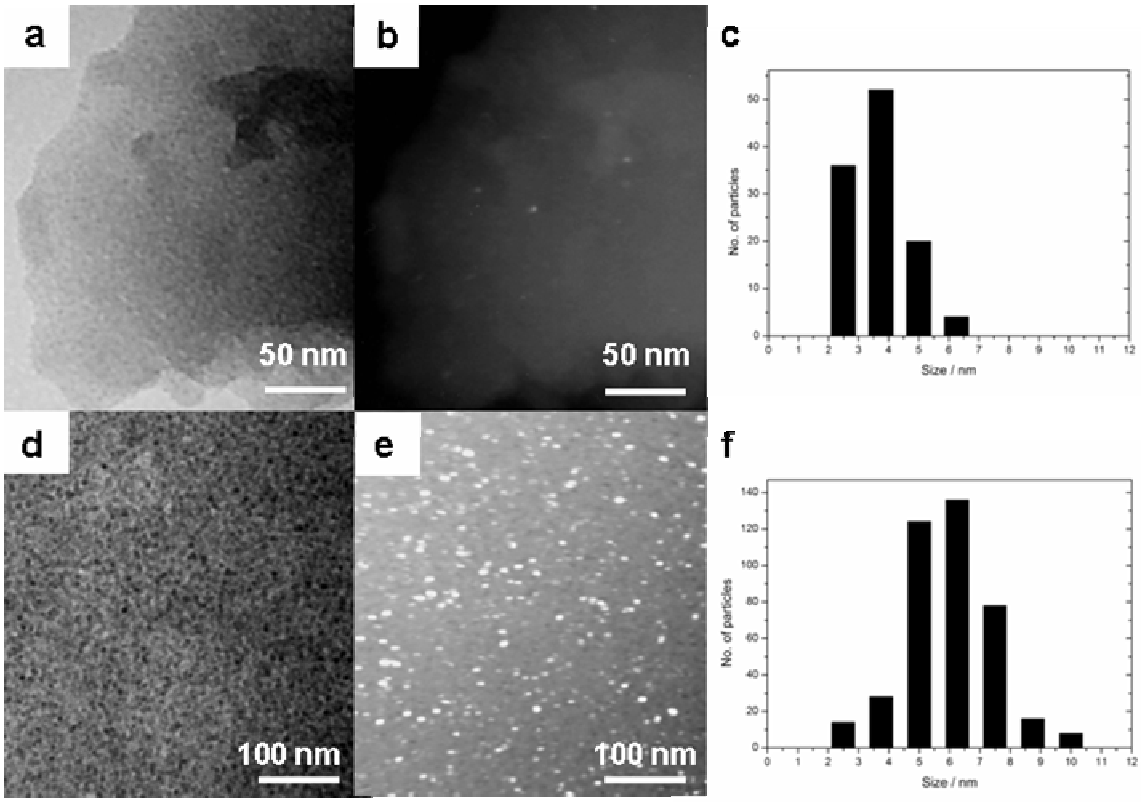


Figure 3.44 Representative TEM bright field and dark field images of the FeCo-F68 (a,b) and FeCo-F127 (d,e) nanocomposites. Nanoparticle size distribution analysis plots are shown in c and f for the FeCo-F68 and FeCo-F127 nanocomposites, respectively.

This effect is even more evident in the dark field images (**Figure 3.44b and e**) which also show that the nanoparticles are single crystals. In fact, the dark spots in the bright field images correspond to the bright spots in the dark field images, indicating that the whole nanoparticle corresponds to a single crystalline domain. The size distribution obtained from dark field images analysis shows that the nanocrystal size is monodisperse in both samples and is centred at 5 and 7 nm in the FeCo-F68 and FeCo-F127 samples, respectively. In both samples no aggregated nanoparticles or nanoparticles outside the mesopores of the silica matrix have been observed.

To sum up, silica mesoporous films have shown to be an effective matrix for the preparation of nanoparticles requiring high crystallisation temperatures (> 600 °C). The films maintain their porosity even after thermal treatment at 600 °C and show only a

slight shrinkage after the impregnation process. The mesoporous silica films used as the matrix have either spherical or cylindrical pores, depending on the templating agent used in the synthesis. We have shown that the growth of the FeCo nanocrystals in the silica films took place inside the mesopores and the pore diameter constitutes an upper limit for the nanocrystal size. Therefore, since mesopores represent a spatial confinement for the growth of the nanocrystals, nanocomposites with different FeCo sizes can be obtained by choosing the appropriate host matrix.

This synthetic approach represents a method for producing magnetic nanocomposites in the form of thin films, which is desirable for perspective integration in technological devices: tuning the magnetic properties of the nanocrystals can be accomplished by selecting the mesopore size of the host mesoporous matrix and this, in turn, can be achieved by using a suitable templating agent.

## 3.5 Pore walls properties: mesoporous $SiO_2$-$GeO_2$ films

We have shown that mesoporous ordered films are a promising category of functional materials for applications in high-technology, such as photonics, sensing, and electronics. This is due to the high specific surface area, pore size that can be tailored in the nanometre range, and possibility to incorporate functional groups or immobilizing active molecules in the mesopores or in the inorganic network. In addition, it is also possible to exploit the physical and chemical properties given by the mesoporous pore walls. Ordered porous titania films, for example, are a very efficient materials to produce electrodes for solar cells because of the peculiar crystallinity (crystal phase, size and texture) which can be induced in the pore walls.[90] Most part of research in the field of mesoporous films has been devoted to silica and titania because of the broad range of applications and because they serve as models to understand the physicochemical phenomena occurring during self-assembly, but other compositions (transition metal oxides, mixed oxides, phosphates, etc.) are also possible. In particular, in this section we report on the functional properties of $SiO_2$-$GeO_2$ mesoporous film. Silica-germania glasses are very important for applications in photonics because they can be processed by UV-light in order to produce Bragg grating fibres[91,92] or optical waveguides with a large second order non-linearity.[93,94] Silica-germania films, in fact, exhibit photoactive properties[95,96] because their divalent $Ge^{2+}$ centres can be photo-

bleached and oxidized to tetravalent $Ge^{4+}$ centres, causing a local densification of the inorganic network, thus increasing the refractive index (typically on the order of $10^{-4}$-$10^{-5}$). In addition, the low phononic energy of germania-based glasses can be used to obtain low-loss optical waveguides and amplifiers in thin silica-germania films.[97]

Sol-gel processing represents an important method to fabricate silica-germania films and several examples have been reported.[98,99] The synthesis is not simple; the high reactivity of germanium precursors needs to be adjusted to that of silicon alkoxides to avoid phase separation.[100] $SiO_2$-$GeO_2$ sol-gel films can be produced as pure oxides or hybrid organic-inorganic films,[101,102] but the film processing has to face several severe problems in order to be used in photonics. The homogeneity of the material and the amount of hydroxyl species has to be carefully evaluated in the case of photonic applications. On one hand, a high temperature is necessary to condensate the oxide structure and to reduce the hydroxyl content; on the other hand, at around 600 °C, germanium oxides crystallizes causing a decrease of oxygen vacancies and, therefore, a decrease of $Ge^{2+}$ centres.[103] Moreover, even if crystallization does not occur below 500 °C, Ge-OH species can be produced via diffusion of hydrogen atoms. A common method to increase the amount of defects[95] enhancing the photoactivity of $SiO_2$-$GeO_2$ materials, is to perform a thermal treatment at ≈ 500 °C in $H_2$ reducing atmosphere. Another parameter to carefully control is the mechanical stress induced in sol-gel films by thermal treatment and not completely released for temperatures around 500 °C:[103] in hybrid organic-inorganic materials, for instance, even low temperatures (between 100 and 300 °C) significantly decrease the concentration of defects.

Therefore, the possibility of producing $SiO_2$-$GeO_2$ films at low processing temperatures, with a small residual stress and a high content of $Ge^{2+}$ centres without using a specific reducing treatment, represents a challenging opportunity to explore. An interesting question is how the presence of a porous structure can affect the optical properties of a silica-germania material. The combination of photoactivity with a mesoporous structure could allow the fabrication of photonic devices with integrated functions and overcome the problems related to sol-gel films processing. In fact, due to the high porosity, the inorganic lattice could increase its density to a higher extent upon UV irradiation.[104] Furthermore, the amount of $Ge^{2+}$ centres is expected to be larger than in dense silica-germania films obtained by sol-gel because of the high specific surface area provided by the mesopores: the mesostructure, in fact, allows locating most of silica and germania units at the solid-air interface where the strain of the chemical bonds are most likely. By

changing the processing parameters of the mesoporous films, such as overall porosity, pore dimension and shape, and pore organization, we can expect to tune the optical properties. This is much more difficult to achieve in dense films; therefore, the presence of mesoporosity is expected to affect the final property of the material and the photoactive response of silica-germania films. Finally, such materials can also be suitable in the viewpoint of fundamental science, because these films are good candidates to investigate surface defects in porous matrix.

Mesoporous $SiO_2$-$GeO_2$ films have been prepared following the recipe described in Section 3.1, page 84. Hereafter samples with increased germanium content will be referred to as SG1, SG2, SG3, and SG4, indicating 0.1, 0.2, 0.3 and 0.4 $GeCl_4$ molar concentrations in the solution of precursors, respectively. Silica-germania films are generally difficult to prepare via the sol-gel processing due to the different hydrolysis and condensation rates of the Si and Ge precursors (chlorides or alkoxides).[100] As a consequence, phase separation may occur and homogeneity is rarely attained;[105] the synthesis is even more complex in the case of $SiO_2$-$GeO_2$ self-assembled mesostructured films because, at the end of the process, ordered porosity must be achieved. We have observed that RH is a very critical parameter, and organization is not obtained when RH is higher than 25%; after dip-coating the films were colourless and transparent, but, after deposition, they quickly turned to white. To avoid this effect, the samples have been stabilized in the deposition room at low RH for a at least 10 minutes.

*- Characterization of the porous structure*

The mesostructure of silica-germania films has been analyzed by combining GISAXS with TEM. The films exhibit a good order with some differences as a function of the composition and temperature. GISAXS measurements have been performed at the European Synchrotron Radiation Facility (ESRF) in Grenoble, France, at the ID01 beamline. An incident X-ray energy of 8 keV ($\lambda$ = 1.54 nm) has been selected, and the glancing angle has been adjusted slightly above the critical angle (≈ 0.2°). The diffraction patterns have been collected with a two-dimensional CCD detector with a typical integration time of 800 ms. GISAXS patterns show well-defined spots even for the second order of diffraction, indicating that the mesostructure has a high degree of order upon thermal treatment at 100 °C (**Figure 3.45**). The GISAXS patterns have been indexed as body-centred tetragonal unit cells belonging to the $I\bar{4}/mmm$ symmetry group, in analogy with the structure of other hybrid mesoporous films obtained using the same

templating agent.[3] The structure is made by ordered mesoporous domains that are randomly oriented around the axis perpendicular to the substrate (*c* axis in the tetragonal system) as it is often the case in mesoporous materials.

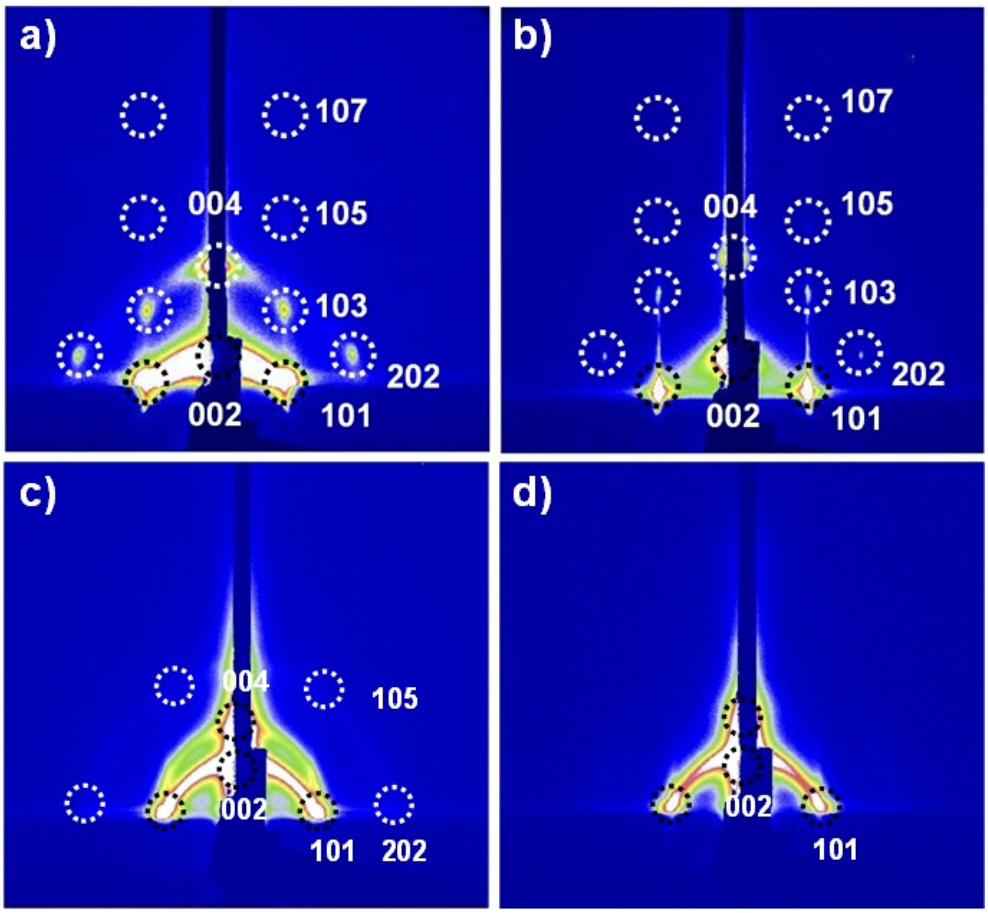


Fig. 3.45 Grazing incidence small-angle X-ray scattering patterns referring to samples SG1 (a), SG2 (b), SG3 (c) and SG4 (d) thermally treated at 100°C.

This is commonly referred to as planar disorder (i.e., the mesostructure has out-of-plane order but lacks in-plane order). The films containing lower Ge content (SG1 and SG2) yielded GISAXS patterns with well defined spots, showing a high degree of order. The cell parameters have been calculated by minimizing an error function defined using the experimental and the theoretical spot positions, following a procedure already reported in literature.[3] In **Table 3.2** are listed the calculated cell parameters as well as the percentage contraction of the out-of-plane *c* parameter for the samples obtained for different Si and Ge compositions, after treatment at 100, 350 and 550 °C.

| Sample | Cell parameters (nm) at 100°C | Cell parameters (nm) at 350°C | Cell parameters (nm) at 550°C |
|---|---|---|---|
| SG1 | $a$ = 18<br>$c$ = 16 | $a$ = 15<br>$c$ = 11 | $a$ = 14<br>$c$ = 9 |
| SG2 | $a$ = 18<br>$c$ = 15 | $a$ = 16<br>$c$ = 10 | N/A |

Table 3.2 Cell parameters of the silica-germania mesoporous films obtained for different [Ge] / [Si] molar ratios, treated at 100, 350, and 550 °C.

The full set of GISAXS patterns of the samples SG1 and SG2 as a function of the thermal treatment is reported in **Figure 3.46**. Samples SG1 and SG2 treated at 350 °C show a contraction of the *c* parameter, while *a* parameter is substantially unaltered within the experimental error, which can be estimated as ± 2 nm. Samples SG3 and SG4 give striped GISAXS patterns when treated at 350 °C; therefore, it is not possible to estimate the cell parameter values, as the error affecting the calculations is too large. GISAXS patterns of films treated at temperatures higher than 350 °C showed a partial or complete loss of order.

Cross-sectional TEM measurements showed a well-ordered porous structure in sample SG1 thermally treated at 550 °C (**Figure 3.47a**). Transmission electron microscopy characterization has been performed with a field-emission gun FEI TECNAI F20 SuperTwin FEG-(S)TEM microscope operating at 200 kV equipped with an EDAX energy dispersive X-ray spectrometer (EDS). The samples have been prepared as cross-sections cutting the mesoporous films along two perpendicular directions with respect to the Si substrate. The ordered porosity of the films has been investigated by acquiring TEM images in scanning mode (STEM) in which a small electron probe (about 1 nm FWHM) has been rastered over the sample. Sample SG2, with respect to SG1, appeared less ordered, even for lower temperatures of annealing (350 °C, **Figure 3.47b**): in the latter case the regions close to the film-air and film-substrate interfaces were more ordered, whereas the central region has been found to be highly porous but with a wormlike structure. This is an indication that the formation of ordered micellar arrays is nucleated at the interfaces of the film during EISA. Pore morphology is ellipsoidal with the minor axis oriented perpendicular to the substrate; this is because structural shrinkage occurred during drying and calcination. Film thickness has been estimated by TEM measurements as 209 ± 3 nm for SG1 sample and 181 ± 3 nm for SG2 sample.

Film thickness has been also measured by spectroscopic ellipsometry using a α-SE Wollam instrument and assuming a Cauchy model for the samples (Cauchy dispersion relation, see note page 136).

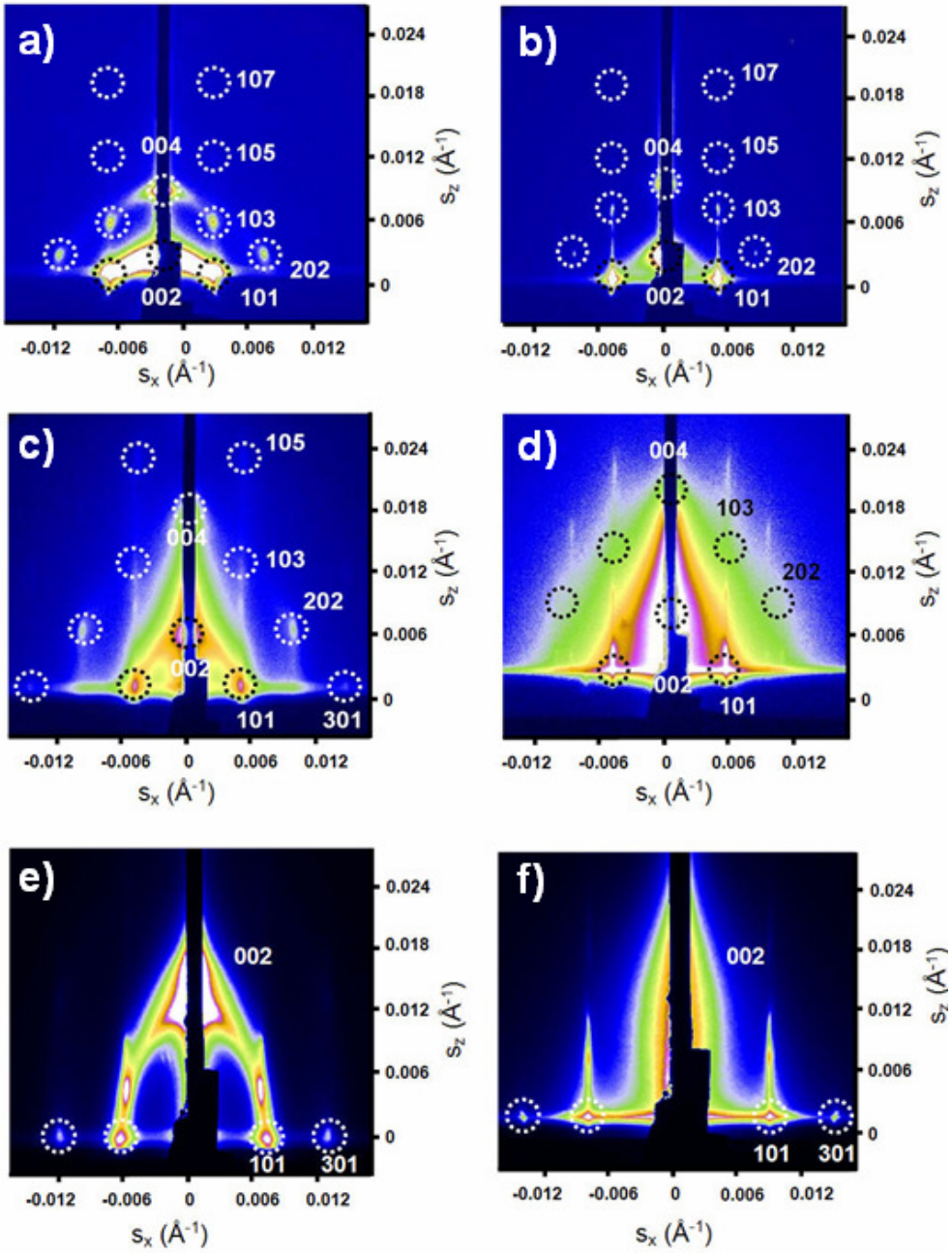


Fig. 3.46 GISAXS patterns referring to sample SG1, treated at 100 (a), 350 (c) and 550 °C (e). Sample SG2, treated at 100 (b), 350 (d) and 550 °C (f).

The thicknesses estimations are well in accordance with the TEM values; for the films treated at 350 °C, we calculated 208 ± 8 (SG1), 206 ± 6 (SG2), 198 ± 8 (SG3), and 172 ± 6 nm (SG4) respectively. In the SG1 sample treated at 350 °C, the pore dimensions

measured from the TEM images are 9.0 ± 1.0 nm along the major axis $a_1$, parallel to the surface, and nm 5.0 ± 1.0 nm along the minor axis $a_2$, perpendicular to the substrate. In the SG2 sample treated at 350 °C, the pore dimensions are $a_1$ = 2.5 ± 0.8 nm and $a_2$ = 2.0 ± 0.9 nm.

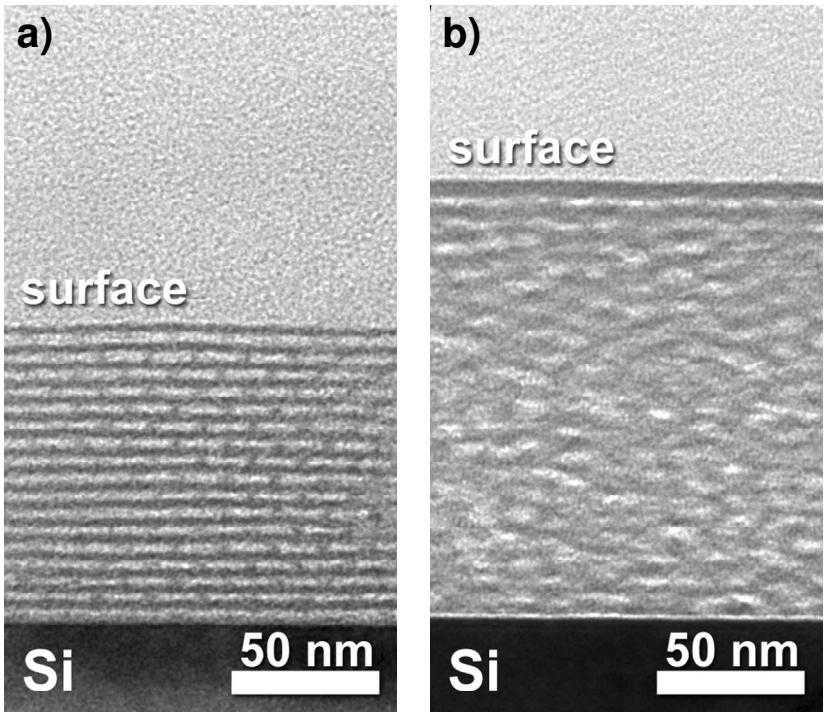


Fig. 3.47 Bright-field cross-section TEM images referring to sample SG1, thermally treated at 550 °C (a) and to SG2, thermally treated at 350 °C (b).

X-ray photoelectron spectroscopy (XPS) has been performed at Kyoto University thanks to a collaboration with Prof. Masahide Takahashi group. The chemical analysis of the mesoporous silica-germania films has been carried out by using an ULVAC-PHI 5500 X-ray photoelectron spectrometer with Mg Kα radiation operated at 15 kV and 20 mA. **Figure 3.48** shows the wide scan XPS spectra of sample SG1 treated at 350 °C. In particular, the Si 2p and Ge 3d XPS peaks have been used to estimate the atomic concentration, obtaining an average composition of [Ge] : [Si] = 13 : 87. The chemical composition has been found to be close to the nominal composition, indicating that the final material is not phase-separated along the film thickness; similar results have been obtained for the other compositions.

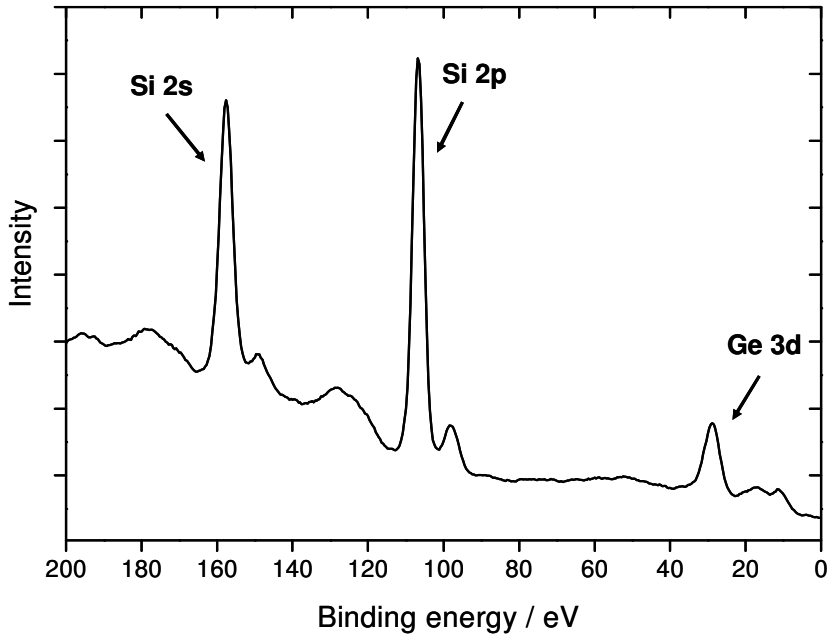


Fig. 3.48 XPS scan of the SG1 sample treated at 350 °C in the 200 - 0 eV range.

We have also used FTIR analysis to study the structure of the mesoporous silica-germania films at the different compositions. Fourier transform infrared spectroscopy (FTIR) has been performed with a Nicolet Nexus FTIR spectrometer equipped with a DTGS detector and a KBr beamsplitter, in the 4000 - 400 $cm^{-1}$ range. The spectra have been recorded in transmission mode on films deposited on Si wafers and the background has been recorded using a Si substrate. Each acquisition is the average of 256 scans collected with a resolution of 4 $cm^{-1}$. FTIR spectroscopy can give information on the presence and nature of surface hydroxyl groups in the material. **Figure 3.49a** shows the FTIR absorption spectra in the 1280-870 $cm^{-1}$ range of the films after treatment at 350 °C. The surfactant is almost completely removed, as we deduce from the absence of any related absorption mode; the silica antisymmetric stretching mode at 1075 $cm^{-1}$ indicates the formation of a highly interconnected silica backbone[23] and the band at 970 $cm^{-1}$ is attributed to Ge-O-Ge antisymmetric stretching.[102,106] We do not detect the presence the Si-OH and Ge-OH bands,[23] which should be present around 930 (Si-OH stretching) and 750 $cm^{-1}$ (not shown in figure: Ge-OH stretching); this is an indication of the good condensation degree reached by the inorganic silica-germania backbone upon thermal calcination. **Figure 3.49b** shows the infrared spectra in the 3800-2800 $cm^{-1}$ interval which is in the range of the stretching modes of O-H groups.

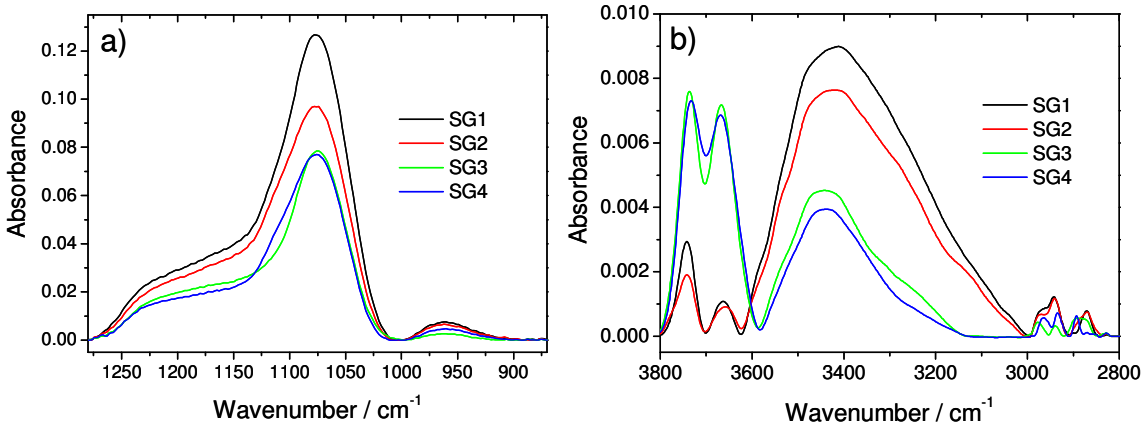


Fig. 3.49 Fourier-transform infrared spectra of the silica-germania films treated at 350 °C in the 1280–870 $cm^{-1}$ (a) and 3800–2800 $cm^{-1}$ (b) range.

The weak intensity of these bands indicates that most of the hydroxyls have been condensed during calcination. However, the low intensity bands detected in this range give information on the nature of the pore surface after thermal treatment, and in general, single and geminal silanols bands (see Section 3.3) can be observed. The FTIR spectra show three vibrational modes which change in intensity with the composition at 3670, 3737, and around 3450 $cm^{-1}$. The 3670 $cm^{-1}$ band is assigned to OH stretching of Si-OH with a contribution from antisymmetric stretching of hydrogen bonded molecular water ($\lambda_{as}(H_2O)$).[24] We attribute the 3737 $cm^{-1}$ band to isolated silanols[27] and the band around 3450 $cm^{-1}$ to OH stretching of silanols that are hydrogen bonded to the oxygen of neighbouring silanols ($\lambda_s(OH^{\cdot\cdot\cdot H}OSi)$). The FTIR data suggest that higher concentrations of germania induce a higher silanol condensation because the 3450 $cm^{-1}$ band shifts to higher wavenumbers (which indicates the presence of shorter silanols chains) while the band of isolated silanols increase in intensity. FTIR spectra of **Figure 3.49b** give also a good indication of surfactant removal upon thermal treatment at 350 °C: the C-H stretching bands around 2700 $cm^{-1}$, which are the typical signature of the surfactant, almost disappear.

*- Luminescence and photoactive properties*

The UV-Vis absorption spectra have been performed in transmission mode on films deposited on fused silica substrates. Absorption spectra have been measured in 190-310 nm wavelength (6.5 – 4 eV) range using a UV-Vis Nicolet Evolution 300

spectrophotometer, at 500 nm·min$^{-1}$ scan rate. Each acquisition is the average of 3 different scans collected with a bandwidth of 1.5 nm. The samples with different compositions, after thermal treatment at 350 °C (**Figure 3.50a**), showed a band around 5 eV, which has been associated with Ge oxygen-deficient centres (GeODC), responsible for photorefractive effects upon irradiation with high power UV source.[107]

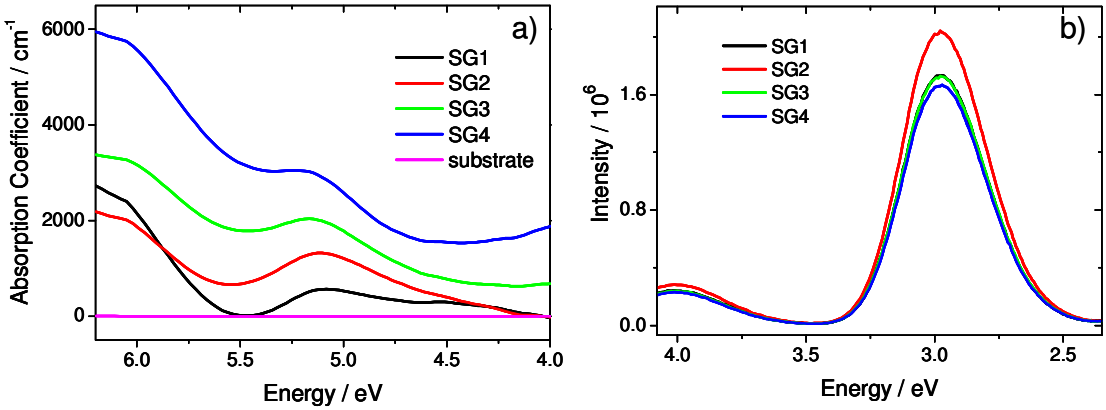


Fig. 3.50 UV-Vis absorption (a) and photoluminescence spectra (b) of mesoporous silica-germania films with four different Si and Ge concentrations treated at 350 °C.

These defects mainly consist of twofold coordinated, sp$^2$-hybridized, Ge$^{2+}$ centres with a lone pair of electrons.[108] Upon UV irradiation, one of these electrons is at first excited to the conduction band, forming a positively charged Ge centre, and then transferred to an adjacent tetravalent Ge. Two paramagnetic Ge *E′* centres are eventually formed as a result of an electron-hole recombination: this process gives rise to a change in refractive index, due to structural rearrangement and densification of the inorganic network. Therefore, the existence of the 5 eV band suggests the photoactivity of the films. The band around 5 eV can be observed in all mesoporous silica-germania samples obtained with different [Ge] / [Si] ratios, even though it is more intense in the samples with lower Ge content (SG1 and SG2). This result shows that there is not a linear dependence of the absorption coefficient on the Ge concentration in mesoporous silica-germania films. By a comparison with the films structural characterization, we can correlate this property with a lower order of the films at higher Ge content (**Figure 3.45**) and a different nature of the pore surface (**Figure 3.49**). The order of the mesophase and the [Ge] / [Si] ratio can affect the arrangement of Ge atoms and density of Ge$^{2+}$ and Ge$^{4+}$ species in the samples. This point needs a further specific study

because the understanding of the defects origin in mesoporous silica-germania films is of paramount interest to develop future applications.

**Figure 3.50b** shows the emission photoluminescence (PL) spectrum of the mesoporous silica-germania films with different compositions ($\lambda_{ex}$ = 245 nm). Intense emission bands at 3.02 eV, together with a less intense peak at 4.07 eV, have been observed when the excitation wavelength ranged from 200 to 300 nm. The band at 3.02 eV is attributed to the singlet-triplet emission (β-band) of the $Ge^{2+}$ centres, whereas the band at 4.07 eV is assigned to the singlet-singlet emission of the $Ge^{2+}$ centres ($\alpha$-band).[109,110] To elucidate the origin of the absorption band around 5 eV, the SG2 sample has been treated at different temperatures. The absorption spectra relative to the SG2 sample showed a decrease in intensity of the ≈ 5 eV band with higher temperatures (**Figure 3.51a**). This decrease can be explained by the oxidation of the oxygen-deficient $Ge^{2+}$ centres occurring at higher temperatures: the two-coordinated defects become four-coordinated Ge connected to bridging oxygens. The PL spectra of the SG2 sample treated at different temperatures are shown in **Figure 3.51b**. The decrease in intensity of the emitted PL shows that the thermal treatment decreases the concentration of GeODC in the film. This is consistent with an oxidation treatment, which causes the transformation of Ge(II) to Ge(IV).

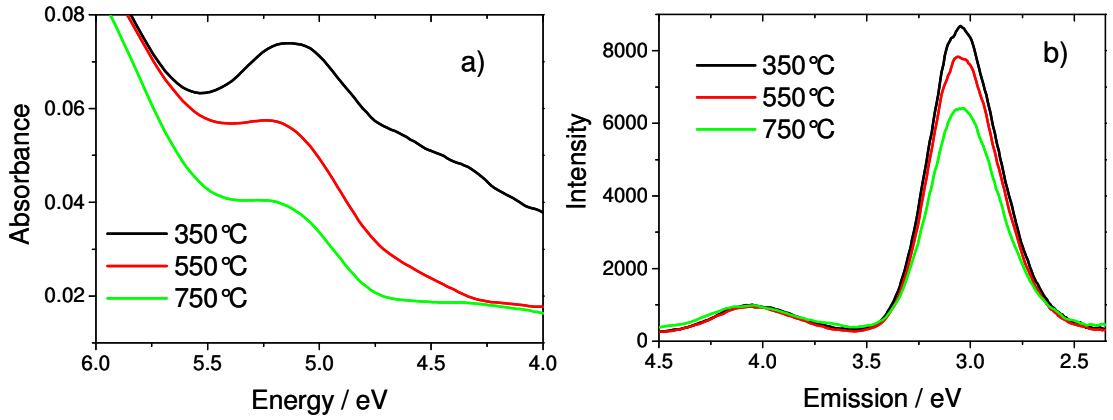


Fig. 3.51 UV-Vis absorption (a) and photoluminescence spectra (b) of mesoporous silica-germania SG2 film after thermal treatment at 350, 550, and 750 °C.

To demonstrate the possibility of producing photoactive silica-germania mesoporous thin films, preliminary experiments have been performed by irradiating the sample SG2 with a KrF excimer laser source (λ = 248 nm, 5.0 eV) having an irradiation power of ≈ 220 $mJ \cdot cm^{-2}$. **Figure 3.52** shows the absorbance spectra of the films before and after

irradiation. The decrease of the 5 eV absorbance peak can be observed; this is accompanied by an increase in the band around 6.3 eV, which is associated with photochemical conversion of divalent Ge defects to Ge *E'* or Si *E'*.

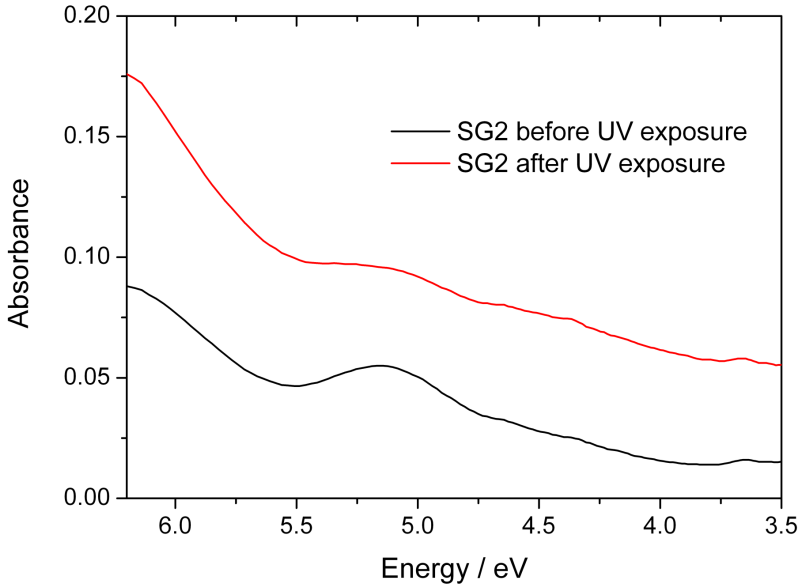


Fig. 3.52 UV-Vis absorption spectra of SG2 film before (black line) and after (red line) UV-laser exposure (λ = 248 nm).

To resume, in this section we have shown that mesoporous mixed silica-germania films can be used as photoactive optical materials thanks to their specific structure and pore walls chemical composition. GISAXS and TEM measurements pointed out that the porous ordered structure in the samples is tetragonal with a lattice constant on the order of 10 nm. The films with lower Ge have a high degree of order, which is retained even at 550 °C. The silica-germania films after calcinations at 350 °C have low amount of residual hydroxyls, which appear as isolated silanols and hydrogen bonded short hydroxyl chains. UV-Vis absorption and photoluminescence showed that the films possess divalent $Ge^{2+}$ centres, this defects can be used to "pattern" by UV the porous coating inducing local changing in the refractive index.

## 3.6 Self-assembled hierarchical materials

Controlling the self-assembly on multiple length scale is a natural evolution of EISA process and, nowadays, fabrication of complex nanoscale porous materials through co-assembly of inorganic and organic species is a current trend in chemistry and nanomaterials science. The importance of materials with different ranges of porosity is based on the expectation of a new generation of "smart" materials based on hierarchical systems, which should be able to play a specific function at every different pore scale. For this purpose an important issue is controlling the order and topology of the porosity; an ordered porosity is, in fact, a great advantage for applications where diffusion processes are involved.

In this section, we present three main approaches to modulate porosity into mesoporous films: direct templating by the addition of fluorinated nanobeads into the precursors solution; controlled swelling and/or phase separation by the use of a co-solvent and a co-templating agent; and nanocrystallization of inorganic salt during the self-assembly of the mesostructured films. All the three approaches allow a fine tuning of the porosity even tough each route gives peculiar properties to the final materials. The direct templating approach with nanosized polymer beads allows adding a highly hydrophobicity to the organosilica films; with the controlled swelling and/or phase separation route more than two types of porosity can be obtained in one step; finally, the nanocrystallization allows a selective opening and functionalization of the pores depending of their size and shape.

### 3.6.1 Mesopores and direct templating

To date, the rising interest of the scientific community to hierarchical systems has allowed to induce multirange porosity in a material with the possibility to select the pore dimensions from a few nanometers up to micrometers. In all the length scales, the larger pores should be connected through the smaller pores and the shape and the connection with the bigger pores has to be controlled,[111] in agreement with the definition of hierarchical porous architecture as "a 3D arrangement of well-defined pores of different sizes, the smaller ones being located in the walls between the larger pores, thereby also establishing the connectivity".[112]

Several examples of hierarchical porous materials have been reported so far, but if we focus the attention on thin films with at least one range of porosity showing an ordered structure, we do not find so many examples.[113,114] In the case of bulk or powdered materials, two kind of processes have been reported: the addition of a block copolymer and a small surfactant or co-solvent to the sol-gel solution;[115,116] the infiltration of sol-gel solution containing block copolymers in a pre-synthesized polymeric colloidal crystal structure.[117,118] In general, two main strategies can be envisaged, controlled phase separation or addition of surfactant templates of different dimensions to control the pores. Here a different approach to obtain hierarchical porous thin film is reported: the use of predefined nano-objects such as nanoparticles of controlled dimension as template for the pore of bigger dimensions. The main advantage of this strategy is the easy removal of the template without disrupting the host material.

We have used a self-assembled mesostructured hybrid organic-inorganic thin film as the matrix of the nanoparticles (the details of the synthesis are available in Section 3.1 page 84). The recipe has allowed us to introduce removable nano-objects into a mesoporous material, which gives, after thermal treatment at 350 °C, bimodal porous films. The optimization of a suitable nanoparticles solution has played a pivotal role to obtain monodisperse macroporosity without interferences to self-assembly on mesoscale. The nanoparticles colloidal solution (NCS) has developed in collaboration with CIVEN (Centro Interuniversitario Veneto per le Nanotecnologie) researchers. Evaporation-induced self-assembly has been used to obtain highly organized mesostructured films templated by block copolymers with an ordered mesophase in the 8-10 nm range and polymeric nanospheres to produce pores of around 50-60 nm within the mesostructured films.

*- SAXS and TEM characterization*

The introduction of the nanospheres, especially at high concentrations, could potentially interfere with self-assembly. We have, therefore, used SAXS analysis to study the mesophase formation in hybrid organic-inorganic films synthesized via EISA and the effect of nanospheres on self-organization. GISAXS characterization has been performed at the Austrian SAXS beamline at Elettra with an incident wavelength of 1.54 Å. A 2D detector has been used to acquire the scattering patterns: the acquisition procedure consisted is an average of 10 measures with integration time of 500 ms. **Figure 3.53a** shows a typical GISAXS pattern of a sample prepared with 3 $cm^3$ of NCS

and treated at 350 °C. The presence of well-defined spots is a clear indication of an ordered mesostructure within the hybrid film. The pattern can be assigned to a tetragonal symmetry (space group $I\bar{4}/mmm$) with the (100) plane oriented perpendicular to the substrate (**Figure 3.53b**), in accordance with previous findings.[19] This organization corresponds to an ordered stack of spherical pores with a body-centred tetragonal primitive cell. Comparing these results with those of hybrid MTES-TEOS mesoporous films, we can observe that the presence of NCS, even at high concentrations, does not affect the self-assembly: no appreciable variations in terms of degree of order or mesophase symmetry are detectable by changing the relative amount of NCS in hierarchical films.

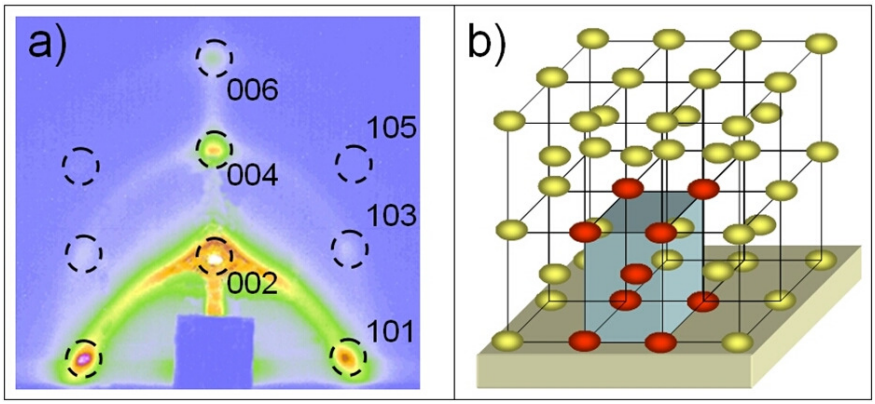


Figure 3.53 a) (a) GISAXS pattern of a hierarchical mesoporous hybrid film treated at 350 °C (3 $cm^3$ of NCS in the precursor sol). (b) Body-centred tetragonal porous structure image.

We have obtained a direct visualization of the film porous structure using transmission electron microscopy (TEM) in conventional and high-resolution mode. At first a JEOL 200C× microscope equipped with a tungsten cathode operating at 200 kV has been used. Finely ground films scratched from the silicon substrate have been dispersed in *n*-octane by sonication, and then have been dropped on a carbon-coated copper grid and dried for TEM observations. **Figure 3.54** shows the TEM image of a scratched fragment of the porous film after thermal treatment at 350 °C. The mesophase organization is well-preserved, even after calcination, and the nanoparticles are dispersed within the matrix. The hierarchical structure that appears from this image is shown in **Figure 3.54b** and is made from an ordered distribution of mesopores and a random distribution of pores of

larger dimensions (around 60 nm) produced by the thermal removal of the polymeric nanoparticles.

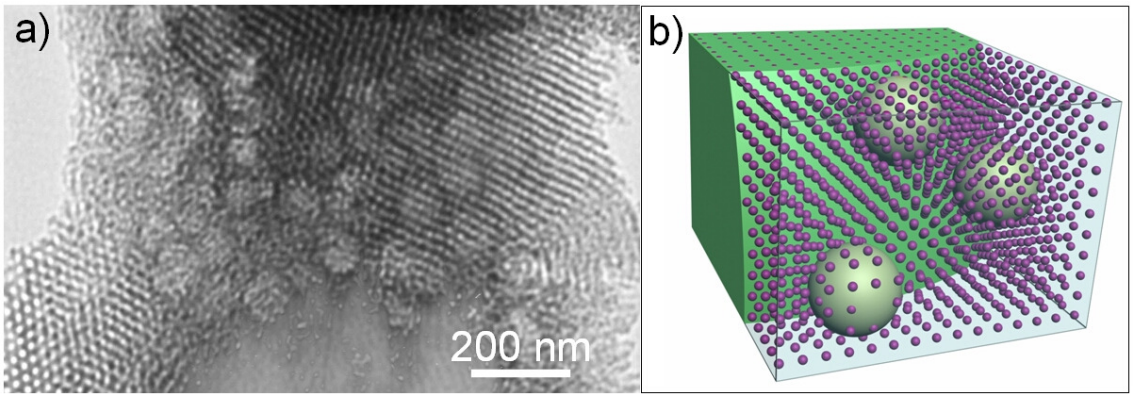


Figure 3.54 Bright-field TEM image of a hierarchical porous thin film treated at 350 °C (a) and a representative picture of the hierarchical structure (b).

To have a more precise characterization of the porous structure, we have then used high-resolution transmission electron microscopy obtained by a JEOL 2100F microscope equipped with a field emission electron gun and operating at 200 kV. The samples have been prepared for cross-section or planar view analysis: two small plates have been obtained by cutting the sample at a fixed height of the substrate. A roughly mechanical polishing procedure has been carried out on all the samples to achieve around 50 μm in thickness: in the direction parallel to the substrate cut, for the cross-section sample, and in the direction perpendicular to the substrate cut, for the planar view sample. Final thinning to ensure electron transparency has been achieved by precision ion milling with a JEOL Ion Slicer. **Figure 3.55a and b** shows a HRTEM cross-section image of the film at 350 °C; a planar section of the same sample is shown in **Figure 3.55c and d**. A bimodal pore distribution is clearly detected from both cross and planar sections; the film is characterized by an ordered lattice of 9 nm pores and a random distribution of 60 nm pores. The HRTEM figures show an apparent coalescence of close pores, which is however due to the artefact of TEM images that merge a three-dimensional structure in a plane. The different grey scale of the larger pores indicates that they are spatially separated. The mesopores are highly ordered within a range of some micrometers; the cross section shows that the film maintains a well-ordered structure along all the directions normal to the substrate (**Figure 3.55a**). The planar

view shows that the surface has domains of organized pores at micrometer scale (**Figure 3.55c**).

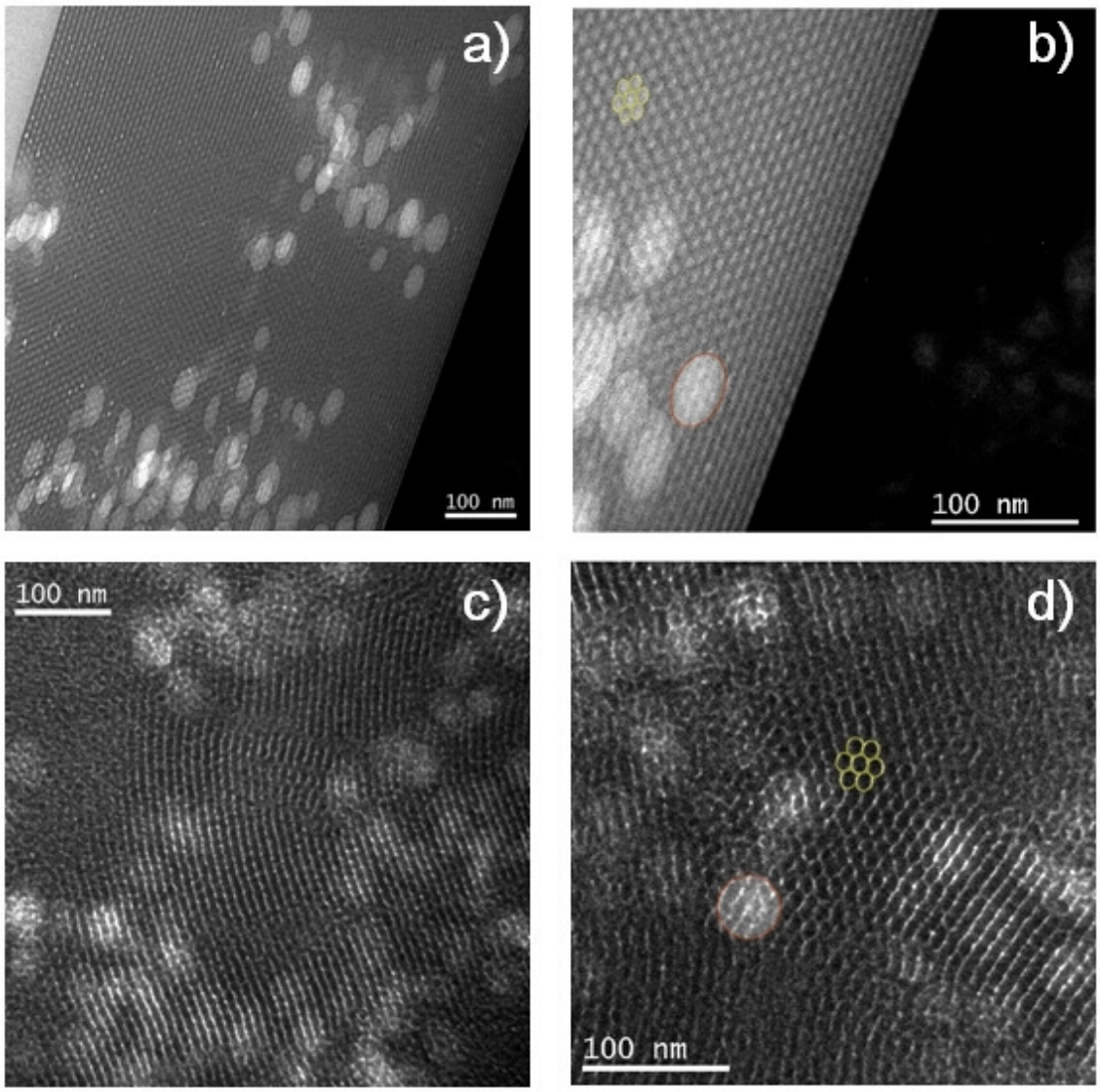


Figure 3.55 Bright-field cross-section (a and b) and dark-field planar view (c and d) HRTEM images of a hierarchical porous thin film treated at 350 °C. The macropores produced by the nanospheres appear as white spots in the images.

No effects induced by polymer nanoparticles on the ordered mesophase have been observed: in the range of composition investigated, NCS and the surfactant work separately. If we look at the pores in the planar section image, we can observe that they have a regular and circular shape (**Figure 3.55d**), whereas an elliptical shape is visible from the HRTEM cross-section image (**Figure 3.55b**). The pore dimensions have been calculated from the cross-section HRTEM images: along the direction parallel to the

substrate, the average size of pores templated by the nanoparticles is 55 ± 10.4 nm; along the direction perpendicular to the substrate, the average size is 26 ± 3.7 nm. We have also calculated the dimensions of mesopores: in this case the average size in the directions perpendicular and parallel to the substrate are 8.8 ± 0.9 and 4.8 ± 1.2 nm, respectively. Therefore, comparing the cross section to the planar view, we observe that the thermal calcination induces a shrinkage in the direction normal to the substrate; this affects the shape of smaller and bigger pores, producing an ellipsoidal shape.

The average ratio between the shorter axis (perpendicular to the substrate) and the longer axis (parallel to the substrate) of the different ranges of pores has been calculated by HRTEM; we have obtained a value of 0.47 for the larger pores and 0.54 for the smaller pores. This indicates that the thermal shrinkage of the films induces similar eccentricity on both the pore distributions. Besides, in the present case the thermal shrinkage produces a deformation of the pore shape with a contraction in the direction normal to the substrate without a change in the organization (see Paragraph 1.3.1), which maintains a tetragonal symmetry after calcination, in both the mesoporous and the hierarchical films.

*- Spectroscopic characterizations*

The SAXS and TEM analysis show that this single-step synthesis produces a bimodal pore distribution with 9 nm ordered pores of tetragonal symmetry and 60 nm randomly dispersed pores in the film. The fabrication of this bimodal hierarchical porous film has been achieved by removal of the templates, i.e. the micelles for mesopores and the nanoparticles for the macropores, by thermal treatment. We have, therefore, observed by FTIR analysis and spectroscopic ellipsometry the effect of the thermal calcination on composition and properties of the films. In particular, we have compared the data of 60 °C stabilized and 350 °C calcined samples to assess the removal of the templates. The infrared spectra have been recorded with a Nicolet Nexus instrument working in the 400-5000 $cm^{-1}$ range, by averaging 256 scans with 4 $cm^{-1}$ resolution; a silicon wafer has been used as substrate to measure the background. **Figure 3.56** show the FTIR spectra of mesoporous and hierarchical films, respectively, before (60 °C) and after thermal treatment (350 °C). We have taken the signal around 1700 $cm^{-1}$, which is assigned to carbonyl groups (C=O stretching), as a signature of the presence of the polymeric nanoparticles (**Figure 3.56b**);[119] the FTIR spectrum of the nanoparticles alone is reported as a reference (green line). The thermal treatment at 350 °C removes the

nanoparticles and the surfactant, as respectively shown by the disappearance of the signals at 1700 $cm^{-1}$ and at 2900 $cm^{-1}$ (the latter is due to the $CH_2$ stretching bands which indicate the presence of the block copolymers).[119]

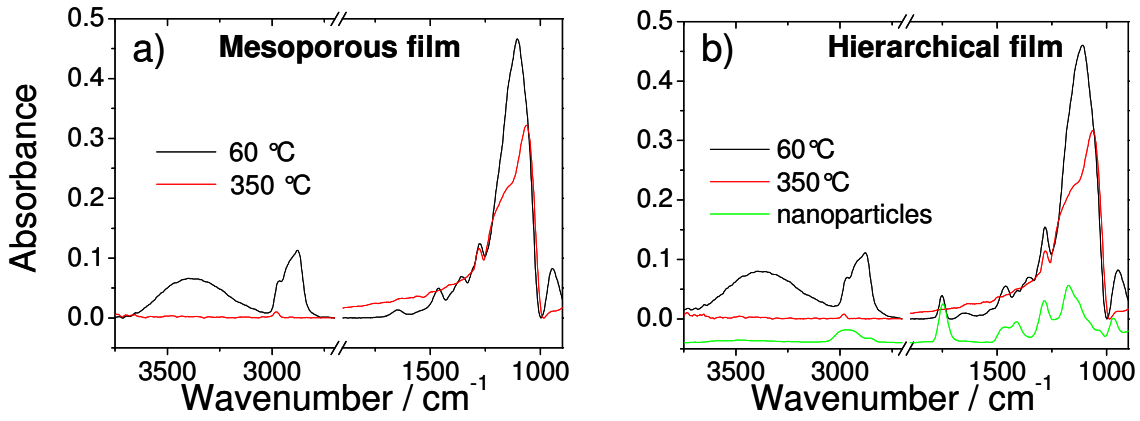


Figure 3.56 FTIR absorption spectra of mesoporous hybrid (a) and hierarchical porous film (b) after thermal treatment at 60 °C (black line) and 350 °C (red line). The reference spectrum of nanoparticles (green line) is shown in (b).

Another effect of the thermal treatment is the removal of silanols; in fact the wide OH stretching band around 3300 $cm^{-1}$ disappears.[23] Noteworthy, the methyl groups are still present in the films after calcination at 350 °C, as revealed by the band at 1276 $cm^{-1}$ attributed to $CH_3$ deformation; this is correlated with the absence of adsorbed molecular water.

Ellipsometric data have been obtained by a α-SE Wollam spectroscopic instrument working at room temperature. *n*, *k* have been calculated by 2.03 α-SE Wollam software by assuming a Bruggeman effective medium approximation layer (see note page 144) with two components (non absorbing Cauchy film and void) based on the assumption of transparent films[‡] on silicon. The quality of the fitting has been evaluated on the ground of the mean square error. The change in refractive index between the samples treated at 60 and 350 °C (**Figure 3.57**) reflects the thermal shrinkage and the removal of the organic components; after calcination, the hierarchical porous films have a lower refractive index that we attribute to a higher porosity. The refractive index values

[‡] The measurements have been done in the 390-900 nm ranges, in this interval the mesoporous and hierarchical films do not absorb.

measured at 632.8 nm are 1.14 and 1.17 for the hierarchical porous and monomodal mesoporous films, respectively.

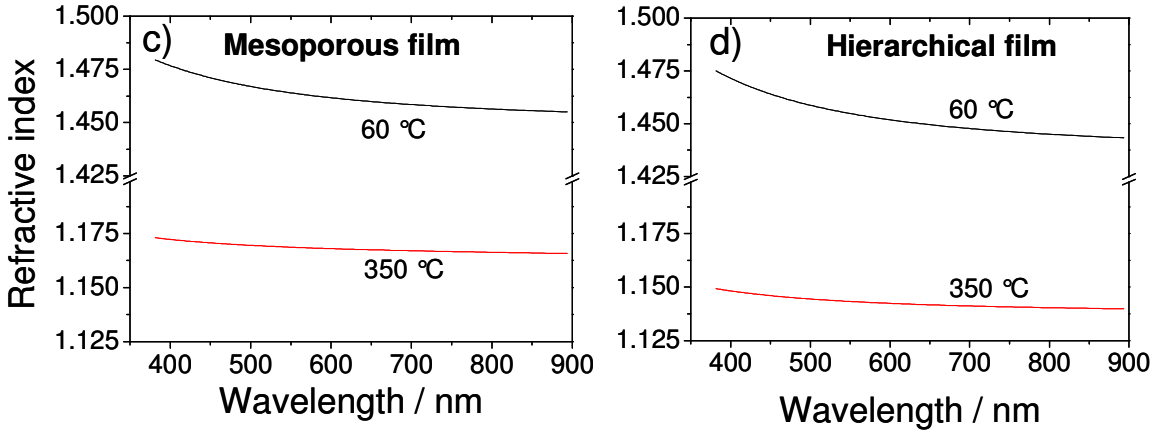


Figure 3.57 The refractive index as a function of the wavelength for a mesoporous film (c) and a hierarchical porous film (d) after thermal treatment at 60 °C (black line) and 350 °C (red line).

The thickness changes from 815 to 628 nm in the mesoporous film and from 1185 to 975 nm in the hierarchical film (6 $cm^3$ of NCS in the precursor sol). The residual porosity after the thermal calcination is still high, around 60% in volume for the mesoporous film and 69% in volume for the hierarchical sample (6 $cm^3$ of NCS in the precursor sol). The amount of nanoparticles affects the films properties; higher contents of nanoparticles increase the thickness and the residual porosity. **Figure 3.58** shows the film thickness as a function of NCS volume introduced in the precursors solution for films treated at 60 and 350 °C; the values have been calculated by the ellipsometric data. In the inset of **Figure 3.58** is shown the dependence of the porosity on the amount of nanoparticles for the films calcined at 350 °C. The properties of these mesoporous and hierarchical porous films after calcination appear particularly interesting; the presence of residual methyl groups upon calcination at 350 °C inhibits the adsorption of water from the external environment and they exhibit an ultralow refractive index, among the lowest values reported in the literature for silica-based porous materials.[73,120,121] For comparison, a value of $n$ = 1.18 in the 350-800 nm visible range and $n$ = 1.14 at $\lambda$ = 1300 nm has been reported for hierarchical porous silica films,[122] $n$ = 1.21-1.23 for silica mesoporous films prepared using an ionic surfactant[121] and 1.17 at $\lambda$ = 500 nm in the case of MTES-TEOS mesoporous films.[123] These results show that a lower

refractive index and a higher residual porosity can be obtained in hierarchical porous films, which have applications as ultralow $k$[124] and ultralow refractive index materials.[125]

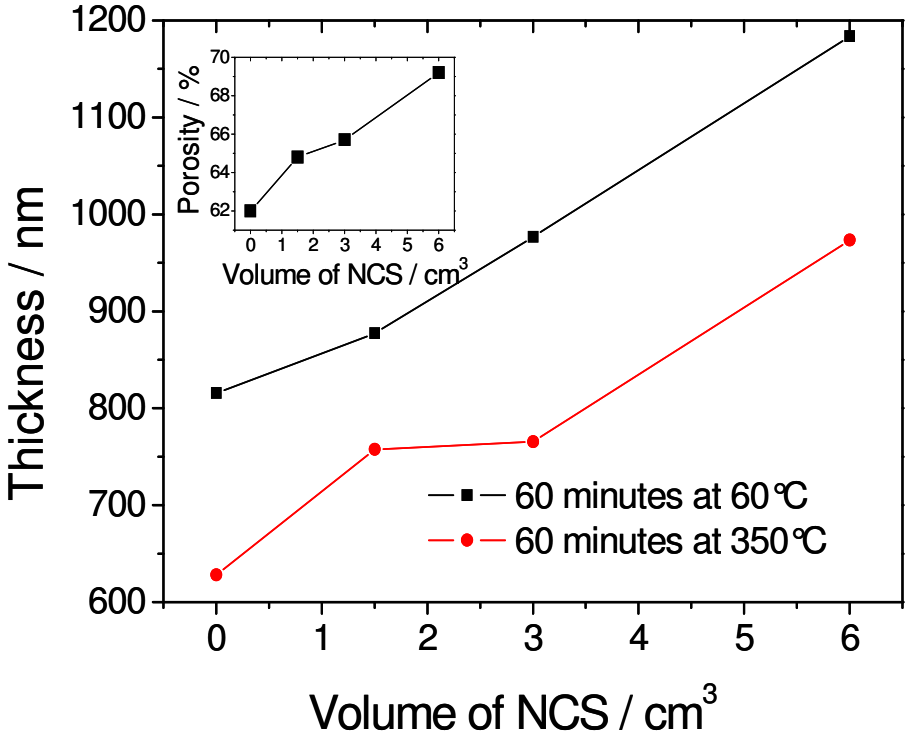


Figure 3.58 Variation of film thickness as a function of nanoparticles content in the precursors solution after thermal treatment at 60 °C (black line) and 350 °C (red line). In the inset is shown the dependence of the porosity on the nanoparticles content for hierarchical porous films treated at 350 °C.

To summarize the obtained results, we have shown that hierarchical mesoporous thin films can be obtained by using block-copolymer micelles and organic polymer nanoparticles of 70 nm as templates of pores of different dimensions. Evaporation-induced self-assembly has been used to prepare a mesoporous matrix for the nanoparticles that are entrapped and well-dispersed within the film. The introduction of the nanoparticles into the precursor solution does not affect the self-assembly process; a tetragonal mesostructure with $I\bar{4}/mmm$ symmetry is obtained in the films. A thermal treatment at 350 °C removes the organic template and the nanoparticles without cracking the films and leaving a bimodal porous hierarchical structure. Two ranges of well-defined porosities are produced: (1) mesoporosity due to the organic templating micelles with an average pore dimension of 9 nm (these pores are also well-ordered

following a tetragonal unit cell); a porosity in the 60 nm range, which is produced by the thermal removal of the polymeric nanoparticles (these pores are not ordered, but are well-dispersed within the mesoporous matrix). The process that we have developed allows obtaining hierarchical porous films with an ultralow refractive index combined with hydrophobicity.

### 3.6.2 Controlled phase-separation

Ordered mesoporous materials obtained by micelle templating have a monodisperse pore diameter which is generally restricted within the 2-10 nm range,[126] well below the 50 nm upper limit defined by IUPAC. Therefore, this "10 nm barrier" represents a severe limitation for developing novel applications of ordered mesoporous thin films, such as those in nanobiotechnology, for immobilization of biomolecules, large molecule analysis or sensing. This limitation triggers the need of new multipore materials produced by reproducible soft chemistry routes.[127] Although the EISA is a very flexible and well developed synthetic method, large pores (up to 50 nm) have only been obtained in ultrathin oxide films by using custom-designed polymer templates and very dilute precursors concentrations. In these conditions, template micelles seem to spread over the substrate and exhibit a higher range of open porosities; these pores can be better defined as craters in patterned monolayers[128] whose size can be controlled as a function of the molecular weight of the template.[129]

Hierarchical porous structures, presenting nested pores with different sizes and functions, are a natural evolution of advanced nanoporous materials.[130,111] The possibility of obtaining such hierarchical structures through one-pot assembly processes is a tempting challenge so far. Crossing the "10 nm barrier" in mesoporous self-assembled films, and obtaining at the same time an accurate control of the pore size, up to a hierarchical and multimodal pore distribution, represents an important breakthrough in the field. Previous reports of hierarchically porous films rely on a combination of techniques. Yang et al. demonstrated the possibility of producing three-length-scale templated oxide films (silica, niobia, or titania) by the combined use of micromolding, latex beads, and surfactant templating.[130] Macro-mesoscale templated films or gels can also be obtained by concurrent sol-gel transition and phase separation, which can be induced by the incorporation of supramolecular templates or polymers. In this case, macropores arise from phase separation, and small-size mesopores ( $\approx$ 2-3 nm) are

generated after the elimination of polymers strongly embedded into a sol-gel matrix.[131] The use of functional nanoparticles as inorganic precursors has been also reported; macro-mesoporous ceria can be generated by phase separation processes induced by the presence of a functional polymer.[132] More recently, the use of breath figures processing (high humidity conditions) in combination with functional nanobuilding blocks allowed the preparation a wide range of nanoparticle-based macro-mesoporous thin films.[133] In these two cases, mesopores are generated from the textural
porosity derived from interparticle spaces; therefore, the mesopore range is limited by the nanoparticle precursor size.

*- Films preparation and morphological characterization*

We have found a simple and reproducible one-pot synthesis to produce titania thin films with hierarchical porous structures, formed by nested meso- and macropores, with
diameters controllable in the 10-200 nm range. A fine tuning of the pore size can be attained through the control of the synthesis parameters. We have used a triblock copolymer template, Pluronic F127, combined with a pore enhancing agent, poly(propylene glycol) (PPG) to obtain monomodal or multimodal pore systems. Different precursor compounds have been selected on the basis of a specific design of the solution; we have used a low weight (MW ≈ 4000) simple polymer such as PPG as a molecule that swells the template micelles at lower concentrations or induces a phase separation at higher concentrations. Butanol (BuOH) has been used as a solvent to adequately dissolve PPG; Pluronic F127, besides being the templating agent during self-assembly, played also a fundamental role in increasing the solubility of PPG. This approach is simple and employs commercial, low budget, and easily removable templating agents. We have systematically changed the synthesis parameters, such as the relative amount of the templates, the content of water and tetrahydrofuran (THF) co-solvent, to modulate the pore size and pore distribution. The films have shown a high tuning in terms of their porosity properties; large mesopores or bimodal porous distribution can be obtained as a function of the synthesis parameters. These films can be easily deposited on silicon and glass substrates without cracking and maintaining a high optical transparency. Besides, titania films are useful for molecule or ion trapping, selective molecule detection, catalysis, photocatalysis, and dye-sensitized solar cells. Titania is also known to be stable in aqueous solutions, under conditions comparable to biological media, where mesoporous silica stability is limited.[134] This last feature is

important for applications in nanobiotechnology (microarrays, ultrasensitive detection, molecule imaging) or nanomedicine (controlled delivery, implants).

The film synthesis and the preparation of precursor sols containing the titania source is reported in Section 3.1, page 86. Hereafter the molar ratio between PPG and $TiCl_4$, and between Pluronic F127 and $TiCl_4$ will be referred to as *P* and *S* respectively. The percentage volume ratio between the volume of THF and the final volume of the solution will be also referred to as $V_{THF}$. The films have been deposited by dip-coating at low withdrawal rates that allows to produce crack-free thin films with excellent adhesion to substrates in a reproducible way. After deposition, ageing and thermal treatment, robust films with excellent adhesion to the substrate (i.e. they do not detach after peeling off Scotch tape at 90°) and well defined mesoporous structure have been obtained. The films are also crack-free and highly transparent, as shown by UV-Vis transmission spectra in **Figure 3.59.** Spectra have been recorded in the 300–900 nm range by using a with a Hewlett-Packard 8453 spectrophotometer from samples deposited on soda-lime glass slides.

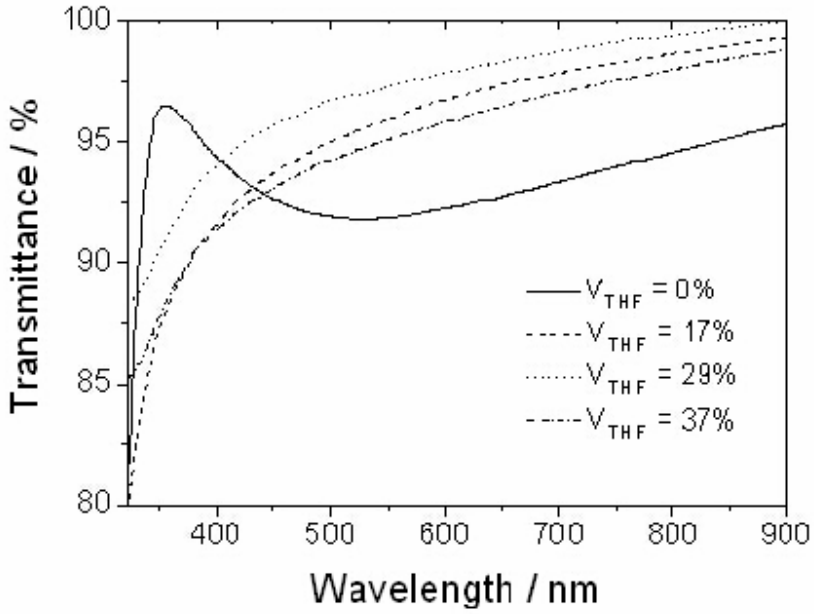


Figure 3.59 UV-Vis transmission spectra (300 – 900 nm range) of self-assembled hierarchical titania porous films deposited on silica glass slides. The samples have been prepared as a function of $V_{THF}$ maintaining constant the other synthesis parameters ($P = 6.25 \cdot 10^{-3}$, $S = 4 \cdot 10^{-3}$).

We have used Field Emission-Scanning Electron Microscopy (FE-SEM) to study the surface morphology of the samples; images have been taken with a ZEISS LEO 982

GEMINI FE-SEM in the secondary-electron mode, using an in-lens detector to improve resolution. **Figure 3.60a** shows a top-view of a film obtained from a butanol solution containing $TiCl_4$, water ($h$ = [$H_2O$] / [Ti] = 10) and Pluronic F127, with no addition of PPG or THF; under these conditions, similar to those reported for pure mesoporous titania films,[135] a homogeneous pore structure with a local hexagonal organization has been obtained.

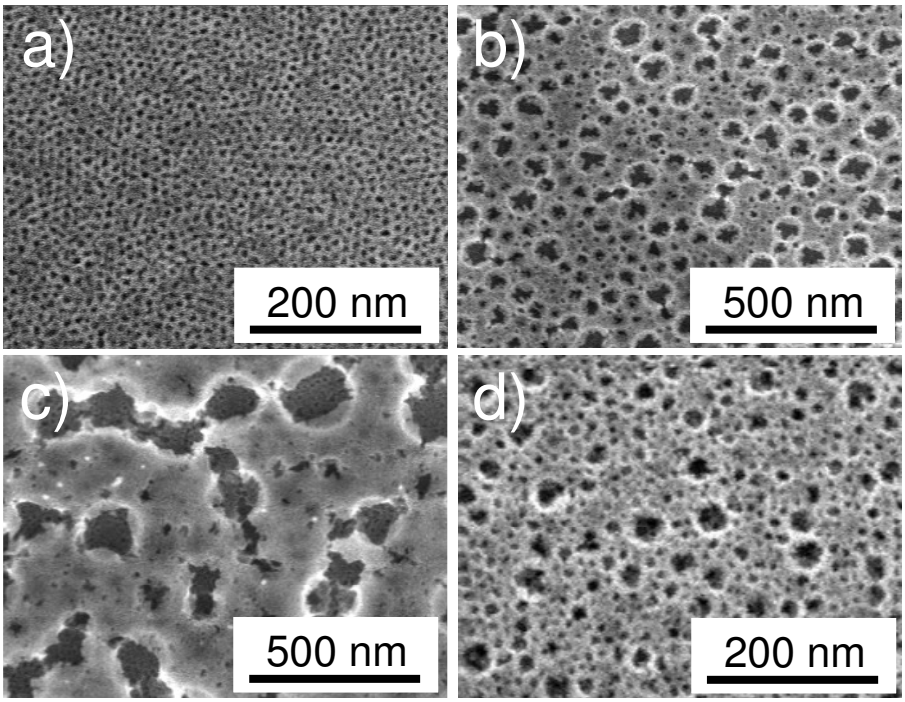


Figure 3.60 FE-SEM micrographs of typical self-assembled hierarchical titania porous films. The samples have been prepared starting from different precursors solutions: (a) $P$ = 0, $S$ = $4 \cdot 10^{-3}$, $V_{THF}$ = 0%; (b) $P$ = $1.5 \cdot 10^{-2}$, $S$ = $4 \cdot 10^{-3}$, $V_{THF}$ = 29%; (c) $P$ = $1.5 \cdot 10^{-2}$, $S$ = $4 \cdot 10^{-3}$, $V_{THF}$ = 0%; (d) $P$ = $1.5 \cdot 10^{-2}$, $S$ = $4 \cdot 10^{-3}$, $V_{THF}$ = 37%.

Addition of PPG and THF to the same precursors solution results in the appearance of a bimodal distribution of pores. A population of smaller pores with diameters centred at 15 nm and larger pores with an average diameter of 90 nm have been observed (**Figure 3.60b**). Higher concentrations of PPG in the absence of THF produce even larger pores (150-200 nm diameter, **Figure 3.60c**) that coexist with smaller mesopores and tend towards coalescence.

As a general trend, the addition of THF to the latter system allows to control the pore size distribution and dimension. When this co-solvent has been added, two populations

of well-defined pores with diameters 15 and 35 nm have been obtained (**Figure 3.60d**). A preliminary observation of these systems suggested that the presence of two different pore populations could be due to two different processes taking place concurrently upon film formation and processing: mesoscale templating and phase separation.

By changing the external synthesis parameters, we have been able to control pore sizes and distribution: the average pore size has been estimated by processing FE-SEM micrographs with a software for image analysis (Image J[136]). **Figure 3.61** shows the dramatic effect of the THF amount added to the precursor solution on the film porosity for PPG-containing systems. We have prepared the samples with fixed contents of F127 and PPG ($P = 6.25 \cdot 10^{-3}$, $S = 4 \cdot 10^{-3}$) and variable amount of THF. In this case, in the absence of THF, a bimodal pore distribution is reproducibly obtained throughout the samples. **Figure 3.61a and b** show a small pore population with centre-to-centre interpore distance ($d_{ip}$) peaking at 15 nm and a well-defined fraction of larger mesopores with 38 nm average diameter. The larger pores are evident on the film surface, and the lower dimension mesopores decorate the walls. For larger $V_{THF}$ values (**Figure 3.61c-f**), a continuous change in the pore system morphology has been observed, and both pore distributions partially overlapped, attaining closer diameter values. In the extreme of $V_{THF} = 37\%$, a large distribution of mesopores, with average diameter centred at 20 nm has been obtained (**Figure 3.61g and h**).

The films porous structure has been analyzed by SAXS in collaboration with Dr. Galo Soler-Illia research groups at the at the D11A-SAXS2 line of LNLS synchrotron (Campinas, Brazil). SAXS patterns have been collected on glass-cover supported films using a wavelength of $\lambda = 1.608$ Å at normal (90°) and glancing (3°) incidence with different integration time. 2D-SAXS patterns present rings at 90° incidence on glass cover supported films; the well-defined signals are indicative of pore order at the mesoscale. **Figure 3.62** shows the radial integrated intensity of 90° incidence SAXS data of the same series of films shown in **Figure 3.61**; the pattern of a titania film without PPG and THF is reported as a reference. SAXS results indicate that a higher amount of THF in the precursor solution results in lower scattering and a shift of the scattering angle to lower $q$ values, reflecting a higher average $d_{ip}$.

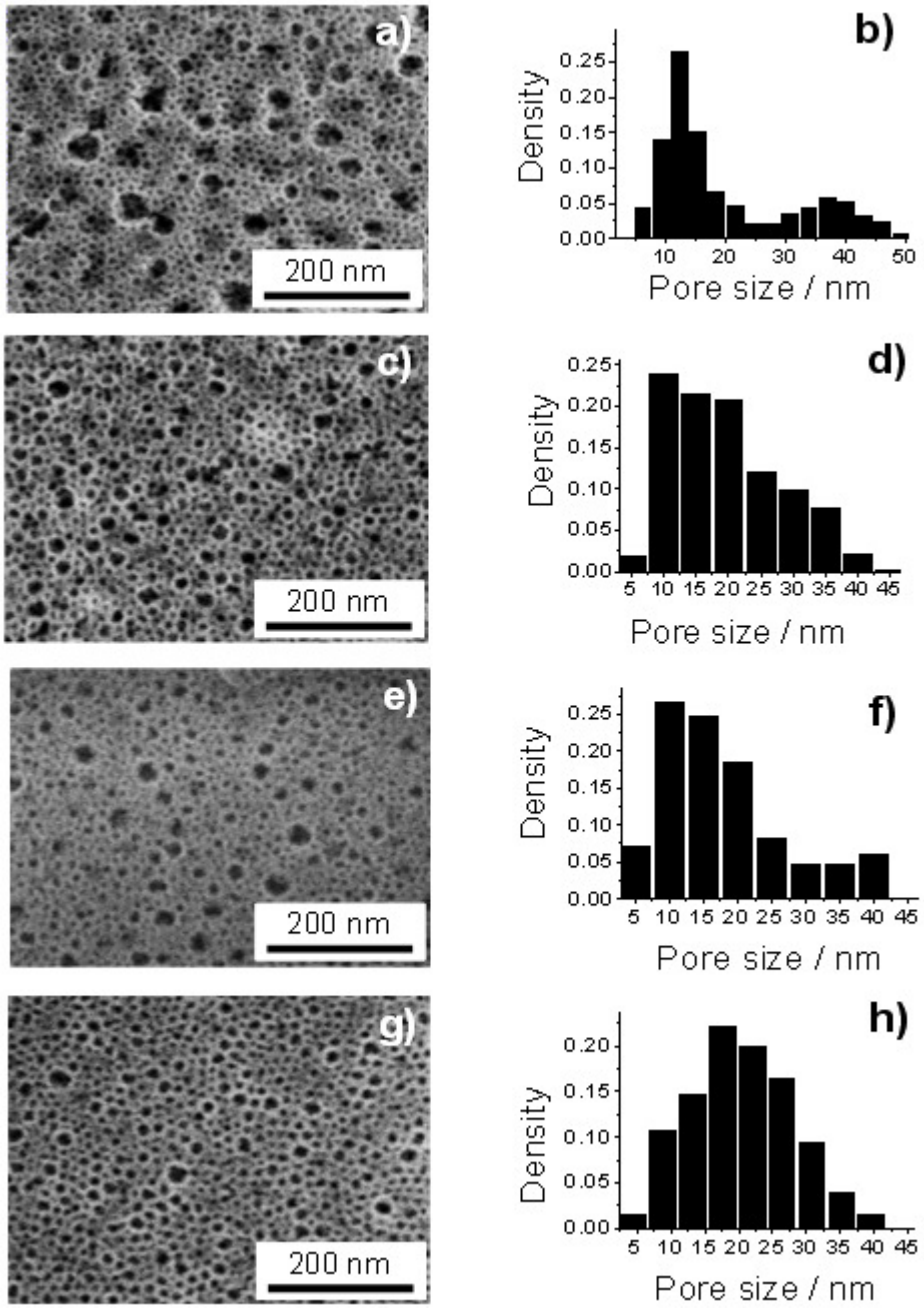


Figure 3.61 FE-SEM micrographs and relative pore size distributions of samples prepared as a function of $V_{THF}$ maintaining constant the other synthesis parameters ($P$ = 6.25·10$^{-3}$, $S$ = 4·10$^{-3}$): (a) $V_{THF}$ = 0%; (c) $V_{THF}$ = 17%; (e) $V_{THF}$ = 29%; (g) $V_{THF}$ = 37%.

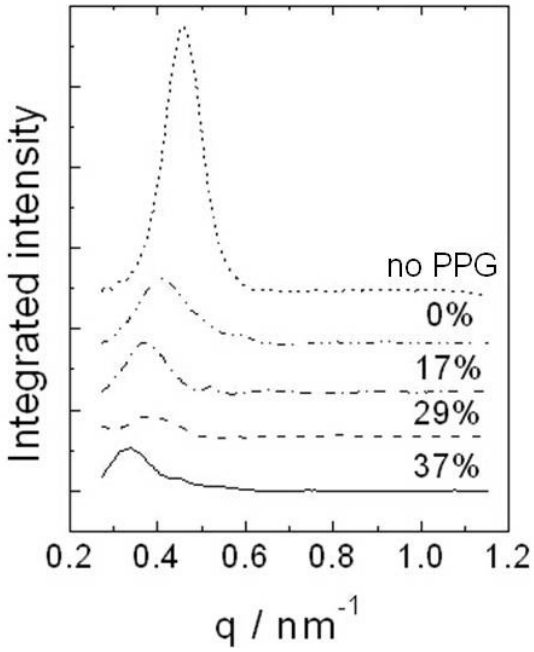


Figure 3.62 Radial integrated intensity of SAXS patterns at normal incidence as a function of $V_{THF}$. The data are referred to the same series of Figure 3.61.

The values obtained from SAXS correspond to $d_{ip}$; an excellent agreement is found between the $d_{ip}$ values calculated by SAXS and those obtained by FE-SEM image analysis of the smaller pores.[‡] Patterns collected at 3° incidence show only weak signals because of the low quantity of matter, the patterns are indicative of local pore organization (not shown); the scattering intensity of the SAXS patterns decreases in intensity with the increase of $V_{THF}$.

Film thickness of hierarchical titania samples have been also measured by α-SE Wollam instrument and assuming a Cauchy model for the samples (Cauchy dispersion relation, see note page 136). Film thickness estimated at λ = 632.8 nm by ellipsometry decreases with increasing $V_{THF}$, as shown in **Figure 3.63**. The smaller quantity of matter deposited with increasing dilution explains the observed trend in X-ray scattering intensity of **Figure 3.62**. The size of the large pore population has been found to be dependent on $V_{THF}$; this feature, in combination with the SAXS analysis of the smaller pores, suggests

[‡] It is important to note that under our SAXS conditions (camera length 584 mm), any periodic feature larger that 25 nm cannot be detected, for it falls inside the beam stopper.

that the interplay of PPG and THF is a determinant in the solubility of PPG in the micelles, which seems to be crucial for pore size control (see below).

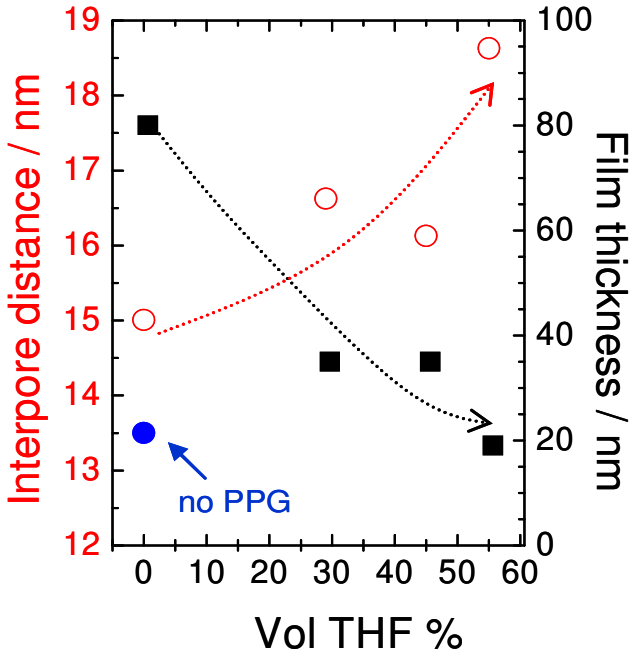


Figure 3.63 Interpore distance estimated by SAXS (red hollow circles) and film thickness estimated by ellipsometry (black squares) as a function of $V_{THF}$. The data are referred to the same series of Figure 3.61. The blue dot value corresponds to the reference sample shown in Figure 3.60a.The dotted arrows are a guide for the eye.

**Figure 3.64** shows the effect of increasing PPG quantities for systems with a constant $V_{THF}$ = 29%: no large mesopores have been observed in the absence of the pore enhancing agent (**Figure 3.64a and b**). Addition of small amounts of PPG ($P$ = 6.25·$10^{-3}$) increases the size of the smaller mesopores and the interpore distance (from 13.5 to 15 nm) according to FE-SEM and SAXS data. Furthermore, a population of large pores of 30 - 40 nm diameter appears in these conditions (**Figure 3.64c and d**). For higher PPG added quantities, the diameter of the small mesopore population remains around 16 nm, almost reaching a plateau. On the other hand, the average diameter of the large pore population increases in a sustained way, to about 100 nm (**Figure 3.64e and f**), and to more than 200 nm for higher PPG concentrations (not shown). In some cases, a third population of pores is observed, producing complex "flower-like" patterns such as those shown in the **Figure 3.65**.

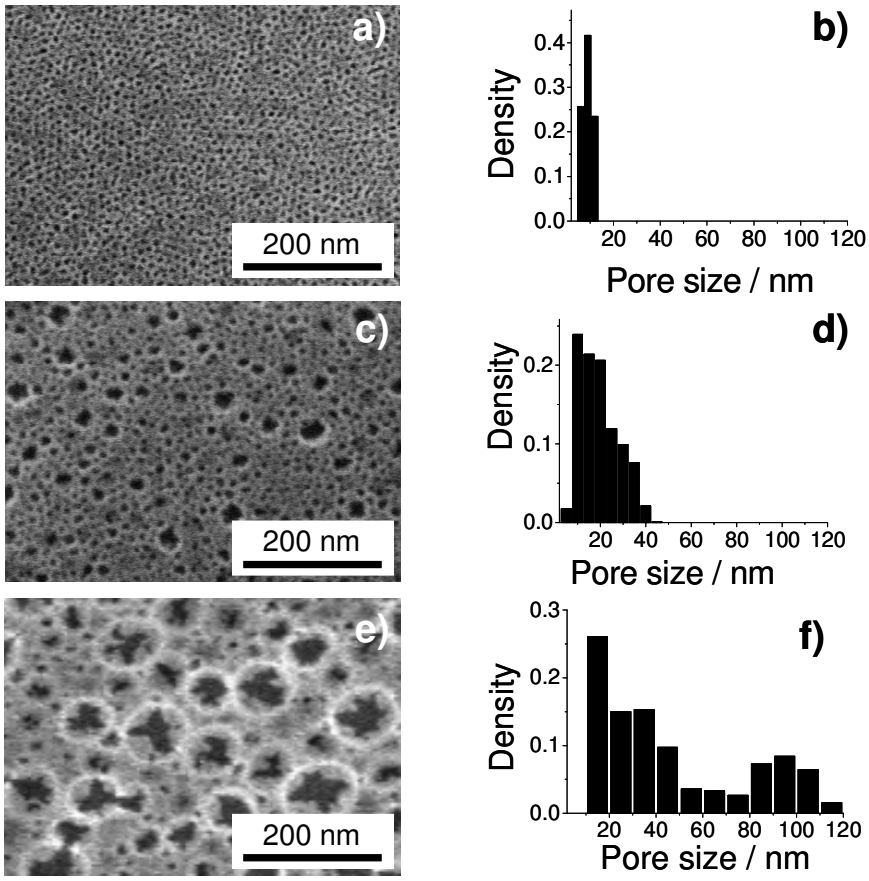


Figure 3.64 FE-SEM micrographs and relative pore size distributions of samples prepared as a function of *P* maintaining constant the other synthesis parameters ($S = 4 \cdot 10^{-3}$, $V_{THF} = 29\%$): (a) $P = 0$; (c) $P = 6.25 \cdot 10^{-3}$; (e) $P = 1.5 \cdot 10^{-2}$.

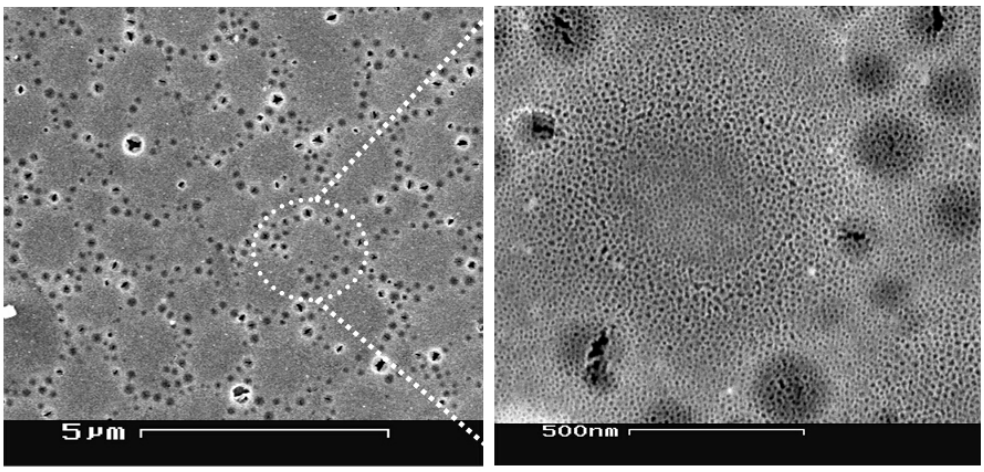


Figure 3.65 FE-SEM micrographs of "flower-like" patterns formed by 3 populations of pores: 15, 40 and 120 nm respectively from the inner to the outer part of the "flower". This porous structure has been obtained using the following conditions: $S = 4 \cdot 10^{-3}$, $V_{THF} = 17\%$, $P = 2 \cdot 10^{-2}$.

Interestingly, the films are not formed by a monolayer of large mesopores; a close FE-SEM examination of the surface in **Figure 3.66a** reveals that a mesoporous layer is present beneath the large pore openings.

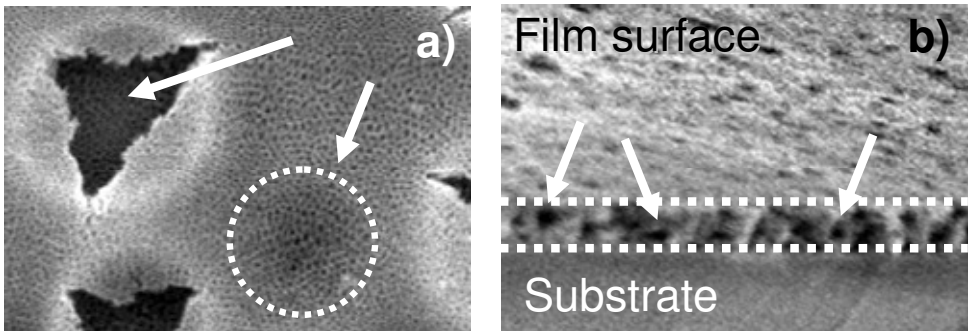


Figure 3.66 a) Detail of a FE-SEM micrograph that shows small pores (arrow) and large pores (dotted circles) beneath the first porous layer. The circle diameter is around 200 nm. b) FE-SEM cross section of a 80 nm thick film. The white arrows indicate macropores along the film thickness.

The same phenomenon has been observed in all the bimodal pore size samples, which display a hierarchical structure where the large pore population (> 80 nm) is generally connected by the smaller pores. A second important point is that the large mesopores are not restrained to the surface; FE-SEM images in **Figure 3.66a and b** (surface and cross section views) of a 80 nm thick films show that both mesopore populations coexist all along the film thickness. In the particular case of **Figure 3.66b**, directly interconnected large pores can be observed.

*- Origin of the hierarchical multiporous texture*

As shown before, the presented method allows the production of titania thin films with homogeneously dispersed large pore size, permitting a fine-tuning of the porosity in terms of the pore size and monomodal / bimodal distribution by varying $V_{THF}$ and PPG concentration. It is also clear from these experiments that the presence of PPG influences the size of mesopores at two different length scales. The information presented in **Figure 3.65**, in particular, reinforces the hypothesis that the role of PPG is crucial in the development of the larger pore population, probably by triggering a phase separation process. The observed crossed effect of the co-solvent and PPG in the swelling of the smaller mesopores suggests a complex synergy between these two

components. **Figure 3.67** summarizes the pore size diameters for the larger pore population (**Figure 3.67a**) and the $d_{ip}$ interpore distances for the smaller one (**Figure 3.67b**), obtained from the analysis of SAXS and FE-SEM data. The global trends in pore size are now clearly observed when data are organized in this representation.

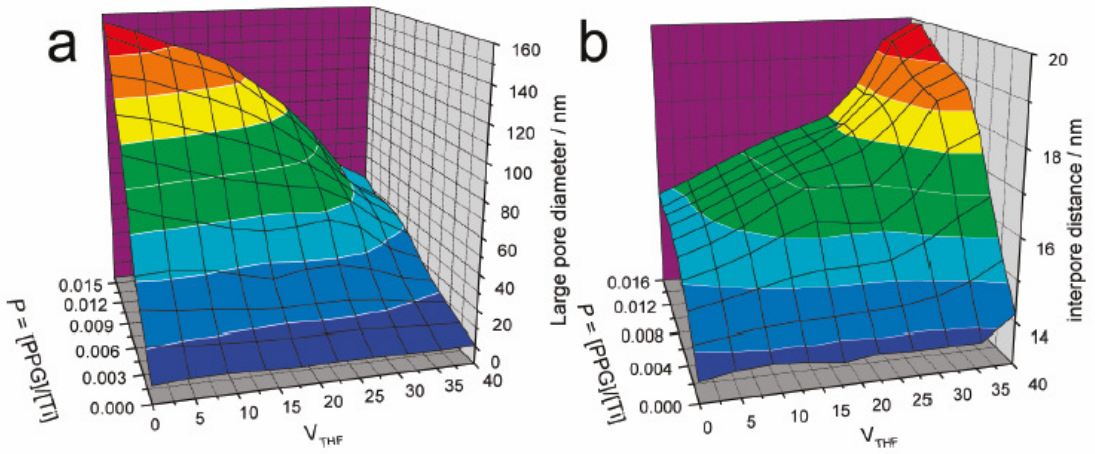


Figure 3.67 (a) Pore diameters and (b) interpore distances, for large and small pore population respectively, obtained by SAXS and FE-SEM analysis of multiporous titania films calcined at 350 °C, as a function of synthesis parameters $V_{THF}$ and $P$ =[PPG] / [Ti] ($S = 4 \cdot 10^{-3}$).

Addition of PPG at $V_{THF} < 20\%$ results in an appreciable swelling of the small pores, until a levelling off at a 16 nm $d_{ip}$; this saturation of pore size is related to a limited solubility of PPG in the F127 micelles. At the same time, larger mesopores begin to appear; their average size is controlled by the PPG concentration. For $V_{THF} > 25$ - 30%, there is an increase in the small pore diameter up to at least 18 nm; coincidently, a drop in the large pores diameter is observed. This effect can be ascribed to the enhanced solubility of PPG in THF. Considering the increasing pore diameter with $V_{THF}$, it appears that THF assists the dissolution of PPG inside the micelles that are formed at mesoscopic scale, upon solvent evaporation. These PPG-swollen micelles are efficient templates for the smaller mesopore population, which displays pore diameters larger than those usually observed in F127-templated titania thin films.[5] The presence of the larger pore population at low $V_{THF}$ can be ascribed to a controlled phase separation triggered by the increasing concentration of PPG upon film drying. The partition of PPG between the forming micelles and the titania-solvent matrix upon film formation is also a key issue in determining the pore diameter of the large pore population. When PPG is essentially dissolved in the micelles, the phase separation process leading to the

large pore population should be less abrupt, influencing the large pore size. The size of the larger pores should be thus controlled by the dynamics of two processes: the macroscopic phase separation and the increasing viscosity attained upon film formation and drying processes.[137] For higher $V_{THF}$, the co-solvent remains in solution for longer times, kinetically assisting the F127 swelling by PPG.

A complex process, where EISA and macroscopic phase separation run in parallel, appears to be responsible for the observed bimodal film porosity. The balance between micelle formation and swelling, micelle organization, and macroscopic phase separation is a key point for the design of these films with multiporous textures. **Figure 3.67** demonstrates that these features can be indeed controlled by adjusting external synthesis and processing parameters. In the precursors solution, PPG can play two different roles, depending on the co-solvent. The relatively high solubility of small size PPG molecules in a solvent with an intermediate hydrophobic character, such as THF, leads to a complex behaviour[§]. In absence of the co-solvent, some of the PPG molecules enter the micelles and act as a pore swelling agent; the remaining PPG triggers de-mixing, originating the large mesopores observed. This phase separation process can take place by either an entropic or enthalpic mechanism;[137] the collected data are not enough to discern between both alternatives. On the other hand, larger amounts of THF enhance the solubility of PPG in the micelles, but it is still unclear if PPG is located in the corona or in the hydrophobic core. This leads to a higher swelling of the smaller pores; at the same time, less PPG is available in the extramicellar space. Therefore, phase separation is less likely, and the system tends to produce one pore size population. These two are examples of extreme conditions; in intermediate situations, we observed a combination of these possibilities. At this point, the combination of species of intermediate hydrophilic / hydrophobic behaviour such as THF and moderate weight PPG appears very important, as far as it determines the dynamics of the evolution. Using this method, we have obtained pore dimensions with the upper limit of around 200 nm. In principle, varying the hydrophobic character (either by changing the PPG size or the monomer) can lead to control of pore size in other length scales. We have also controlled how a higher content of THF in the absence of PPG can affect the porosity of the titania films; a higher dilution of the solution gives a thinner film with slightly larger mesopores, in good agreement with the literature.[129]

[§] Partition coefficients $P_{o/w}$ for THF and butanol are 2.9 and 7.4, respectively.[138]

In summary a one-pot strategy has been reported that is able of producing hierarchically nanoporous oxide thin films with highly and rationally controlled pore size and spatial distribution. This recipe allows the preparation of transparent titania thin films with hierarchical mesoporosity from commercially available, non-toxic templates and simple inorganic precursors. The straightforward preparation conditions reported mask a complex underlying physical-chemical process, which has to be systematically studied to obtain total control of the material features.

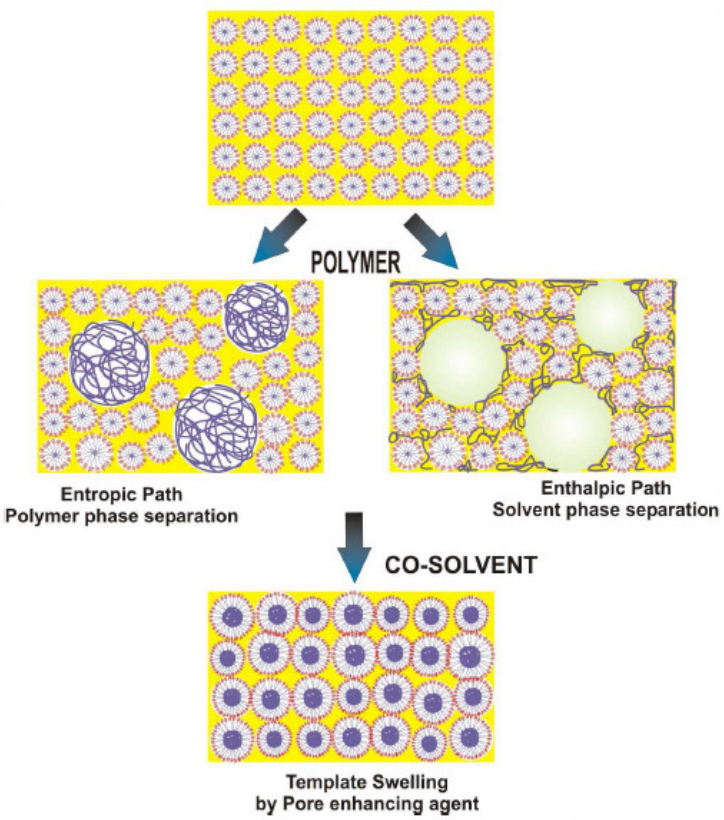


Figure 3.68 Scheme of the possible mechanisms involved in the formation of hierarchical porous titania films.

As resumed in **Figure 3.68**, the key point is mastering the balance among the co-assembly of the inorganic precursors, the supramolecular template, and the behaviour of a pore enhancing agent such as PPG. The addition of PPG to alcohol / water solutions containing titania precursors and template results in the co-existence of smaller and larger mesopores, which are produced by phase separation. Addition of a co-solvent of intermediate hydrophilicity such as THF assists the dissolution of PPG in the micelles, directing to a more uniform population of intermediate size mesopores. An appropriate balance of PPG and THF permits the *in situ* generation of a tailored templating system

with multiple characteristic lengths, obtained by controlling the phase separation and micellar template swelling behaviour of a surfactant / polymer / solvent / co-solvent mixture. The method presented here opens the gate for crossing the 10 nm barrier in mesoporous films and creating multimodal porous thin films with large mesopores.

### 3.6.3 Mesopores and nanoboxes

The strategies to fabricate hierarchical porous materials through self-assembly basically rely on the capability of using templates of different dimensions which are able to organize during solvent evaporation. The choice of the second template to produce a hierarchical material is dictated by the limitation that it should not interfere with the self-assembly process and should allow to control the pore dimension. Easy removal of the template at the end of the process and interconnectivity between smaller and bigger pores are also important requirements to be fulfilled.[111] We have already shown how to produce hierarchical porous materials by introduction of nano-objects of well-defined shape: this approach, however, is limited by the fact that one template, the micelles, self-organizes and forms during EISA while the other one does not really participate to EISA because its formation is not driven by solvent evaporation. We have also shown that hierarchical porous films can be obtained by a controlled phase separation of a co-solvent, but this approach does not allow to obtain a very fine control of the pore shape.
To build up hierarchical highly controlled nanoporous materials it is necessary to control not only pore dimension, but also pore organization and, if possible, pore shape. Moreover, when different types of templates are used, another important requirement is the possibility of achieving a selective templating removal. Taking in mind these strict requirements, we have developed an alternative route to hierarchical nanoporous films through evaporation-induced self-assembly based on forming a second template during EISA that can be easily and selectively removed at the end of film processing. The idea is that the formation of salt nanocrystals acting as porogen materials can be driven by evaporation of the solvent. This approach has been previously used for generating porous materials, but the examples that have been reported are limited to microparticles sinthesized by aerosol.[139]

To prepare the hierarchical porous films, we have followed the procedure reported in Section 3.1, page 86. We have selected the different compounds on the basis of a specific design of the solution: the precursor sol containing MTES and TEOS allows

preparing hybrid organic-inorganic films that exhibit a strong capability to form highly organized mesostructures using both ionic or block copolymer surfactants. Besides, Pluronic F127 is a template which can be easily removed upon calcination of the film in air at temperatures between 150 and 350 °C.[27] This temperature range is low enough to maintain the covalently bonded methyl groups into the film without affecting the organization of the mesophase. The presence of the methyl groups is very important because they limit the absorption of water into the mesopores (see Section 3.3, FTIR of MTES-TEOS membrane).

A set of different samples has been prepared by changing the relative salt concentrations as reported in **Table 3.3**.

| NaCl [M] | $Na_2HPO_4$ [mM] | | |
|---|---|---|---|
| | 32 | 45.5 | 54 |
| 0.49 | *mesopores* | *mesopores* | *mesopores* |
| 0.7 | *mesopores* | *mesopores* + *nanoboxes* | *mesopores* + *nanoflakes* |
| 0.84 | *mesopores* + *salt precipitates on film surface* | *mesopores* + *salt precipitates on film surface* | *mesopores* + *nanoboxes* |

Table 3.3 Summary of the films prepared with different salt concentrations and the phases that have been observed.

The organization of the films porous structure has been evaluated by GISAXS at the Austrian SAXS beamline of ELETTRA synchrotron. An incident energy of 8 keV has been used; the instrumental glancing angle between the incident radiation and the sample has been set slightly above the critical angle (grazing incidence). Typically, each measurement is obtained by the average of 10 acquisitions with integration time ranging from 20 ms to 1 s. We have analyzed by GISAXS the films treated at 350 °C, and we have observed diffraction spots which have been compatible with the formation of an organized cubic mesopores array. The patterns have been assigned to a cubic symmetry (body centred cubic, $Im\bar{3}m$ in the space group) with the (110) plane oriented perpendicular to the substrate ($z$ direction), uniaxially distorted. Following this

attribution, the typical interplanar distances in the films have been estimated as $d_{1\text{-}10}$ = 16.7 ± 1.8 nm and $d_{110}$ = 13.7 ± 2 nm (**Figure 3.69**). Clearly the addition of the salts into the precursor sol does not interfere with the EISA process during the film deposition since all the samples showed the formation of ordered mesopores (**Table 3.3**). Besides, the interplanar distances appear not dependent by the salts concentrations and remain substantially unaltered for all the samples. After the thermal treatment, the typical film thickness, as measured by an α-SE Wollam spectroscopic ellipsometer, is around 400 nm.

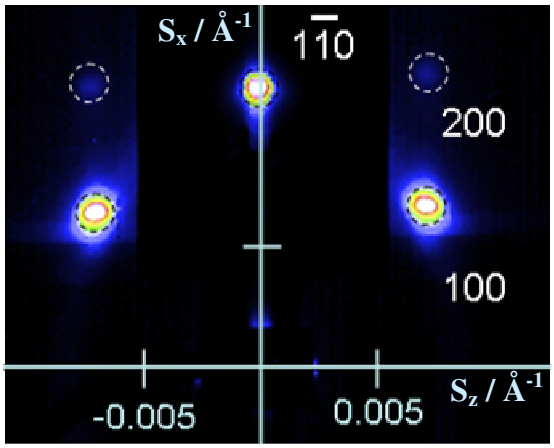


Figure 3.69 GI-SAXS pattern of a mesoporous hybrid thin film (sample 0.7 M NaCl - 45.5 mM $Na_2HPO_4$) after thermal treatment at 350 °C. Indexation of the body centred cubic mesopores array is shown in the figure.

Samples treated ad 350 °C have been also analyzed by TEM using a JEOL 200C× microscope equipped with a tungsten cathode operating at 200 kV. Finely ground films scratched from the silicon substrate have been deposited on a carbon-coated copper grid for TEM observations. The images taken by transmission electron microscopy (sample 0.7 M NaCl - 45.5 mM $Na_2HPO_4$) showed the presence of different types of nanoscale structures. These structures are mesopores of spherical appearance and dimensions of 6.3 ± 0.6 nm and cubic "nanoboxes" of larger dimensions, typically in the range of 100-380 nm (**Figure 3.70**).

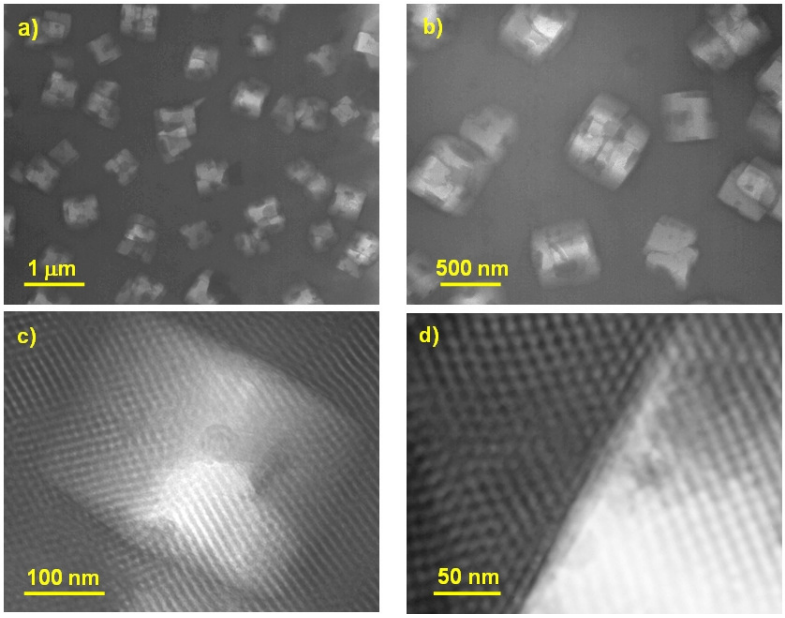


Figure 3.70 TEM images (a-d) at different magnifications of the film (sample 0.7 M NaCl - 45.5 mM $Na_2HPO_4$) showing the presence of mesopores and nanoboxes.

We have used XRD (**Figure 3.71**) and far-infrared (FIR) spectroscopy (**Figure 3.72**) to identify the nature of "nanoboxes" formed during EISA: both the techniques revealed the presence of crystalline sodium chloride.

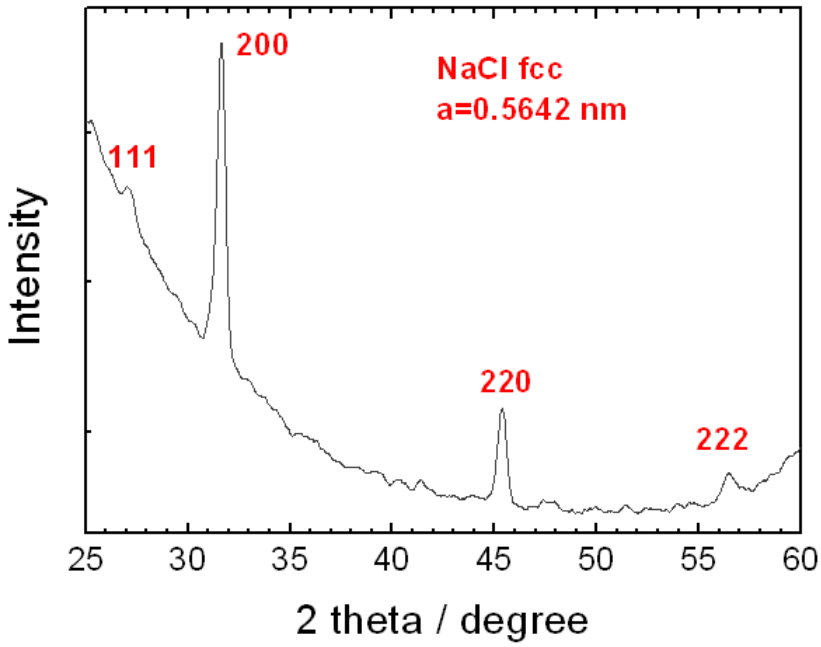


Figure 3.71 XRD pattern of a mesoporous film containing the salt nanocrystals; the indexation of the crystalline phase is shown (sample 0.7 M NaCl - 45.5 mM $Na_2HPO_4$).

XRD measurements have been recorded by a Bruker D8 diffractometer equipped with a scintillator counter. The Cu Kα radiation has been used to perform an ω/2θ scan from 25 to 60° with a resolution of 0.02°. The XRD pattern showed 4 sharp diffraction peaks, which represent the typical signature of crystalline sodium chloride and can be indexed as (111), (200), (220), and (222) reflections. Following this attribution, we have tried to remove the NaCl nanocrystals by washing the films with water; the diffractogram of the samples after washing has shown only the background noise.

We have also compared the FIR spectra of the samples showing nanoboxes before and after washing with the spectrum of a reference mesoporous film prepared without using NaCl and $Na_2HPO_4$. Far infrared spectra have been collected using a Bruker 70v optical bench working under vacuum at a pressure lower than 0.5 hPa. The measurements have been conducted using a Globar source, a Si beamsplitter, and a DTGS detector. The spectra have been recorded in transmission, in the 600-50 $cm^{-1}$ range by averaging 32 scans with 4 $cm^{-1}$ of resolution. An intense absorption band at 440 $cm^{-1}$ which has been assigned to the silica rocking mode is present in all the spectra while another band at 170 $cm^{-1}$, attributed to phononic modes in crystalline NaCl, is only visible in the film with nanocrystals inside. Therefore, also far infrared characterization showed that the washing process completely removes the salt within the film leaving empty nanoboxes.

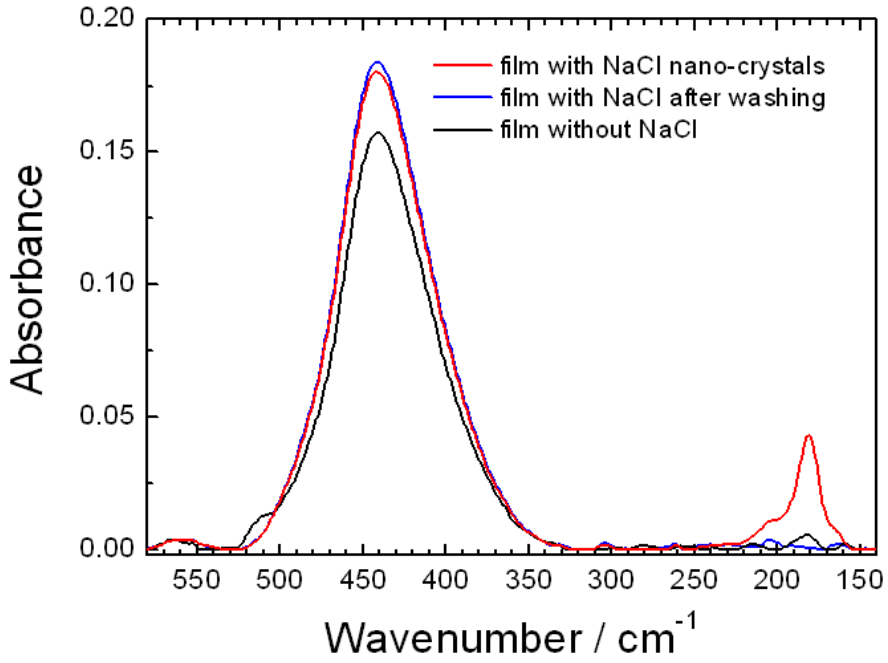


Figure 3.72 Far-infrared spectrum, in the 580-140 $cm^{-1}$ range, of films with different steps of preparation (sample 0.7 M NaCl - 45.5 mM $Na_2HPO_4$).

The experimental results clearly point out the different chemical nature of the two self-assembled templates: mesopores and nanoboxes. The thermal calcination removes the templating organic micelle formed by the block copolymer living a porous organized structure with mesopores of spherical appearance; these pore self-organize into a cubic structure by EISA during film deposition. At the same time the salts added in the precursors solution allows forming another type of nanostructure which appears as a cubic box of larger dimensions. The cubic salt "nanoboxes" can be easily removed by washing the film with water; the salt crystals are water-soluble, and after removal, they leave empty pores. The overall process does not disrupt the mesophase; the ordered porous phase maintains its arrangement after thermal treatment at 350 °C and the following washing process. The evaporation of the ethanol and water during EISA drives self-organization of the templating micelles and also induces precipitation of cubic salt nanocrystals.

A systematic TEM films characterization as a function of the salts concentrations in their solutions of precursors is resumed in **Figure 3.73**. From TEM measurements, we can argue that only some specific compositions allow forming NaCl nanocrystals (**Table 3.3**), while in one case (**Figure 3.73 a and b**, sample 0.7 M NaCl – 54 mM $Na_2HPO_4$) a very peculiar "flake-like" nanostructure formed by piled symmetrical salt nanoboxes of around 100 nm can be obtained. In some other samples, not shown in figure, the formation of white salt precipitates on film surface has been observed (samples 0.84 M NaCl – 32 mM $Na_2HPO_4$ and 0.84 M NaCl - 45.5 mM $Na_2HPO_4$).

**Figure 3.73 c-f** shows the TEM images of the films 0.7 M NaCl - 45.5 mM $Na_2HPO_4$ and 0.84 M NaCl - 54 mM $Na_2HPO_4$. The nanoboxes formed in the 0.7 M NaCl - 45.5 mM $Na_2HPO_4$ film are bigger with respect to the sample prepared at a lower salt concentration. It should be underlined that obtaining NaCl nanocrystals embedded into mesoporous films by EISA is a difficult task because evaporation of the solvent is very fast and the presence of ethanol together with the high acidic conditions in the precursors sol can cause immediate salt crystallization. We have not been able to obtain nanoboxes using only NaCl or $Na_2HPO_4$ as templating agent, even though we have systematically changed the sol composition and the salt concentration. The role of $Na_2HPO_4$ appears critical in avoiding the precipitation of NaCl and seeding the crystal formation. However the crystallized salt shows a well-defined shape and dimension which is an indication that the overall process is controlled. This process is highly reproducible; in fact we have repeated several times the preparation, always obtaining

similar results. The formation of salt nanocrystals gives pores of well defined shape, while a certain control of pore dimension and topological distribution can be achieved by changing the salt concentration and relative salt composition. Nevertheless the peculiarity of this system consists in the effect of $Na_2HPO_4$ which, under particular conditions, appears responsible to the nanoboxes formation.

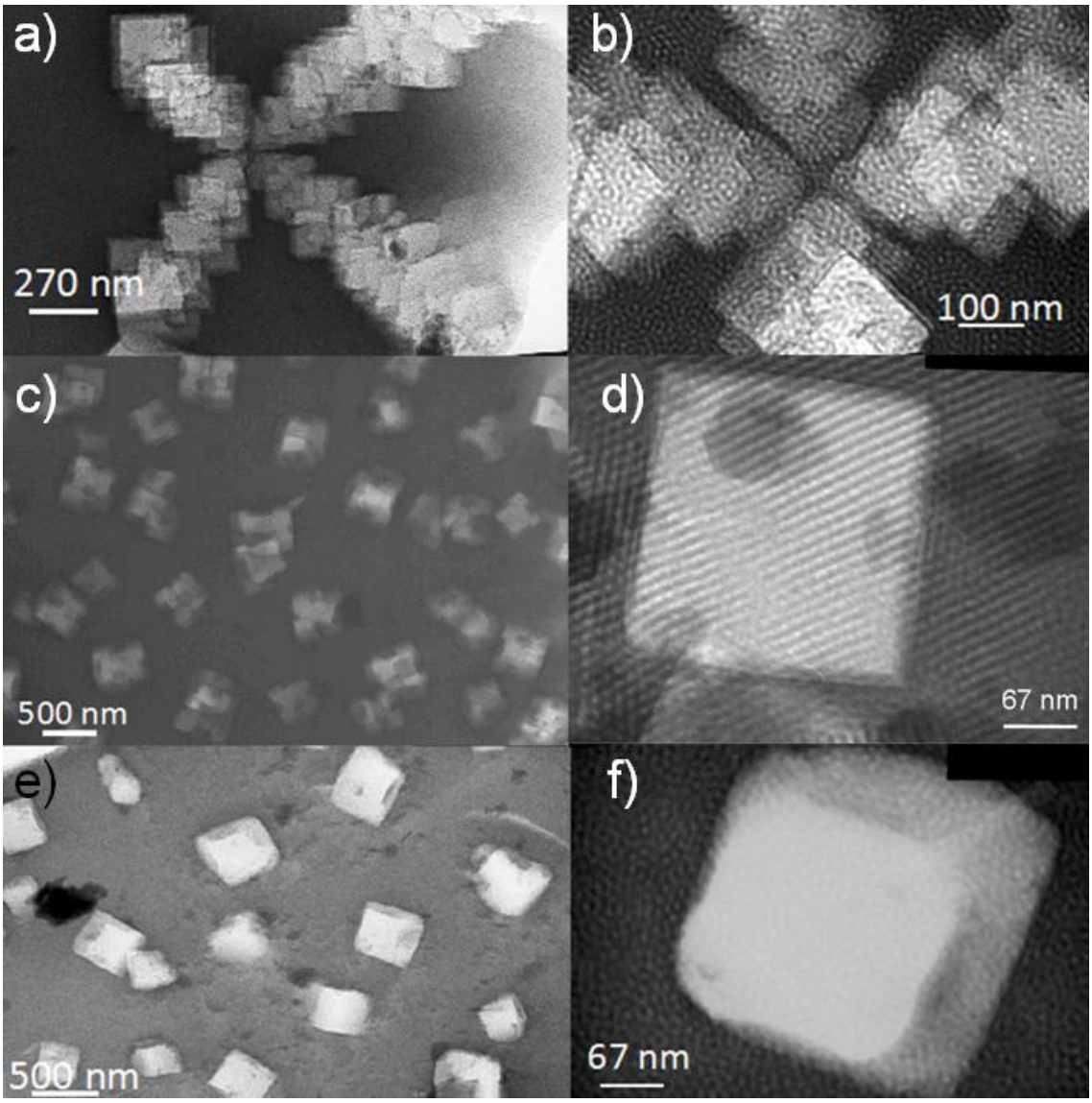


Figure 3.73 TEM images (a-f ) at different magnifications of the films: (a, b) sample 0.7 M NaCl – 54 mM $Na_2HPO_4$; (c, d) sample 0.7 M NaCl - 45.5 mM $Na_2HPO_4$; (e, f) sample 0.84 M NaCl - 54 mM $Na_2HPO_4$.

We suspect that $Na_2HPO_4$ helps the growth of NaCl by a fast seeding during the first stage of evaporation. Once crystal seeds are formed, NaCl growth occurs with the formation of nanoboxes. *In situ* experiments are ongoing in order to clarify this effect.

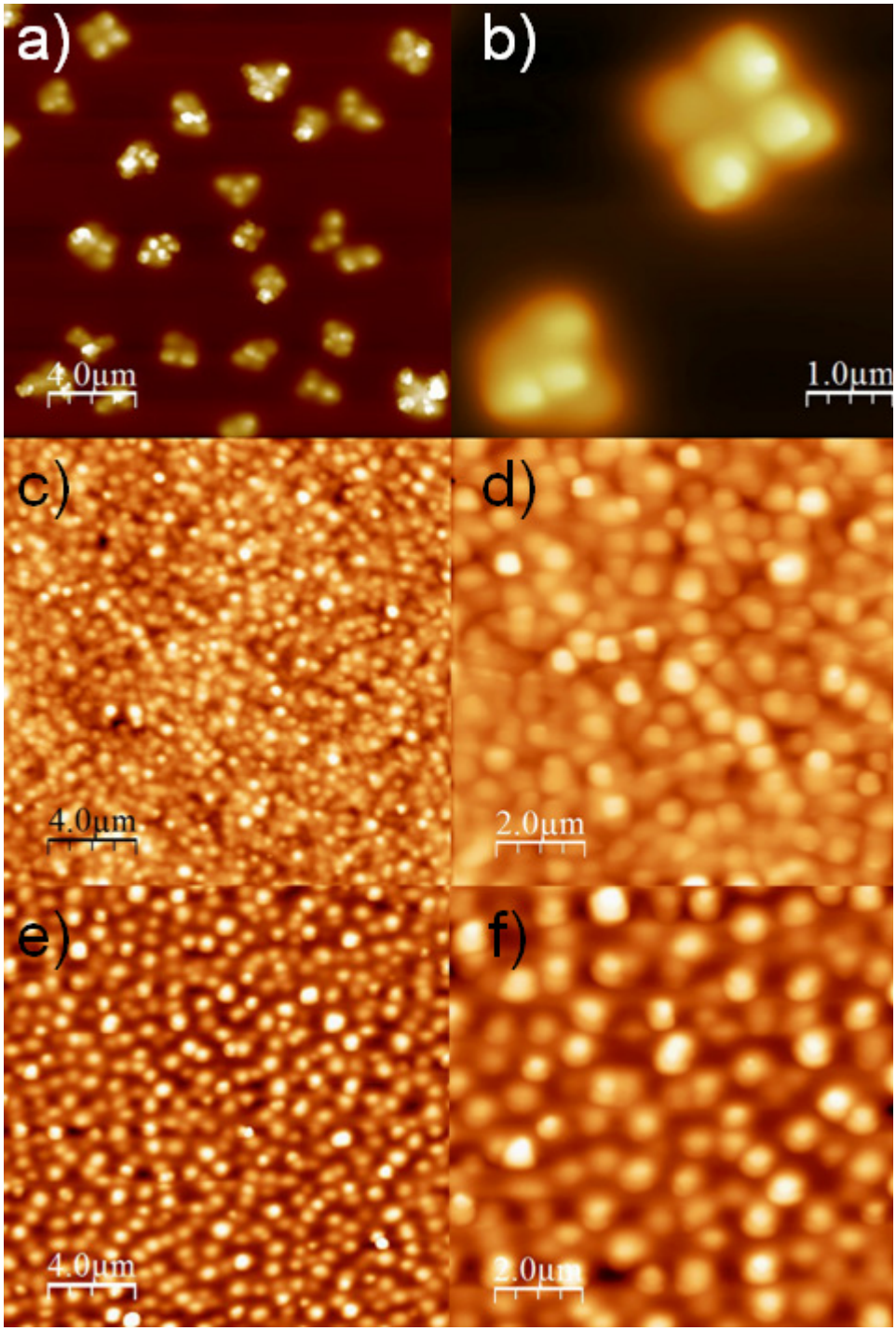


Figure 3.74 AFM images (a-f) at different magnifications of the films: (a, b) sample 0.7 M NaCl – 54 mM $Na_2HPO_4$; (c, d) sample 0.7 M NaCl - 45.5 mM $Na_2HPO_4$; (e, f) sample 0.84 M NaCl - 54 mM $Na_2HPO_4$.

The surface morphology of films has been analysed by atomic force microscopy (AFM) using a NT-MDT Ntegra AFM. Surfaces have been measured at 0.5–1 Hz scan speed in non-contact mode, using a silicon tip with nominal resonance frequency of 150 kHz, 5 $N \cdot m^{-1}$ force constant, and 10 nm typical curvature radius. The AFM images reveal that the "flake-like" salt structure forms a very specific pattern also on the surface, where symmetrical nanostructures, which are due to the piled nanoboxes within the film, can be observed (**Figure 3.74a and b**). Besides this particular pattern, the surface of films prepared with different salts compositions shows a homogeneous distribution of grains that has been correlated to the formation of the salt nanoboxes within the films (**Figure 3.74 c-f**). It is important to observe that the film covers homogeneously these structures and does not form open craters on the surface even after salt washing out. This in accordance to some numerical models performed to simulate the formation of NaCl crystals in the core of mesoporous microparticles.[139] In that case, numerical solutions to the radial gradients in mass and heat for evaporating a $H_2O$-EtOH-NaCl droplets indicate that preferential ethanol evaporation enriches the droplet surface in water. As NaCl is 481 times more soluble in water than in ethanol (at 25 °C), and the ionic diffusivity of $Na^+$ and $Cl^-$ exceeds that of both water and ethanol, supersaturation of $Na^+$ and $Cl^-$ and nucleation of NaCl occurs first at the particle centre, where the EtOH / $H_2O$ ratio is maximized. By adjusting these results to a different geometry, we can conclude that in mesoporous films the probability of NaCl nucleation is higher at the film-substrate interface and this could explain the reason why the salts nanocrystals are always covered by a film layer.

The synthesis we have used allows a selective functionalization of the nanopores through a controlled multistep process of pores opening, as illustrated in **Figure 3.75**. In the first step a mesostructured film is produced by EISA and the film contains mesopores and salt nanoboxes; in the second step the film is fired in air at 350 °C to remove the block copolymer template, the mesopores are now empty, and the nanoboxes are still filled. In the final step the film is washed by water and then dried; this process allows eliminating the salt, leaving empty nanoboxes. The advantage of this procedure is given by the selective control of nanopore formation through film processing during EISA.

To resume, we have developed a new method that allows the formation of two types of pore templates during EISA, spherical micelles from block copolymers and crystalline nanoboxes from salts. Formation of NaCl nanocrystals is driven by the evaporation of

the solvent during film deposition while uncontrolled precipitation of the salt is avoided by the co-addition of $Na_2HPO_4$ in the precursor sol. The nanoboxes are not ordered but appear homogeneously dispersed within the mesoporous matrix.

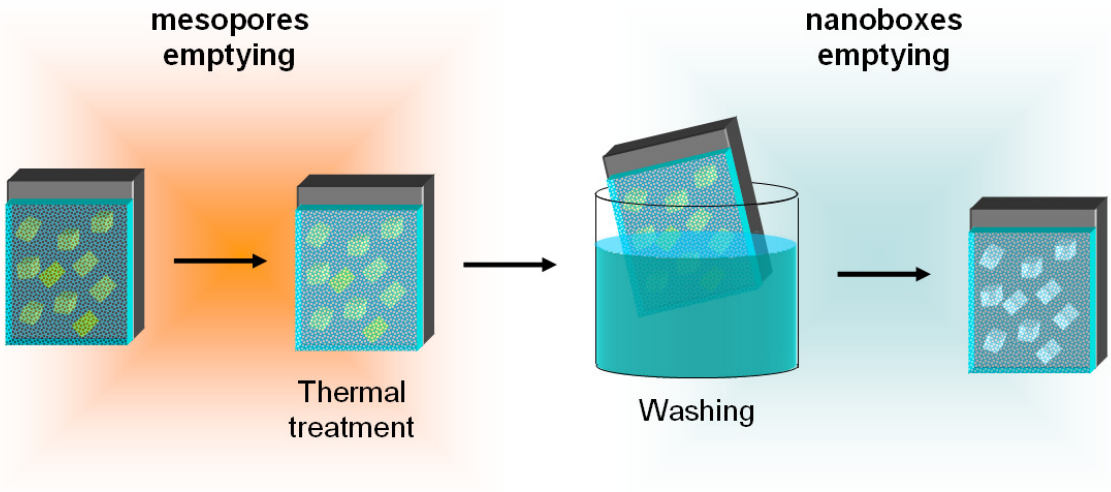


Figure 3.75 Illustration of the different steps to prepare hierarchical porous films with spherical mesopores ( ≈ 6 nm) and cubic pores (100 - 380 nm).

The template removal can be performed in a selective way; block copolymers are eliminated by thermal treatment and salt nanoboxes are removed by a simple water washing of the film. The final material appears as a porous hierarchical film with two ranges of porosities, an ordered array of mesopores with a dimension of around 6 nm, and cubic macropores in the range of 100-380 nm from the salt nanocrystals. This preparation method allows a selective functionalization of the nanopores through a controlled multistep process.

## 3.7 References

[1] T. Sakata, Y. Yan, G. J. Marriott. Family of site-selective molecular optical switches. *J. Org. Chem.* **2005,** *70,* 2009-2013.

[2] V. Castelvetro, C. De Vita, G. Giannini, G. Simone. Role of anionic and nonionic surfactants on the control of particle size and latex colloidal stability in the seeded emulsion polymerization of butyl methacrylate. *J. Appl. Polym. Sci.* **2006**, *102*, 3083-3094.

[3] P. Falcaro, S. Costacurta, G. Mattei, H. Amenitsch, A. Marcelli, M. C. Guidi, M. Piccinini, A. Nucara, L. Malfatti, T. Kidchob, P. Innocenzi. Highly ordered "defect-free" self-assembled hybrid films with a tetragonal mesostructure. *J. Am. Chem. Soc.* **2005**, *127*, 3838-3846.

[4] E. L. Crepaldi, G. Soler-Illia, D. Grosso, C. Sanchez. Nanocrystallised titania and zirconia mesoporous thin films exhibiting enhanced thermal stability. *New J. Chem.*, **2003**, *27*, 9–13.

[5] E. L. Crepaldi, G. Soler-Illia, D. Grosso, F. Cagnol, F. Ribot, C. Sanchez. Controlled formation of highly organized mesoporous titania thin films: from mesostructured hybrids to mesoporous anatase $TiO_2$. *J. Am. Chem. Soc.*, **2003**, *125*, 9770–9786.

[6] G. Soler-Illia, E. Scolan, A. Louis, P.-A. Albouy, C. Sanchez. Design of mesostructured titanium oxo based hybrid organic-inorganic networks. *New J. Chem.*, **2001**, *25*, 156–165.

[7] F. Cagnol, D. Grosso, G. Soler-Illia, E. L. Crepaldi, F. Babonneau, H. Amenitsch, C. Sanchez. Humidity-controlled mesostructuration in CTAB-templated silica thin film processing. The existence of a modulable steady state. *J. Mater. Chem.*, **2003**, *13*, 61–66.

[8] C. J. Brinker, G. W. Scherer. Sol-gel science: The physics and chemistry of sol-gel processing. **1992,** Academic Press, San Diego.

[9] M. P. Tate, V. N. Urade, J. D. Kowalski, T. Wei, B. D. Hamilton, B.W. Eggiman, H. W. Hillhouse. Simulation and interpretation of 2d diffraction patterns from self-assembled nanostructured films at arbitrary angles of incidence: from grazing incidence (above the critical angle) to transmission perpendicular to the substrate. *J. Phys. Chem. B* **2006,** *110*, 9882-9892.

[10] Website: http://cobweb.ecn.purdue.edu/~hgroup/ (accessed November 2009).

[11] C. Hammond. Introduzione alla cristallografia. **1994**, Zanichelli, Bologna.

[12] C. N. Urade, H. W. Hillhouse. Synthesis of thermally stable highly ordered nanoporous tin oxide thin films with a 3D face-centered orthorhombic nanostructure. *J. Phys. Chem. B*, **2005**, *109*, 10538–10541.

[13] C. Sanchez, G. Soler-Illia, F. Ribot, D. Grosso. Design of functional nano-structured materials through the use of controlled hybrid organic-inorganic interfaces. *C. R. Chimie*, **2003**, *6*, 1131–1151.

[14] A. G. Yodh, K.-H. Lin, J. C. Crocker, A. D. Dinsmore, R. Verma, P. D. Kaplan. Entropically driven self-assembly and interaction in suspension. *Phil. Trans. R. Soc. Lond. A*, **2001**, *359*, 921–937.

[15] H. N. W. Lekkerkerker, A. Stroobants. Ordering entropy. *Nature*, **1998**, *393*, 305-306.

[16] J. Murray, E. Garman. Investigation of possible free-radical scavengers and metrics for radiation damage in protein cryocrystallography. *J. Synchrotron Rad.*, **2002**, *9*, 347–354.

[17] A. Cheng, M. Caffrey. Free radical mediated X-ray damage of model membranes. *Biophys. J.*, **1996**, *70*, 2212–2222.

[18] A. G. Richter, J. Wang, R. Guico, K. Shull. X-radiation damage of polymer thin films. **1999**, Argonne National Laboratory Report.

[19] D. Grosso, F. Babonneau, P.-A. Albouy, H. Amenitsch, A. R. Balkenende, A. Brunet-Bruneau, J. Rivory. An in situ study of mesostructured CTAB-silica film formation during dip coating using time-resolved SAXS and interferometry measurements. *Chem. Mater.*, **2002**, *14*, 931–939.

[20] D. A. Doshi, A. Gibaud, V. Goletto, M. Lu, H. Gerung, B. Ocko, S. M. Han, C. J. Brinker. Peering into the self-assembly of surfactant templated thin-film silica mesophases. *J. Am. Chem. Soc.*, **2003**, *125*, 11646–11655.

[21] P. Innocenzi, T. Kidchob, J. Mio Bertolo, M. Piccinini, M. Cestelli Guidi, A. Marcelli. Time-resolved infrared spectroscopy as an in situ tool to study the kinetics during self-assembly of mesostructured films. *J. Phys. Chem. B*, **2006**, *110*, 10837–10841.

[22] S. Besson, T. Gacoin, C. Jacquiod, C. Ricolleau, J.-P. Boilot. 3D periodic arrays of nanoparticles inside mesoporous silica films. *Mat. Res. Soc. Symp. Proc.*, **2002**, 707,119-124.

[23] P. Innocenzi. Infrared spectroscopy of sol-gel derived silica-based films: a spectra microstructure overview. *J. Non-Cryst. Solids*, **2003**, *316*, 309–319.

[24] K. Davis, M. J. Tomozawa. An infrared spectroscopic study of water-relate species in silica glasses. *J. Non-Cryst. Solids*, **1996**, *201*, 177–198.

[25] J. G. Bayly, V. B. Kartha, W. H. Stevens. Absorption spectra of liquid phase $H_2O$, HDO, and $D_2O$ from 0.7 to 10 μ. *Infrared Phys.*, **1963**, *3*, 211–222.

[26] Y. Shen, P. Wu. Two-dimensional ATR-FTIR spectroscopic investigation on water diffusion in polypropylene film: water bending vibration. *J. Phys. Chem. B*, **2003**, *107*, 4224–4226.

[27] P. Innocenzi, P. Falcaro, D. Grosso, F. Babonneau. Order-disorder transitions and evolution of silica structure in self-assembled mesostructured silica films studied through FTIR spectroscopy. *J. Phys. Chem. B*, **2003**, *107*, 4711–4717.

[28] A. Bearzotti, J. Mio Bertolo, P. Innocenzi, P. Falcaro, E. Traversa. Humidity sensors based on mesoporous silica thin films synthesized by block copolymers. *J. Eur. Ceramic Soc.*, **2004**, *24*, 1969–1974.

[29] D. Avnir, D. Levy, R. Reisfeld. The nature of the silica cage as reflected by spectral changes and enhanced photostability of trapped Rhodamine 6G *J. Phys. Chem.* **1984**, *88*, 5956-5959.

[30] E. T. Knobbe, B. Dunn, P. D. Fuqua, F. Nishida. Laser behavior and photostability characteristics of organic dye doped silicate gel materials. *Appl. Opt.* **1990**, *29*, 2729-2733.

[31] C. M. Carbonaro, A. Anedda, S. Grandi, A. Magistris. Hybrid Materials for Solid-State Dye Laser Applications *J. Phys. Chem. B* **2006**, *110,* 12932-12937.

[32] K. Kemnitz, K. Yoshibara. Entropy-driven dimerization of xanthene dyes in nonpolar solution and temperature-dependent fluorescence decay of dimers. *J. Phys. Chem.* **1991**, *95*, 6095-6104.

[33] S. Daré-Doyen, D. Doizi, P. Guilbaud, P., F. Djedaini-Pilard, B. Perly, P. Millié. Dimerization of xanthene dyes in water: experimental studies and molecular dynamic simulations. *J. Phys. Chem. B* **2003**, *107,* 13803-13812.

[34] R. Sasai, N. Iyi, T. Fujita, F. L. Arbeloa, V. M. Martinez, K. Takagi, H. Itoh. Luminescence properties of rhodamine 6g intercalated in surfactant/clay hybrid thin solid films. *Langmuir* **2004,** *20,* 4715-4719.

[35] F. Del Monte, J. D. Mackenzie, D. Levy. Rhodamine fluorescent dimers adsorbed on the porous surface of silica gels *Langmuir* **2000**, 16, 7377-7382.

[36] P. Bojarski, A. Matczuk, C. Bojarski, A. Kawski, B. Kuklinski, G. Zurkowska, H. Diehl. Fluorescent dimers of rhodamine 6G in concentrated ethylene glycol solution *Chem. Phys.* **1996**, *210*, 485-499.

[37] J. Bujdak, N. Iyi, Y. Kanko, A. Czimerova, R. Sasai. Molecular arrangement of rhodamine 6G cations in the films of layered silicates: the effect of the layer charge *Phys. Chem. Chem. Phys.* **2003**, *5*, 4680-4685.

[38] J. M. McKiernan, S. A. Yamanaka, B. Dunn, J. I. Zink. Spectroscopy and laser action of Rhodamine 6G doped aluminosilicate xerogels. *J. Phys. Chem.* **1990**, *94*, 5652–5654.

[39] A. Anedda, C. M. Carbonaro, R. Corpino, P. C. Ricci, S. Grandi, P. Mustarelli, Formation of fluorescent aggregates in Rhodamine 6G doped silica glasses. *J. Non-Cryst. Solids* **2007**, *353*, 481-485.

[40] A. Anedda, C. M. Carbonaro, F. Clemente, R. Corpino, S. Grandi, P. Mustarelli, A. Magistris. Rhodamine 6G–$SiO_2$ hybrids: A photoluminescence study. *J. Non-Cryst. Solids* **2005**, *351*, 1850-1854.

[41] G. J. A. Soler-Illia, P. Innocenzi, P. Mesoporous hybrid thin films: the chemistry beneath. *Chem.: A Europ. J.* **2006**, *12*, 4478-4494.

[42] R. Vogel, P. Meredith, M. D. Harvey, H. Rubinsztein-Dunlop. Absorption and fluorescence spectroscopy of rhodamine 6G in titanium dioxide nanocomposites. *Spectrochimica Acta Part A* **2004**, *60*, 245–249.

[43] P. Yang, G. Wirnsberger, H. C. Huang, S. R. Cordero, M. D. McGehee, B. Scott, T. Deng, G. M. Whitesides, B. F. Chmelka, S. K. Buratto, G. D. Stucky. Mirrorless Lasing from Mesostructured Waveguides Patterned by Soft Lithography. *Science* **2000**, *287*, 465-467.

[44] P. Pal, H. Zeng, G. Durocher, D. Girard, R. Giasson, L. Blanchard, L. Gaboury, L. Villeneuve. Spectroscopic and photophysical properties of some new rhodamine derivatives in cationic, anionic and neutral micelles. *J. Photochem. Photobiol. A: Chem.* **1996**, *98*, 65-72.

[45] M. Harvey, G. Edwards, P. Meredith, N. Heckenberg, M. Trau, H. Rubinsztein-Dunlop. Dimer-to-monomer transformation of rhodamine 6G in aqueous PEO–PPO–PEO block copolymer solutions *Macrom.* **2002**, *35,* 2063-2070.

[46] B. Dunn, J. I. Zink. Molecules in glass: probes, ordered assemblies, and functional materials. *Acc. Chem. Res.* **2007**, *40*, 747-755.

[47] P. N. Minoofar, B. Dunn, J. I. Zink. Multiply doped nanostructured silicate sol−gel thin films: spatial segregation of dopants, energy transfer, and distance measurements. *J. Am. Chem. Soc.* **2005**, *127*, 2656–2665.

[48] G. Wirnsberger, B. J. Scott, B. F. Chmelka, G. D. Stucky. Fast response photochromic mesostructures. *Adv. Mater.* **2000**, *12*, 1450-1454.

[49] D. Grosso, G. J. A. Soler-Illia, F. Babonneau, D. Sanchez, P.-A. Albouy, A. Brunet-Bruneau, A. R. Balkenende. Highly organized mesoporous titania thin films showing mono-oriented 2d hexagonal channels *Adv. Mater.* **2001** *13,*1085-1090.

[50] F. Del Monte, D. Levy. Formation of fluorescent rhodamine B J-dimers in sol−gel glasses induced by the adsorption geometry on the silica surface. *J. Phys. Chem. B* **1998**, *102*, 8036-8041.

[51] C. Bojarski, G. Obermueller. Association and photoluminescence quenching of rhodamine 6G in solutions *Acta Phys. Pol.* **1976**, *A50*, 389-411.

[52] S. Blonski. Aggregation of rhodamine 6G in porous silica gels. *Chem. Phys. Lett.* **1991**, *184*, 229-234.

[53] P. Innocenzi, H. Kozuka, T. Yoko. Dimer-to-monomer transformation of rhodamine 6G in sol—gel silica films. *J. Non-Cryst. Solids* **1996**, *201*, 26-36.

[54] M. Fischer, J. Georges. Use of thermal lens spectrometry for the investigation of dimerization equilibria of rhodamine 6G in water and aqueous micellar solutions. *Spectrochim. Acta A* **1997**, *53*, 1419-1430.

[55] V.I. Minkin. Photo-, thermo-, solvato-, and electrochromic spiroheterocyclic compounds. *Chem. Rev.* **2004,** *104*, 2751-2776.

[56] J.H. Day. Thermochromism. *Chem. Rev.* **1963**, *63*, 65-80.

[57] R.J. Byrne, S.E. Stitzel, D. Diamone. Photo-regenerable surface with potential for optical sensing. *J. Mater. Chem.* **2006,** *16*, 1332-1337.

[58] G. Wirnsberger, B.J. Scott, B.F. Chmelka, G.D. Stucky. Fast Response Photochromic Mesostructures. *Adv. Mater.* **2000,** *12*, 1450-1454.

[59] J.L. Bahr, G. Kodis, G. De la Garza, S. Lin, A.L. Moore, T.A. Moore, D. Gust. Photoswitched singlet energy transfer in a porphyrin−spiropyran dyad. *J. Am. Chem. Soc.* **2001,** *123* ,7124-7133.

[60] T. Minami, N. Tamai, T. Yamazaki, I.J. Yamazaki. Picosecond time-resolved fluorescence spectroscopy of the photochromic reaction of spiropyran in Langmuir-Blodgett films. *J. Phys. Chem.* **1991,** *95*, 3988-3993.

[61] F. Levy, D. Avnir. Effects of the changes in the properties of silica cage along the gel/xerogel transition on the photochromic behavior of trapped spiropyrans. *J. Phys. Chem.* **1988,** *92*, 4734-4738.

[62] M.Q. Zhu, L. Zhu, J.J. Han, W. Wu, J.K. Hurst, A.D.Q. Li. Spiropyran-based photochromic polymer nanoparticles with optically switchable luminescence *J. Am. Chem. Soc.* **2006**, *12,* 4303-4309.

[63] A. Léaustic, A. Dupont, P. Yu, R. Clement. Photochromism of cationic spiropyran-doped silica gels. *New J. Chem.* **2001,** *25*, 1297-1300.

[64] A. Garcia, M. Marquez, T. Cai, R. Rosario, Z. Hu, D. Gust, M. Hayes, S.A. Vail, C. .D. Park, *Langmuir* **2007,** *23*, 224-229.

[65] J. R. Sheats, H. Antoniadis, M. Hueshen, W. Leonard, J. Miller, R. Moon, D. Roitman, A. Stocking. Organic Electroluminescent Devices *Science* **1996,** *273*, 884-888.

[66] A. Karft , A. C. Grimsdale, A. B. Holms. Electroluminescent Conjugated Polymers - Seeing Polymers in a New Light. *Angew. Chem. Int. Ed.* **1998**, *37*, 402-428.

[67] X. T. Tao, H. Suzuki, T. Wada, H. Sasabe, S. Miyata. Lithium tetra-(8-hydroxy-quinolinato) boron for blue electroluminescent applications. *Appl. Phys.* Lett., **1999,** *75*, 1655-1657.

[68] W. H. Zhang , J. L. Shi, L. Z. Wang, D. S. Yan. Preparation and characterization of zno clusters inside mesoporous silica. *Chem. Mater.* **2000,** *12,* 1408-1413.

[69] W. Xu, D. L. Akkins. Absorption and exciton emission by an aggregated cyanine dye occluded within mesoporous SBA-15. *J. Phys. Chem. B* **2002,** *106*, 1991-1994.

[70] K. Moller, T. Bein. Internal modification of ordered mesoporous hosts. *Stud. Surf. Sci. Catal.* **1998,** *117*, 53-64.

[71] D. Trong On, D. Desplantier-Giscard, C. Danumah, S. Kaliaguine. Perspectives in catalytic applications of mesostructured materials. *Appl. Catal. A Gen.* **2001,** *222*, 299-357.

[72] M. La Deda, M. Ghedini, I. Aiello, A. Grisolia. A new blue photoluminescent salen-like zinc complex with excellent emission quantum yield. *Chem. Lett.* **2004,** *33,* 1060-1061.

[73] P. Falcaro, D. Grosso, H. Amenitsch, P. Innocenzi. Silica orthorhombic mesostructured films with low refractive index and high thermal stability. *J. Phys. Chem. B,* **2004**, 108, 10942-10948.

[74] B. J. Scott, M.H. Bartl, G. Wirnsberger, G. D. Stucky. Energy transfer in dye-doped mesostructured composites. *J. Phys. Chem. A* **2003,** *107*, 5499-5502.

[75] S. Besson, T. Gacoin, C. Ricolleau, C. Jacquiod, J.-P. Boilot. 3D quantum dot lattice inside mesoporous silica films. *Nano Lett.*, **2002**, *2*, 409–414.

[76] V. Della Savia, M. C. Marchi, E. H. Otal, B. Bozzano, G. Soler-Illia. Tuned photoluminescence emission of CdS dots embedded in mesoporous silica, *EMRS Spring Meeting*. **2005**.

[77] M. Wark, H. Wellmann, J. Rathousky. Homogeneously distributed CdS and CdSe nanoparticles in thin films of mesoporous silica. *Thin Solid Films*, **2004**, *458*, 20–25.

[78] A. V. Kouzema, M. Fröba. $Cd_{1-x}Mn_xS$ diluted magnetic semiconductors as nanostructured guest species in mesoporous thin-film silica host media. *Adv. Funct. Mater.*, **2005**, *15*, 168–172.

[79] J. P.Waters, D. Smyth-Boyle, K. Govender, A. Green, J. Durrant, P. O'Brien. Simple CVD routes towards infiltration of mesoporous TiO2. *Chem. Vap. Deposition*, **2005**, *11*, 254–260.

[80] D. Buso, P. Falcaro, S. Costacurta, M. Guglielmi, A. Martucci, P. Innocenzi, L. Malfatti, V. Bello, G. Mattei, C. Sada, H. Amenitsch, I. Gerdova, A. Hachè. PbS-doped mesostructured silica films with high optical nonlinearity. *Chem. Mater.*, **2005**, *17*, 4965–4970.

[81] A. M. Saad, A. V. Mazanik, Y. E. Kalinin, J. A. Fedotova, A. K. Fedotov, S. Wrotek, A. V. Sitnikov, I. A. Svito. Structure and electrical properties of CoFeZr-aluminium oxide nanocomposite films. *Rev. Adv. Mater. Sci.*, **2004**, *8*, 152–157.

[82] Z. Turgut, J. H. Scott, M. Q. Huang, S. A. Majetich, M. E. McHenry. Magnetic properties and ordering in C-coated $Fe_xCo_{1-x}$ alloy nanocrystals. *J. Appl. Phys*, **1998**, *83*, 6468–6470.

[83] N. O. Nunez, P. Tartaj, M. Puerto Morales, P. Bonville, C. J. Serna. Yttria-coated FeCo magnetic nanoneedles. *Chem. Mater.*, **2004**, *16*, 3119–3124.

[84] C. Desvaux, C. Amiens, P. Fejes, P. Renaud, M. Respaud, P. Lecante, E. Snoeck, B. Chaudret. Multimillimetre-large superlattices of air-stable iron-cobal nanoparticles. *Nature Materials*, **2005**, *4*, 750–753.

[85] M. F. Casula, G. Concas, F. Congiu, A. Corrias, A. Falqui, G. Spano. Near equiatomic FeCo nanocrystalline alloy embedded in an alumina aerogel matrix: microstructural features and related magnetic properties. *J. Phys. Chem. B*, **2005**, *109*, 23888–23895.

[86] A. F. Gross, M. R. Diehl, K. C. Beverly, E. K. Richman, S. H. Tolbert. Controlling magnetic coupling between cobalt nanoparticles through nanoscale confinement in hexagonal mesoporous silica. *J. Phys. Chem. B*, **2003**, *107*, 5475–5482.

[87] W. S. Seo, J. H. Lee, X. Sun, Y. Suzuki, D. Mann, Z. Liu, M. Terashima, P. C Yang, M. V. McConnell, N. D. G., H. Dai. FeCo/graphitic-shell nanocrystals as advanced magnetic-resonance-imaging and near-infrared agents. *Nature Mater.*, **2006**, *5*, 971–976.

[88] JCDD International Centre for Diffraction Data, *PDF Database*, Card No. 48-1818.

[89] G. Soler-Illia, E. L. Crepaldi, D. Grosso, D. Durand, C. Sanchez. Structural control in self-standing mesostructured silica oriented membranes and xerogels. *Chem. Commun.*, **2002**, 2298–2299.

[90] L. Malfatti, P. Falcaro, H. Amenitsch, S. Caramori, R. Argazzi, C. A. Bignozzi, S. Enzo, M. Maggini, P. Innocenzi. Mesostructured. Self-Assembled Titania Films for Photovoltaic Applications. *Micropor. Mesop. Mater.* **2005**, *88*, 304–311.

[91] K. O. Hill, Y. Fuji, D. C. Johnson, B. S. Kawasaki. Photosensitivity in optical fiber waveguides: Application to reflection filter fabrication. *Appl. Phys. Lett.* **1978**, *32*, 647-648.

[92] A. Othonos, K. Kalli, K. *Fiber Bragg Gratings: Fundamentals and Applications in Telecommunications and Sensing*; Artech House:Norwood, MA, **1999**; Chapter 2.

[93] Y. Hirai, T. Fukuda, K. Kubota. Optical properties of $SiO_2$-$GeO_2$ glasses made by sol-gel method. *J. Non-Cryst. Solids* **1987**, *93*, 431-435.

[94] T. Fujiwara, M. Takahashi, A. J. Ikushima. Second-harmonic generation in germanosilicate glass poled with ArF laser irradiation. *Appl. Phys. Lett.* **1997**, *71*, 1032-1034.

[95] H. Hosono, Y. Abe, D. L. Kinser, R. A. Weeks, K. Murata, H. Kawazoe. Nature and origin of the 5-eV band in $SiO_2$-$GeO_2$ glasses. *Phys. Rev. B* **1992**, *46*, 11445-11451.

[96] J. Nishii, K. Fukumi, H. Yamanaka, K. Kawamura, H. Hosono, H. Kawazoe. Photochemical reactions in $GeO_2$-$SiO_2$ glasses induced by ultraviolet irradiation: Comparison between Hg lamp and excimer laser. *Phys. Rev. B* **1995**, *52*, 1661-1665.

[97] A. Martucci, G. Brusatin, M. Guglielmi, C. Strohhofer, J. Fick, S. Pelli, G. C. Righini. Fabrication and characterization of sol-gel $GeO_2$-$SiO_2$ erbium-doped planar waveguides. *J. Sol-Gel Sci. Technol.* **1998**, *13*, 535-539.

[98] W. X. Que, X. Hu, Q. Y. Zhang. Germania/ormosil hybrid materials derived at low temperature for photonic applications. *Appl. Phys. B: Laser Opt.* **2003**, *76*, 423-427.

[99] Ho Rajni, K. Pita, S. C. Tjin, S. F. Yu, C. H. Kam. Enhanced photosensitivity in sol–gel derived $20GeO_2$:$80SiO_2$ thin films *Appl. Phys. A: Mater. Sci. Process.* **2006**, *82*, 535-541.

[100] B. Alonso, D. Dominique, F. Babonneau, G. Brusatin, G. Della Giustina, T. Kidchob, P. Innocenzi. Structural control in germania hybrid organic–inorganic materials. *Chem. Mater.* **2005**, *17*, 3172-3180.

[101] W. Que,X. Hu. Preparation and characterization of sol–gel processed $GeO_2$ / methyltrimethoxysilane hybrid thin films. *Opt. Mater.* **2004**, *27*, 273-277.

[102] J. H. Jang, J. Koo, B.-S. Bae. Fabrication and ultraviolet absorption of sol–gel-derived germanium oxide glass thin films. *J. Am. Ceram. Soc.* **2000**, *83*, 1356-1360.

[103] H. Kozuka. Stress evolution on gel-to-ceramic thin film conversion. *J. Sol-Gel Sci. Technol.* **2006**, *40*, 287-297.

[104] A Sakoh, M. Takahashi, T. Yoko, J. Nishii, H. Nishiyama, I. Miyamoto. Photochemical process of divalent germanium responsible for photorefractive index change in $GeO_2$-$SiO_2$ glasses. *Opt. Express* **2003**, *11*, 2679-2688.

[105] F. Kirkbir. Sol-gel process for forming a germania-doped silica glass rod. U.S. Patent 5,254,508, **1993**.

[106] K. E. Lipinska-Kalita. FT infrared and laser Raman spectroscopy of amorphous and crystalline germanates. *J. Non-Cryst. Solids* **1990**, *119*, 41-48.

[107] J. Nishii. Permanent index changes in Ge–$SiO_2$ glasses by excimer laser irradiation *Mater. Sci. Eng. B* **1998**, *54*, 1-10.

[108] H. Shigemura, Y. Kawamoto, J. Nishii, M. Takahashi. Ultraviolet-photosensitive effect of sol–gel-derived $GeO_2$–$SiO_2$ glasses. *J. Appl. Phys.* **1999**, *85*, 3413-3418.

[109] T. Uchino, M. Takahashi, T. Yoko. Structure and formation mechanism of Ge E′ center from divalent defects in Ge-doped $SiO_2$ glass. *Phys. Rev. Lett.* **2000**, *84*, 1475-1478.

[110] M. Takahashi, K. Ichii, Y. Tokuda, T. Uchino, T. Yoko, J. Nishii, T. Fujiwara. Photochemical reaction of divalent-germanium center in germanosilicate glasses under intense near-ultraviolet laser excitation: origin of 5.7 eV band and site

selective excitation of divalent-germanium center. *J. Appl. Phys.* **2002**, *92*, 3442-3446.

[111] D. Kuang, T. Brezesinski, B. Smarsly. Hierarchical porous silica materials with a trimodal pore system using surfactant templates. *J. Am. Chem. Soc.* **2004**, *126*, 10534-10535.

[112] O. Sel, A. Brandt, D. Wallacher, M. Thommes, B. Smarsly. Pore hierarchy in mesoporous silicas evidenced by in-situ SANS during nitrogen physisorption. *Langmuir* **2007**, *23*, 4724-4727.

[113] S. Tao, J. Yin, G. Li. High-performance TNT chemosensory materials based on nanocomposites with bimodal porous structures *J. Mater. Chem.* **2008**, *40*, 4872-4878.

[114] R. E. Williford, G. E. Fryxell, X. S. Li, R. S. Addleman. Mechanism of hierarchical porosity formation in silica thin films using cellulose nitrate. *Microporous Mesoporous Mater.* **2005**, *84*, 201-210.

[115] K. Nakanishi, Y. Kobayashi, T. Amatani, K. Hirao, T. Kodaira. Spontaneous formation of hierarchical macro–mesoporous ethane–silica monolith. *Chem. Mater.* **2004**, *16*, 3652-3658.

[116] B. Smarsly, S. Polarz, M. Antonietti. Preparation of porous silica materials via sol–gel nanocasting of nonionic surfactants: a mechanistic study on the self-aggregation of amphiphiles for the precise prediction of the mesopore size. *J. Phys. Chem. B* **2001**, *105*, 10473-10483.

[117] F. Li, Z. Wang, N. S. Ergang, C. A. Fyfe, A. Stein. Controlling the shape and alignment of mesopores by confinement in colloidal crystals: designer pathways to silica monoliths with hierarchical porosity. *Langmuir* **2007**, *23*, 3996-4004.

[118] M. Antonietti, B. Berton, C. Goltner, H. P. Hentze. Synthesis of mesoporous silica with large pores and bimodal pore size distribution by templating of polymer latices. *Adv. Mater.* **1998**, *10*, 154-159.

[119] N. B. Colthup, L. H. Daly, S. E. Wiberley. *Introduction to Infrared and Raman Spectroscopy*. **1990,** San Diego, Academic Press.

[120] T. Maruo, S. Tanaka, H. W. Hillhouse, N. Nishiyama, Y. Egashira, K. Ueyama. Disordered mesoporous silica low-k thin films prepared by vapor deposition into a triblock copolymer template film. *Thin Solid Films* **2008**, *516*, 4771-4776.

[121] A.-L. Pénard, T. Gacoin, J.-P. Boilot. Functionalized sol–gel coatings for optical applications. *Acc. Chem. Res.* **2007**, *40*, 895-902.

[122] D. Konjhodzic, H. Bretinger, U. Wilczok, A. Dreier, A. Ladenburger, M. Schmidt, M. Eich, F. Marlow. Low-*n* mesoporous silica films: structure and properties. *Appl. Phys. A: Mater. Sci. Process.* **2005**, *81*, 425-432.

[123] A. R. Balkenende, F. K. De Theije, J. C. K. Kriege. Controlling dielectric and optical properties of ordered mesoporous organosilicate films. *Adv. Mater.* **2003**, *15*, 139-143.

[124] B. D. Hatton, K. Landskron, W. J. Hunks, M. R. Bennett, D. Shukaris, D. D. Perovic, G. A. Ozin. Materials chemistry for low-k materials. *Mater. Today* **2006**, *9*, 22-31.

[125] D. Grosso, C. Boissiere, C. Sanchez. Ultralow-dielectric-constant optical thin films built from magnesium oxyfluoride vesicle-like hollow nanoparticles *Nat. Mater.* **2007**, *6*, 572-575.

[126] G. J. A. A. Soler-Illia, E. Crepaldi, D. Grosso, C. Sanchez. Block copolymer-templated mesoporous oxides. *Current Op. Colloid Interf. Sci.* **2003**, *8*, 109-126.

[127] M. Tortajada, D. Ramòn, D. Beltràn, P. Amoròs. Hierarchical bimodal porous silicas and organosilicas for enzyme immobilization. *J. Mater. Chem.* **2005**, *15*, 3859-3868.

[128] A. Fischer, M. Kuemmel, M. Järn, M. Lindén, C. Boissière, L. Nicole, C. Sanchez, D. Grosso. Surface nanopatterning by organic/inorganic self-assembly and selective local functionalization *Small* **2006**, *4*, 569-574.

[129] T. Brezesinski, M. Groenewolt, A. Gibaud, N. Pinna, M. Antonietti, B. M. Smarsly. Evaporation-Induced Self-Assembly (EISA) at its limit: ultrathin, crystalline patterns by templating of micellar monolayers. *Adv. Mater.* **2006**, *18*, 2260-2263.

[130] P. Yang, T. Deng, D. Y. Zhao, P. Feng, D. Pine, B. Chmelka, G. M. Whitesides, G. D. Stucky. Hierarchically Ordered Oxides. *Science* **1998**, *282*, 2244-2246.

[131] M. C. Fuertes, G. J. A. A. Soler-Illia. Processing of macroporous titania thin films: from multiscale functional porosity to nanocrystalline macroporous $TiO_2$. *Chem. Mater.* **2006**, *18*, 2109-2117.

[132] A. Bouchara, G. J. A. A. Soler-Illia, J.-Y. Chane-Ching, C. Sanchez. Nanotectonic approach of the texturation of $CeO_2$ based nanomaterials *Chem. Commun.* **2002**, 1234-1235.

[133] Y. Sakatani, C. Boissière, D. Grosso, L. Nicole, G. J. A. A. Soler-Illia, C. Sanchez. Coupling nanobuilding block and breath figures approaches for the

designed construction of hierarchically templated porous materials and membranes. *Chem. Mater.* **2008**, *20*, 1049-1056.

[134] J. D. Bass, D. Grosso, C. Boissière, E. Belamie, T. Coradin, C. Sanchez. Stability of mesoporous oxide and mixed metal oxide materials under biologically relevant conditions. *Chem. Mater.* **2007**, *19*, 4349-4356.

[135] S. Y. Choi, B. Lee, D. B. Carew, M. Mamak, F. C. Peiris, S. Speakman, N. Chopra, G. A. Ozin. 3D Hexagonal (*R3m*) Mesostructured Nanocrystalline Titania Thin Films: Synthesis and Characterization . *Adv. Funct. Mater.* **2006**, *16*, 1731-1738.

[136] http://rsbweb.nih.gov/ij/ (accessed November 2009)

[137] K. Nakanishi. Pore structure control of silica gels based on phase separation. *J. Porous Mater.* **1997**, *4*, 67-112.

[138] O. Sterner. *Chemistry Health and the Environment*, **1999**, p 42, Wiley, Weinheim.

[139] X. Jiang, C. J. Brinker. Aerosol-assisted self-assembly of single-crystal core/ nanoporous shell particles as model controlled release capsules *J. Am. Chem. Soc.* **2006**, *128*, 4512-4513.

# 4. Conclusions

During the three years of this doctoral work we have tried to explore the most important aspects and potentialities offered by mesoporous thin films. These systems, in fact, give the possibility to tailor several of their characteristic features such as chemical composition of the pore walls, pore structure and arrangement making them ideal matrixes for host-guest systems with organic or inorganic functionalities into the pores. We started from *in situ* experiments in order to increase the basic knowledge of the evaporation-induced self-assembly process and reveal the chemical behaviour of the pore walls, then we gave an attempt to exploit the mesoporous materials by functionalization with dyes, organic photoactive molecule and inorganic complexes. We also tried to use the porous organized phase as a nanoreactor for controlled growth of nanoparticles. The particular morphology of porous ordered thin films gave us the opportunity to use the high surface area and tunable chemical composition of the inorganic pore walls in order to prepare photoactive films that could be useful for optical applications. Finally we explored the possibility of inducing more than one degree of self-organization in the same film. This approach, which is a natural evolution of evaporation-induced self-assembly, led to hierarchical porous thin films that were prepared following different strategies; from direct templating, to controlled phase separation until controlled nanocrystallization.

The obtained results show the versatility of the mesoporous thin films and, more in general, the EISA technique to produce advanced functional materials with a wide range of tunability in terms of properties and morphology. These results justify the increasing interest that mesoporous systems are knowing in the last years.

We think new important achievements in the field of nanotechnology will be obtained by pushing the self-assembly techniques beyond their actual limits and combining *bottom-up* and *top-down* techniques to envisage new fabrication technologies of functional multiporous materials.

# Appendix

## Publications in peer review journals

1. *Highly ordered self-assembled mesostructured hafnia thin films: an entropy driven rewritable mesostructure* L. Malfatti, T. Kidchob, S. Costacurta, P. Falcaro, P. Schiavuta, H. Amenitsch, P. Innocenzi **Chemistry of Materials** 2006, 18, 4553-4560.
2. *Thermal Stability of Lysozyme Langmuir-Schaefer Films by FTIR Spectroscopy* E. Pechkova, P. Innocenzi, L. Malfatti, T. Kidchob, L. Gaspa, C. Nicolini **Langmuir** 2007, 23, 1147-1151.
3. *Hafnia sol-gel films synthesised from $HfCl_4$: changes of structure and properties with the temperature* T. Kidchob, L. Malfatti, F. Serra, P. Falcaro, S. Enzo, P. Innocenzi **Journal of Sol-Gel Science and Technology** 2007, 42, 89–93.
4. *Highly ordered self-assembled mesostructured membranes: Porous structure and pore surface coverage* L. Malfatti, T. Kidchob, P. Falcaro, S. Costacurta, M. Piccinini, M. C. Guidi, A. Marcelli, A. Corrias, M. F. Casula, H. Amenitsch, P. Innocenzi **Microporous and Mesoporous Materials** 2007, 103, 113-122.
5. *Time-Resolved Simultaneous Detection of Structural and Chemical Changes during Self-Assembly of Mesostructured Films* P. Innocenzi, L. Malfatti, T. Kidchob, S. Costacurta, P. Falcaro, M. Piccinini, A. Marcelli, P. Morini, D. Sali, H. Amenitsch **Journal of Physical Chemistry C** 2007, 111, 5345-5350.
6. *Photocurable silica hybrid organic-inorganic films for photonic applications* S. Costacurta, L. Malfatti, P. Falcaro, P. Innocenzi **Journal of Sol-Gel Science and Technology** 2007, 44, 59–64.
7. *Confined growth of iron cobalt nanocrystals in mesoporous silica thin films: $FeCo$-$SiO_2$ nanocomposites* S. Costacurta, L. Malfatti, P. Innocenzi, H. Amenitsch, A. Masili, A. Corrias, M. F. Casula **Microporous and Mesoporous Materials** 2008, *115*, 338.
8. *Self-Assembled Mesoporous Silica−Germania Films* S. Costacurta, L. Malfatti, T. Kidchob, M. Takahashi, G. Mattei, V. Bello, C. Maurizio, P. Innocenzi, **Chemistry of Materials** 2008, *20*, 3259.
9. *In-situ study of sol–gel processing by time-resolved infrared spectroscopy* P. Innocenzi, T. Kidchob, L. Malfatti, S. Costacurta, M. Takahashi, M. Piccinini, A. Marcelli, **Journal of Sol-Gel Science and Technology**, 2008, 48, 253.
10. *Mesoporous Aluminophosphate Thin Films with Cubic Pore Arrangement* M. Mazaj, S. Costacurta, N. Zabukovec Logar, G. Mali, N. Novak Tušar, P. Innocenzi, L. Malfatti, F. Thibault-Starzyk, H. Amenitsch,V. Kaucic, G. J. A. A. Soler-Illia, **Langmuir** 2008, 24, 6220.
11. *Bottom-up and top-down approach for periodic microstructures on thin oxide films by controlled photo-activated chemical processes* M. Takahashi, K. Uemura, T. Maeda, J. Yao, Y. Tokuda, T. Yoko, S. Costacrta, L. Malfatti, P. Innocenzi, **Journal of Sol-Gel Science and Technology**, 2008, 48, 182.
12. *Fabrication of Mesoporous Functionalized Arrays by Integrating Deep X-Ray Lithography with Dip-Pen Writing* P. Falcaro, S. Costacurta, L. Malfatti, M.

Takahashi, T. Kidchob, M. F. Casula, M. Piccinini, A. Marcelli, B. Marmiroli, H. Amenitsch, P. Schiavuta, P. Innocenzi, **Advanced Materials**, 2008, 20, 1864.

13. *Blue-emitting mesoporous films prepared via incorporation of luminescent Schiff base zinc(II) complex* D. Aiello, L. Malfatti, T. Kidchob, R. Aiello, F. Testa, I. Aiello, M. Ghedini, M. La Deda, T. Martino, M. Casula, P. Innocenzi **Journal of Sol-Gel Science and Technology**, 2008 47, 283
14. *Evaporation of Ethanol and Ethanol−Water Mixtures Studied by Time-Resolved Infrared Spectroscopy* P. Innocenzi, L. Malfatti, S. Costacurta, T. Kidchob, M. Piccinini, A. Marcelli **Journal of Physical Chemistry A**, 2008, 112, 6512.
15. *Aggregation States of Rhodamine 6G in Mesostructured Silica Films* L. Malfatti, T. Kidchob, D. Aiello, R. Aiello, P. Innocenzi **Journal of Physical Chemistry C,** 2008, *112*, 16225.
16. *Stain Effects Studied by Time-Resolved Infrared Imaging* P. Innocenzi, L. Malfatti, M. Piccinini, D. Grosso, A. Marcelli, **Analytical Chemistry,** 2009, 81, 551-556
17. *Mesostructured self-assembled silica films with reversible thermo-photochromic properties* L. Malfatti, S. Costacurta, T. Kidchob, P. Innocenzi, M. Casula, H. Amenitsch, D. Dattilo, M. Maggini **Microporous and Mesoporous Materials** 2009, 120, 375-380.
18. *Absolute emission quantum yield determination of self-assembled mesoporous titania films grafted with a luminescent zinc complex* D. Aiello, F. Testa, R. Aiello, L. Malfatti, T. Kidchob, P. Innocenzi, I. Aiello, T. Martino, M. La Deda **Inorganic Chemistry Communications**, 2009 12, 237-239.
19. *Water Evaporation Studied by In Situ Time-Resolved Infrared Spectroscopy* P. Innocenzi, L. Malfatti, M. Piccinini, A. Marcelli, D. Grosso **Journal of Physical Chemistry A,** 2009, 113, 2745-2749.
20. *Hierarchical Porous Silica Films with Ultralow Refractive Index* P. Falcaro, L. Malfatti, T. Kidchob, G. Giannini, A. Falqui, M. F. Casula, H. Amenitsch, B. Marmiroli,G. Grenci, P. Innocenzi **Chemistry of Materials** 2009, *21*, 2055-2061.
21. *Order-Disorder in Self-Assembled Mesostructured Silica Films: A Concepts Review* P. Innocenzi, L. Malfatti, T. Kidchob, P. Falcaro **Chemistry of Materials** 2009, *21,* 2555.
22. *A one-pot route to produce hierarchically porous titania thin films by controlled self-assembly, swelling and phase separation* L. Malfatti, M. G. Bellino, P. Innocenzi, G. J. A. A. Soler-Illia **Chemistry of Materials** 2009, *21*, 2763-2769.
23. *Application Of Terahertz Spectroscopy To Time dependent Chemical-Physical Phenomena* P. Innocenzi, L. Malfatti, M. Piccinini, D. Salic, U. Schaded, A. Marcelli **Journal of Physical-Chemistry A** 2009, *113*, 9418–9423.
24. *SR a brilliant sources for solid-state researches in the IR energy domain* A. Marcelli, M. C. Guidi, M. Piccinini, P. Innocenzi, L. Malfatti, W. Xu **Physica Status Solidi C** 2009, *6*, 1999-2007.
25. *Formation of cerium titanate, $CeTi_2O_6$, in sol–gel films studied by XRD and FAR infrared spectroscopy* T. Kidchob, L. Malfatti, D. Marongiu, S. Enzo, P. Innocenzi **Journal of Sol-Gel Science and Technology** 2009, *52*, 356-361.
26. *Self-assembly of Shape Controlled Hierarchical Porous Thin Films: Mesopores and Nano-boxes* L. Malfatti, P. Falcaro, D. Marongiu, M. F. C., H. Amenitsch, P. Innocenzi. **Chemistry of Materials** 2009, *21*, 4864-4850.
27. *Fabrication of Advanced Functional Devices Combining Soft Chemistry with X-ray Lithography in One Step* P. Falcaro, L. Malfatti, L. Vaccari, H. Amenitsch, B. Marmioli, G. Grenci, P. Innocenzi **Advanced Materials** 2009, *21*, 4932–4936.